

SEARCH FOR HEAVY TOP QUARK PARTNERS WITH CHARGE 5/3 AND ANOMALOUS HIGGS ($\rightarrow b\bar{b}$) COUPLINGS TO VECTOR BOSONS

by

Sinan Sagir

M.Sc. in Physics, Brown University, 2013

B.Sc. in Physics, Selcuk University, 2008

A DISSERTATION SUBMITTED IN PARTIAL FULFILLMENT OF THE REQUIREMENTS

FOR

THE DEGREE OF DOCTOR OF PHILOSOPHY

IN THE DEPARTMENT OF PHYSICS AT BROWN UNIVERSITY

Providence, Rhode Island

May 2017



© Copyright 2017 by Sinan Sagir

Abstract of “Search for Heavy Top Quark Partners with Charge 5/3 and Anomalous Higgs ($\rightarrow b\bar{b}$) Couplings to Vector Bosons ” by Sinan Sagir, Ph.D., Brown University, May 2017

In this thesis, we present two searches for new physics performed using the data collected by the CMS experiment at the LHC at two different center of mass energies.

In the first part, we present a search for anomalous Higgs couplings. In 2012, the ATLAS and CMS experiments at the LHC discovered a new boson. This discovery completed a long search for the final missing piece of the standard model (SM). The measurements so far confirm that the new boson is consistent with the Higgs boson predicted by the SM. However, there are decay channels that are yet to be confirmed experimentally; e.g., the decay to a pair of bottom quarks. In addition, precision measurements of the Higgs couplings to all SM particles need to be performed in order to make sure there is no deviation from the predictions of the SM. We present the first search at the LHC for anomalous couplings of the Higgs boson H to vector bosons V ($= W$ or Z) using associated Higgs production with the Higgs boson decaying to a pair of bottom quarks. We use the data collected with the CMS detector from proton-proton collisions in 2012 at a center of mass energy of 8 TeV. Even though the exclusion limit derived from this production channel alone is at the 68% CL using the 2012 data, we demonstrate the power of this channel in constraining very small anomalous Higgs couplings to vector bosons. Combining the results from this channel with the previously published $H \rightarrow VV$ channels, we put more stringent constraints on anomalous Higgs couplings to vector bosons.

The second part of the thesis deals with the so called hierarchy problem, caused by quadratically divergent radiative corrections to the Higgs mass at higher energy scales. The corrections are many orders of magnitude larger than the observed mass and it requires unnatural fine-tuning to cancel out these contributions. There are different models that attempt to address this problem, one of which is the Composite

Higgs Model that predicts a very heavy fermionic partner of the top quark with an electric charge of $5/3$ ($X_{5/3}$). $X_{5/3}$ decays into a W boson and a top quark, which then decays into a bottom quark and a W boson. We analyze the events in which one of the W bosons in the $X_{5/3}$ pair production final state decays into leptons and the remaining three W's decay hadronically. We present here the first study of $X_{5/3}$ at the LHC in the lepton + jets decay channel using events from the data collected in 2015 with the CMS detector at a center of mass energy of 13 TeV in Run 2 of the LHC. The results are also combined with the more sensitive same-sign dilepton channel.

This dissertation by Sinan Sagir is accepted in its present form by
the Department of Physics as satisfying the
dissertation requirement for the degree of
Doctor of Philosophy

Date
Meenakshi Narain, Advisor

Recommended to the Graduate Council

Date
Ulrich Heintz, Reader

Date
David Cutts, Reader

Approved by the Graduate Council

Date
Andrew G. Campbell
Dean of the Graduate School

Sinan Sagir

Curriculum Vitae

Physics Department
Barus and Holley Building
Brown University
182 Hope Street
Providence, RI 02906

Sinan_Sagir@brown.edu
sinan.sagir@cern.ch
s.sagir42@gmail.com
401-863-6788 (office)
205-413-9296 (cell)

Education

- **Brown University**, Graduate Studies in Physics, Providence, RI
 - Doctor of Philosophy in Physics, Sep 2013 – August 2016
 - * Thesis: “Search for Heavy Top Quark Partners with Charge 5/3 and Anomalous Higgs ($\rightarrow b\bar{b}$) Couplings to Vector Bosons”
 - * Advisor: Prof. Meenakshi Narain
 - Master of Science in Physics, Sep 2011 – May 2013
- **Selcuk University**, Faculty of Arts and Sciences, Konya, TURKEY
 - Bachelor of Science in Physics with Honors, Sep 2004 – July 2008

Research Experience

- **Search for Heavy Fermionic Top Quark Partners with Charge 5/3**

A new boson has been discovered at the LHC by both ATLAS and CMS experiments. Studies so far have shown that the new boson is as predicted by the SM. However, the mass of this particle (125 GeV) is significantly lighter than new physics scales and causes the so called Hierarchy problem. There are different models that attempt to address this problem, one of which is the Composite

Higgs Model that predicts a very heavy fermionic partner to top quark with a charge of $5/3$ ($X_{5/3}$). With this motivation, I have led a search for this particle where it is produced in pairs at center-of-mass energy of $\sqrt{s} = 13$ TeV with the CMS detector in Run 2 of LHC using the data collected in 2015. $X_{5/3}$ is expected to decay into a W boson and a top quark, which then decays into a bottom quark and a W boson. We analyze the events where one of the W bosons in the final state decays into a lepton and a neutrino and the rest of the three W's decay hadronically. This is the first study of $X_{5/3}$ at the LHC using the semi-leptonic decay channel. The results are combined with the more sensitive same-sign dilepton channel and presented in a Physics Analysis Summary (PAS). Recently, we have also implemented the top tagging in the analysis and improved the contribution from semi-leptonic channel.

- **Search for Vector-Like Quarks**

Another model that attempts to address the Hierarchy problem is the Little Higgs Model, which predicts vector-like quarks. One of the particles predicted in this model is T' , which decays into a b-quark and a W boson, a top quark and a Z boson, or a top quark and a Higgs boson. Building on the experience on the $X_{5/3}$ search, I made significant contributions to this analysis in the single lepton channel and we have extended the search conducted in Run 1 of the LHC using 8 TeV data. Using the single lepton channel alone and the data collected in 2015 at $\sqrt{s} = 13$ TeV with the CMS detector, we were able to put stronger limits on the T' mass and the results are presented in a Physics Analysis Summary.

- **Search for Anomalous HVV Couplings**

With the discovery of a new particle at the Large Hadron Collider (LHC) in 2012, the focus of interest now moved on to understanding the physics behind this particle, in particular whether it is the Higgs boson as predicted by the standard model (SM) or it has some theory beyond the SM. In order to find out if it is a Higgs boson or the Higgs boson, we need to characterize its full properties such as spin and parity. The studies so far have shown that the new particle is a scalar particle with a spin of 0 as predicted by the SM. However, these results did not exclude very small anomalous couplings to other particles. In this work, we search for anomalous Higgs couplings to vector bosons in VH associated Higgs production channel with Higgs decaying to a pair of bottom quarks and vector boson decaying leptonically using the data collected with the Compact Muon Solenoid (CMS) detector at the LHC from proton-proton collisions in 2012 at center-of-mass energy of $\sqrt{s} = 8$ TeV. We demonstrate that the VH channel is very powerful to put limits on very small anomalous Higgs couplings to vector bosons. This analysis is the first study of anomalous Higgs couplings at the LHC in VH associated Higgs production channel and the first study in Higgs fermionic decay channel. The resulting paper is published in PLB.

- **Radiation Hard Detectors for Phase-II Upgrade of CMS Detector**

This project is a research into the development of radiation hard silicon sensors to be used in the CMS tracker during the high luminosity phase of the LHC (HL-LHC) that will take place after 2020. Given the very high radiation environment with increased luminosity, it is very crucial to develop new sensor technologies as the current detector will not be able to survive in the presence of high radiation conditions during HL-LHC. To contribute to this project as part of the large CMS collaboration, together with my colleagues, I have built experimental setups at Brown University to perform tests on prototype silicon detectors and to investigate their radiation hardness. We have studied more than 60 sensors on these experimental setups both before and after 800 MeV proton irradiations at LANSCE (Los Alamos National Lab). We have also extended our studies by performing an isothermal annealing study at different temperatures. The results of these studies help understand more about the radiation damage dependency on particle type (protons, neutrons, muons) and/or different energies (23MeV and 23GeV). This work has been presented at different workshops and meetings.

- **Monitoring, Commissioning and Maintenance of the CMS Strip Tracker**

CMS strip tracker is an important part of the CMS detector. It is built at the innermost layer of the CMS detector, providing the tracks of particles originating from the proton-proton collisions and assigning vertex that is very important for physics analyses. Being very close to the interaction point, it is exposed to very high radiation. In order to make sure that CMS detector provides high quality data that is crucial for physics analyses, the tracker needs to be monitored. We perform simulations of different detector properties using the temperature and fluence history of the CMS strip tracker. These simulations are then compared to real measurements to determine the performance of the detector. We later use these simulations to estimate detector lifetime and improve the annealing so that the tracker will continue taking high quality data for a longer term. These simulations are also important for testing models that are developed from experimental studies and the results of our experimental studies on prototype silicon detectors are directly applicable in this project.

- **Simulations of New Sensor Designs for Phase-II Upgrade of CMS Detector**

Another important part of sensor development for the Phase-II upgrade of the CMS detector is to perform simulations on different design technologies. These simulations provide us more information on how to improve our designs and understand more about the radiation damage in silicon detectors. I have been involved in simulations of different sensor structures on new wafer designs that can be a potential candidate for high energy physics detectors in future colliders. These wafer designs are already manufactured by Novati Technologies and I have performed quality measurements using our experimental setups at Brown

Silicon Lab. The results of these measurements are very useful for improving the wafer designs.

Publications

- CMS Collaboration, “Search for top quark partners with charge $5/3$ at $\sqrt{s} = 13$ TeV,” in preparation, (2016).
- CMS Collaboration, “Combined search for anomalous pseudoscalar HVV couplings in VH production and $H \rightarrow VV$ decay,” arXiv:1602.04305, Phys. Lett. B759 (2016).
- B. Asavapibhop, A. Garabedian, U. Heintz, A. Junkes, M. Narain, S. Sagir, N. Sophonrat and D. Tersegno, “Effect of A Double Metal Layer on the Performance of CMS Silicon Sensors: A Preliminary Study,” in *Thai Journal of Physics (TJP)* 10, 24001, (Jun 2014).
- Co-author of the CMS Collaboration since 2015. See SPIRE for the full list of publications in refereed journals.

CMS Physics Analysis Summaries

- CMS Collaboration, “Search for pair production of vector-like T quarks in the lepton plus jets final state,” CMS Physics Analysis Summary CMS PAS B2G-16-002 (2016).
- CMS Collaboration, “Search for top quark partners with charge $5/3$ at $\sqrt{s} = 13$ TeV,” CMS Physics Analysis Summary CMS PAS B2G-15-006 (2015).

CMS Analysis Notes

- “Search for heavy top quark partners with charge $5/3$ in the single lepton final state with boosted top tagging,” CMS AN-16-205, June 2016.
- “Search for top quark partners with charge $5e/3$ in the same-sign dilepton final state with the CMS detector,” CMS AN-16-210, June 2016.
- “Search for pair production of a vector-like T quark in the single lepton final state,” CMS AN-15-161, March 2016.
- “Search for heavy top quark partners with charge $5e/3$ in the single lepton final state,” CMS AN-15-171, December 2015.
- “Search for top quark partners with charge $5e/3$ in the same-sign dilepton final state with the CMS detector,” CMS AN-15-148, December 2015.

- “Search for anomalous HVV couplings in associated Higgs production with $h \rightarrow b\bar{b}$,” CMS AN-14-127, November 2015.

Presentations

- S. Sagir, “Search for heavy top quark partners with charge $5e/3$ in the single lepton final state,” in *APS April Meeting*, Salt Lake City, UT, USA, April 2016.
- C. Barth, E. Butz, M. Narain, S. Sagir, D. Zhong, “CMS Silicon Strip Tracker: Radiation Damage Monitoring: Leakage Current,” in *Tracker DPG - Tracking POG General Meeting*, CERN, Geneva, SWITZERLAND, Sep 2015 and Mar 2016.
- A. Avetisyan, T. Bose, U. Heintz, J. Hogan, M. Narain, C. Richardson, S. Sagir, “Search for heavy top quark partners with charge $5e/3$ in the single lepton final state,” in *CMS Physics Week (B2G-15-006 Lepton + Jets Approval Presentation)*, CERN, Geneva, SWITZERLAND, Dec 2015.
- A. Avetisyan, T. Bose, U. Heintz, J. Hogan, M. Narain, C. Richardson, S. Sagir, “Search for heavy top quark partners with charge $5e/3$ in the single lepton final state,” in *B2G (B2G-15-006 Lepton + Jets Pre-approval Presentation)*, CERN, Geneva, SWITZERLAND, Nov 2015.
- A. Avetisyan, T. Bose, U. Heintz, J. Hogan, M. Narain, C. Richardson, S. Sagir, “ $X5/3$ in single lepton final state,” in *B2G/TOP Run2 Workshop*, CERN, Geneva, SWITZERLAND, Oct 2015.
- N. Bower, U. Heintz, N. Khishigsuren, M. Narain, S. Sagir, E. Spencer, J. Trenado, “Measurements on 8” Novati Wafer,” in *US-CMS Outer Tracker Workshop*, Brown University, Providence, RI, USA, June 2015.
- J. Berryhill, A. Garabedian, B. Kreis, J. Li, Q. Li, J.F. Low, Y. Mao, M. Narain, N. Parashar, S. Sagir, J. Stupak III, N. Tran, C. Vernieri, Q. Wang, A. Whitbeck, M. Xiao, Z. Xu, “Search for Anomalous HVV Couplings in $VH(b\bar{b})$,” in *US-CMS Annual Meeting*, Cornell University, Ithaca, NY, USA, May 2015.
- S. Sagir, “Search for anomalous HVV couplings in associated Higgs production with $H \rightarrow b\bar{b}$,” in *APS April Meeting*, Baltimore, MD, USA, April 2015.
- B. Asavapibhop, A. Garabedian, U. Heintz, A. Junkes, M. Narain, S. Sagir, N. Sophonrat and D. Tersegno, “Effect of Double Metal Layer on the Performance of CMS Silicon Sensors: A Preliminary Study,” in *SPC2014: Siam Physics Congress*, Rajamangala University of Technology Isan, Nakhon Ratchasima, Thailand, March 2014.
- S. Sagir, Z. Mao, A. Junkes, U. Heintz, M. Narain, A. Garabedian, “Radiation Damage Induced by 800 MeV Protons in Silicon PAD Diodes,” in *22nd RD50 Workshop*, Albuquerque, NM, USA, June 2013.

- S. Sagir, “A Study of the Charge Collection Efficiency (CCE) of the Silicon Detectors (Poster Presentation),” in *Turkish Physical Society 27th International Physics Congress*, Istanbul, Turkey, Sep 2010.
- Several related presentations at various CMS internal meetings and workshops.

Workshops & Schools

- The European School of High-Energy Physics (ESHEP), Skeikampen, NORWAY, 15-28 June 2016.
- CMS Data Analysis School (CMSDAS), Fermi National Lab., Batavia, IL, USA, Jan 2016 (Facilitator).
- Computing and Applications in Accelerator and Particle Physics IV (HPFBU IV), Anadolu University, Eskisehir, TURKEY, Feb 2015.
- CMS Data Analysis School (CMSDAS), Fermi National Lab., Batavia, IL, USA, Jan 2015 (Facilitator).
- Beyond Standard Model (BSM) Higgs Workshop at LPC, Fermi National Lab., Batavia, IL, USA, Nov 2014.
- Tracker Upgrade + Hardware "experience" HATS@LPC, Fermi National Lab., Batavia, IL, USA, July 2014 (Facilitator).
- Statistics HATS@LPC, Fermi National Lab., Batavia, IL, USA, June 2014.
- CMS Data Analysis School (CMSDAS), Fermi National Lab., Batavia, IL, USA, Jan 2014.
- CMS Data Analysis School (CMSDAS), Fermi National Lab., Batavia, IL, USA, Jan 2012.
- CERN International Summer Student Programme for Non-Member State Students, CERN, Geneva, SWITZERLAND, June 2009 – Aug 2009.
- GSI International Summer Student Programme, GSI, Darmstadt, GERMANY, Aug 2008 – Sep 2008.

Work Experience

- Research Assistant, Brown University, Department of Physics, Providence, RI, USA, Sep 2012 – Present.

- 2012 – 2015 Organized the research activities in Silicon Lab at Brown University and supervised several Brown University undergraduates which provided them an opportunity to contribute to a research in their early career in physics. During this time, I also helped with the thesis work of two master’s students.
 - Feb 2016 – May 2016 Supervised Brown University undergraduate Joseph Van der List on the implementation of top tagging in heavy top quark partner search with charge $5e/3$ in single lepton channel. This work became his senior thesis.
 - Sep 2015 – May 2016 Supervised Brown University graduate student Dewen Zhong on the leakage current monitoring and simulation of the CMS Strip Tracker.
- Research & Teaching Assistant, Selcuk University, Department of Physics, Konya, TURKEY, Dec 2008 – Sep 2010.

Professional Affiliations

- Full Member of Society of the Sigma Xi, Brown Chapter (nominated by the Brown University Physics Department), 2016 – Present.
- Member of American Physical Society (APS), 2011 – Present.

Awards

- LPC Guests and Visitors program, 2015.
- LPC Guests and Visitors program, 2014.
- Graduate Research Fellowship, Brown University, 2011 – 2016.
- Scholarship for M.Sc. and Ph.D. studies in the USA, Turkish Ministry of Education, 2010 – 2016.

Languages

- Turkish: Mother tongue.
- English: Fluent.

Skills

- ROOT, C++, Python, LabVIEW, UNIX, L^AT_EX, MATLAB, Fortran, Mathematica, TCAD, CTSim, SIMION 3D

Preface and Acknowledgments

A lot of people have contributed in one way or another to the completion of this thesis. It is impossible to thank everyone individually; however, I would like to mention a few of them.

First and foremost, I would like to thank my advisor Professor Meenakshi Narain for her continuous support during my studies both at Brown University and CMS collaboration. I have learned a great deal from her knowledge, experience, and wisdom and admire her dedication to her students' education. I'm especially grateful for the excellent research opportunities that she provided me. I have greatly enjoyed my time working with her.

I would like to thank the rest of my thesis committee, Professors David Cutts and Ulrich Heintz for being in my committee and all the useful advice they gave me. The detailed comments they provided helped highly improve both the writing and presentation of this dissertation. I worked very closely with Professor Heintz throughout my studies at Brown and I would like to mention that I am grateful for his support and sharing his knowledge and wisdom.

I would like to thank everyone in the large CMS collaboration for their hard work in running the experiment throughout the years and helping to collect the data used in this thesis.

From Brown Silicon Lab, I would like to thank my colleagues Alex Garabedian, Robert Harrington, Alexandra Junkes, Zaixing Mao, Nanta Sophonrat, Eric Spencer,

Juan Trenado, and Brown undergraduates who performed a lot of measurements, in particular, Jamelle Watson-Daniels, Nomin Khishigsuren, Joseph van der List, and Jovan Nelson. I would also like to thank Christian Barth and Erik Butz for their help with the radiation damage simulations of the CMS Strip Tracker.

During my anomalous Higgs coupling studies, I worked with post-docs at Fermilab. In particular, I would like to thank Ben Kreis, John Stupak, and Nhan V. Tran for their great collaboration. I've learned a great deal from them about CMS software tools and programming, physics data analysis, or physics in general.

From my X5/3 search, I would like to thank Julie Hogan, and our colleagues from Boston University; Clint Richardson and Tulika Bose. I am in particular grateful to Professor Narain and Julie for their tireless help while I was working day and night on the first 13 TeV physics results with very tight deadlines.

I also would like to thank the rest of my colleagues at Brown who are not mentioned above; in particular, Juliette Alimena, Altan Allawalla, Saptaparna Bhattacharya, Mary Hadley, Edward Laird, Jangbae Lee, and Rizki Syarif. Barbara Dailey had been very helpful with handling my administrative paperwork, especially by smoothly resolving conflicts between my scholarship and Brown administrative rules and I owe thanks to her. I also thank to Professor Valles for his encouragement.

Last but not least, I would like to thank my parents and family for raising and supporting me all these years. Even though they were physically apart, I have always felt their support. Finally, I thank to Habibe for her constant support, encouragement, and love throughout my life both within and outside physics.

Contents

Curriculum Vitae	iv
Preface and Acknowledgments	xi
Contents	xiii
List of Tables	xviii
List of Figures	xxi
1 Theory Background	1
1.1 The Standard Model of Particles	1
1.1.1 Particle Families	2
1.1.2 Particle Interactions	4
1.1.2.1 Strong Interactions	5
1.1.2.2 Electroweak Interactions	5
1.2 Electroweak Symmetry Breaking and the Higgs Boson	7
1.3 The Hierarchy Problem	10
2 The Compact Muon Solenoid Experiment at the Large Hadron Col-	
lider	13
2.1 The Large Hadron Collider	13
2.2 The Compact Muon Solenoid	17

2.2.1	Tracker	19
2.2.2	Electromagnetic Calorimeter	21
2.2.3	Hadronic Calorimeter	23
2.2.4	Muon System	25
2.2.5	Trigger System	27
3	Radiation Damage Monitoring of Leakage Currents in the CMS	
	Strip Tracker	28
3.1	Parameterization of leakage current evolution with fluence and annealing	29
3.2	Monitoring tools in the CMS tracker	31
3.3	Simulation Tool	32
3.3.1	Fluence Estimation	33
3.3.2	Temperature Estimation	34
3.4	Comparison of simulated and measured leakage currents	37
3.4.1	Correlation on a given date	37
3.4.2	Evolution in time	38
3.4.3	Evolution with luminosity	38
3.5	Investigation of outlier modules	45
4	Radiation Damage Studies for the CMS Strip Tracker	49
4.1	LHC Operations and Upgrades	49
4.2	Phase-II Upgrade of the CMS Strip Tracker	50
4.3	Test Structures and Irradiations	51
4.4	Experimental Setup	52
4.5	Depletion Voltage	54
4.6	Annealing	55
4.7	Hamburg Model	58
4.8	Damage Rate	62

4.9	Effective Doping Concentration	64
4.10	Comparison with 23 MeV and 23 GeV Proton Irradiations	66
5	Physics Object Definitions	68
5.1	Primary vertex and pile-up	68
5.2	Electrons	69
5.3	Muons	71
5.4	Jets	72
5.5	b tagging	73
5.6	Missing transverse energy	74
5.7	Large radius jets and substructure	75
6	Search for Anomalous Higgs Couplings in $VH(\rightarrow b\bar{b})$	76
6.1	Introduction and Theory	76
6.2	Analysis Strategy	79
6.3	Data and Monte Carlo	80
6.4	Event Selection	82
6.5	Background Modeling	83
6.6	Systematic Uncertainties	84
6.7	Parameter Scan	86
6.7.1	Combine Physics Model	87
6.7.2	Presentation of results	90
6.7.3	Templates	91
6.8	Results	94
6.8.1	Tevatron-Style Scans	94
6.8.2	CMS-Style Scans	97
6.8.3	2D Scans	102
6.8.4	Form Factor Scans	106

6.9	Conclusion	107
7	Search for Heavy Top Quark Partners with Charge 5/3	108
7.1	Motivation	108
7.2	Data and Monte Carlo	109
7.2.1	Data Samples	109
7.2.2	Background Samples	110
7.2.3	Signal Samples	111
7.3	Event Selection	112
7.4	Categorization and Discriminants	116
7.4.1	Event Categories	116
7.4.2	Discriminating Variables	120
7.5	Selection Optimization	122
7.6	Background Modeling	123
7.7	Systematic Uncertainties	125
7.7.1	Uncertainty in the normalization	131
7.7.2	Uncertainties in the shape of the distributions	131
7.8	Results	132
7.8.1	Kinematics with optimized selection	136
7.8.2	Kinematics with final event selection	139
7.8.3	Categorized discriminant templates	139
7.8.4	Final results	141
7.9	Combination with Same-Sign Dilepton Channel	148
8	Summary and Outlook	150
	Bibliography	153

A Chapter 6 Appendix	166
A.1 Control Region Plots	166
A.2 Signal Region Plots	179
A.3 Template Binning and Statistical Uncertainty	192
A.4 Fit Validation	194
A.5 Background Modeling Crosscheck	195

List of Tables

2.1	The nominal LHC parameters.	14
3.1	Mapping of the tracker operational states from DCS to tracker states used in the simulation tool.	34
3.2	The availability of the PLC temperature probes at different locations in the tracker [1].	37
4.1	Comparison of nominal LHC parameters to those of HL-LHC [2, 3]. .	50
4.2	The basic properties of investigated detectors.	52
4.3	Fluences achieved for test structures with 800 MeV protons.	52
4.4	Comparison of nominal and normalized (from Fig. 4.8.1) fluences for HPK test structures with 800 MeV protons.	64
4.5	Fitting values for Neff vs Fluence parameters.	65
4.6	Space charge sign inversion in physically thinned FZ and MCz materi- als after proton irradiations at different energies.	67
6.1	Additional MC samples used in the analysis not described in Ref. [4].	81
6.2	Event selection criteria. Numbers in parentheses refer to the high boost region.	83

6.3	Summary of the sources of systematic uncertainty on the background and signal yields. The size of the uncertainties that only affect normalizations are given. Uncertainties that also affect the shapes are implemented with template morphing, a smooth vertical interpolation between the nominal shape and systematic shape variations.	85
6.4	Signal strength parameters for the various Higgs production processes. In a given row, μ values with a common subscript but primed are related via Eq. 6.7.4.	90
6.5	The best fit value of f_{0-} and 95% CL intervals derived from fixed- μ profile likelihood scans. The ranges are truncated at the physical boundaries.	97
6.6	The best fit values of f_{a3} and 95% CL intervals derived from floating- μ profile likelihood scans. The ranges are truncated at the physical boundaries. All scans which involve both VH and $H \rightarrow VV$ channels are performed with and without enforcing the correlation between the μ parameters given in Equation 6.7.4.	102
6.7	The observed and expected intervals derived from floating- μ profile likelihood scans. Parentheses contain 68% CL intervals, and brackets contain 95% CL intervals. The ranges are truncated at the boundaries $0 < f_{a3} < 1$. All scans which involve both VH and $H \rightarrow VV$ channels are performed with and without enforcing the correlation between the μ parameters given in Equation 6.7.4.	106
7.1	Data sample definitions.	110
7.2	Background MC sample definitions.	111
7.3	$X_{5/3}$ signal MC samples for both LH and RH chiralities at various mass points. These samples were generated with inclusive decays of the $X_{5/3}$	112

7.4	Observed (expected) number of data (background) events in electron and muon channels after the initial selection cuts, with an integrated luminosity of 2.2 fb^{-1} . Uncertainties include all statistical and normalization uncertainties described in Table 7.8.	117
7.5	Definitions of W+jets and $t\bar{t}$ control regions.	125
7.6	Observed (expected) number of data (background) events in the $t\bar{t}$ + jets control region, with an integrated luminosity of 2.2 fb^{-1} . Uncertainties include statistical and all normalization uncertainties except those derived from data/MC agreement in the CR.	127
7.7	Observed (expected) number of data (background) events in the W+jets control region, with an integrated luminosity of 2.2 fb^{-1} . Uncertainties include statistical and all normalization uncertainties except those derived from data/MC agreement in the CR.	129
7.8	Summary of all systematic uncertainties considered.	132
7.9	Observed (expected) number of data (background) events when requiring lepton $p_T > 80 \text{ GeV}$ and 4 or more AK4 jets, but before applying the final cuts on $\Delta R(\ell, \text{sub-leading jet})$. Uncertainties include all statistical and normalization uncertainties (Table 7.8).	138
7.10	Expected (observed) number of background (data) events for the electron channel in the four analysis categories, with an integrated luminosity of 2.2 fb^{-1} . Uncertainties include all statistical and normalization uncertainties (Table 7.8).	139
7.11	Expected (observed) number of background (data) events for the muon channel in the four analysis categories, with an integrated luminosity of 2.2 fb^{-1} . Uncertainties include all statistical and normalization uncertainties (Table 7.8).	140

List of Figures

1.1.1	The Standard Model Particles [5].	3
1.2.1	The Higgs potential [6].	8
1.3.1	Radiative corrections to the Higgs mass: (top-left) self-interactions, (top-right and bottom-left) interactions with gauge bosons, and (bot- tom right) interactions with fermions [6].	11
2.1.1	A superconducting dipole magnet of LHC.	14
2.1.2	CERN accelerator complex with details of the various pre-accelerators before the proton beam enters the LHC ring.	15
2.1.3	Total integrated luminosity delivered by the LHC to the CMS detector during (left) Run 1 from 2010 to 2012 at $\sqrt{s} = 7$ TeV and $\sqrt{s} = 8$ TeV and (right) Run 2 in 2015 at $\sqrt{s} = 13$ TeV.	16
2.2.1	A three dimensional sketch of the CMS detector.	18
2.2.2	A slice of the CMS detector with different particle interactions with the sub-detectors.	18
2.2.3	Schematic cross section through the CMS tracker in the r-z plane [7].	20
2.2.4	(Left) Layout of the CMS ECAL with the crystal module arrangements and (right) schematic cross section of one quarter of the ECAL showing the barrel and end cap regions.	22

2.2.5	A schematic drawing of one quarter of the HCAL in the $r - \eta$ plane. Four HCAL parts are shown: the HCAL barrel (HB), the HCAL end-caps (HEs), the HCAL forward calorimeter (HF), and the HCAL outer calorimeter (HO).	24
2.2.6	A longitudinal diagram of the CMS Muon system. The three sub-detectors DT, CSC, and RPC are shown along with their coverage indicated as dashed lines at fixed η values.	25
3.1.1	Current related damage rate as a function of annealing time for different annealing temperatures [8].	30
3.3.1	Map of the tracker modules with their temperature readings on 3/19/2011, when the tracker was on at the beginning of Run 1. Hot modules can be seen in TIB Layers 1 and 2 due to back-to-back mounting of the modules and in Layers 3 and 4 due to bad cooling contacts. White regions correspond to missing or uncalibrated DCU readings. The z-axis is in Celsius.	35
3.4.1	Comparison between simulated and measured (left) leakage currents and (right) temperatures on 11/15/2011, the beginning of Run 1. Each point in the correlation plot represents a module in the tracker, with different colors representing different partitions. The bottom plots show histograms of the relative deviation between the simulated and measured quantities.	39
3.4.2	Comparison between simulated and measured (left) leakage currents and (right) temperatures on 1/30/2013, the end of Run 1. Each point in the correlation plot represents a module in the tracker, with different colors representing different partitions. The bottom plots show histograms of the relative deviation between the simulated and measured quantities.	40

3.4.3	Comparison between simulated and measured (left) leakage currents and (right) temperatures on 6/21/2015, the end/beginning of LS1/Run 2. Each point in the correlation plot represents a module in the tracker, with different colors representing different partitions. The bottom plots show histograms of the relative deviation between the simulated and measured quantities.	41
3.4.4	Comparison between simulated and measured (left) leakage currents and (right) temperatures on 12/11/2015, the end of 2015 data-taking in Run 2. Each point in the correlation plot represents a module in the tracker, with different colors representing different partitions. The bottom plots show histograms of the relative deviation between the simulated and measured quantities.	42
3.4.5	Comparison between simulated and measured leakage currents as a function of time for example modules in (top) TIB and (bottom) TID partitions.	43
3.4.6	Comparison between simulated and measured leakage currents as a function of time for example modules in (top) TOB and (bottom) TEC partitions.	44
3.4.7	Leakage current as a function of luminosity. Each layer of (top) TIB and (bottom) TOB is shown in its own color. The dotted (solid) lines show the simulated (measured) data. See text for the details about how the measured lines are produced.	46
3.4.8	Normalized leakage current versus fluence for (left) TIB and (right) TOB with the effective alpha fits. Each data point corresponds to a module in (left) Layer 4 in TIB and (right) Layer 6 in TOB, measured at two different integrated luminosities of $14.1fb^{-1}$ and $20.1fb^{-1}$. . .	47

3.5.1	Comparison between simulated and measured (top) leakage currents and (bottom) temperatures as a function of time for an example outlier module in the TEC partition, compared to its neighbor.	48
4.4.1	CV-IV setup for electrical characterization in the Brown Silicon Lab.	53
4.5.1	Illustration of two methods used to determine the depletion voltage from capacitance voltage measurements; (left) inverse square of the capacitance versus bias voltage and (right) capacitance versus voltage in logarithmic scale.	55
4.6.1	Depletion voltage as a function of annealing time at 80 ⁰ C after 800 MeV proton irradiation: (top-left) FZ, (top-right) DOFZ, (bottom-left) MCz and (bottom-right) Epi - 150 μ m.	57
4.6.2	Depletion voltage as a function of annealing time at 80 ⁰ C after 800 MeV proton irradiation for (top) FTH-200 μ m and (bottom) MCz-200 μ m detectors with (left) n- and (right) p-type polarities.	59
4.7.1	Hamburg model parameterization of FZ and DOFZ detectors after 800 MeV proton irradiation.	60
4.7.2	Hamburg model parameterization of (left) MCz and (right) Epi-150 μ m detectors after 800 MeV proton irradiation.	61
4.7.3	Hamburg model parameterization of (top) FTH-200 μ m and (bottom) MCz-200 μ m detectors for (left) n- and (right) p-type after 800 MeV proton irradiation.	61
4.8.1	Volume leakage current (corresponding to depletion voltage) as a function of fluence after 800 MeV proton irradiation for (left) RD50 and (right) HPK diodes. The dashed line shows the expected behavior from [8]. The leakage current is scaled to its reference value at 20 ⁰ C from its measurement temperature at (left) room temperature and (right) -20 ⁰ C.	63

4.9.1	Depletion voltage as a function of 1 MeV neutron equivalent fluence for (left) RD50 and (right) HPK diodes. Solid lines show the fits using Eq. 4.9.2.	65
5.1.1	Distributions of (left) mean number of interactions per bunch crossing in data and MC at 13 TeV. The ratio of these histograms is shown in (right) and used to weight MC events.	69
5.1.2	Distribution of the number of primary vertices per event after pileup reweighting at 13 TeV. Uncertainties include all statistical and systematic uncertainties described in sec. 7.7.	70
5.5.1	Distributions of (left) efficiency of tagging a jet with b quark flavor using the pfCombinedInclusiveSecondaryVertexV2BJetTags medium working point, and (right) efficiency of tagging a light flavor jet with the same working point. Both distributions are calculated using the $t\bar{t}$ MC sample for 13 TeV collisions.	74
6.1.1	Higgs boson produced in association with a vector boson	77
6.3.1	The ratio of the NLO POWHEG and LO JHUGEN V transverse momentum shapes, applied as a k-factor to signal MC. The k-factors are derived separately in WH (left) and ZH (right) MC.	82
6.7.1	Various Feynman diagrams relevant to the analysis; quark initiated VH production (upper left), gluon initiated ZH production via a fermion triangle (upper right) and box (lower right), and gluon fusion with $H \rightarrow VV$ (lower left).	88
6.7.2	Closure test of the $gg \rightarrow ZH$ reweighting procedure. Histograms constructed directly from LHEs generated with various a_1 and b values (dots) are compared to those constructed from a linear combination of box-only, triangle-only, and box+triangle LHEs (dashed lines). . .	91

6.7.3	The shape of the BDT discriminant in selected events for the 0^+ , 0^- , and 50/50 signals compared to background, normalized to unit area. The top (bottom) row shows the electron (muon) channel. The left (right) column shows the medium (high) boost region.	92
6.7.4	The shape of the m (VH) distribution in selected events for the 0^+ , 0^- , and 50/50 signals compared to background, normalized to unit area. The top (bottom) row shows the electron (muon) channel. The left (right) column shows the medium (high) boost region.	93
6.7.5	The 2D templates used for hypothesis testing in the $W \rightarrow e\nu$ channel, high boost region. From upper left to lower right: 0^+ signal, 0^- signal, total background, and data.	94
6.7.6	The distribution of (top) m (VH) in the (left) $W \rightarrow \mu\nu$ and (right) $Z \rightarrow ee$ channels and (bottom) BDT discriminant in the (left) $W \rightarrow e\nu$ and (right) $Z \rightarrow \mu\mu$ channels in selected events for the 0^+ , and 0^- signals compared to background, normalized to $18.9fb^{-1}$. All distributions are from the high boost region.	95
6.7.7	Unrolled 2D templates in the (left) $W \rightarrow e\nu$ and (right) $Z \rightarrow \mu\mu$ channels of the high boost region.	96
6.8.1	Results of the fixed- μ profile likelihood scans in the WH, ZH, and VH (WH +ZH) channels. The dashed (solid) line shows the expected (observed) $-2\Delta\ln\mathcal{L}$ value as a function of f_{0-} . Expected results are derived from Asimov data for a pure scalar Higgs with $\mu = 1$	96
6.8.2	Results of the floating- μ profile likelihood scans for the WH and ZH channels, as well as their combination (VH). The dotted (solid) lines show the expected (observed) $-2\Delta\ln\mathcal{L}$ value as a function of f_{a3}^{ZH} . Expected results are derived from Asimov data for a pure scalar Higgs with $\mu = 1$. The horizontal dashed line represents the 68% CL.	98

6.8.3	Results of the floating- μ profile likelihood scans for the VH and $H \rightarrow$ VV channels, plus their combination. The top (bottom) plots show results which exclusively depend on the HWW (HZZ) couplings. The dotted (solid) lines show the expected (observed) $-2\Delta\ln\mathcal{L}$ value as a function of (top) f_{a3}^{WW} and (bottom) f_{a3}^{ZZ} . The full range of f_{a3} is shown on the left, with the low f_{a3} region highlighted on the right. Expected results are derived from Asimov data for a pure scalar Higgs with $\mu = 1$. The horizontal dashed lines represent the 68%, 95%, and 99% CL.	99
6.8.4	Results of the floating- μ profile likelihood scans for the VH and $H \rightarrow$ VV channels, as well as their combination. The dotted (solid) lines show the expected (observed) $-2\Delta\ln\mathcal{L}$ value as a function of f_{a3}^{ZZ} . The full range of f_{a3}^{ZZ} is shown on the left, with the low f_{a3}^{ZZ} region highlighted on the right. The bottom plots contain the results of correlated- μ scans. Expected results are derived from Asimov data for a pure scalar Higgs with $\mu = 1$. The horizontal dashed lines represent the 68%, 95%, and 99% CL. In the legends, VH refers to the combination of the WH and ZH channels, and VV refers to the combination of the $H \rightarrow$ WW and $H \rightarrow$ ZZ channels.	100
6.8.5	Results of the floating- μ profile likelihood scans for the ZH and $H \rightarrow$ ZZ channels, as well as their combination. These channels exclusively probe the HZZ coupling, and therefore the results do not include any assumption on the relationship between the HWW and HZZ couplings. The dotted (solid) lines show the expected (observed) $-2\Delta\ln\mathcal{L}$ value as a function of f_{a3}^{ZH} . Expected results are derived from Asimov data for a pure scalar Higgs with $\mu = 1$. The horizontal dashed lines are shown, representing the 68% and 95% CL.	101

6.8.6	Results of expected (left) and observed (right) two-dimensional profile likelihood scans in the μ^{ZH} versus f_{a3}^{ZH} plane using the combination of WH and ZH channels. The z -axis represents $-2\Delta\ln\mathcal{L}$ calculated with respect to the global minimum with a linear (log) scale on the top (bottom) row. The scan minimum is indicated by a white dot. The 68% and 95% CL contours at $-2\Delta\ln\mathcal{L} = 2.30$ and 5.99, respectively, are shown. Expected results are derived from Asimov data for a pure scalar Higgs with $\mu = 1$	103
6.8.7	Results of expected (left) and observed (right) two-dimensional profile likelihood scans in the μ^{ZH} versus f_{a3}^{ZH} plane using the ZH channel. The z -axis represents $-2\Delta\ln\mathcal{L}$ calculated with respect to the global minimum with a linear (log) scale on the top (bottom) row. The scan minimum is indicated by a white dot. The 68% and 95% CL contours at $-2\Delta\ln\mathcal{L} = 2.30$ and 5.99, respectively, are shown. Expected results are derived from Asimov data for a pure scalar Higgs with $\mu = 1$. . .	104
6.8.8	Results of expected (left) and observed (right) two-dimensional profile likelihood scans in the μ^{WH} versus f_{a3}^{WH} plane using the WH channel. The z -axis represents $-2\Delta\ln\mathcal{L}$ calculated with respect to the global minimum with a linear (log) scale on the top (bottom) row. The scan minimum is indicated by a white dot. The 68% and 95% CL contours at $-2\Delta\ln\mathcal{L} = 2.30$ and 5.99, respectively, are shown. Expected results are derived from Asimov data for a pure scalar Higgs with $\mu = 1$. . .	105
6.8.9	Results of CMS-style expected (left) and observed (right) f_{a3} scans based on a combination of the WH and ZH channels, shown for various new physics scales Λ	107
7.1.1	Pair production of $X_{5/3}$ and its decay into a top quark and a W boson.	109

7.3.1	Distributions of (top) electron and (bottom) muon, showing (left) $ \eta $ and (right) p_T in data and MC after the initial selection. Uncertainties include all statistical and systematic uncertainties described in Section 7.7.	113
7.3.2	Distributions of (left) p_T and (right) $ \eta $ of all AK4 jets with $p_T > 30$ GeV in data and MC after the initial selection. Uncertainties include all statistical and systematic uncertainties described in Section 7.7. .	114
7.3.3	Distributions of p_T for the four highest p_T jets in data and MC after the initial selection. Uncertainties include all statistical and systematic uncertainties described in Section 7.7.	115
7.3.4	Distributions of (left) the number of AK4 jets and (right) the number passing the medium b tag working point in data and MC after the initial selection. Uncertainties include all statistical and systematic uncertainties described in Section 7.7.	116
7.3.5	Distributions of (top left) H_T , (top right) S_T , and (bottom) E_T^{miss} in data and MC after the initial selection. Uncertainties include all statistical and systematic uncertainties described in Section 7.7. . .	117
7.4.1	Distributions of (left) the number of AK8 jets, (right) AK8 jet p_T , and (bottom) AK8 jet $ \eta $ in data and MC after the initial selection. Uncertainties include all statistical and systematic uncertainties described in Section 7.7.	118
7.4.2	Distributions of (left) the n-subjettiness τ_2/τ_1 ratio, (right) AK8 jet pruned mass, and (bottom) the number of W tagged jets in data and MC after the initial selection. Uncertainties include all statistical and systematic uncertainties described in Section 7.7.	119

7.4.3	Distributions of (left) $\min[M(\ell, b)]$, (right) $M[W(\ell, \nu) + \text{all AK4 jets}]$, and (bottom) $\Delta R(\ell, \text{sub-leading jet})$ in data and MC after the initial selection. Uncertainties include all statistical and systematic uncertainties described in Section 7.7.	121
7.5.1	Optimization results, from varying all combinations of selection cuts.	123
7.5.2	Optimization results from varying (top left) jet p_T , (top right) number of jets, (bottom left) E_T^{miss} , and (bottom right) lepton p_T . In each plot the other cuts are held constant at the optimal cut points returned by the algorithm.	124
7.6.1	Distributions of $\min[M(\ell, b)]$ in the $t\bar{t} + \text{jets}$ control region, for (top/bottom) electron/muon plus (left/right) 1/2+ b tag categories. Uncertainties include all uncertainties except those derived from data/MC agreement in the CR.	126
7.6.2	Distributions of $\min[M(\ell, b)]$ in the $W + \text{jets}$ control region, for (top/bottom) electron/muon plus (left/right) 0/1+ W tag categories. Uncertainties include all uncertainties except those derived from data/MC agreement in the CR.	128
7.6.3	Distributions of $\min[M(\ell, b)]$ in the (top) $t\bar{t} + \text{jets}$ control region, for one b tagged jet (top left) and 2+ b tagged jets (top right) categories, and of $\min[M(\ell, b)]$ in the $V + \text{jets}$ control region, for zero W tagged (bottom left) and 1+ W tagged jet (bottom right) categories for combined electron and muon event samples. Uncertainties include statistical and all systematic uncertainties except those which are derived from the control regions. For each category, the QCD contribution is not displayed if it is less than 0.5% of the total background.	130

7.7.1	Distributions of $\min[M(\ell, b)]$ for total background with $\pm 1\sigma$ variations for (top-left) jet energy scale, (top-right) jet energy resolution, (bottom-left) b tag scale factor, and (bottom-right) pileup reweighting uncertainties after combining all channels.	133
7.7.2	Distributions of $\min[M(\ell, b)]$ for total background with $\pm 1\sigma$ variations for (top-left) renormalization scale, (top-right) factorization scale, (bottom-left) PDF uncertainties, and (bottom-right) parton shower energy scale after combining all channels.	134
7.7.3	Distributions of $\min[M(\ell, b)]$ for total background with $\pm 1\sigma$ variations for (top-left) pruned jet mass resolution, (top-right) pruned jet mass scale, (bottom-left) τ_2/τ_1 efficiency uncertainty, and (bottom-right) top quark p_T reweighting.	135
7.8.1	Distributions of (left) lepton p_T and (right) $ \eta $ in (top) electron and (bottom) muon channels in data and MC after the optimized selection. Uncertainties include all statistical and systematic uncertainties. . . .	136
7.8.2	Distributions of (left) p_T (right) $ \eta $ of all AK4 jets with $p_T > 30$ GeV in data and MC after the optimized selection. Uncertainties include all statistical and systematic uncertainties.	137
7.8.3	Distributions of b-tagged and W-tagged jet multiplicity in data and MC after the optimized selection. Uncertainties include all statistical and systematic uncertainties.	137
7.8.4	Distribution of $\min[M(\ell, b)]$ in data and MC after the optimized selection. Uncertainties include all statistical and systematic uncertainties.	138
7.8.5	Distributions of (left) lepton p_T and (right) $ \eta $ in (top) electron and (bottom) muon channels in data and MC after the final selection for the $\min[M(\ell, b)]$ discriminant. Uncertainties include all statistical and systematic uncertainties.	140

7.8.6	Distributions of (left) p_T (right) $ \eta $ of all AK4 jets with $p_T > 30$ GeV in data and MC after the final selection for the $\min[M(\ell, b)]$ discriminant. Uncertainties include all statistical and systematic uncertainties. . . .	141
7.8.7	Distributions of p_T for the four highest p_T jets in data and MC after the final selection for the $\min[M(\ell, b)]$ discriminant. Uncertainties include all statistical and systematic uncertainties.	142
7.8.8	Distributions of (left) H_T , (right) S_T , and E_T^{miss} in data and MC after the final selection for the $\min[M(\ell, b)]$ discriminant. Uncertainties include all statistical and systematic uncertainties.	143
7.8.9	Distributions of b tagged and W tagged jet multiplicity in data and MC after the final selection for the $\min[M(\ell, b)]$ discriminant. Uncertainties include all statistical and systematic uncertainties.	144
7.8.10	Distribution of $\min[M(\ell, b)]$ in data and MC after the final selection for the $\min[M(\ell, b)]$ discriminant. Uncertainties include all statistical and systematic uncertainties.	144
7.8.11	Distributions of $\min[M(\ell, b)]$ in the electron channel in categories with (top) 0 or (bottom) 1+ boosted W-tagged jets and (left) 1 or (right) 2+ b-tagged AK4 jets. Uncertainties include all statistical and systematic uncertainties.	145
7.8.12	Distributions of $\min[M(\ell, b)]$ in the muon channel in categories with (top) 0 or (bottom) 1+ boosted W-tagged jets and (left) 1 or (right) 2+ b-tagged AK4 jets. Uncertainties include all statistical and systematic uncertainties.	146

7.8.13	Distributions of $\min[M(\ell, b)]$ for combined electron and muon channels in categories with (top) 0 or (bottom) 1+ boosted W-tagged jets and (left) 1 or (right) 2+ b-tagged AK4 jets. Uncertainties include all statistical and systematic uncertainties. For each category, the QCD contribution is not displayed if it is less than 0.5% of the total background.	147
7.8.14	95% CL expected and observed upper limits (Bayesian) on the cross section of (left) left-handed and (right) right-handed $X_{5/3}$, after combining electron/muon, 0/1+ W-tagged jets, and 1/2+ b-tagged jets channels at an integrated luminosity of 2.2 fb^{-1}	148
7.9.1	95% CL expected and observed upper limits (Bayesian) after combining the same-sign dileptons, and the lepton+jets signatures for an integrated luminosity of 2.2 fb^{-1} for left handed (left) and right handed (right) $X_{5/3}$ signals.	149
8.0.1	Results of expected profile likelihood scans for the WH and ZH channels, as well as their combination (WH + ZH), corresponding to 100 fb^{-1} at $\sqrt{s} = 13 \text{ TeV}$. The horizontal magenta lines represent the 68% and 95% CL.	151
A.1.1	The distribution of the BDT discriminant in the W+LF control region for the 0^+ and 0^- signals, expected background, and data. The top (bottom) row shows the electron (muon) channel. The left (right) column shows the medium (high) boost region. The binning choice is from the 2D templates in the corresponding signal regions.	167

A.1.2	The m (VH) distribution in the W+LF control region for the 0^+ and 0^- signals, expected background, and data. The top (bottom) row shows the electron (muon) channel. The left (right) column shows the medium (high) boost region. The binning choice is from the 2D templates in the corresponding signal regions.	168
A.1.3	The distribution of the BDT discriminant in the Z+LF control region for the 0^+ and 0^- signals, expected background, and data. The top (bottom) row shows the electron (muon) channel. The left (right) column shows the medium (high) boost region. The binning choice is from the 2D templates in the corresponding signal regions.	169
A.1.4	The m (VH) distribution in the Z+LF control region for the 0^+ and 0^- signals, expected background, and data. The top (bottom) row shows the electron (muon) channel. The left (right) column shows the medium (high) boost region. The binning choice is from the 2D templates in the corresponding signal regions.	170
A.1.5	The distribution of the BDT discriminant in the W+HF control region for the 0^+ and 0^- signals, expected background, and data. The top (bottom) row shows the electron (muon) channel. The left (right) column shows the medium (high) boost region. The binning choice is from the 2D templates in the corresponding signal regions.	171
A.1.6	The m (VH) distribution in the W+HF control region for the 0^+ and 0^- signals, expected background, and data. The top (bottom) row shows the electron (muon) channel. The left (right) column shows the medium (high) boost region. The binning choice is from the 2D templates in the corresponding signal regions.	172

A.1.7	The distribution of the BDT discriminant in the Z+HF control region for the 0^+ and 0^- signals, expected background, and data. The top (bottom) row shows the electron (muon) channel. The left (right) column shows the medium (high) boost region. The binning choice is from the 2D templates in the corresponding signal regions.	173
A.1.8	The $m(\text{VH})$ distribution in the Z+HF control region for the 0^+ and 0^- signals, expected background, and data. The top (bottom) row shows the electron (muon) channel. The left (right) column shows the medium (high) boost region. The binning choice is from the 2D templates in the corresponding signal regions.	174
A.1.9	The distribution of the BDT discriminant in the $t\bar{t}$ control region of the WH channel for the 0^+ and 0^- signals, expected background, and data. The top (bottom) row shows the electron (muon) channel. The left (right) column shows the medium (high) boost region. The binning choice is from the 2D templates in the corresponding signal regions. .	175
A.1.10	The $m(\text{VH})$ distribution in the $t\bar{t}$ control region of the WH channel for the 0^+ and 0^- signals, expected background, and data. The top (bottom) row shows the electron (muon) channel. The left (right) column shows the medium (high) boost region. The binning choice is from the 2D templates in the corresponding signal regions.	176
A.1.11	The distribution of the BDT discriminant in the $t\bar{t}$ control region of the ZH channel for the 0^+ and 0^- signals, expected background, and data. The top (bottom) row shows the electron (muon) channel. The left (right) column shows the medium (high) boost region. The binning choice is from the 2D templates in the corresponding signal regions. .	177

A.1.12	The $m(\text{VH})$ distribution in the $t\bar{t}$ control region of the ZH channel for the 0^+ and 0^- signals, expected background, and data. The top (bottom) row shows the electron (muon) channel. The left (right) column shows the medium (high) boost region. The binning choice is from the 2D templates in the corresponding signal regions.	178
A.2.1	The 2D templates used for profile likelihood scans in the $W \rightarrow e\nu$ channel, medium boost region. From upper left to lower right: 0^+ signal, 0^- signal, total background, and data.	179
A.2.2	The 2D templates used for profile likelihood scans in the $W \rightarrow e\nu$ channel, high boost region. From upper left to lower right: 0^+ signal, 0^- signal, total background, and data.	180
A.2.3	The 2D templates used for profile likelihood scans in the $W \rightarrow \mu\nu$ channel, medium boost region. From upper left to lower right: 0^+ signal, 0^- signal, total background, and data.	181
A.2.4	The 2D templates used for profile likelihood scans in the $W \rightarrow \mu\nu$ channel, high boost region. From upper left to lower right: 0^+ signal, 0^- signal, total background, and data.	182
A.2.5	The 2D templates used for profile likelihood scans in the $Z \rightarrow ee$ channel, medium boost region. From upper left to lower right: 0^+ signal, 0^- signal, total background, and data.	183
A.2.6	The 2D templates used for profile likelihood scans in the $Z \rightarrow ee$ channel, high boost region. From upper left to lower right: 0^+ signal, 0^- signal, total background, and data.	184
A.2.7	The 2D templates used for profile likelihood scans in the $Z \rightarrow \mu\mu$ channel, medium boost region. From upper left to lower right: 0^+ signal, 0^- signal, total background, and data.	185

A.2.8	The 2D templates used for profile likelihood scans in the $Z \rightarrow \mu\mu$ channel, high boost region. From upper left to lower right: 0^+ signal, 0^- signal, total background, and data.	186
A.2.9	The distribution of the BDT discriminant in selected events in the WH channel for the 0^+ and 0^- signals compared to background, normalized to $18.9fb^{-1}$. The top (bottom) row shows the electron (muon) channel. The left (right) column shows the medium (high) boost region. . . .	187
A.2.10	The m (VH) distribution in selected events in the WH channel for the 0^+ and 0^- signals compared to background, normalized to $18.9fb^{-1}$. The top (bottom) row shows the electron (muon) channel. The left (right) column shows the medium (high) boost region.	188
A.2.11	The distribution of the BDT discriminant in selected events in the ZH channel for the 0^+ and 0^- signals compared to background, normalized to $18.9fb^{-1}$. The top (bottom) row shows the electron (muon) channel. The left (right) column shows the medium (high) boost region. . . .	189
A.2.12	The m (VH) distribution in selected events in the ZH channel for the 0^+ and 0^- signals compared to background, normalized to $18.9fb^{-1}$. The top (bottom) row shows the electron (muon) channel. The left (right) column shows the medium (high) boost region.	190
A.2.13	Unrolled 2D templates in the WH channel. The top (bottom) row shows the electron (muon) channel. The left (right) column shows the medium (high) boost region.	191
A.2.14	Unrolled 2D templates in the ZH channel. The top (bottom) row shows the electron (muon) channel. The left (right) column shows the medium (high) boost region.	192

A.3.1	Total background distribution in the medium boost $W \rightarrow e\nu$ channel, before (left) and after (right) rebinning in order to ensure non-zero background expectation in every bin.	193
A.4.1	Results of observed scans to data with signal injected at various values of f_{a3} . The top (bottom) left plot shows the results from WH (ZH) channel only. A zoom into the y-axis is also shown on the right. . . .	194
A.5.1	The $m(\text{VH})$ distribution in the WH signal regions, with the requirement that the BDT discriminant is smaller than -0.3. The top (bottom) row shows the electron (muon) channel. The left (right) column shows the medium (high) boost region.	196
A.5.2	The $m(\text{VH})$ distribution in the WH signal regions, with the requirement that the BDT discriminant is greater than -0.3. The top (bottom) row shows the electron (muon) channel. The left (right) column shows the medium (high) boost region.	197
A.5.3	The $m(\text{VH})$ distribution in the ZH signal regions, with the requirement that the BDT discriminant is smaller than -0.3. The top (bottom) row shows the electron (muon) channel. The left (right) column shows the medium (high) boost region.	198
A.5.4	The $m(\text{VH})$ distribution in the ZH signal regions, with the requirement that the BDT discriminant is greater than -0.3. The top (bottom) row shows the electron (muon) channel. The left (right) column shows the medium (high) boost region.	199

A.5.5	Simultaneous fits to the m (VH) data/background ratio across the electron and muon channels, in the medium (left) and high (right) boost signal regions with $\text{BDT} < -0.3$. The top plots show the WH channel, while the bottom plots show the ZH channel. The left (right) half of each plot shows the data/background ratio vs m (VH) from 0 to 2 TeV in the muon (electron) channel. A nuisance parameter is added to the physics model which allows for a linear correction of the background templates in accord with the fitted ratios in each SR.	200
-------	---	-----

Chapter 1

Theory Background

This chapter gives a brief discussion of the standard model of particles and the underlying theories behind it, along with its theoretical problems.

1.1 The Standard Model of Particles

The standard model (SM) is a mathematical theory that describes the behavior of all known elementary particles [9, 10]. The SM has so far proven to be the most accurate theory of the fundamental interactions in nature. The model is built upon the non-Abelian $SU_C(3) \times SU_L(2) \times U_Y(1)$ gauge symmetry group, where $SU_C(3)$ is the color group, $SU_L(2)$ is the weak isospin group, and $U_Y(1)$ is the hyper charge group. There are two underlying theories of the SM: the electroweak (Glashow-Weinberg-Salam) theory combining the weak and electromagnetic interactions, and the Quantum Chromo-dynamics (QCD) of strong interactions.

The gauge theories, describing the electroweak and strong interactions in the SM, are renormalizable, which is why these are used for combining different interactions. Quantum Electro-dynamics (QED) is described by an Abelian $U_Y(1)$ gauge symmetry. After the construction of a gauge theory with non-Abelian $SU_L(2)$ weak isospin group by Yang-Mills [11], Sheldon Lee Glashow, Abdus Salam, and Steven Weinberg

constructed the Glashow-Weinberg-Salam theory of electroweak interactions [12–16] during the early 1960s, combining the electromagnetic and weak interactions under $SU_L(2) \times U_Y(1)$ gauge theory. Initially, the gauge fields and the fermion fields were assumed to be massless as a requirement for gauge invariance. In 1964, Higgs [17]; Brout & Englert [18]; and Guralnik, Hagen, & Kibble [19] discovered a way to describe massive particles without breaking the gauge invariance of the theory using spontaneous symmetry breaking. This resulted in the prediction of an additional particle which is now known as the Higgs boson, and was recently discovered at the LHC [20–22]. The strong interactions between quarks, on the other hand, is described by a gauge theory with the non-Abelian $SU_C(3)$ color group.

1.1.1 Particle Families

The SM particles can be divided into two groups: matter particles and gauge bosons (see Fig. 1.1.1). The matter particles are fermions with half integer spins and they obey the Fermi-Dirac statistics. The gauge bosons on the other hand have integer spins and are also the force carriers of the fundamental interactions.

The matter particles or fermions are classified as leptons or quarks:

Leptons consist of the electron (e^-), the muon (μ^-), and the tau (τ^-) with an electrical negative unit charge and corresponding to each of these particles three neutrinos with no electrical charge; ν_e , ν_μ , ν_τ . In the SM, the left-handed and right-handed components of these particles interact differently; however, there are only left-handed neutrinos. Leptons don't interact through strong interactions as they don't carry the color quantum number. Neutrinos interact only through weak interactions as they are neutral, while electron, muon, and tau interact both weakly and electromagnetically. Even though there are indications that neutrinos have mass because of recently observed neutrino oscillations [23, 24], they are assumed to be massless in the SM.

Quarks were introduced by Gell-Mann [25, 26] to explain the structure of hadrons

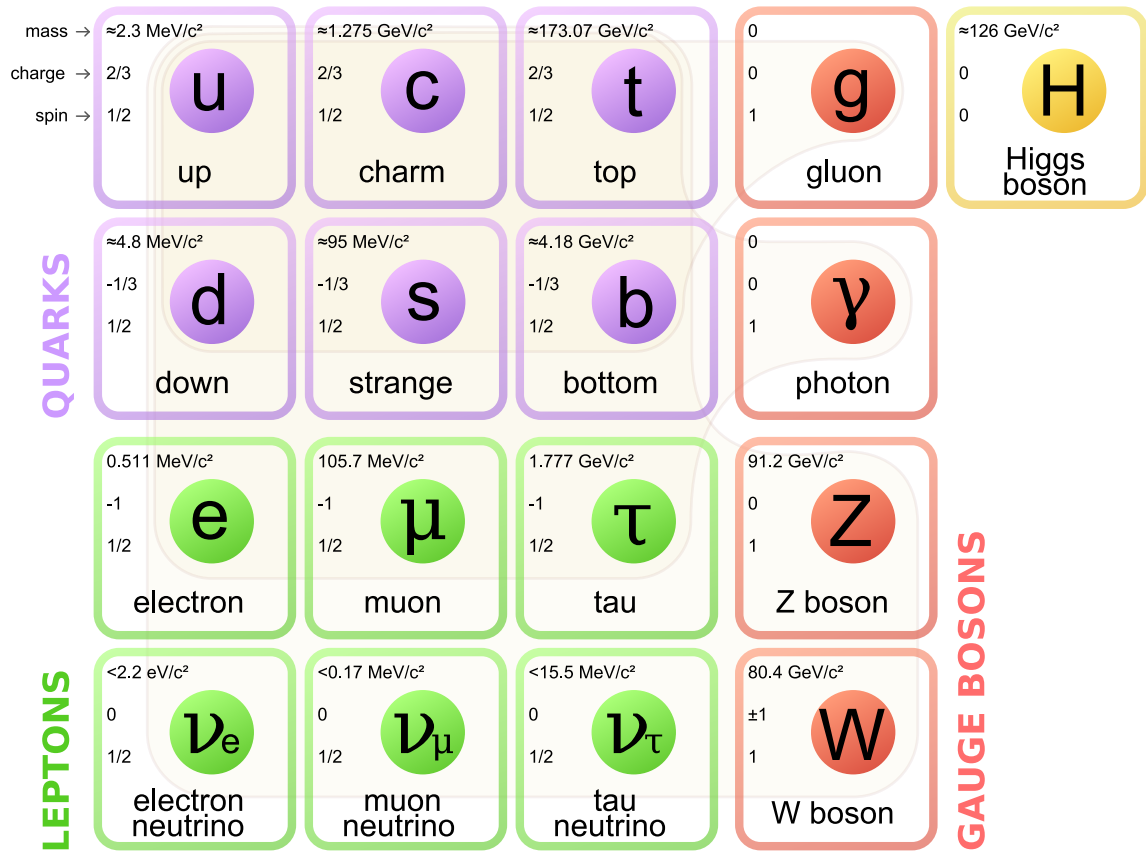


Figure 1.1.1: The Standard Model Particles [5].

and later observed experimentally. There are six quarks grouped into two categories: up-type and down-type quarks. The up-type quarks are up (u), charm (c), and top (t), each with an electrical charge of $2/3$ of the electron charge. The down-type quarks on the other hand are down (d), strange (s), and bottom (b), each with an electrical charge of $-1/3$ of the electron charge. Quarks have three different color quantum numbers and cannot be observed directly as they are trapped in hadrons, which are colorless. The hadrons are divided into baryons and mesons. Baryons (proton, neutron, etc) consist of three quarks, whereas mesons (pion, etc) are made out of a quark and an anti-quark pair.

The second type of fundamental particles in the SM are gauge bosons. Apart from the gravitational interactions, all interactions in particle physics happens through exchange of these spin-1 gauge bosons. There are 8 gluons for the $SU_C(3)$ gauge bosons and W^\pm , Z , and γ for $SU_L(2) \times U_Y(1)$ gauge bosons. Photons are the force carriers of the electromagnetic interactions, gluons are the force carriers of the strong interactions, and W^\pm and Z bosons are the force carriers of the weak interactions. Gluons are massless and neutral particles, but they have color quantum number. They provide the interaction between quarks and also have self-interaction. W^\pm and Z bosons are massive particles and W^\pm bosons have electrical charge, while Z boson is neutral. W^\pm and Z bosons carry weak hypercharge and therefore interact with each other. Photons on the other hand are massless and neutral particles and do not self-interact.

1.1.2 Particle Interactions

The particle interactions include electromagnetic, weak, strong, and gravitational forces. The only missing piece in the SM currently is the gravitational force.

1.1.2.1 Strong Interactions

Quantum Chromo Dynamics (QCD) is a well-established gauge theory of strong interactions between quarks and gluons, which bind together to make hadrons such as protons and neutrons in the atomic nuclei. All mesons and baryons can be obtained from a quark-anti-quark pair and three quarks respectively [26]. However, a new color quantum number needs to be introduced in order to be able use the Fermi-Dirac statistics in baryonic systems.

The gauge symmetry of strong interactions is constructed upon local color exchanges that make the Lagrangian invariant. This gauge symmetry is a non-Abelian $SU_C(3)$ Lie group [27], where C stands for color and 3 is the number of possible color states of the quarks [28]. Gluons (8 of them) are the gauge bosons of this gauge symmetry.

The Lagrangian density for the strong interactions:

$$\mathcal{L}_{QCD} = \bar{\psi}_q(i\not{D} - m_q)\psi_q - \frac{1}{4}F_{\mu\nu}^\alpha F_{\alpha}^{\mu\nu}, \quad (1.1.1)$$

where the sum is over all quark flavors q and $SU_C(3)$ generators α . The gluon field tensor $F_{\mu\nu}^\alpha$ is:

$$F_{\mu\nu}^\alpha = \delta_\mu G_\nu^\alpha - \delta_\nu G_\mu^\alpha - g_s f^{\alpha\beta\gamma} G_{\mu\beta} G_{\nu\gamma}, \quad (1.1.2)$$

where g_s is the coupling constant, $f^{\alpha\beta\gamma}$ are the structure constants of the $SU_C(3)$ group, and G_μ^α are the gluon fields.

1.1.2.2 Electroweak Interactions

All fundamental particles in the SM (leptons and quarks) interact via weak interactions. Additionally, electrically charged particles also interact via electromagnetic

interactions. The electroweak model that describes the electromagnetic and weak interactions between leptons and quarks is a $SU_L(2) \times U_Y(1)$ symmetry group of Yang-Mills gauge theory. The Lagrangian that defines the electroweak interactions must be invariant under $SU_L(2) \times U_Y(1)$ gauge group. The electroweak Lagrangian in the SM is:

$$\mathcal{L}_{EWK} = \mathcal{L}_{gauge} + \mathcal{L}_{fermion} + \mathcal{L}_{scalar} + \mathcal{L}_{Yukawa}. \quad (1.1.3)$$

The gauge part includes the kinetic energy and self-interaction of the gauge fields and is given by

$$\mathcal{L}_{gauge} = -\frac{1}{4}F_{\mu\nu}^i F^{\mu\nu i} - \frac{1}{4}B_{\mu\nu}B^{\mu\nu}, \quad (1.1.4)$$

where F_{μ}^i ($i = 1, 2, 3$) and B_{μ} are $SU_L(2)$ and $U_Y(1)$ gauge fields, respectively, and their strength tensors are

$$\begin{aligned} B_{\mu\nu} &= \partial_{\mu}B_{\nu} - \partial_{\nu}B_{\mu} \\ F_{\mu\nu}^i &= \partial_{\mu}W_{\nu}^i - \partial_{\nu}W_{\mu}^i - g\epsilon_{ijk}W_{\mu}^jW_{\nu}^k, \end{aligned} \quad (1.1.5)$$

where g is the $SU_L(2)$ gauge coupling constant. B_{μ} is the $U_Y(1)$ gauge field with weak hypercharge $Y = Q - I_3$, where Q and I_3 are electric charge operator and the third component of the $SU(2)$ gauge group. Because B_{μ} is a gauge field of a Abelian group, it doesn't self-interact. $SU(2)$ gauge fields on the other hand belongs to non-Abelian group and therefore W^{\pm} bosons self-interact.

The fermion part of the electroweak Lagrangian is

$$\mathcal{L}_{fermion} = \sum_{families} \left[i\bar{l}_L \not{D} l_L + i\bar{q}_L \not{D} q_L + i\bar{e}_R \not{D} e_R + i\bar{u}_R \not{D} u_R + i\bar{d}_R \not{D} d_R \right], \quad (1.1.6)$$

where L and R represent respectively the left-handed and right-handed chiralities

which are obtained by applying the chirality operator γ_5 to spinor $\psi_{R(L)} = (1 \pm \gamma_5)\psi$. l_L and q_L are the weak isospin SU(2) doublets of the left-handed leptons and quarks, respectively, while the right-handed fields e_R , u_R , and d_R are singlets. The covariant derivatives of these fields are given by

$$\begin{aligned} D_\mu f_L &= \left(\partial_\mu + \frac{ig}{2} \sigma \cdot W_\mu + \frac{ig'}{2} Y B_\mu \right) f_L \\ D_\mu f_R &= \left(\partial_\mu + \frac{ig'}{2} Y B_\mu \right) f_R, \end{aligned} \tag{1.1.7}$$

where σ_i are the Pauli matrices. Plugging Eq. 1.1.7 in Eq. 1.1.6, one can read off all the possible interactions between fermions and W_μ and B_μ gauge fields. It can be seen that both the right- and left-handed leptons and quarks interact with B_μ field, while only left-handed fermions interact with the W_μ field. Because of the chiral symmetry, the fermion Lagrangian does not have a mass term for fermions and they get the mass with Yukawa term in the electro-weak Lagrangian.

The last two terms in Eq. 1.1.3 provide the mass for the weak bosons and fermions and are discussed in the next section.

1.2 Electroweak Symmetry Breaking and the Higgs Boson

The scalar part of the Lagrangian in Eq. 1.1.3 is

$$\mathcal{L}_{scalar} = |D_\mu \phi|^2 - V(\phi), \tag{1.2.1}$$

where ϕ is the complex Higgs scalar field that is a doublet under the SU(2) group, with a hypecharge of $Y = 1$. The scalar field and its covariant derivative are

$$\phi = \begin{pmatrix} \phi^+ \\ \phi^0 \end{pmatrix} = \frac{1}{\sqrt{2}} \begin{pmatrix} \phi_1 - i\phi_2 \\ \phi_3 - i\phi_4 \end{pmatrix}, \quad D_\mu \phi = \left(\partial_\mu + \frac{ig}{2} \sigma \cdot W_\mu + \frac{ig'}{2} Y B_\mu \right) \phi, \quad (1.2.2)$$

where the covariant derivative provides the interaction between the scalar field and the W_μ and B_μ gauge fields and the square of it in the Lagrangian gives three and four-point interactions between the scalar and gauge fields.

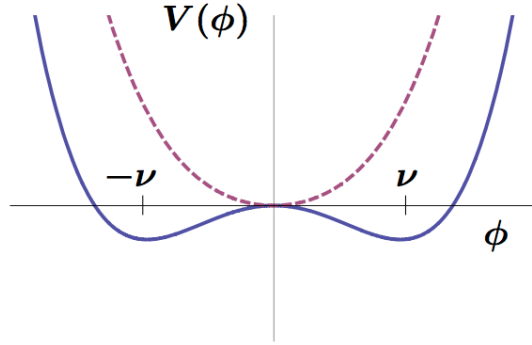


Figure 1.2.1: The Higgs potential [6].

$V(\phi)$, shown in Fig. 1.2.1, is called the Higgs potential and is the simplest renormalizable potential given by

$$V(\phi) = \mu^2 \phi^\dagger \phi + \lambda (\phi^\dagger \phi)^2, \quad (1.2.3)$$

where the μ and the λ terms are respectively the bare mass and self-interaction terms of the Higgs fields. There are two vacuum expectation values that minimize the Higgs potential depending on the sign of the μ term:

- If $\mu^2 > 0$, the vacuum expectation value is $\langle 0 | \phi | 0 \rangle = 0$. In this case, there is no symmetry breaking as the vacuum is symmetric under $SU_L(2) \times U_Y(1)$.

- If $\mu^2 < 0$,

$$|\langle 0|\phi|0\rangle| = \frac{1}{\sqrt{2}} \begin{pmatrix} 0 \\ \nu \end{pmatrix}, \quad (1.2.4)$$

where ν is the vacuum expectation value of the Higgs field and the symmetry is broken spontaneously.

The quantum mechanical interpretation is obtained by considering fluctuations around the classical minimum ν :

$$\phi = e^{i\frac{\xi\cdot\sigma}{\nu}} \frac{1}{\sqrt{2}} \begin{pmatrix} 0 \\ \nu + h \end{pmatrix}, \quad (1.2.5)$$

where h is a Hermitian physical Higgs scalar and ξ are fields that disappear from the physical spectrum when we apply a unitary gauge transformation, $U(\xi) = e^{-i\frac{\xi\cdot\sigma}{\nu}}$. After the gauge transformation, the covariant derivative becomes

$$(D_\mu\phi)^\dagger D^\mu\phi = M_W^2 W^{+\mu}W_\mu^- + \frac{1}{2}M_Z^2 Z^\mu Z_\mu + h \text{ terms}, \quad (1.2.6)$$

where $M_W = g\nu/2$ and $M_Z = \sqrt{g^2 + g'^2}\nu/2$ are the masses of the W and Z bosons. Using the weak eigenstates in the Lagrangian, the mass eigenstates of the physical gauge boson fields are

$$W_\mu^\pm = \frac{1}{\sqrt{2}}(W_\mu^1 \pm W_\mu^2) \quad (1.2.7)$$

$$Z_\mu = -\sin\theta_W B_\mu + \cos\theta_W W_\mu^3 \quad (1.2.8)$$

$$A_\mu = \cos\theta_W B_\mu + \sin\theta_W W_\mu^3, \quad (1.2.9)$$

where the A_μ and Z_μ fields, given in terms of weak angle $\tan\theta \equiv g'/g$, are the physical neutral fields for the massless photon (γ) and the massive weak boson (Z^0),

respectively.

The Higgs potential in Eq. 1.2.3 after gauge transformations becomes

$$V(\phi) = -\frac{\mu^4}{4\lambda} - \mu^2 h^2 + \lambda \nu h^3 + \frac{1}{4}\lambda h^4. \quad (1.2.10)$$

The second term in this potential represents the mass of the scalar Higgs field:

$$M_h = \sqrt{-2\mu^2} = \sqrt{2\lambda\nu}, \quad (1.2.11)$$

which is the mass of the well-known Higgs boson. The weak scale is given as $\nu = 2M_W/g \simeq 246$ GeV; however, the quadratic Higgs coupling λ is unknown. Therefore, the Higgs mass M_H is not predicted by the SM.

The Higgs boson was observed in 2012 [20, 21] and its mass is measured to be 125.09 ± 0.21 (stat) ± 0.11 (syst) GeV [22] using the combination of ATLAS and CMS results. The precision measurements of the properties of this particle such as spin and parity show that the new boson is consistent with the SM Higgs prediction. However, more precise measurements are still needed. In Chapter 6, we present a search for a very small anomalous Higgs couplings to vector bosons in the associated Higgs production channel with Higgs decaying to a pair of bottom quarks using the 8 TeV p-p collision data collected by the CMS detector in 2012 [29].

1.3 The Hierarchy Problem

In the previous section, an elementary Higgs field is introduced in order to give mass to W, Z bosons and fermions. The measured mass of the Higgs boson is close to the W boson mass, which make the model self-consistent. However, the mass scale of the electroweak interactions $\mathcal{O}(10^2)$ GeV is orders of magnitude smaller than the Planck scale $\mathcal{O}(10^{19})$ GeV, which is the mass scale at which the gravitational

interactions become important or the energy scale of the Grand Unification Theory (GUT) $\mathcal{O}(10^{15})$ GeV. In order to have a valid theory up to the Planck scale or GUT scale, very large fine tuning is necessary to the Higgs mass due to the effect of radiative loop corrections. This is known as the hierarchy (fine-tuning) problem.

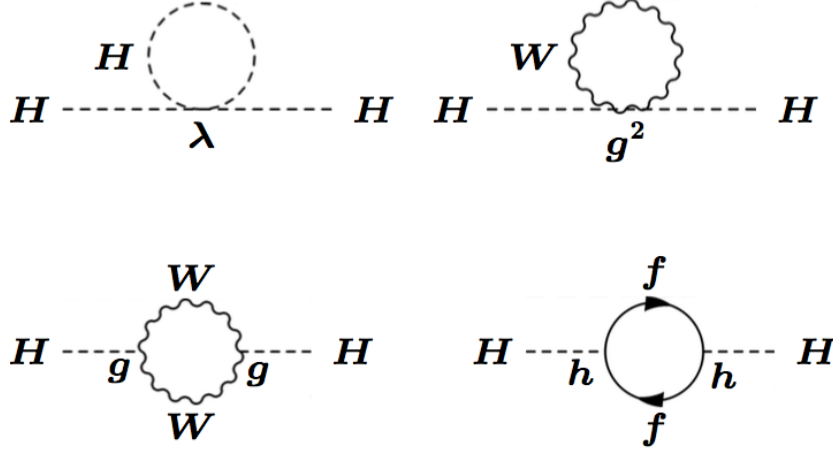


Figure 1.3.1: Radiative corrections to the Higgs mass: (top-left) self-interactions, (top-right and bottom-left) interactions with gauge bosons, and (bottom right) interactions with fermions [6].

All SM particles receive radiative loop corrections to their mass

$$M_h^2 = M_{h,bare}^2 + \mathcal{O}(\lambda_f, g^2, h^2)\Lambda^2, \quad (1.3.1)$$

where Λ is the energy scale that should at least be the new physics energy scale. While mass of the fermions gets logarithmic corrections, the scalar particles receive quadratic corrections. When these corrections are applied to the bare (tree-level) Higgs mass from the loop diagrams in Fig. 1.3.1, the Higgs mass quadratically diverges. The largest corrections to Higgs mass come from the heaviest particle in the SM; the top quark, which can be expressed as

$$M_h^2 = 2\lambda\nu + \frac{\lambda_t^2}{8\pi^2}\Lambda^2 + \dots, \quad (1.3.2)$$

where λ_t is the coupling constant between the Higgs boson and the top quark. If there is no physics beyond the standard model, the next energy scale will be the Planck scale, Λ_P , and an unnatural fine-tuning is required to cancel out this contribution from the loop-corrections to order of $M_h^2/\Lambda_P^2 = \mathcal{O}(10^{34})$.

Many extensions of the SM suggest new physics at the TeV scale to address this hierarchy problem. For example, Supersymmetry introduces a new heavy scalar partner called "stop" to the SM fermionic top quark, which cancels out the top quark loop corrections to the Higgs mass. There are also non-supersymmetric models that predict heavier partners to top quark. In Little Higgs models, several heavy top quark partners (also called vector-like quarks) are introduced which cancel the quadratic divergence.

Another possibility to address the hierarchy problem is to assume the Higgs boson to be a composite particle as in the composite Higgs models, rather than an elementary particle as predicted in the SM. In these composite Higgs models, a Higgs boson may have decays as predicted by the SM. Some of these models predict a heavy fermionic partner to the SM top quark with a charge of $5e/3$ and a search for this model is presented in Chapter 7 using the 13 TeV p-p collision data collected by the CMS detector in 2015 [30].

Chapter 2

The Compact Muon Solenoid Experiment at the Large Hadron Collider

2.1 The Large Hadron Collider

The Large Hadron Collider (LHC) is one of the most important recent projects in particle physics. It was built in the existing Large Electron Positron (LEP) collider tunnel at CERN which straddles the border of Switzerland and France. It has a circumference of 27 km and is 50 to 200 m underground. It is designed to accelerate two proton beams up to 7 TeV in opposite directions and collide them at a center-of-mass energy of 14 TeV at four interaction points. As many as 1232 superconducting dipole magnets are used to keep the proton beams in a circular trajectory (Fig. 2.1.1). There are 2808 bunches of protons circulating around the LHC in each direction with each bunch containing around 10^{11} protons. In each beam, the bunches are grouped into 39 trains [31]. Within each train successive bunches are spaced apart by 25 ns. Thus collisions occur at a maximum frequency of 40 MHz. The instantaneous

luminosity of the LHC is on the order of $10^{34} \text{cm}^{-2} \text{s}^{-1}$. The nominal LHC parameters are given in Table 2.1.

Table 2.1: The nominal LHC parameters.

Parameter	Value
Circumference	26.7 km
C.M. energy	14 TeV
Luminosity	$10^{34} \text{cm}^{-2} \text{s}^{-1}$
Time between collisions	25 ns
Number of bunches	2808
Number of particles per bunch	10^{11}

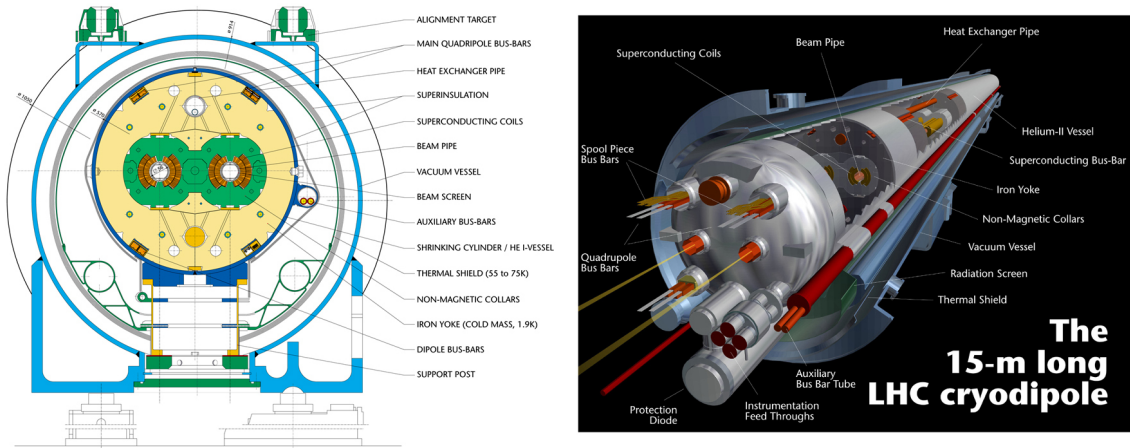


Figure 2.1.1: A superconducting dipole magnet of LHC.

The LHC is only the final stage of a series of accelerators which accelerate the protons to increasingly higher energies. The full accelerator complex is shown in Fig. 2.1.2. The protons are obtained by stripping the electrons from Hydrogen atoms and are injected into the first stage of the accelerator complex, Linac 2, which is a linear accelerator and accelerates the protons to 50 MeV. The protons are then transferred into the PS Booster, where their energy is increased to 1.4 GeV. The next stage after the PS Booster is the Proton Synchrotron where protons are accelerated to 26 GeV. The protons are then injected into the Super Proton Synchrotron (SPS)

which accelerates them to 450 GeV before they enter the LHC. The final stage of the accelerator complex, the LHC, can accelerate the proton beams up to 7 TeV.

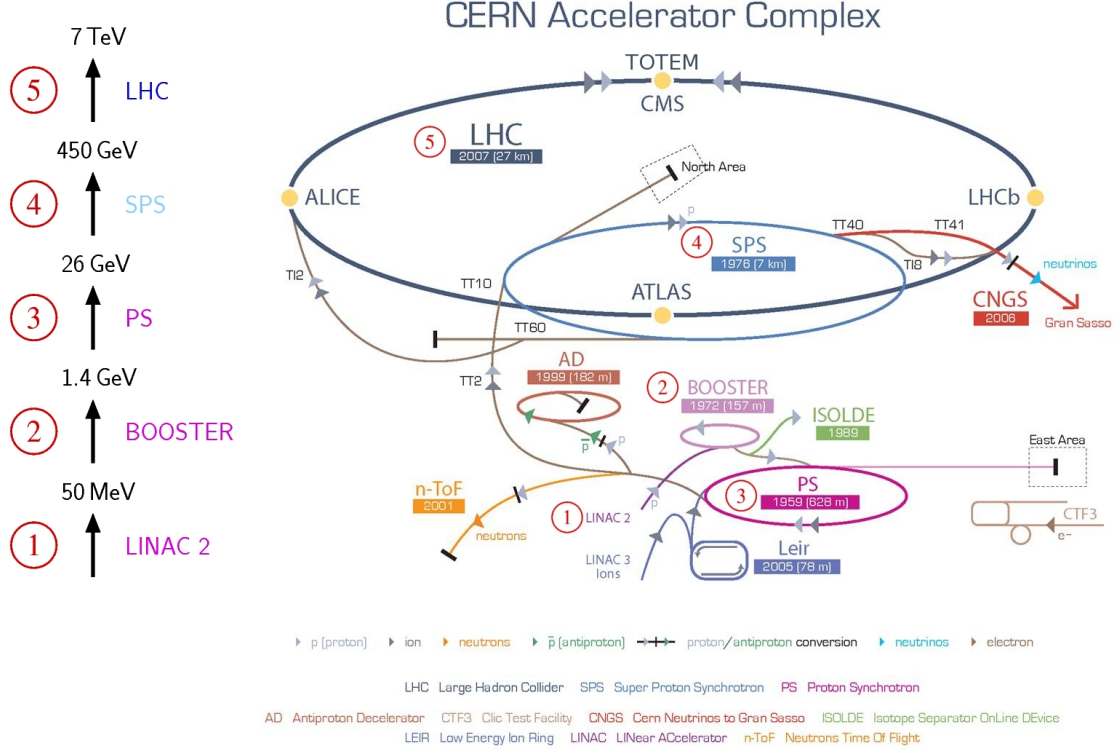


Figure 2.1.2: CERN accelerator complex with details of the various pre-accelerators before the proton beam enters the LHC ring.

There are four main experiments at the LHC: the Compact Muon Solenoid (CMS), A Toroidal LHC Apparatus (ATLAS), A Large Ion Collider Experiment (ALICE), and Large Hadron Collider beauty (LHCb). CMS and ATLAS are the two general purpose detectors, designed for physics studies at the highest LHC luminosity. The other two experiments, ALICE and LHCb, are designed for heavy ion physics and B meson physics at lower luminosities, respectively.

The number of events generated at the LHC for a particular interaction is

$$N = \sigma_{int} \int \mathcal{L} dt, \quad (2.1.1)$$

where \mathcal{L} is the instantaneous luminosity and σ_{int} is the cross section of the particular interaction process. When two bunches, each containing N_b particles, collide with revolution frequency f_{rev} , their instantaneous luminosity is given by

$$\mathcal{L} = \frac{N_b^2 n_b f_{rev} \gamma}{4\pi \epsilon_n \beta^*} R, \quad R = \frac{1}{\sqrt{1 + \left(\frac{\theta_c \sigma_z}{2\sigma_x} \right)^2}}, \quad (2.1.2)$$

where n_b is the number of bunches in each beam, γ is the relativistic factor of protons, β^* is beam beta function or the focal length at the collision point, ϵ_n is the transverse normalized emittance, and R is a luminosity geometrical reduction factor that is dependent on the crossing angle between the colliding beam θ_c and the transverse and longitudinal beam sizes.

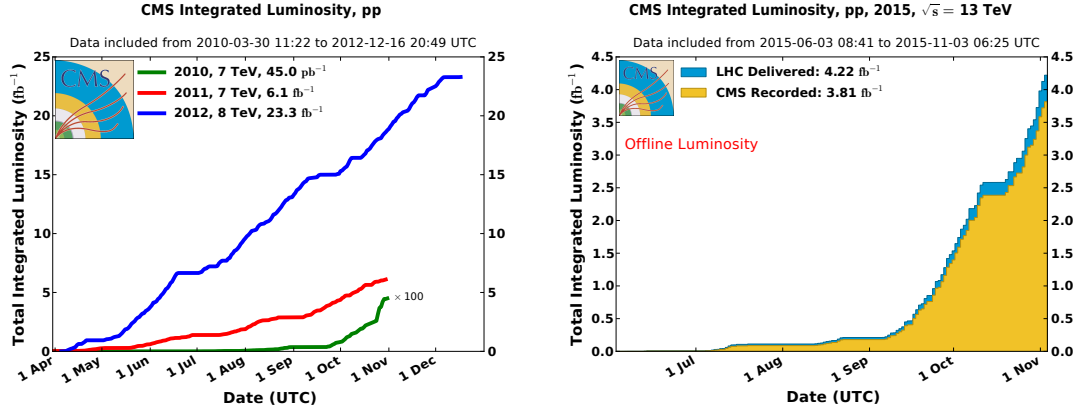


Figure 2.1.3: Total integrated luminosity delivered by the LHC to the CMS detector during (left) Run 1 from 2010 to 2012 at $\sqrt{s} = 7$ TeV and $\sqrt{s} = 8$ TeV and (right) Run 2 in 2015 at $\sqrt{s} = 13$ TeV.

The LHC was designed to run at $\sqrt{s} = 14$ TeV. However, during the initial run in 2008, one of the superconducting dipole magnets failed because of a faulty solder connection, leading to an explosion and damaging several other magnets. After the repairs, it was decided to run the LHC at lower energies. In 2010 and 2011, the LHC was operated at $\sqrt{s} = 7$ TeV and produced data sets of 45 pb^{-1} and 6 fb^{-1} , respectively. In the following year, 2012, the center-of-mass energy was increased to

8 TeV and the LHC delivered an integrated luminosity of 23 fb^{-1} . After a long shut-down in 2013 and 2014 for upgrades and maintenance, the LHC started operating again in 2015 at $\sqrt{s} = 13 \text{ TeV}$, which is close to design energy of the LHC and the highest energy ever reached at a collider. In 2015, the LHC delivered an integrated luminosity of 4.2 fb^{-1} (see Fig. 2.1.3).

2.2 The Compact Muon Solenoid

The Compact Muon Solenoid (CMS) Experiment [32], shown in Fig. 2.2.1, is designed as a general-purpose detector in order to meet the physics goals of the LHC. The central feature of the CMS detector is a superconducting solenoid that provides a magnetic field of 3.8 T. CMS is 28.7 m long, and 15 m high. It weights approximately 14000 tonnes. The beam pipe runs through the center of the detector as seen in the figure. The detector is centered on one of the LHC collision points. CMS has been designed to record the paths and energies of the particles emerging in all directions from the collisions at the center of the detector.

CMS features a series of concentric sub-systems, each sensitive to different types of particles produced in the collisions (see Fig. 2.2.2). The tracker is closest to the interaction point and measures the trajectories of charged particles. Surrounding the tracker is the calorimeter system. The calorimeter system is composed of the crystal electromagnetic calorimeter (ECAL), the hadron calorimeter (HCAL), and two forward calorimeters (HF), as indicated in Fig. 2.2.1. The calorimeters are designed to measure the energy of photons, electrons, and both charged and neutral hadrons. The tracker and the calorimeter system are surrounded by the superconducting solenoid which generates a magnetic field of 3.8 T allowing the momentum measurement of charged particles. The muon system is the outermost layer of the CMS detector and designed to measure the trajectory of the muons escaping the calorimeters.

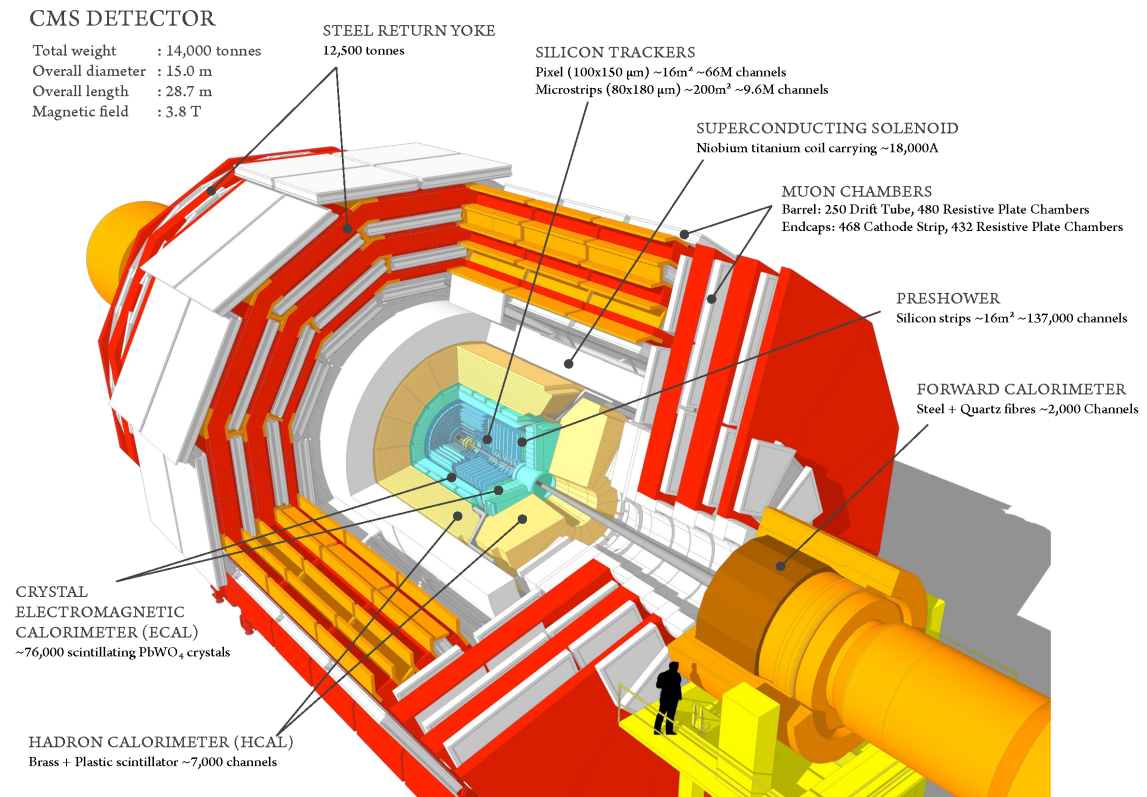


Figure 2.2.1: A three dimensional sketch of the CMS detector.

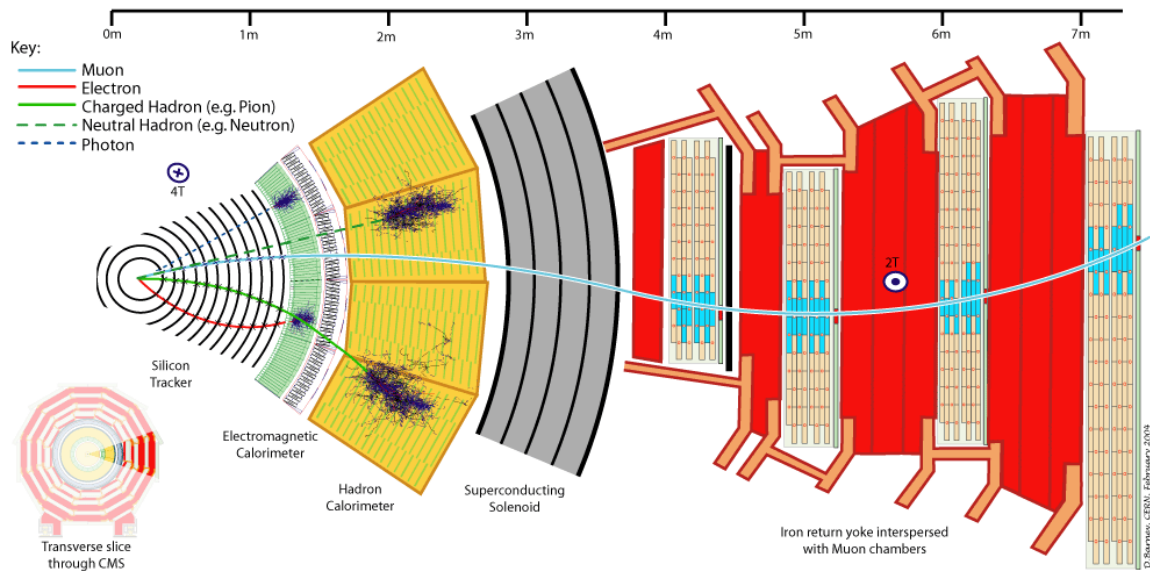


Figure 2.2.2: A slice of the CMS detector with different particle interactions with the sub-detectors.

A common coordinate system is used throughout CMS. The center of the detector (interaction point) is defined as the origin of the coordinate system. The z-axis runs along the anticlockwise beam direction. The x-y plane is perpendicular to the beam line, and is referred to as the transverse plane. The positive x-axis points from the interaction point to the center of the LHC ring; the positive y-axis points upward to the surface of the earth (perpendicular to the plane of the LHC). The transverse plane is often described in terms of $r - \phi$ coordinates. The azimuthal angle ϕ is measured relative to the x-axis in the transverse plane, around the beam. The radial dimension, r , measures the polar distance from the beam line. The polar angle θ is defined as the angle from the positive z-axis. The θ is often reported in terms of pseudorapidity, defined as

$$\eta = -\ln \tan \frac{\theta}{2}. \quad (2.2.1)$$

The distance ΔR is defined in $\eta - \phi$ plane as

$$\Delta R = \sqrt{\Delta \eta^2 + \Delta \phi^2}. \quad (2.2.2)$$

2.2.1 Tracker

The tracker, shown in Fig. 2.2.3, is the closest sub-detector to the interaction point. It is designed to measure the position, charge, and momentum of charged particles. The tracker is 5.8 m in length and 2.5 m in diameter. It operates in a 3.8 T magnetic field provided by the superconducting solenoid. The goal is to measure charged particles with transverse momentum between 100 MeV and 1 TeV.

Two types of semiconductor detector technologies are used in the CMS tracker: silicon pixels and silicon strips. Sensors consist of p-n junctions that are reverse biased up to high enough a voltage to deplete the entire sensor of free charge carriers.

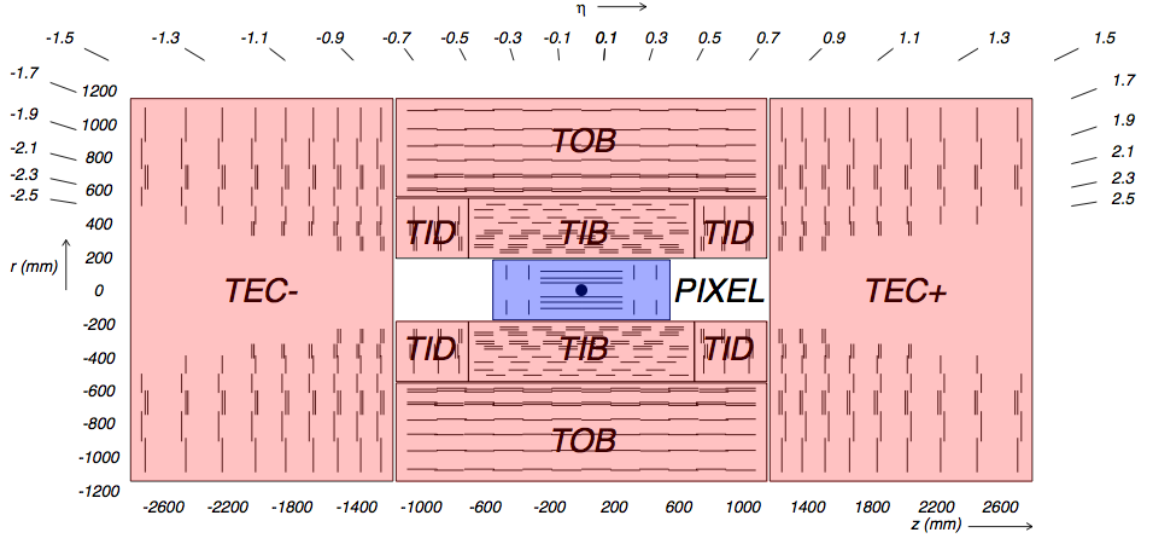


Figure 2.2.3: Schematic cross section through the CMS tracker in the r - z plane [7].

When charged particles pass through the silicon detectors, they produce electron-hole pairs, which are accelerated towards their electrodes with an applied electric field and produce a current. This current is recorded locally in the sensor, and used to identify the position of the particles passing through.

The silicon pixel detector is the closest detector to the collision point and provides the highest granularity which is important for vertex reconstruction. It is composed of 1,440 pixel modules in 3 barrel layers and 2 end cap disks on each side. These pixel modules cover an area of about 1 m^2 . There are over 66 million pixels. Each pixel has a rectangular dimension of $100 \times 150 \text{ } \mu\text{m}^2$ and provides position measurements of the charged particles passing through. The spatial track resolution of the pixel detector is about $20 \text{ } \mu\text{m}$.

The silicon strip tracker surrounds the pixel detectors. It consists of ten barrels in the central region and twelve end cap disks on each side, with a total of 15,148 silicon strip modules. The silicon strip tracker consists of four partitions: the tracker inner barrels (TIB), the tracker inner disks (TID), the tracker outer barrels (TOB), and the tracker end caps (TEC). The central region is divided into 4 layers of TIB

which are closed by 3 layers of TID on each side along the beam axis. In both TIB and TID partitions, each module has one sensor with a thickness of $320\text{ }\mu\text{m}$ and strip length of up to 12 cm . The TIB and TID partitions are surrounded by 6 layers of TOB which are closed by 9 layers of TEC on each side along the beam axis. In the TOB partition, each module has two sensors bonded together with a thickness of $500\text{ }\mu\text{m}$ and total strip length of up to 19 cm . The TEC partition employs both $320\text{ }\mu\text{m}$ (for the first 4 disks) and $500\text{ }\mu\text{m}$ (for the last 5 disks) thick sensors. The active silicon area of the CMS tracker is about 198 m^2 and it is the largest silicon tracker ever built.

2.2.2 Electromagnetic Calorimeter

After the particles pass through the tracker, they encounter the electromagnetic calorimeter (ECAL), which is designed to measure the energy of electrons and photons. The ECAL is a homogeneous, fine-grain, hermetic and compact calorimeter made out of 75848 lead tungstate (PbWO_4) scintillating crystals. In order to meet the LHC physics program goals, the ECAL was required to have good electromagnetic energy resolution, di-photon and di-electron mass resolution, coverage up to $|\eta| < 2.5$, measurement of photon direction, rejection of π^0 , and efficient photon and lepton isolation at high luminosities. Therefore, the ECAL is placed inside the superconducting solenoid magnet in order to reduce the material in front of it which would cause energy loss. This is achieved by a compact and homogeneous design using PbWO_4 crystals with high density of 8.28 g/cm^3 , a short radiation length of $X_0 = 0.89\text{ cm}$ (where X_0 is defined as $E(x) = E_0 e^{-x/X_0}$), and small Moliere radius of 2.2 cm .

The CMS ECAL consists of a barrel section (EB) and end caps (EE) on each side as shown in Fig. 2.2.4.

The ECAL barrel section covers a pseudorapidity range up to $|\eta| < 1.479$ and

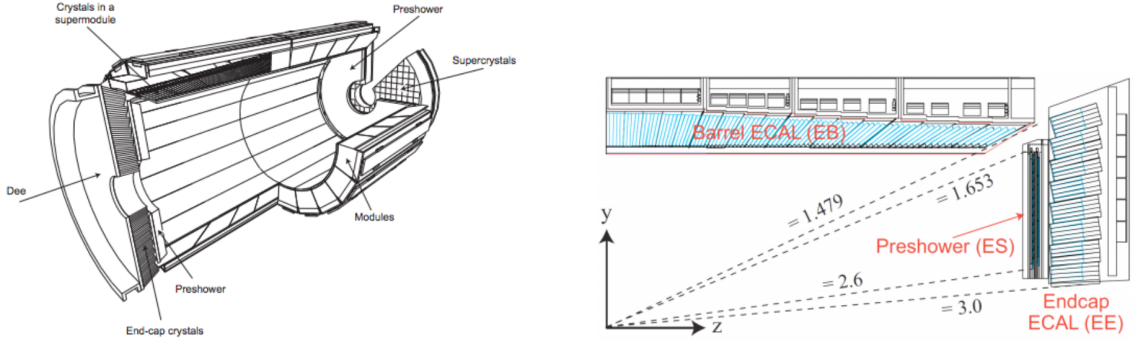


Figure 2.2.4: (Left) Layout of the CMS ECAL with the crystal module arrangements and (right) schematic cross section of one quarter of the ECAL showing the barrel and end cap regions.

contains 61,200 crystals. Each crystal is 23 *cm* long (or $25.8 X_0$) and has a front face cross section of around $2.2 \times 2.2 \text{ cm}^2$. This results in a solid angle coverage of 0.0174×0.0174 in the $\eta - \phi$ plane. In order to optimize the detector hermeticity to prevent particle disappearance between the crystals, each crystal is slightly tapered towards the collision point with an angle that points 3° away from the interaction point. The ECAL barrel section energy resolution for electrons is measured as a function of electron energy [33]:

$$\frac{\sigma_E}{E} = \frac{2.8\%}{\sqrt{E(\text{GeV})}} \oplus \frac{12\%}{\sqrt{E(\text{GeV})}} \oplus 0.3\%, \quad (2.2.3)$$

where the first term is the stochastic term caused by event-to-event fluctuations in the energy deposition, the second term is the noise term caused by the noise in the electronics, and the last term is a constant term mainly coming from non-uniformity of longitudinal light collection and energy leakage from the back of the ECAL crystals. For each EB crystal, scintillation light is read-out by avalanche photodiodes (APDs).

The ECAL end caps cover a pseudorapidity range $1.479 < |\eta| < 3.0$, placed at $|z| > 315.4 \text{ cm}$, and contain 7324 crystals on each side. EE crystals are identical, each measuring $2.86 \times 2.86 \text{ cm}^2$ and $3 \times 3 \text{ cm}^2$ at the inside and outside face, respectively,

with a length of 22 *cm* (or $24.7 X_0$). They are arranged into 5×5 supercrystals. For each EE crystal, scintillation light is read-out by vacuum phototriodes (VPTs).

The last element of the CMS ECAL is the preshower detector (ES) that helps with the separation of $\pi^0 \rightarrow \gamma\gamma$ from prompt photons. The ES detectors are located in front of the end caps and cover a pseudorapidity range $1.65 < |\eta| < 2.6$, contain silicon strip sensors to measure the deposited energy, and backed up by two layers of lead radiators to initiate electromagnetic showers.

2.2.3 Hadronic Calorimeter

The hadronic calorimeter (HCAL) is the outermost subdetector placed inside the superconducting magnet and surrounding the ECAL. The HCAL is a crucial part of the CMS detector and measures the energy and directions of particle jets and of missing transverse energy, which are essential for the identification of quarks, gluons, and neutrinos. In order to achieve good missing energy resolution, the hadronic calorimetry is required to cover a range $|\eta| < 5$.

The HCAL is separated into four subdetectors: the HCAL barrel (HB), the HCAL endcaps (HEs), the HCAL forward calorimeter (HF), and the HCAL outer calorimeter (HO). Figure 2.2.5 shows a schematic overview of the CMS HCAL with its four subdetectors. The HB covers a pseudorapidity range up to about $|\eta| < 1.4$ and consists of 18 azimuthal wedges of absorbers for each half-barrel (HB+ and HB-). The HE covers the pseudorapidity range $1.3 < |\eta| < 3.0$ and the range between 1.3 and 1.4 is shared by HB and HE. The HF extends the coverage to range $3.0 < |\eta| < 5.0$. Since the depth of a hadronic shower is typically greater than that of an electromagnetic shower, the HO is placed outside of the solenoid in order to increase the thickness of the calorimeter in the central pseudorapidity region.

The HB and HE are sampling calorimeters with plastic scintillator layers as active material and brass layers as absorbers. In order not to disturb the magnetic field from

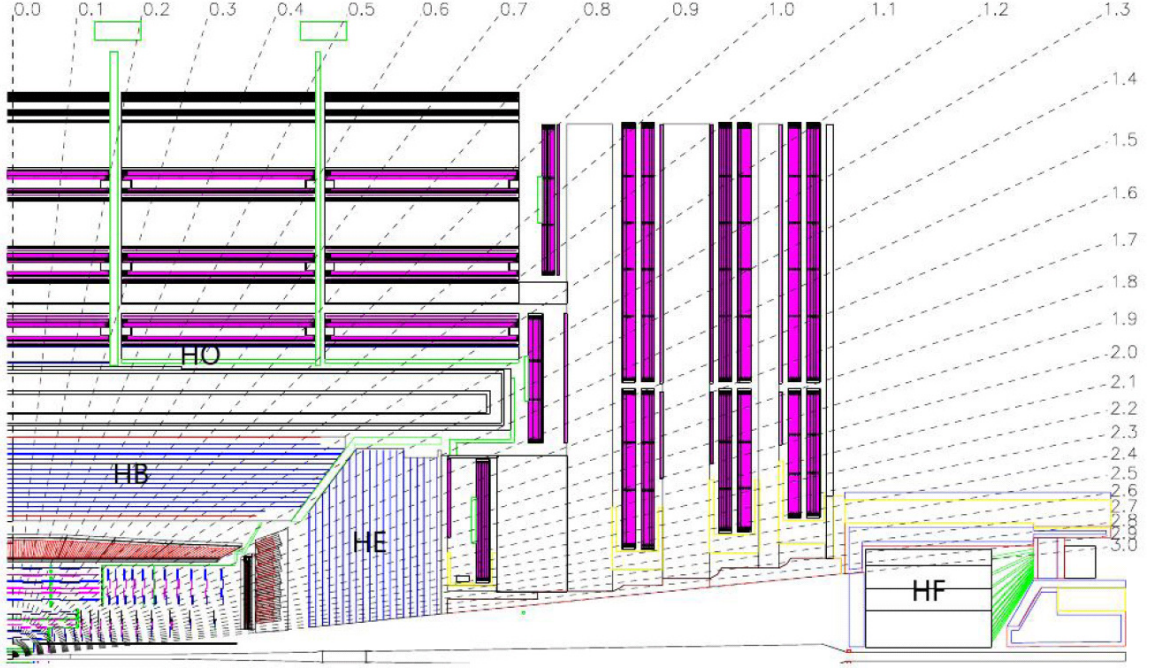


Figure 2.2.5: A schematic drawing of one quarter of the HCAL in the $r - \eta$ plane. Four HCAL parts are shown: the HCAL barrel (HB), the HCAL endcaps (HEs), the HCAL forward calorimeter (HF), and the HCAL outer calorimeter (HO).

the solenoid, non-magnetic material is chosen. The calorimeter tower granularity in η and ϕ for HB, HE, and HO is 0.087×0.087 . For HE however the granularity is approximately 0.17×0.17 for $|\eta| > 1.6$.

The HCAL energy resolution can be parameterized as was the ECAL energy resolution in the previous section. The energy resolution for HB and HE is given by

$$\frac{\sigma_E}{E} = \frac{90\%}{\sqrt{E(\text{GeV})}} \oplus 4.5\%, \quad (2.2.4)$$

and the HF energy resolution is

$$\frac{\sigma_E}{E} = \frac{172\%}{\sqrt{E(\text{GeV})}} \oplus 9.0\%, \quad (2.2.5)$$

where the first term is the stochastic term and the second term is the constant term.

2.2.4 Muon System

Muons interact weakly with ordinary matter and can travel through the CMS subdetectors, passing all the calorimetric systems without leaving a large fraction of their energy. Therefore, the muon system of the CMS detector is a tracking system located in the outermost region. A dedicated muon system is required to have hermetic coverage, properly identify muons, measure their momentum, and provide fast triggering for interesting events.

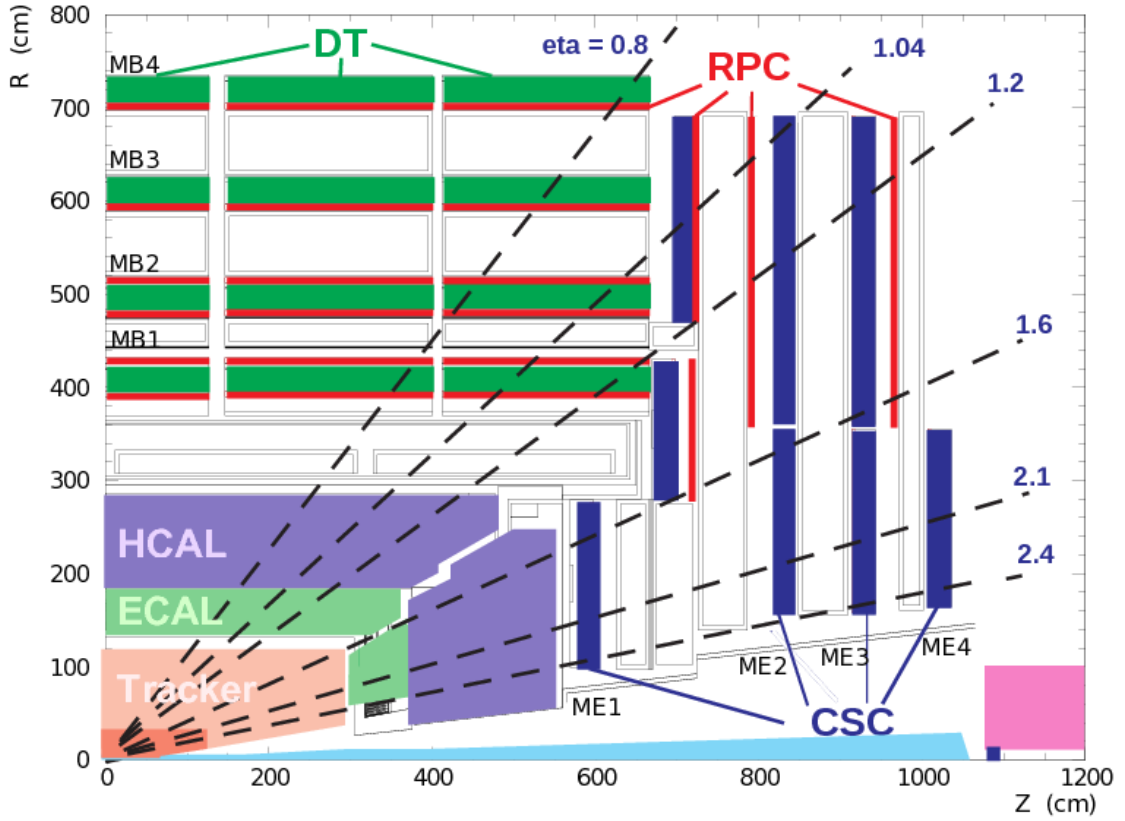


Figure 2.2.6: A longitudinal diagram of the CMS Muon system. The three subdetectors DT, CSC, and RPC are shown along with their coverage indicated as dashed lines at fixed η values.

The CMS muon system consists three types of gaseous detectors that are interleaved with iron return yoke of the solenoid: drift tube (DT) chambers, cathode strip chambers (CSC), and resistive plate chambers (RPC). The muon system uses DT

chambers in the barrel region covering the range $|\eta| < 1.2$, where the magnetic field is low. The CSC is used in the end cap regions covering the range $0.9 < |\eta| < 2.4$, where the magnetic field is high. The RPC system covers the region of $|\eta| < 1.6$ and is used both in the barrel and endcaps, providing fast, independent and highly segmented transverse momentum measurement. A schematic view of the CMS muon system can be seen in Fig. 2.2.6.

The barrel muon system has four stations (MB1 to MB4), each of which is arranged in twelve segments (each covering 30 azimuthal degrees) forming concentric cylinders with the beam line. The stations are interleaved with the layers of the flux return plates. There are a total of 60 aluminum drift chambers in the 3 inner cylinders and 70 chambers in the outer cylinder. The gas in the DT consists of 85% argon (Ar) and 15% carbon dioxide (CO₂) and is ionized when a charged particle traverses the chamber.

The endcap muon system also consists of four stations (ME1 to ME4) on each endcap with a total of 468 cathode strip chambers arranged in groups and overlapping in azimuth to maintain full coverage. The CSC chambers are also ionizing gas detectors, whose operating gas consists of 40% Ar, 50% CO₂, and 10% carbon tetrafluoride (CF₄).

The RPCs are designed as a complementary system in order to tag a signal faster than 25 ns, the LHC bunch crossing, and are placed both in the barrel and endcaps. Although they cover almost the same area as DTs and CSCs they do not provide as precise a measurement of the position and momentum, but instead a fast response. Thus, RPCs provide critical information for the Level 1 trigger and relate particles to their own bunch crossings.

2.2.5 Trigger System

The LHC delivers p-p collisions to CMS at high interaction rates, with bunch crossing intervals of 25 ns, corresponding to a bunch crossing frequency of 40 MHz. However, CMS can read out the detector only at a maximum frequency of up to 1 kHz. Therefore, the data from the detector needs to be reduced to a manageable level, which can be achieved by using a dedicated trigger design. CMS uses a two stage trigger system; the Level-1 trigger (L1) which is implemented at the hardware level, and the High Level Trigger (HLT) which is implemented in software.

The L1 trigger consists of custom designed and largely programmable hardware systems. Since there is a very limited time ($3.2 \mu s$) to make a decision at the L1 level, the triggering is done based on energy and momentum thresholds, specified by physics interests, using the information from the local energy deposits in calorimeter trigger towers and hits in muon chambers. The L1 trigger system reduces the event rate of 40 MHz to 100 kHz.

The next stage of the CMS trigger system is the HLT, which takes the input from the L1 trigger and makes further decisions at the software level. HLT is an on-line processing farm and has more time to make decisions. Complex reconstruction algorithms are executed at this level using information from all subdetectors. The HLT reduces the event rate of 100 kHz from L1 trigger down to $\mathcal{O}(100)$ Hz.

Chapter 3

Radiation Damage Monitoring of Leakage Currents in the CMS Strip Tracker

In this chapter, radiation damage monitoring studies of the CMS Strip Tracker are presented. As discussed in Chapter 2, the silicon strip tracker is located at the inner region of the CMS detector. Because it is close to the interaction point, the tracker is damaged due to radiation from hadrons and energetic leptons. In addition, the tracker was designed to run a 10 years of operational lifetime at an operational temperature of -10°C , which was not possible during Run 1 of the LHC due to sealing problems that led to condensations and the tracker needed to be operated at a higher temperature of 4°C . Therefore, it became more important to monitor the evolution of the detector properties with radiation damage and subsequent annealing. In this Chapter, we present simulations of the leakage current using well-known models parameterized from experimental studies [34] and environmental history of the detector such as temperature and fluence. The simulations are then compared to leakage current data from the CMS strip tracker. These simulations are useful for

estimating detector lifetime, optimizing detector lifetime with controlled annealing, and validating experimental parameterizations.

3.1 Parameterization of leakage current evolution with fluence and annealing

The change in the total leakage current with radiation damage and annealing is experimentally well-parameterized [8] and can be given by

$$I = I_0 + \alpha(t, T)\Phi_{eq}V, \quad (3.1.1)$$

where I_0 is the initial leakage current, Φ_{eq} is the 1 MeV neutron equivalent fluence, V is the volume of the sensor bulk, and $\alpha(t, T)$ is known as the current related damage rate dependent on the annealing time and the temperature during annealing process. After the removal of the unstable damage (see Chapter 4 for more detailed discussion), this parameter is a constant and has been confirmed in laboratory experiments where the fluence exposure is well-controlled. However, in a running experiment the fluence is distributed over long periods of an experimental run. The experimental parameterization of the current related damage rate is given by [8]:

$$\alpha(t, T) = \alpha_0(T) + \alpha_I \exp\left(-\frac{t}{\tau_I(T)}\right) - \beta \ln \frac{t}{t_0}. \quad (3.1.2)$$

Figure 3.1.1 shows the behavior of $\alpha(t, T)$ at different annealing temperatures. The value of $\alpha(t, T)$ and thus the leakage current decreases over time with annealing as a result of the recombination of defects from radiation damage, which is a desired

effect. The extracted parameters of Eq. 3.1.2 are as follows [8]:

$$\begin{aligned}
\alpha_0(T) &= -(8.9 \pm 1.3) \times 10^{-17} \text{ A/cm} + \frac{1}{T} (4.6 \pm 0.4) \times 10^{-14} \text{ AK/cm} \\
\alpha_I &= (1.23 \pm 0.06) \times 10^{-17} \text{ A/cm} \\
\frac{1}{\tau_I(T)} &= k_{0I} \times \exp\left(-\frac{E_I}{k_B T}\right) \text{ with } \begin{cases} k_{0I} = 1.2^{+5.3}_{-1.0} \times 10^{13} \text{ s}^{-1} \\ E_I = 1.11 \pm 0.05 \text{ eV} \end{cases} \quad (3.1.3) \\
\beta &= (3.07 \pm 0.18) \times 10^{-18} \text{ A/cm} \\
t_0 &= 1 \text{ min.}
\end{aligned}$$

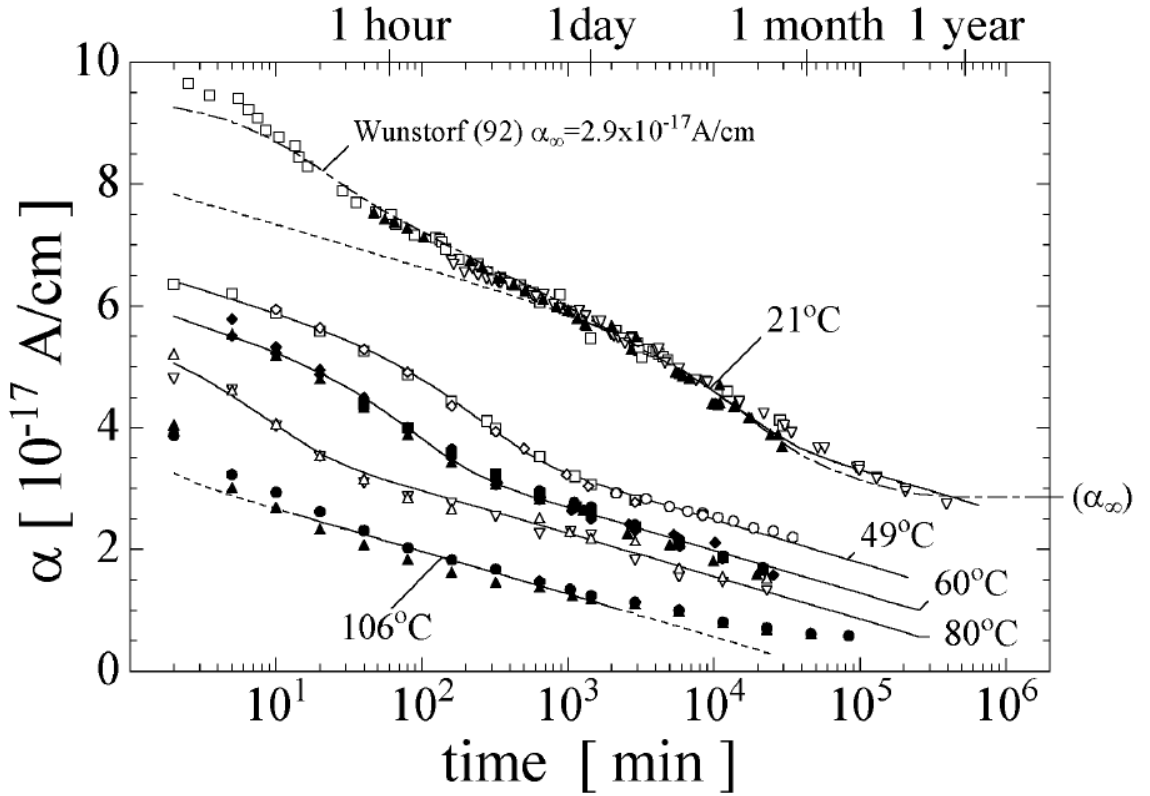


Figure 3.1.1: Current related damage rate as a function of annealing time for different annealing temperatures [8].

The leakage current is strongly dependent on the temperature at which it is measured. Therefore, it is useful to describe the temperature dependency of the leakage

current. In order to scale the leakage current measured at temperature T_0 to its equivalent at temperature T , we use

$$I(T) = I_0(T_0) \frac{T^2}{T_0^2} \exp \left[-\frac{E_{g,eff}}{2k_B} \left(\frac{1}{T} - \frac{1}{T_0} \right) \right], \quad (3.1.4)$$

where k_B is the Boltzmann constant and $E_{g,eff}$ is an effective band gap energy for silicon, which is measured to be 1.21 eV [35] using experimental data.

3.2 Monitoring tools in the CMS tracker

The leakage current is linearly dependent on the fluence and thus a significant limiting factor for the detector lifetime. High leakage current also results in higher detector noise and worse data quality. Therefore, a significant effort has been put into the development of the leakage current monitoring with high resolution. The environmental variables such as temperature, dew point, and relative humidity are also important to monitor. CMS tracker has different monitoring tools that are summarized below:

- **Detector Control System (DCS)** is the main interface to the hardware of the tracker and used for managing the operational states of the tracker, monitoring the voltages, currents, temperatures, and relative humidities as well as storing all this information in a dedicated database.
- **Detector Control Unit (DCU)** is an integrated circuit mounted on each silicon strip tracker modules, providing temperature and leakage current measurement from the sensor as well as operational low voltage measurement with very high granularity for each module of the strip tracker separately.
- **Power Supply Unit (PSU)** is the unit that provides voltage to bias the sensors. The leakage current can also be retrieved from PSU; however, the

PSUs are connected to multiple modules and therefore provide the total leakage current of the corresponding power group.

- **Programmable Logic Controller (PLC)** provides continuous measurement of the environmental variables. Even though the PLC readings are more stable compared to DCU readings, the PLCs are not available at the module level, but located at different position in the tracker volume; on the silicon, on the cooling pipes, or in the air.

3.3 Simulation Tool

In order to estimate the evolution of the leakage current in the tracker, a simulation tool [36] is built using Python programming language. The tool is an improved version of the tool originally developed by Christian Barth [1] using ROOT framework based on programming language C++.

The estimation of the leakage current is based on the parameterization described in the previous section. The input parameters required for the simulation are the fluence and the temperature history of the tracker. While an average fluence is calculated for each day, the temperature resolution of the simulation is increased by considering four different temperatures for each day depending on the tracker state.

The DCU readings from the beginning of the 2011 operations are taken to be the initial leakage current of the modules, where the raw leakage current readings are scaled to their reference value at $20^{\circ}C$ using Eq. 3.1.4. The impact of fluence is then calculated using the annealing time constants based on the given temperature on the respective day. The integrated sum over all days prior to a given day gives the resulting leakage current.

3.3.1 Fluence Estimation

The full fluence that the modules in the tracker are exposed to is calculated using the particle flux information from FLUKA [37], a general purpose Monte Carlo code to compute particle interactions with matter and electromagnetic fields, the inelastic p-p cross section, and the total integrated luminosity. The FLUKA simulations estimate the particle flux per p-p collisions for the whole tracker volume with 2.5 *cm* resolution in both the *r* and *z* directions. The total exposure of each module is calculated using the module position and volume information.

The p-p cross section is assumed to be 73.5 mb [38] for the Run 1 portion of the simulations. Even though this value is calculated for p-p collisions at 7 TeV, the same cross section is used for both the 7 and 8 TeV collisions as the reported values are consistent within uncertainties [39]. For the 13 TeV collisions, we assume a cross section of 79.1 mb decided from internal discussions with the FLUKA experts. This is in agreement with the recent ATLAS measurement [40]. Because it is a challenging measurement, the measurements of the cross sections from different experiments and collaborations are within ~ 10 mb.

The final piece of the fluence estimation is the luminosity. Two different luminosity values are stored in the CMS database; delivered and recorded luminosity. The delivered luminosity is the raw luminosity delivered by the LHC, while the recorded luminosity depends on the data taking efficiency of the CMS detector. However, the total damage on the tracker is described by the delivered luminosity. We extract the total integrated luminosity per day from the CMS database using the delivered luminosity. The full information is then used to estimate the total fluence for each day in the tracker history.

Table 3.1: Mapping of the tracker operational states from DCS to tracker states used in the simulation tool.

State	ON	OFF	STANDBY	SHUT-DOWN
ON	1	0	0	0
OFF	0	1	0	0
ERROR	0	1	0	0
DEAD	0	1	0	0
OFF-LOCKED	0	1	0	0
STANDBY	0	0	1	0
HVMIXED	0.5	0.5	0	0
LVMIXED	0.5	0.5	0	0
ON_CTRL	0	0.5	0.5	0
CTRLMIXED	0	0.5	0.5	0

3.3.2 Temperature Estimation

Estimation of the tracker temperature history is more difficult than the estimation of the fluence. Extracting the full temperature data for all the modules in the tracker for the entire tracker history is not practical. Therefore, the assessment of the temperature is done by defining certain operational tracker states in which the cooling plants in the tracker are set to a constant temperature and the module temperatures are approximately constant.

For each day in the simulation tool, we consider four tracker states: ON, OFF, STANDBY, and SHUT-DOWN. The states are defined by first checking the Low Voltage (LV) status in Power Supply Units (PSUs). If the LV is off, the tracker state is assumed to be SHUT-DOWN and the tracker is assumed to be at a constant temperature as the cooling plants are also shut-down during this time. If however the LV status is on, then the tracker is either in ON, OFF, or STANDBY state. These three states are further distinguished using the data from the DCS which manages the operational state of the tracker. The different operational states from DCS are mapped into tracker states used in the simulation as shown in Table 3.1.

The estimation of the temperature for the full history of the tracker depends on the four tracker states described above. When the tracker state is ON, we use

temperature readings from the DCUs, extracted from the beginning of Run 1 as shown in Fig. 3.3.1. Since the cooling plants are set to a temperature of 4°C during Run 1, these readings are assumed to be valid whenever the tracker state is ON, and shifted by -19°C for the Run 2 portion of the simulations as the tracker is cooled down to -15°C in Run 2 of LHC. The temperature map in Fig. 3.3.1 is extracted from readings on 3/19/2011. However, a slight temperature increase was found for some of the TID modules shortly after this date and therefore, TID module temperatures are updated from the readings on 4/25/2011 to cover this effect. We also use the DCU readings for the STANDBY state after shifting the values by -3°C , where the offset is determined from the average temperature difference between the DCU and PLC readings.

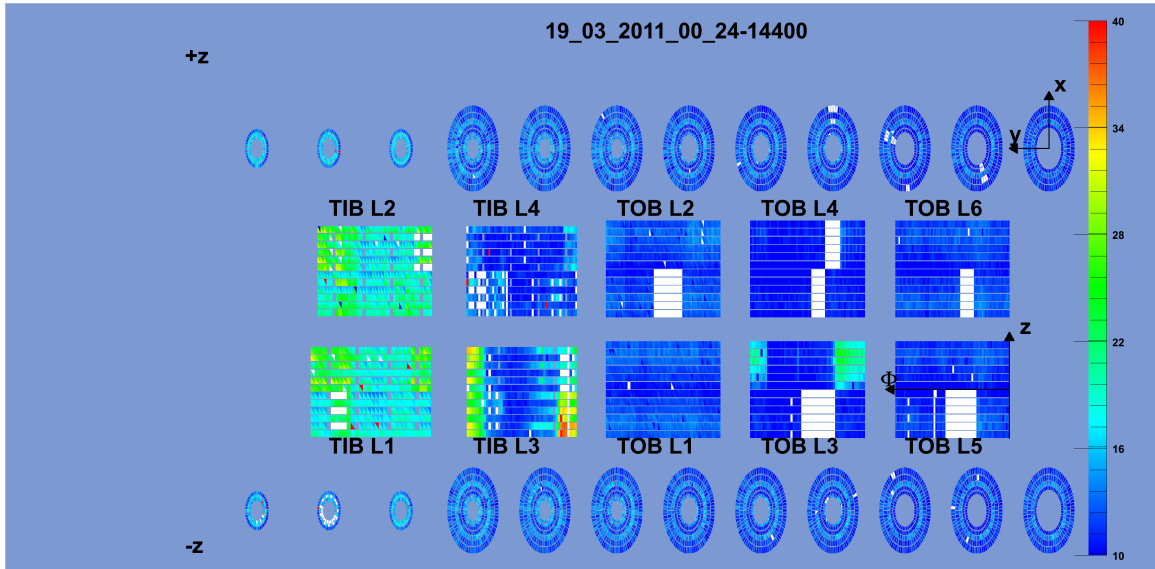


Figure 3.3.1: Map of the tracker modules with their temperature readings on 3/19/2011, when the tracker was on at the beginning of Run 1. Hot modules can be seen in TIB Layers 1 and 2 due to back-to-back mounting of the modules and in Layers 3 and 4 due to bad cooling contacts. White regions correspond to missing or uncalibrated DCU readings. The z-axis is in Celsius.

The temperature of the modules are set to a single temperature value averaged from the PLC readings when the tracker state is OFF or SHUT-DOWN. The average

temperature is calculated using several PLC temperature probes located on the silicon or in the air. The availability of the temperature probe locations for different tracker partitions are collected in Table 3.2. The average temperature is calculated using four probes located on the silicon in the TEC partition:

- TEC_minus_1.2.4.2.3_PLC_TSil
- TEC_minus_2.1.1.1.3_PLC_TSil
- TEC_plus_3.1.2.2.3_TSil
- TEC_plus_8.8.4.2.3_TSil

chosen from both +z and -z directions. Even though the PLC readings are more stable compared to DCU readings, there are still corrupted readings that need to be filtered out before averaging temperature. The filtering is done initially by removing the temperature values $> 30^0C$ and $< -20^0C$. Further filtering is done by comparing the temperature values from the above probes on the silicon to an average temperature reading calculated from the following probes in the air, which are more reliable.

- Monitor_PT1000_Minus_Bottom_Mid_TEC_TAir
- Monitor_PT1000_Minus_Top_Mid_TEC_TAir
- Monitor_PT1000_Plus_Bottom_Mid_TEC_TAir

The readings from silicon sensors that differ by more than 10^0C from the air temperature are also removed from averaging.

It is also important to consider the increase in the temperature of the sensor as a result of increased leakage current (thermal runaway). A finite thermal contact to the cooling system won't be able to control the sensor temperature at high leakage currents. Therefore, a dedicated measurement of this effect has been done and the details can be found in [1].

Table 3.2: The availability of the PLC temperature probes at different locations in the tracker [1].

Partition	on the silicon	on the cooling pipes	in the air
TIB	✗	✓	✗
TID	✗	✓	✗
TOB	✗	✓	✓
TEC	✓	✗	✓

3.4 Comparison of simulated and measured leakage currents

The performance of the simulation can be checked by comparing the simulated and measured leakage currents. Three types of plots have been considered in order to compare the simulation to measurements:

- A correlation plot between simulation and measurement including all the simulated modules. The correlation plots are produced for a given date.
- An overlay of simulated and measured leakage currents as a function of time for a given module.
- Average leakage current of each layer in TIB and TOB partitions as a function of luminosity.

The measured data used in the comparison to simulation are extracted from the DCU readings.

3.4.1 Correlation on a given date

Figures 3.4.1, 3.4.2, 3.4.3, and 3.4.4 show the simulated leakage current versus the measured DCU leakage current for several different dates. For each correlation plot a histogram of the relative deviation between simulation and measurement is also shown. The performance of the simulation is shown for different periods including the

beginning and end of Run 1 and LS1 and 2015 data-taking in Run 2. The simulated leakage current values are scaled to the measured temperature of the corresponding date, although modeled temperature already well-predicts the measured temperature of the respective date (see temperature correlation plots in Figs. 3.4.1 - 3.4.4).

As seen from the correlation plots, the majority of the modules are described by the simulation within $\sim 20\%$. A small fraction of the modules are outliers mostly due to corrupted DCU readings on the respective date and thus they are only local outliers. These are investigated in more detail in the following sections.

3.4.2 Evolution in time

The evolution of simulated and measured leakage current values over time is shown in Figs. 3.4.5 and 3.4.6, starting from 2011 operations at 7 TeV until the end of 2015 data-taking of Run 2 at 13 TeV. Each plot shows an example module chosen from each of the tracker partitions; TIB, TID, TOB, and TEC. The high fluctuations in the measured leakage current from DCU data are due to corrupted readings. Apart from the the fluctuations, it is visible that the overall behavior of the leakage current measurements is well described by the simulation. The sudden drop in leakage current near the right end of the plots is due to temperature change of the tracker in Run 2, when the detector cooling plant set temperature was changed to $-15^{\circ}C$ from $4^{\circ}C$.

3.4.3 Evolution with luminosity

In Fig. 3.4.7, average leakage current of each layer in the TIB and TOB partitions of the strip tracker as a function of integrated luminosity is shown. The leakage current values are scaled to their reference values at $0^{\circ}C$. The simulated leakage current is plotted in solid lines using directly the simulated data. The sudden drops in the leakage current corresponds to different technical stops or shut-down, during which the leakage current is annealed.

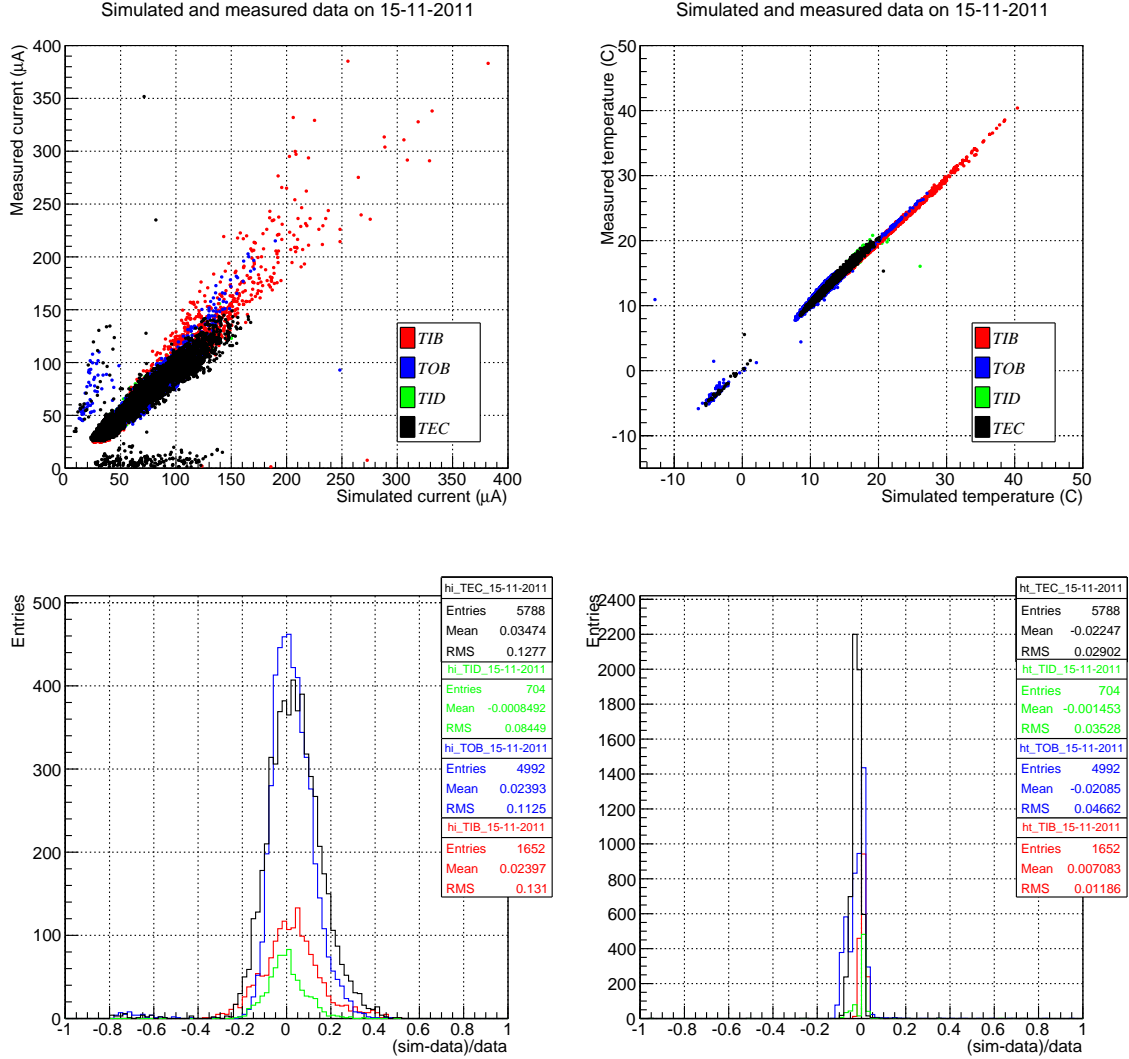


Figure 3.4.1: Comparison between simulated and measured (left) leakage currents and (right) temperatures on 11/15/2011, the beginning of Run 1. Each point in the correlation plot represents a module in the tracker, with different colors representing different partitions. The bottom plots show histograms of the relative deviation between the simulated and measured quantities.

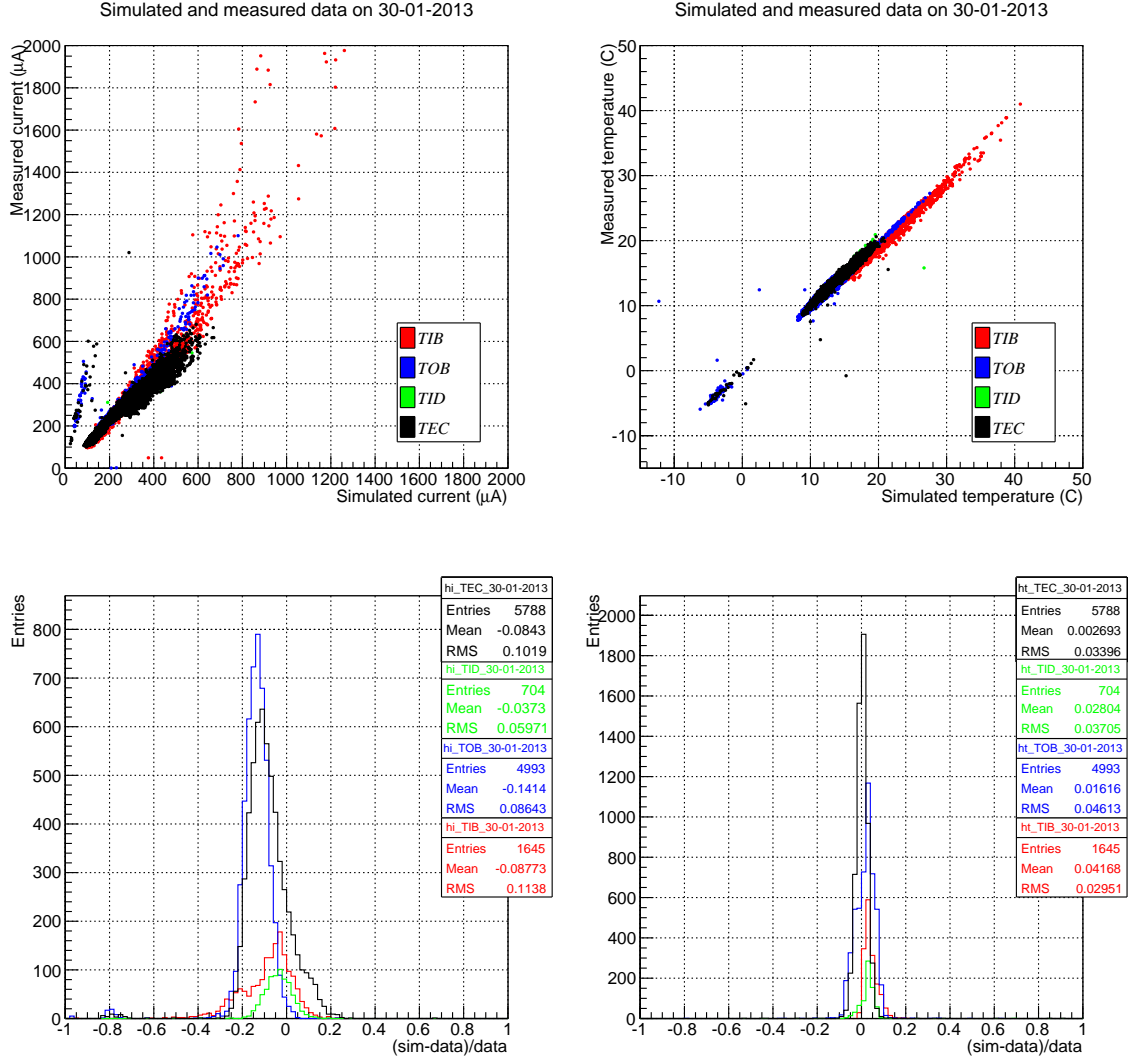


Figure 3.4.2: Comparison between simulated and measured (left) leakage currents and (right) temperatures on 1/30/2013, the end of Run 1. Each point in the correlation plot represents a module in the tracker, with different colors representing different partitions. The bottom plots show histograms of the relative deviation between the simulated and measured quantities.

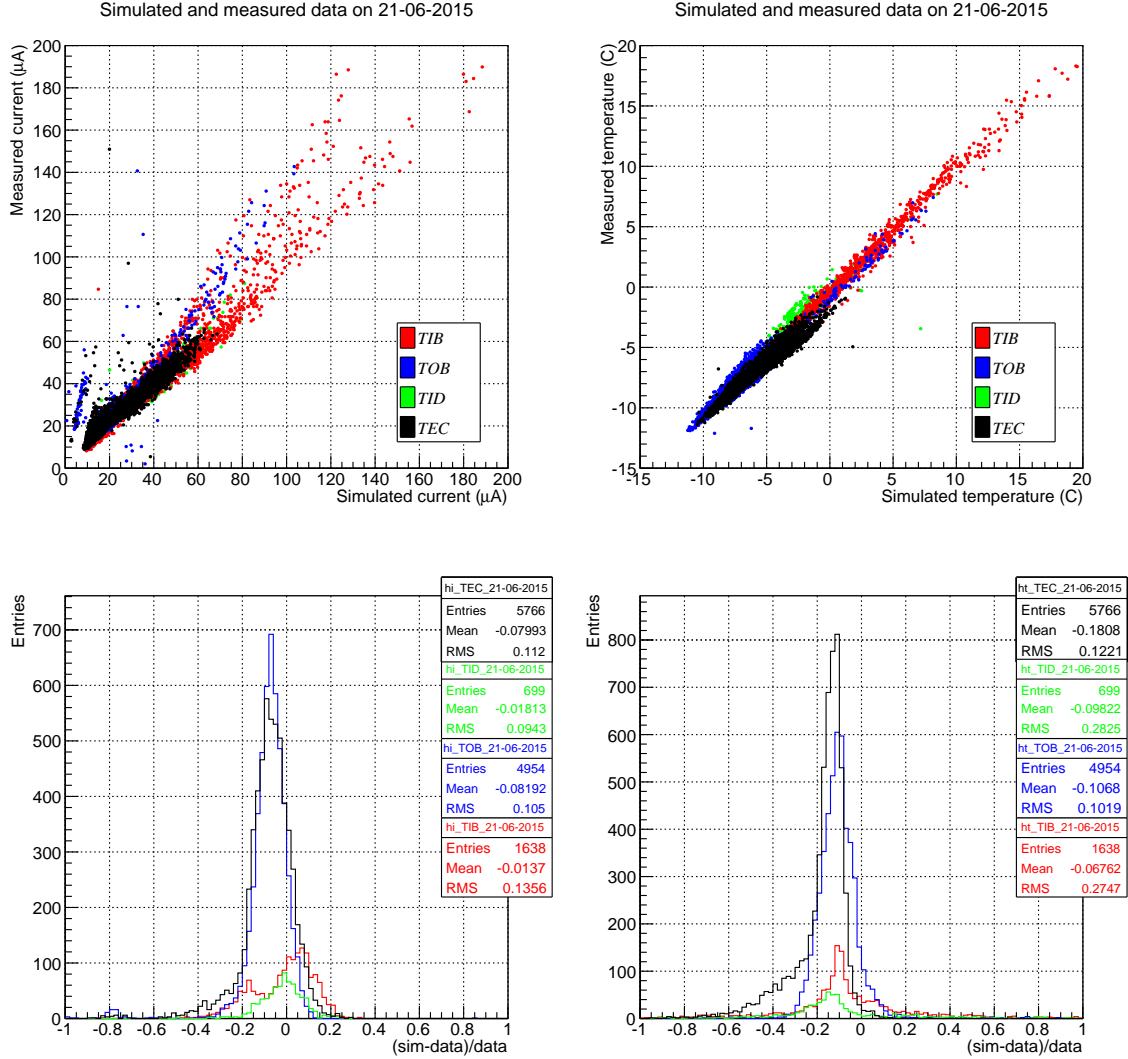


Figure 3.4.3: Comparison between simulated and measured (left) leakage currents and (right) temperatures on 6/21/2015, the end/beginning of LS1/Run 2. Each point in the correlation plot represents a module in the tracker, with different colors representing different partitions. The bottom plots show histograms of the relative deviation between the simulated and measured quantities.

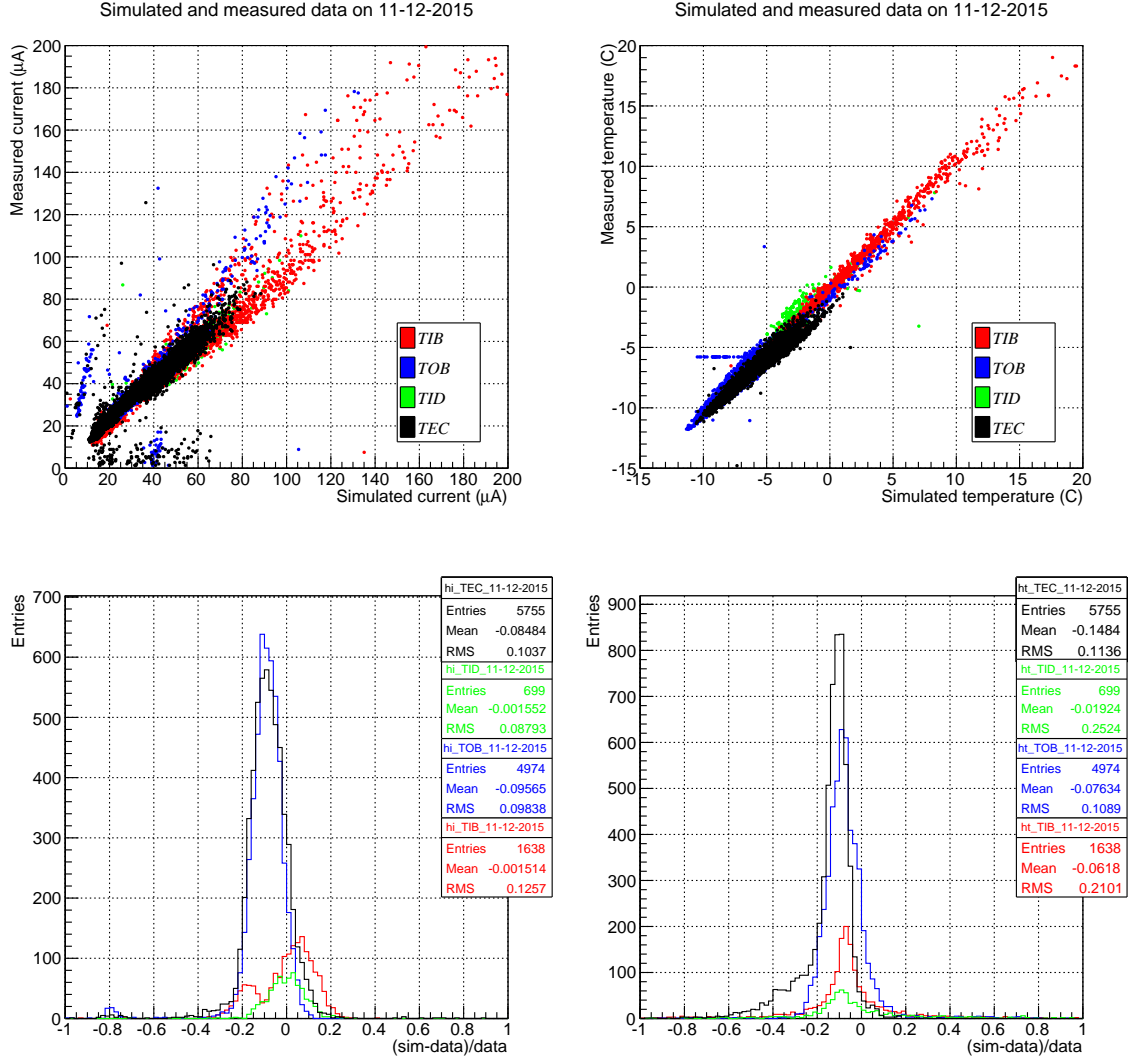


Figure 3.4.4: Comparison between simulated and measured (left) leakage currents and (right) temperatures on 12/11/2015, the end of 2015 data-taking in Run 2. Each point in the correlation plot represents a module in the tracker, with different colors representing different partitions. The bottom plots show histograms of the relative deviation between the simulated and measured quantities.

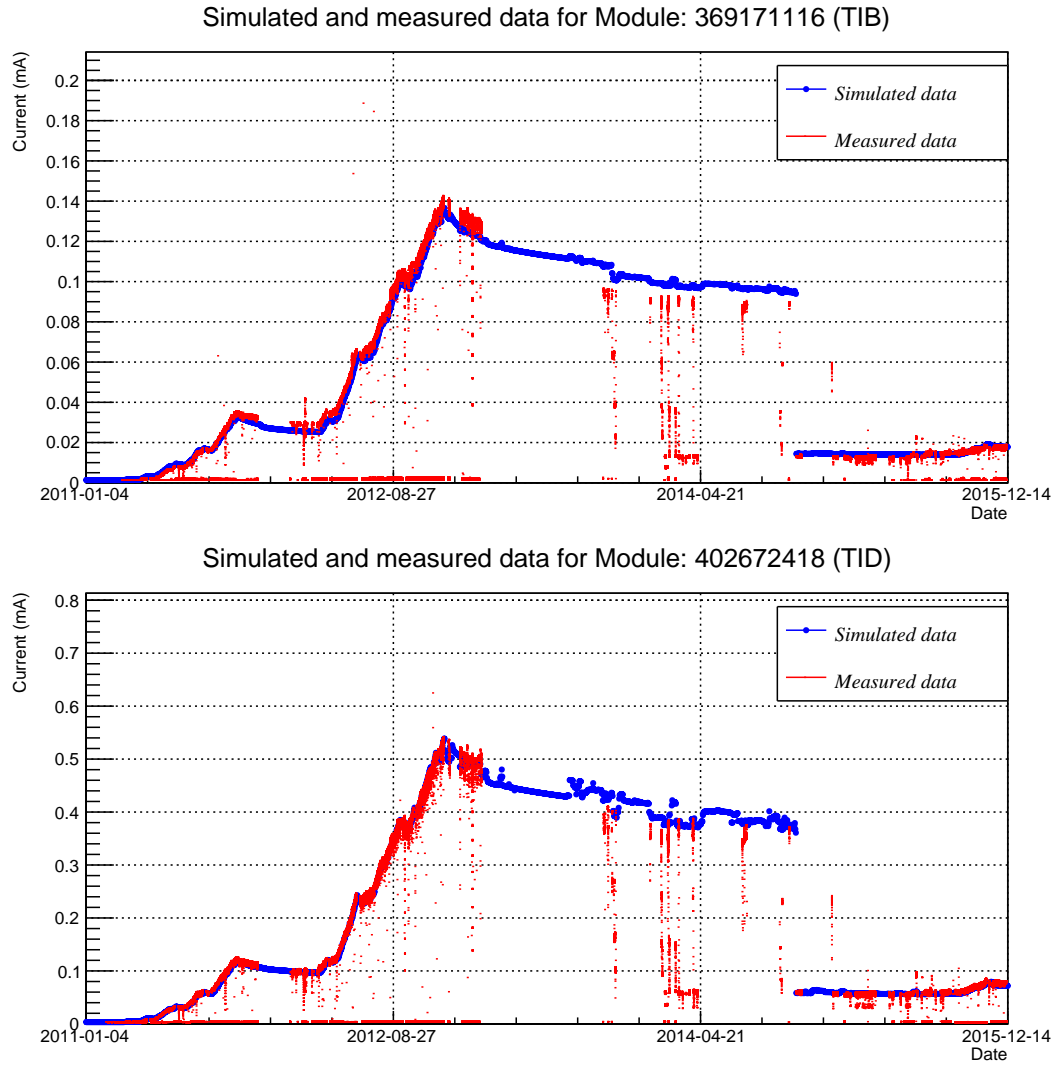


Figure 3.4.5: Comparison between simulated and measured leakage currents as a function of time for example modules in (top) TIB and (bottom) TID partitions.

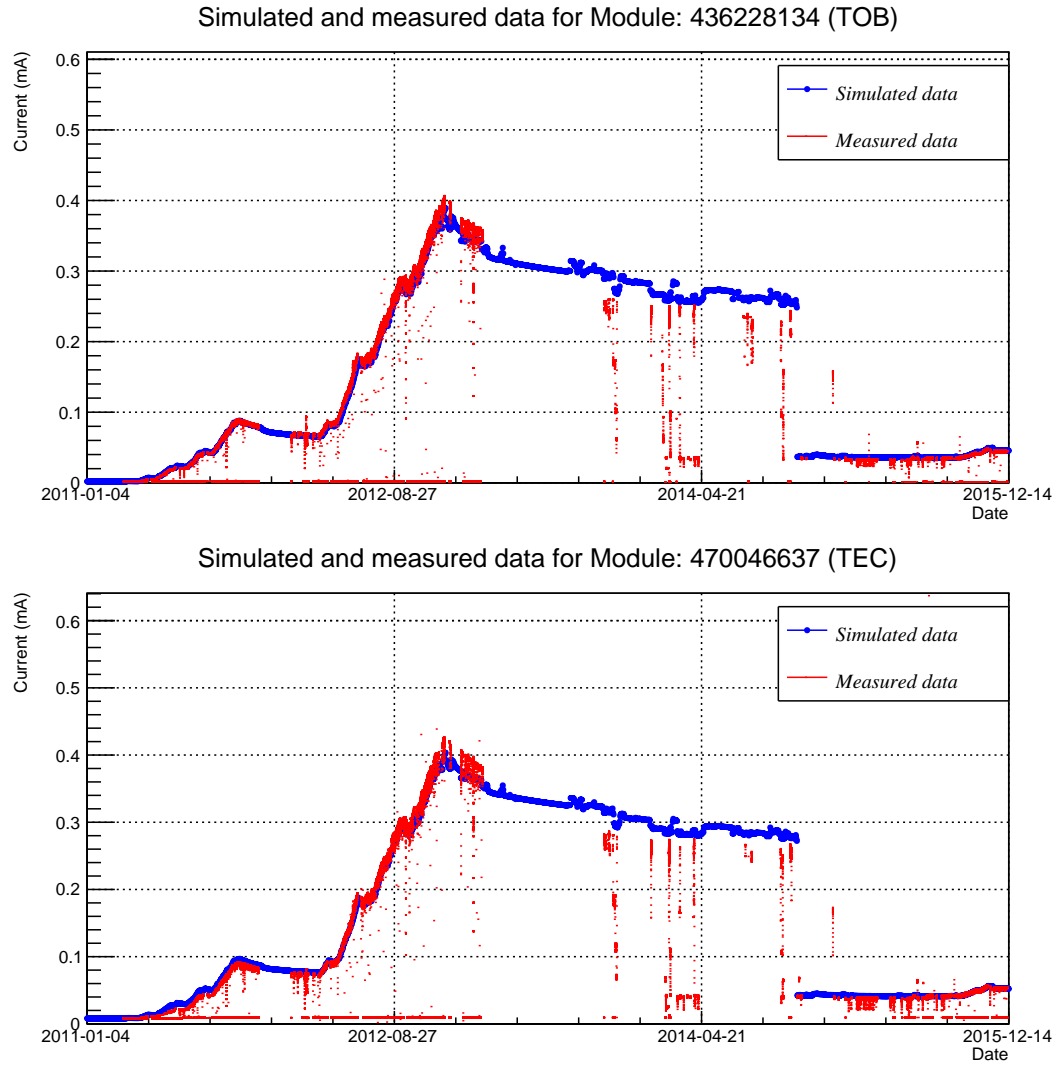


Figure 3.4.6: Comparison between simulated and measured leakage currents as a function of time for example modules in (top) TOB and (bottom) TEC partitions.

Due to technical difficulties with the extraction of the measured leakage current data from DCU readings, the measured leakage current, shown in Fig. 3.4.7 in dotted lines, are produced by deriving effective alpha values at various integrated luminosities. In Fig. 3.4.7, five periods where the leakage current increases linearly with the luminosity can be seen. Two or more different integrated luminosity values are chosen in order to extract an effective alpha value for each of these periods using the DCU readings at the luminosities shown with vertical dashed lines. These effective alpha values are then linearly extrapolated to represent the measured leakage current, shown with solid lines in Fig. 3.4.7.

In order to calculate the effective alpha values, DCU leakage current readings are extracted for all modules on given dates corresponding to integrated luminosities shown in Fig. 3.4.7 with vertical lines. The DCU leakage currents are scaled to their reference values at $0^{\circ}C$ and averaged over sensor volume of the module. Two example fits are shown in Fig. 3.4.8 for TIB and TOB, corresponding to fits for the effective alpha of the third period in Fig. 3.4.7. The effective alpha is defined as follows:

$$\frac{\Delta I}{V} = offset + \alpha_{eff}\Phi_{eq}. \quad (3.4.1)$$

Even though the effective alpha approach is an approximation of the real measured data, it can be seen that the performance is reasonably good especially for the TOB partition. The disagreement in the TIB partition is mainly due to hot modules. With the extraction of full DCU leakage current data, this discrepancy might go away, which is currently under study.

3.5 Investigation of outlier modules

A small portion of tracker modules are outliers as seen in Figs. 3.4.1 - 3.4.4. These outlier modules are often due to corrupted DCU readings for the time that the scatter

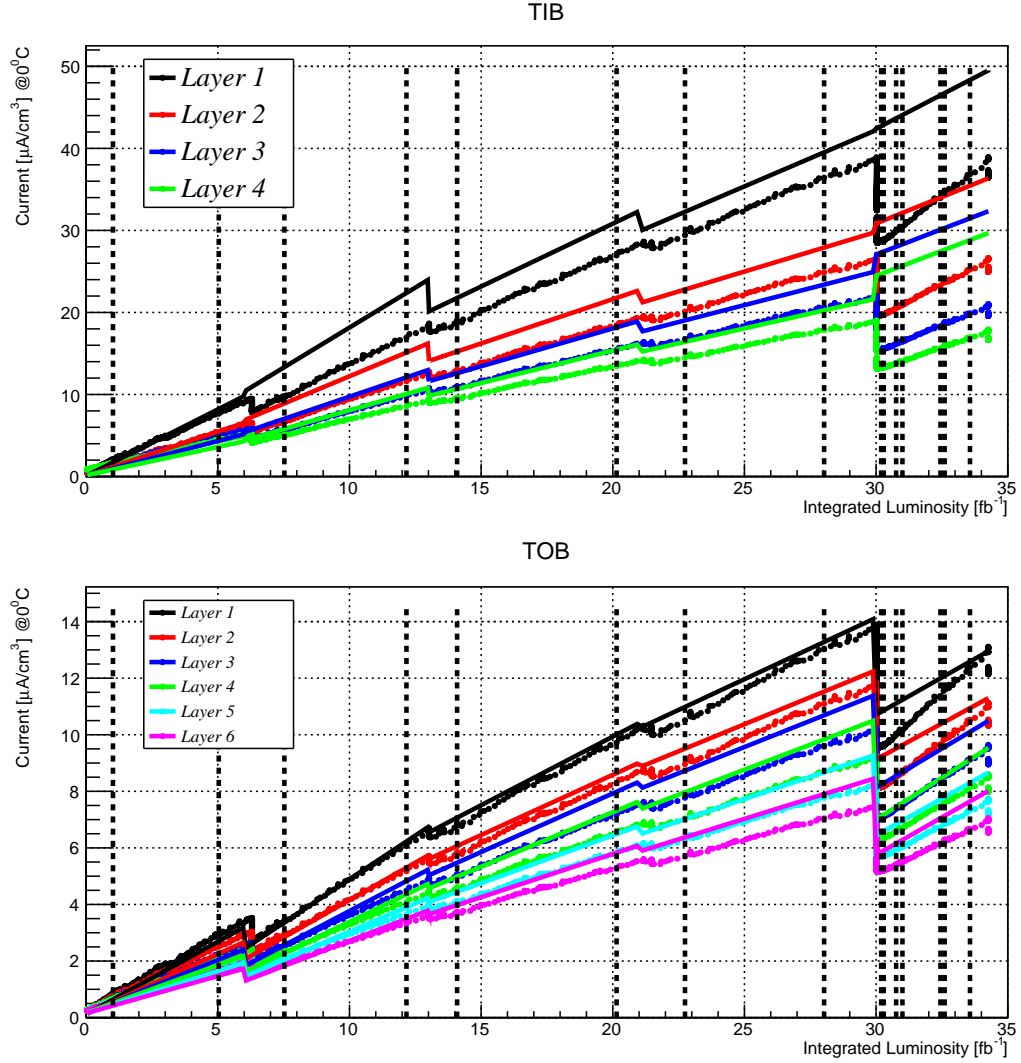


Figure 3.4.7: Leakage current as a function of luminosity. Each layer of (top) TIB and (bottom) TOB is shown in its own color. The dotted (solid) lines show the simulated (measured) data. See text for the details about how the measured lines are produced.

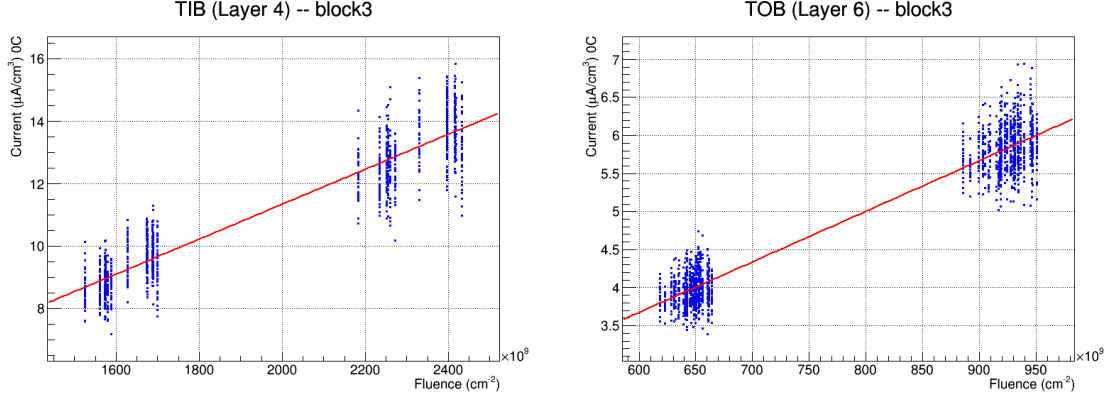


Figure 3.4.8: Normalized leakage current versus fluence for (left) TIB and (right) TOB with the effective alpha fits. Each data point corresponds to a module in (left) Layer 4 in TIB and (right) Layer 6 in TOB, measured at two different integrated luminosities of $14.1 fb^{-1}$ and $20.1 fb^{-1}$.

plot between simulated and measured leakage current data is made. Therefore, we have compared several correlations for different dates and picked the modules that are often outliers (i.e., they are global outliers rather than a local outlier at a specific time). We found around 90 such modules and investigated them in more detail. In order to understand the behavior of these modules, we compare their simulated and measured leakage current and temperature data to their neighbor in Fig. 3.5.1, where the neighbor module is taken to be the spatially closest module.

From Fig. 3.5.1, it can be seen that the neighboring modules have good agreement between their simulated and modeled temperatures, while the simulated leakage current describes the measured data only for one of them. The measured leakage currents of the neighboring modules are also close to each other as expected. However, the large temperature difference between these modules suggest that one of the temperature readings are wrong or uncalibrated. Because the modeled temperature also uses the DCU temperature readings, the leakage current simulation underestimates the measured data.

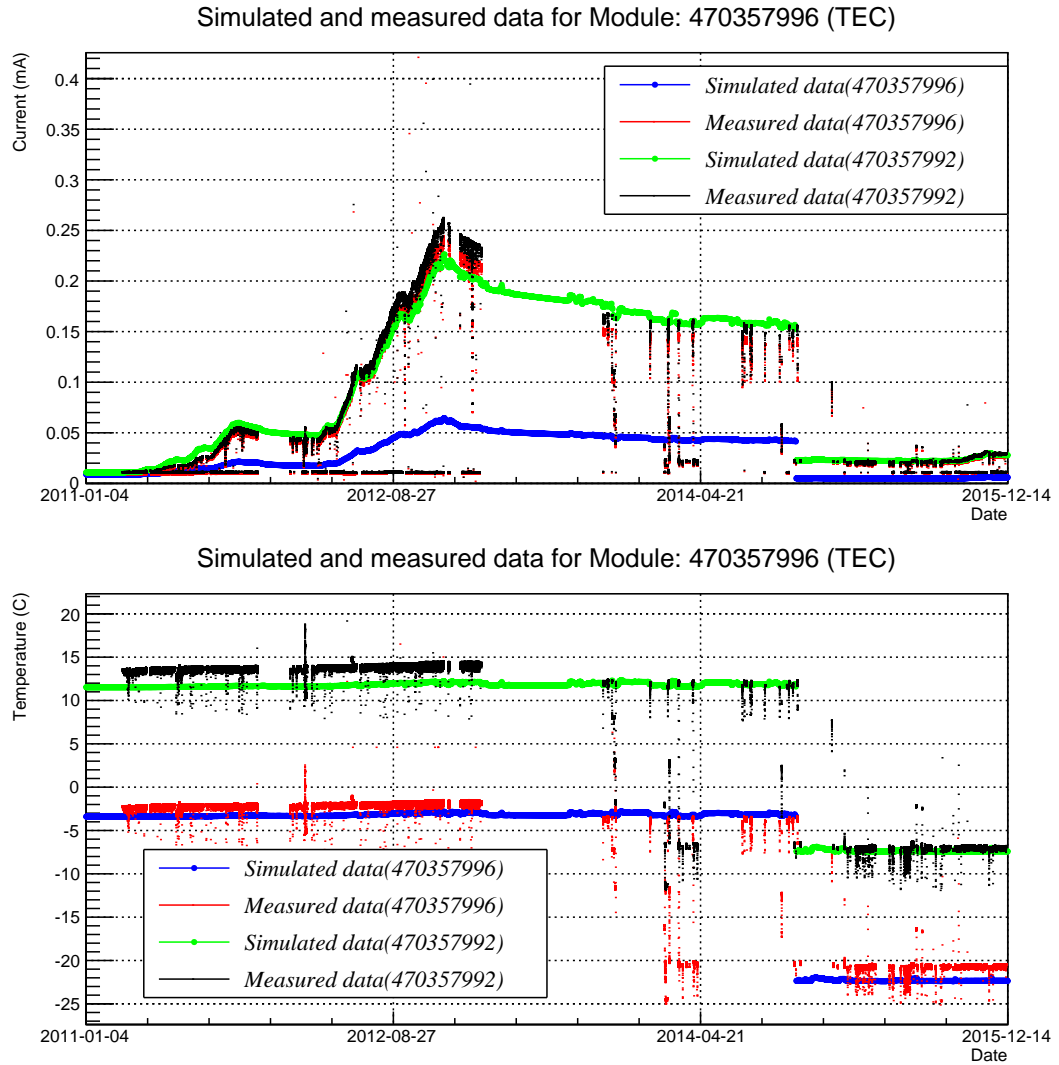


Figure 3.5.1: Comparison between simulated and measured (top) leakage currents and (bottom) temperatures as a function of time for an example outlier module in the TEC partition, compared to its neighbor.

Chapter 4

Radiation Damage Studies for the CMS Strip Tracker

In this chapter, radiation damage studies for the Phase-II Upgrade of the CMS detector performed in the Brown Silicon Lab is presented.

4.1 LHC Operations and Upgrades

In order to maintain and improve the performance the LHC has an upgrade plan with three phases: Phase-0, Phase-I, and Phase-II. From 2010 to early 2013, LHC operated successfully and delivered p-p collisions to the experiments at $\sqrt{s} = 7$ and 8 TeV. In 2013 and 2014, the first long shut-down, LS1, took place and during this time Phase-0 upgrade is done and COM energy is increased to $\sqrt{s} = 13$ TeV, the number of bunches per beam is increased to 2808 from 1380, and the bunch spacing is reduced to 25 ns from 50 ns. After the current run (Run 2) of the LHC, there will be a second long shut-down, LS2, in 2018 during which the Phase-I upgrade will take place. In Phase-I, the LHC peak instantaneous luminosity will be increased to $2.2 \times 10^{34} \text{ cm}^{-2}\text{s}^{-1}$, which is approximately twice the nominal value. The LHC is expected to deliver an integrated luminosity around 300-400 fb^{-1} by 2022.

The third stage of the upgrade plan is the Phase-II upgrade, which is anticipated to take place from 2023 through 2025. This third stage is also called the third long shut-down, LS3. This last upgrade will open up the so called High Luminosity LHC (HL-LHC) era. There will be major upgrades to the accelerator complex as well as the detectors. The LHC plans to upgrade its peak instantaneous luminosity to $2 \times 10^{35} \text{ cm}^{-2} \text{ s}^{-1}$ (which is 10 times the value before the upgrade) with an operational instantaneous luminosity of $5 \times 10^{34} \text{ cm}^{-2} \text{ s}^{-1}$ with a capability to deliver 250 fb^{-1} per year for a further 10 years of operation during HL-LHC. A comparison of nominal LHC and HL-LHC parameters is shown in Table 4.1.

Table 4.1: Comparison of nominal LHC parameters to those of HL-LHC [2, 3].

Parameter	LHC	HL-LHC
COM energy [TeV]	14	14
Peak luminosity [$\text{cm}^{-2} \text{ s}^{-1}$]	10^{34}	5×10^{34}
Maximum integrated luminosity per year [fb^{-1}]	40	>250
Bunches per beam	2808	2808
Bunch spacing [ns]	25	25
Protons per bunch	1.15×10^{11}	2×10^{11}
Average pile-up	27	140

4.2 Phase-II Upgrade of the CMS Strip Tracker

By the end of Phase-I by 2022 after about ten years of operation, the innermost subdetectors of the two general purpose detectors, ATLAS [41] and CMS [42], in particular the pixel and the strip detectors will reach the end of their lifetime mainly because of radiation aging. Therefore, a complete replacement of these current detector components will be necessary. Higher luminosity at the HL-LHC and thus higher fluence requires new detector design that is more radiation hard and has higher granularity due to the increased pile-up and thus the track density. Therefore, the limiting factors for the operability of the detectors need to be pushed further in order to meet the requirements of future experiments during the high luminosity phase at the LHC

(HL-LHC).

In this chapter, several different silicon detector designs are studied for the Phase-II upgrade of the CMS silicon tracker. Pad sensors made of different silicon materials and geometries were irradiated with 800 MeV protons. The change of the effective doping concentration resulting from the radiation damage was analyzed and Space Charge Sign Inversion (SCSI) of initially n-type sensors, to p-type-like sensors was observed. The influence of the beneficial annealing on the effective doping concentration and the sign of the space charge were investigated. Electrical properties were characterized before and after irradiation and during a subsequent isothermal annealing treatment. Depletion voltages and leakage currents were extracted from Capacitance-Voltage and Current-Voltage (CV-IV) measurements and the results were analyzed by means of the "Hamburg Model" [8].

4.3 Test Structures and Irradiations

Test structures we studied include pad detectors (diodes) produced from Float Zone (FZ), Oxygen Enriched FZ (DOFZ), Magnetic Czochalski (MCz) and Epitaxially (Epi) grown silicon, manufactured by CiS (Erfurt) and provided by RD50 collaboration as well as Thinned FZ (FTH) and MCz manufactured by Hamamatsu [43] and provided by the CMS HPK Campaign (discussion of silicon growth techniques can be found elsewhere; i.g., [8]). The test structures from RD50 collaboration have n-type silicon bulk, while HPK diodes are made of both n-type and p-type bulk silicon. The test structures have a variety of geometries with sensor thicknesses ranging from 50 μm to 300 μm and active areas of 25 mm^2 and 6.25 mm^2 . Various electrical characteristics can be found in Table 4.2. The initial depletion voltages before irradiation were measured using the experimental technique described in the following sections and other characteristics are calculated using the measurement results.

Table 4.2: The basic properties of investigated detectors.

Material	RD50 Collaboration					HPK Campaign			
	FZ	DOFZ	MCz	Epi	Epi	FTH	FTH	MCz	MCz
Type	N	N	N	N	N	N	P	N	P
Thickness [μm]	285	285	300	150	50	200	200	200	200
Active Area [mm^2]	25	25	6.25	6.25	25	25	25	25	25
Initial Dep. Vol. [V]	46	76	281	146	125	89	112	146	92
Initial N_{eff} [$\times 10^{11} \text{cm}^{-3}$]	12.4	7.5	41.3	80.5	657.3	29.3	36.9	48.1	30.2
Resistivity [$\text{k}\Omega\text{cm}$]	3.71	5.56	1.05	0.53	0.07	1.49	3.67	0.91	4.49

Table 4.3: Fluences achieved for test structures with 800 MeV protons.

Material	RD50 Collaboration					HPK Campaign			
	FZ	DOFZ	MCz	Epi	Epi	FTH	FTH	MCz	MCz
$1.7 \times 10^{13} n_{eq}/\text{cm}^2$	✗	✗	✗	✗	✗	✓	✓	✓	✓
$1.8 \times 10^{13} n_{eq}/\text{cm}^2$	✓	✓	✓	✓	✓	✗	✗	✗	✗
$4.3 \times 10^{13} n_{eq}/\text{cm}^2$	✓	✓	✓	✓	✓	✗	✗	✗	✗
$1.0 \times 10^{14} n_{eq}/\text{cm}^2$	✗	✗	✗	✗	✗	✓	✓	✓	✓
$1.3 \times 10^{14} n_{eq}/\text{cm}^2$	✓	✓	✓	✓	✓	✗	✗	✗	✗
$3.0 \times 10^{14} n_{eq}/\text{cm}^2$	✗	✗	✗	✗	✗	✓	✓	✓	✓
$4.6 \times 10^{14} n_{eq}/\text{cm}^2$	✗	✗	✓	✓	✓	✗	✗	✗	✗
$1.5 \times 10^{15} n_{eq}/\text{cm}^2$	✗	✗	✗	✗	✗	✓	✓	✓	✓

These proto-type detectors were then irradiated with 800 MeV protons at the LANSCE proton facility in Los Alamos, NM. The fluences that the test structures were exposed to are listed in Table 4.3 and the highest fluence achieved for the RD50 diodes is $4.6 \times 10^{14} \text{ MeV } n_{eq}/\text{cm}^2$, while for HPK diodes higher fluences up to $1.5 \times 10^{15} \text{ MeV } n_{eq}/\text{cm}^2$ was achieved.

After the irradiation the structures were stored in a freezer at temperature below -20°C to avoid uncontrolled annealing. The detectors were then studied during a subsequent isothermal annealing treatment by taking a series of IV-CV measurements at selected representative annealing steps.

4.4 Experimental Setup

In order to characterize the electrical properties of silicon materials such as full depletion voltage, leakage current, end capacitance, effective doping concentration, etc., we

have built a Capacitance vs. Voltage and Current vs. Voltage (CV-IV) measurement setup. Figure 4.4.1 shows a picture of the setup in the Brown Silicon Lab.

The detectors are biased from the rear electrode by applying a high voltage to the chuck to which the sensor is pressed by vacuum pumping. The bias voltage is applied by a Keithley 6517B HV source (+/-1000V) and the leakage current is measured using the same instrument. The connections to the front of the sensors are made with probes of a tip size of $7\text{ }\mu\text{m}$ and these probes can be moved in 3D using micro manipulators. The measurements can be performed at various temperatures ranging from over 80°C down to around -30°C using four Peltier elements and liquid coolant as heat sink for the Peltiers.

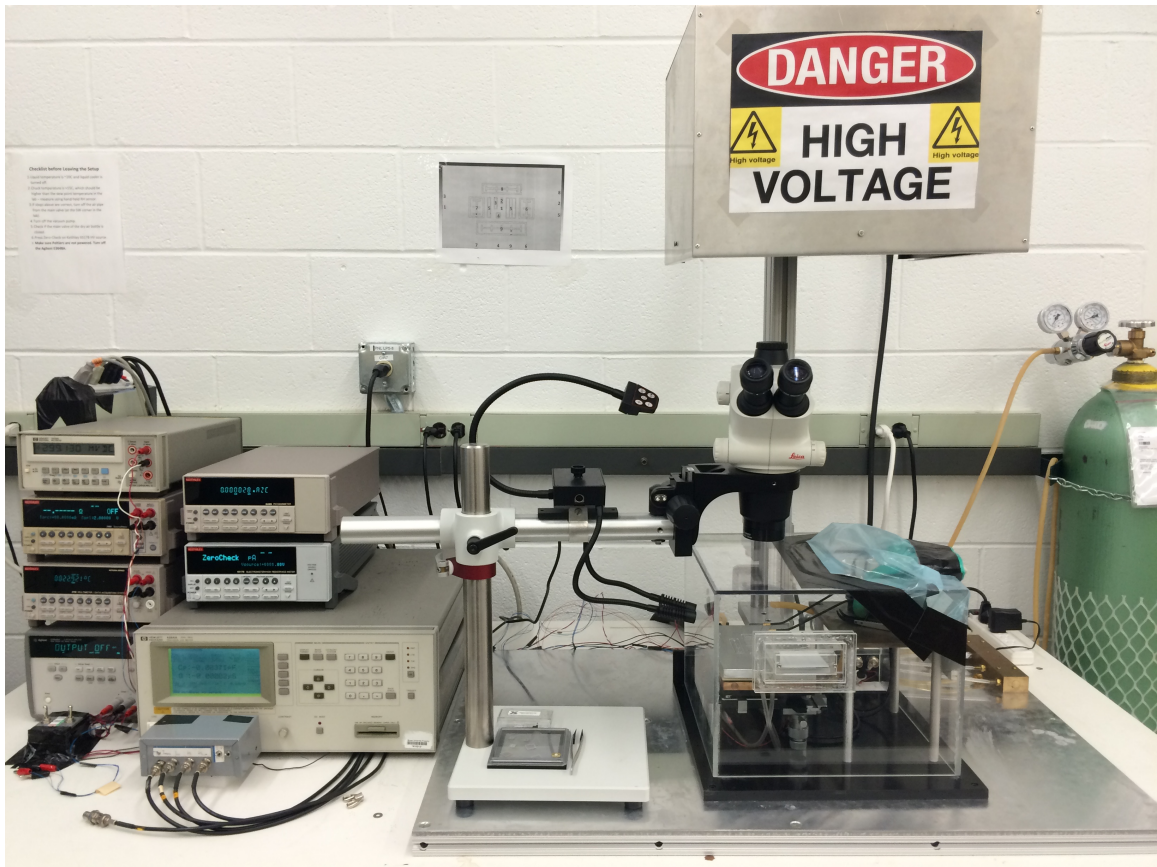


Figure 4.4.1: CV-IV setup for electrical characterization in the Brown Silicon Lab.

A large aluminum box encloses the chuck and micro manipulators to create a

dark environment during measurements in order to prevent the current created by light. Inside the aluminum box, there is a glove-box that also encloses the probe station and enables the inspection of the setup and changing the sensors between measurements without disturbing the dew point temperature inside. To prevent condensation problems at low temperatures, dry air is flushed inside the glove-box during low temperature measurements.

The measurement equipment is connected to a PC via a General Purpose Interface Bus (GPIB). The setup is fully controllable by a dedicated LabView program.

4.5 Depletion Voltage

The measurement of capacitance voltage characteristics of the diodes was used to extract full depletion voltage by performing two linear fits (before and after saturation) both to plots of $1/C^2$ vs bias voltage and to plots of $\log(C)$ vs $\log(V)$. However, only the results from the latter are presented as the two methods give similar results within uncertainties. Figure 4.5.1 shows an initial linear increase (decrease) in $1/C^2$ ($\log(C)$) with increasing bias voltage and reaches a near-horizontal plateau (saturation of capacitance) when the sensor is fully depleted. Therefore, the intersection of the two linear fits before and after the saturation is taken as the depletion voltage.

The leakage current is extracted from the current voltage measurements as the current corresponding to full depletion voltage. Since the current does not fully saturate even after full depletion (see Fig. 4.5.1), the leakage current is measured at 1.2 times the depletion voltage for HPK diodes, following the HPK campaign specifications. The measurements were taken at room temperature (without temperature control, but stable around $\pm 0.1^\circ\text{C}$) for the RD50 diodes, while the HPK diodes were measured at 0°C and -20°C , again following the HPK campaign specifications. The leakage current was then scaled to its reference value at 20°C [34].

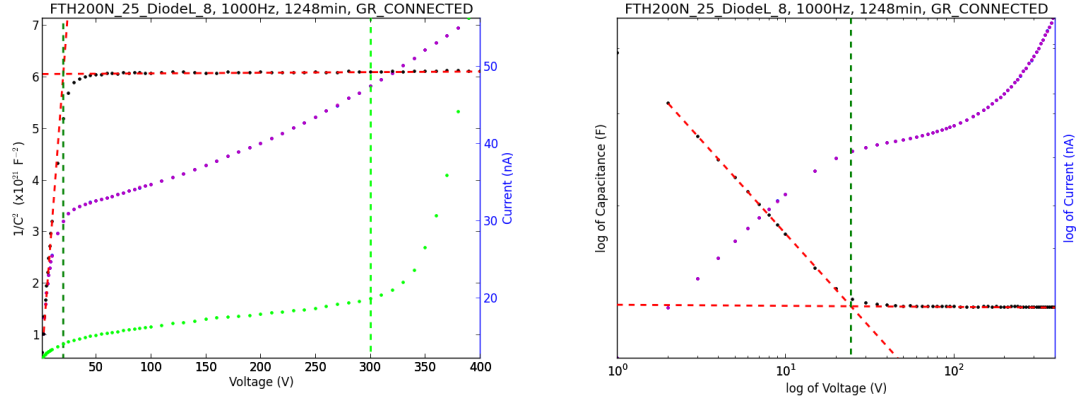


Figure 4.5.1: Illustration of two methods used to determine the depletion voltage from capacitance voltage measurements; (left) inverse square of the capacitance versus bias voltage and (right) capacitance versus voltage in logarithmic scale.

4.6 Annealing

It is important to investigate the detector characteristics during annealing as it gives important information about the lifetime and certain properties of the silicon detectors after irradiation. To study the annealing behavior of the detectors, an annealing experiment was performed using selected representative annealing steps up to 10,000 minutes. The experiment was performed by heating the sensors in an oven at 60°C for the initial short annealing steps, which allowed slower annealing and more time to better control the process. For longer annealing steps on the other hand we use a higher annealing temperature of 80°C, which allows faster annealing in shorter time as the annealing is strongly dependent on the temperature (for a comparison; removal of unstable damage (see Section 4.7) takes only about 8 minutes with annealing at 80°C, while this takes about 80 minutes at 60°C). After each annealing step capacitance voltage and current voltage measurements were taken to extract the sensor characteristics such as depletion voltage and leakage current at V_{dep} .

The typical annealing behavior of semiconductor detectors depends on the polarity of the detector after the radiation damage; n- or p-type. An n-type detector has a

bulk with positive effective doping concentration, the difference between donor and acceptor concentrations in the space charge region, while a p-type detector has a negative effective doping concentration. The radiation damage removes donors and/or introduces new acceptors in the bulk of the detector. In other words, it reduces the effective doping concentration. During annealing however, initially an annealing of acceptors takes place and the effective doping concentration increases. This means that the absolute value of the effective doping concentration thus depletion voltage (see Eq. 4.9.1) increases for an n-type sensor, whereas it decreases for a p-type sensor. This initial annealing of acceptors is usually rather fast, but it continues until the unstable damage is removed or reversed. After this initial annealing process, the space charge starts to become more negative; i.e., the effective doping concentration decreases. This means that the depletion voltage decreases for an n-type sensor and increases for a p-type sensor. This second part of the annealing takes longer and is not completely understood. However, there are indications that this process is due to acceptor build up [8], while this could also be as a result of annealing of donors or formation of divacancies or other defect complexes.

The annealing behaviors of FZ and DOFZ detectors from RD50 are shown in Fig. 4.6.1. The least irradiated diodes from both FZ and DOFZ materials show n-type annealing behavior, increasing V_{dep} during short term annealing (up to a local maximum) and decreasing V_{dep} during long term annealing (after the local maximum). However, all of the other diodes from these materials with two higher fluences show p-type-like annealing behavior, decreasing V_{dep} during short-term annealing and increasing V_{dep} during long-term annealing, confirming a type-inversion on these detectors after irradiation. In addition, V_{dep} starts to rise up for not-type-inverted FZ and DOFZ diodes after around 160 minutes annealing at 80°C, which shows space charge sign inversion to p-type-like detectors during annealing. It should also be noted that, as expected from previous studies, 800 MeV protons also caused less damage to

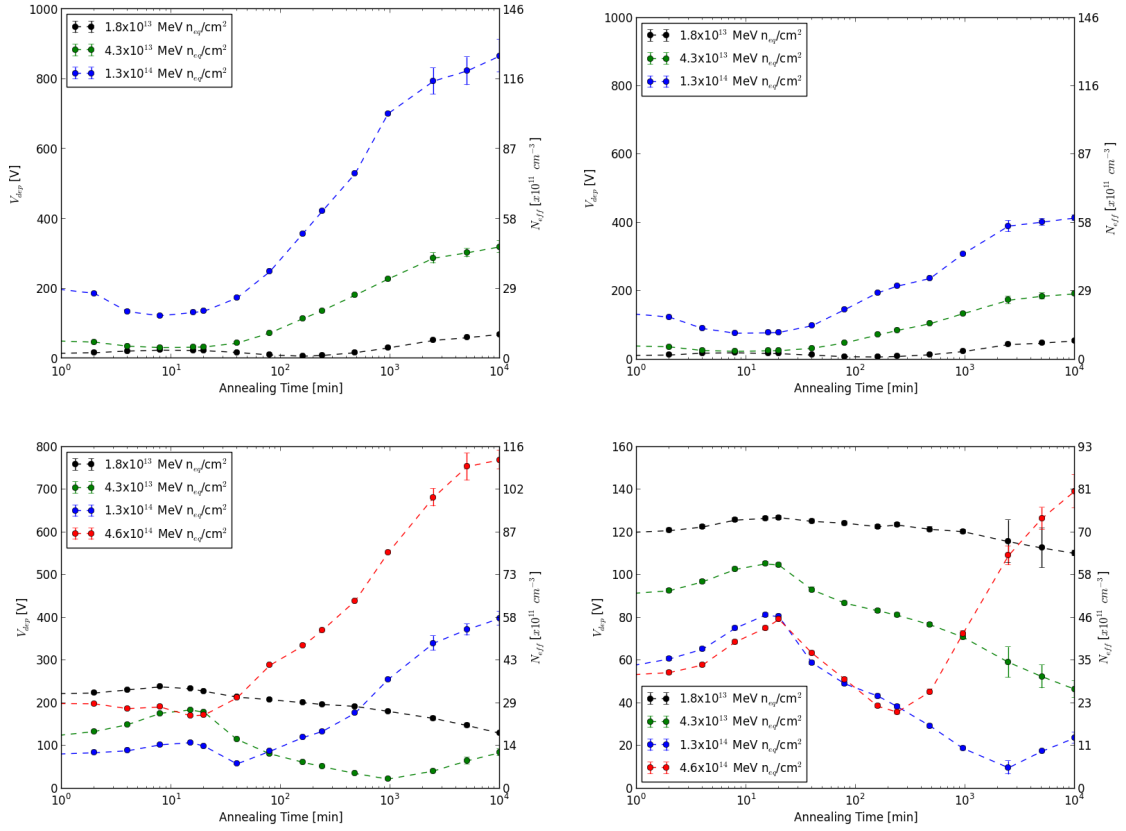


Figure 4.6.1: Depletion voltage as a function of annealing time at 80°C after 800 MeV proton irradiation: (top-left) FZ, (top-right) DOFZ, (bottom-left) MCz and (bottom-right) Epi - 150 μ m.

the DOFZ detectors comparing to the FZ detectors, which can be seen by comparing the increases in the depletion voltages in the long-term annealing.

The same annealing plots are also shown for MCz and Epi (150 μm) detectors from RD50 in Fig. 4.6.1. The two MCz detectors with lower fluence display n-type annealing behavior, but the diode ($4.3 \times 10^{13} \text{ MeV } n_{eq}/\text{cm}^2$) with higher fluence inverted after around 1,000 minutes of annealing. The MCz diodes with higher fluence on the other hand have an unclear short term annealing behavior although their long term annealing behaviors are p-type-like, confirming type-inversion after irradiation. Even though it is less pronounced in the annealing behaviors, it looks like these diodes were p-type as they were irradiated, but they quickly type-inverted back to n-type during short-term annealing and continued as p-type during long-term annealing. On the Epi (150 μm) diodes no type-inversion was observed after irradiation within the fluence range achieved, but the two diodes with the highest fluences show space charge sign inversion to p-type like diodes during the annealing process.

The annealing behaviors of FTH detectors from HPK are shown in Fig. 4.6.2. The n-type FTH sensors shows very similar behavior to the FZ sensors from RD50 as they also go through SCSI after being exposed to similar fluence. However, FTH has lower depletion voltage compared to FZ and similar depletion voltage compared to DOFZ. The p-type FTH on the other hand does not undergo type-inversion, which has also been observed by the previous studies [44] after irradiations with different beam energies (see Section 4.10).

4.7 Hamburg Model

The annealing behavior of silicon detectors has been well parameterized with the Hamburg model, which divides the change in the effective doping concentration into

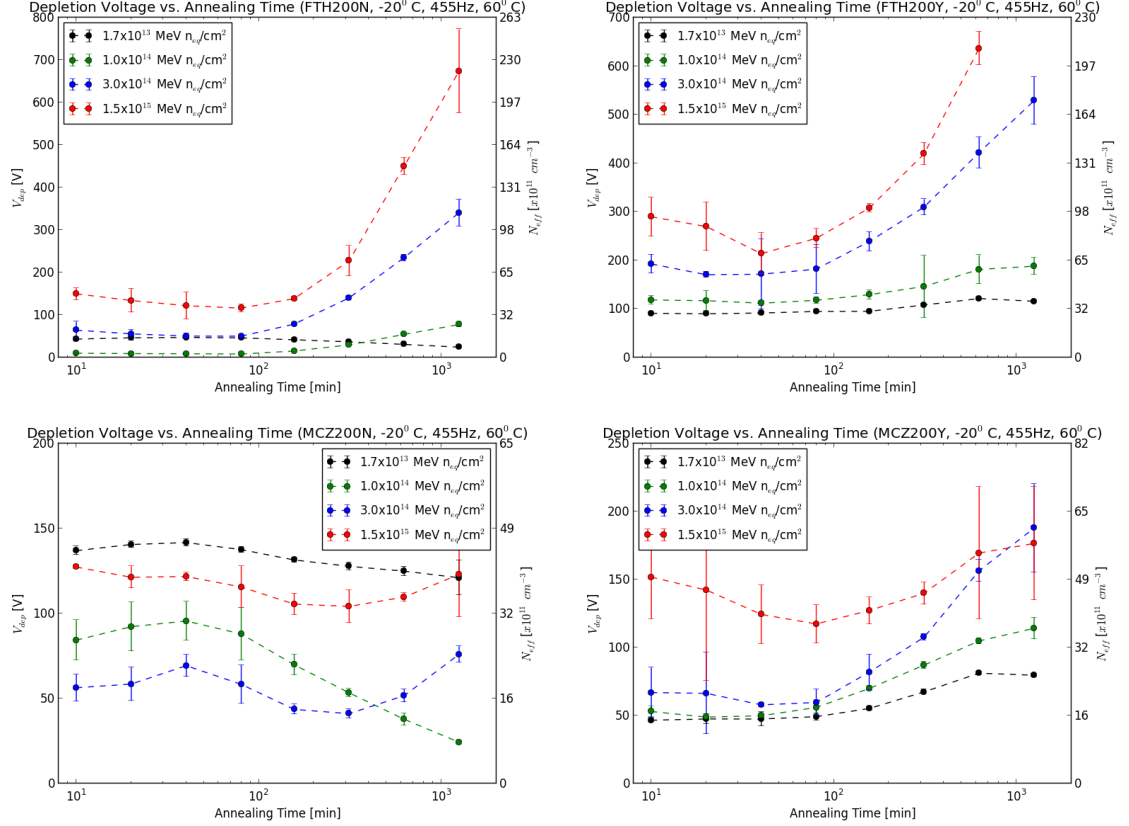


Figure 4.6.2: Depletion voltage as a function of annealing time at 80°C after 800 MeV proton irradiation for (top) FTH-200 μ m and (bottom) MCz-200 μ m detectors with (left) n- and (right) p-type polarities.

three parts by

$$\begin{aligned}\Delta N_{eff}(\Phi_{eq}, t) &= N_{eff,0} - N_{eff}(\Phi_{eq}, t) \\ &= N_A(\Phi_{eq}, t) + N_C(\Phi_{eq}) + N_Y(\Phi_{eq}, t)\end{aligned}\tag{4.7.1}$$

where N_A is short-term beneficial annealing describing the removal of acceptors, N_C is the stable damage component that is independent of annealing time and N_Y is the long-term reverse annealing component describing the generation of acceptors. A detailed discussion of these components can be found in [8]. Using this model the results in the previous section are parameterized. To do so, the stable damage part N_C was fixed to a single parameter for all the Hamburg model fits presented here as it is independent of annealing time. Before calculating ΔN_{eff} a negative space charge sign (SCS) was introduced for all the diodes that type-inverted after irradiation. In

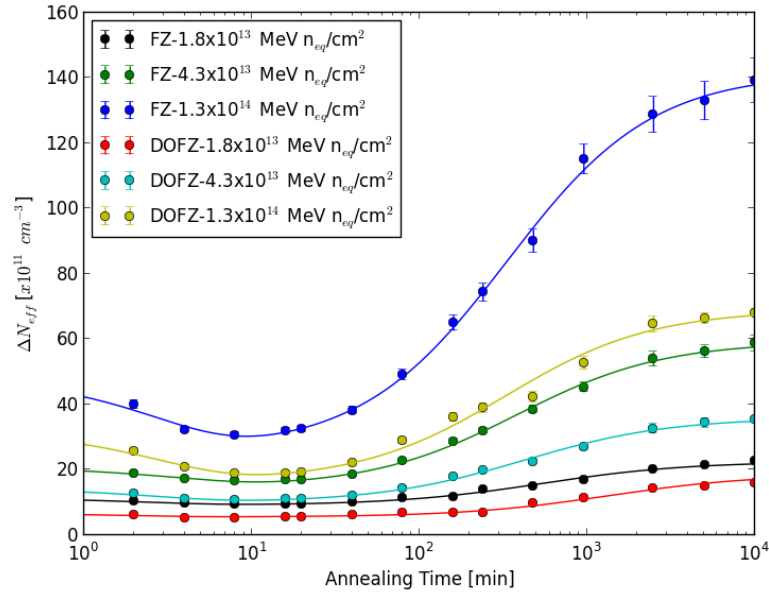


Figure 4.7.1: Hamburg model parameterization of FZ and DOFZ detectors after 800 MeV proton irradiation.

addition, for the diodes that type-inverted during the annealing process a negative

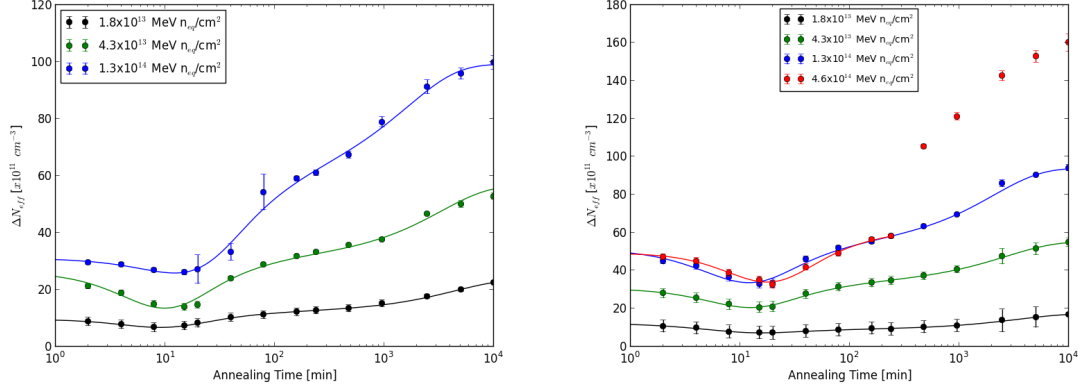


Figure 4.7.2: Hamburg model parameterization of (left) MCz and (right) Epi-150 μ m detectors after 800 MeV proton irradiation.

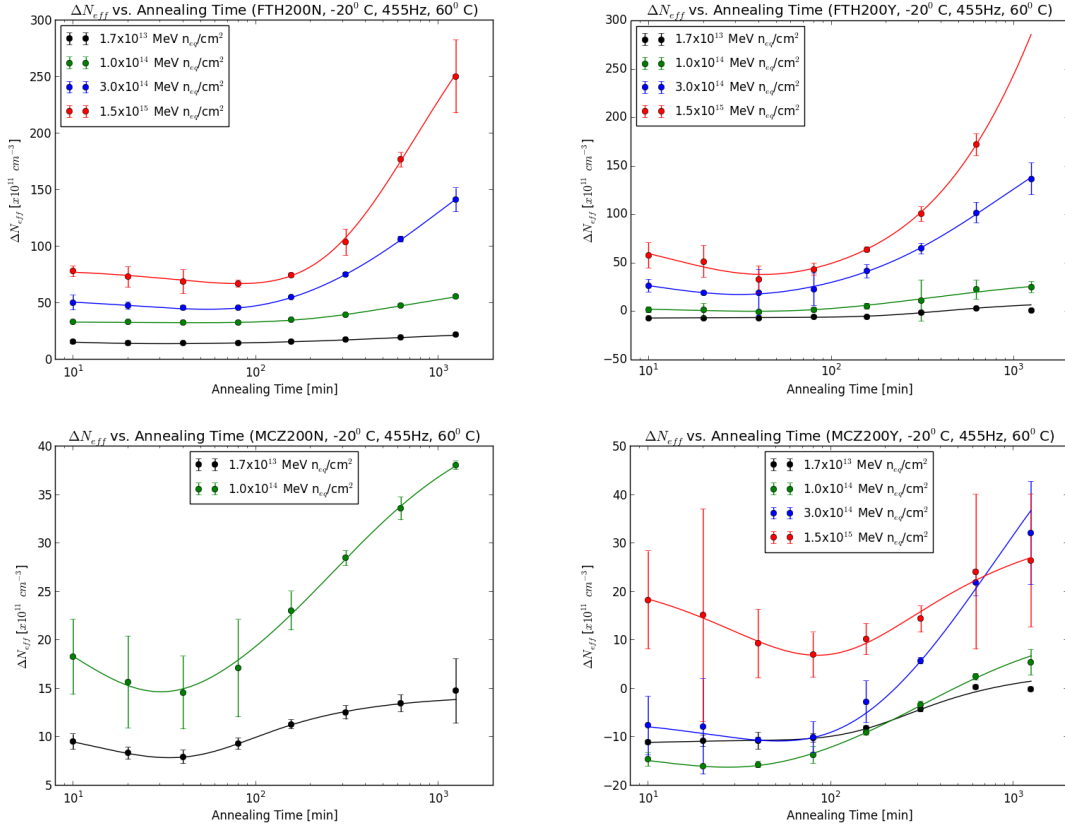


Figure 4.7.3: Hamburg model parameterization of (top) FTH-200 μ m and (bottom) MCz-200 μ m detectors for (left) n- and (right) p-type after 800 MeV proton irradiation.

SCS was only introduced for the annealing data points after the inversion. It was found that the results from FZ and DOFZ diodes can be best described by the second order long term annealing process (Fig. 4.7.1). MCz-300 μm and Epi-150 μm diodes show a second kink in the long-term annealing part and a fit to data could not be done using a single reverse annealing term as for FZ and DOFZ detectors (Fig. 4.7.2). Therefore, the long term annealing part for these diodes can be described both with first and second order processes. The Epi-150 μm diode with the highest fluence could not be fitted using the full data and the fit shown in Fig. 4.7.2 on the right is only up to 240 minutes of annealing time. The MCz-300 μm diode with the highest fluence on the other hand has inconclusive short-term annealing behavior and a fit could not be achieved.

Figure 4.7.3 shows the Hamburg model parameterization for the HPK diodes. As is the case for RD50 FZ diodes, FTH materials of HPK can be well parameterized with the Hamburg model. Because of SCSI during long-term annealing, a good parameterization with the Hamburg model was not achieved with the two n-type MCz-200 μm HPK detectors with the highest fluence.

4.8 Damage Rate

The change in the total leakage current after irradiation is linearly dependent on the fluence by [8] (after the unstable damage is annealed out, which is the main difference that makes the α constant compared to the one described in Eq. 3.1.1, which is dependent on the annealing time and temperature)

$$\frac{\Delta I}{V} = \alpha \Phi_{eq} \quad (4.8.1)$$

where α is a constant and known as current related damage rate, V is the volume of the detector, ΔI is the increase in the leakage current after irradiation and Φ_{eq} is 1

MeV neutron equivalent fluence Φ which is related to proton fluence by $\Phi_{eq} = \kappa\Phi$ and $\kappa = 0.72$ [45] is the hardness factor for 800 MeV protons. The proportionality factor α is known to be independent of the silicon material, particle type and energy [8]. Therefore, leakage current can be used to cross-check irradiation fluences after the unstable damage is annealed out.

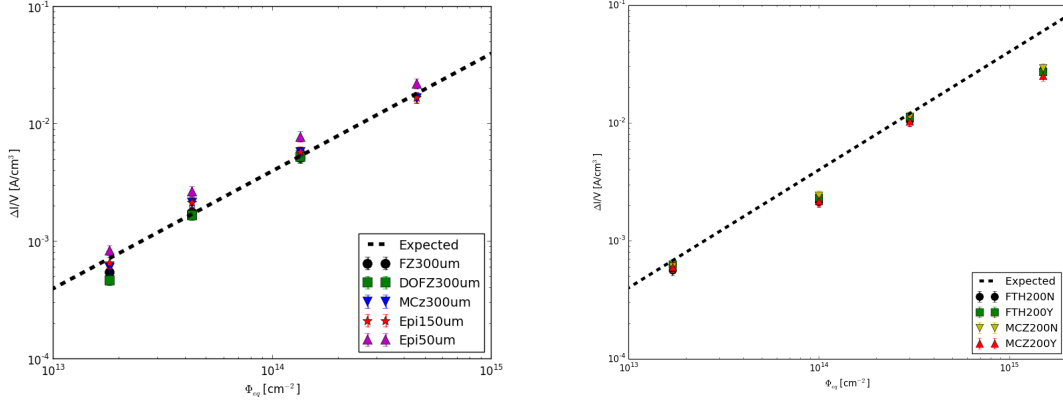


Figure 4.8.1: Volume leakage current (corresponding to depletion voltage) as a function of fluence after 800 MeV proton irradiation for (left) RD50 and (right) HPK diodes. The dashed line shows the expected behavior from [8]. The leakage current is scaled to its reference value at 20°C from its measurement temperature at (left) room temperature and (right) -20°C .

Figure 4.8.1 shows the volume leakage current of the investigated diodes in this work as a function of fluence. The results are in agreement with the expected leakage current behavior (dashed line in Fig. 4.8.1) within the error margins for the RD50 diodes. Therefore, these results also confirm that the leakage current is independent of silicon material. In addition, this also shows that the 800 MeV proton irradiation create the same current related damage rate (independent of particle energy).

On the other hand, the results from the HPK diodes show deviation from the expected behavior, in particular for the second highest and the highest fluences. As these measurements are often used to cross-check the fluence measured during irradiation and the actual fluence achieved, we attribute this discrepancy to wrong fluence

measurement and normalize the HPK fluences to the expectations from experimentally well-confirmed current related damage rate as shown in Table 4.4.

Table 4.4: Comparison of nominal and normalized (from Fig. 4.8.1) fluences for HPK test structures with 800 MeV protons.

Nominal $\Phi_{eq} [\times 10^{13} n_{eq}/cm^2]$	Normalized $\Phi_{eq} [\times 10^{13} n_{eq}/cm^2]$
1.7	1.4
10	5.4
30	26
150	71

4.9 Effective Doping Concentration

The effective doping concentration is calculated from the measured depletion voltage using

$$|N_{eff}| = \frac{2\varepsilon V_{dep}}{q_0 d^2} \quad (4.9.1)$$

where ε is the permittivity of silicon, d is the geometrical thickness of the detector and q_0 is the unit charge. In Fig. 4.9.1 the effective doping concentrations of investigated detectors are plotted as a function of fluence after 8 min of anneal time at 80°C for the RD50 diodes and 80 min of anneal time at 60°C for the HPK diodes when the short term annealing is approximately completed and the only contribution to N_{eff} comes from the stable damage. A fit to this data is performed using

$$N_{eff}(\Phi) = N_{eff,0} e^{-c\Phi} + \beta_{eff} \Phi \quad (4.9.2)$$

where $N_{eff,0}$ is initial doping concentration, c is the donor removal cross section and β_{eff} is the probability to create an acceptor state. This equation corresponds to the stable damage component of the Hamburg model in Eq. 4.7.1. For all investi-

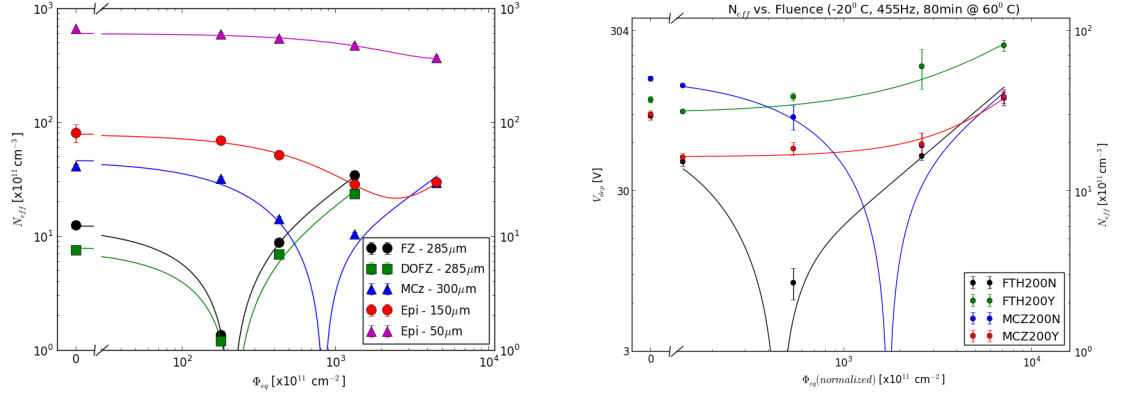


Figure 4.9.1: Depletion voltage as a function of 1 MeV neutron equivalent fluence for (left) RD50 and (right) HPK diodes. Solid lines show the fits using Eq. 4.9.2.

gated sensors with an initial polarity of n-type the depletion voltage decreases in the lower fluence range as a result of dominant donor removal. However, as the fluence increases acceptor generation becomes more important and the sensors type-invert to p-type-like sensors. Type inversion happens around $2(4.5) \times 10^{13}$ MeV n_{eq}/cm^2 for FZ and DOFZ (FTH) detectors, and around $8.5(10.5) \times 10^{13}$ MeV n_{eq}/cm^2 for MCz-300 μm (MCz-200 μm) detectors (these type-inversions are confirmed with the annealing study as discussed in Section 4.6). Epi sensors did not type-invert within the fluence range that was achieved in this work. The p-type materials show a continuous increase in the depletion voltage as a function of fluence. The values of the fit parameters are collected in Table 4.5.

Table 4.5: Fitting values for N_{eff} vs Fluence parameters.

Sensor	N_{eff} [$10^{11} cm^{-3}$]	c [$10^{-14} cm^{-2}$]	β_{eff} [$10^{-2} cm^{-1}$]
FZ	12.4 ± 0.1	4.07 ± 0.04	-2.54 ± 0.01
DOFZ	7.9 ± 1.2	3.01 ± 1.14	-1.90 ± 2.66
MCz (300 μm)	46.2 ± 8.2	2.41 ± 0.62	-0.74 ± 0.12
Epi (150 μm)	79.0 ± 2.9	1.04 ± 0.06	0.63 ± 0.02
Epi (50 μm)	604.4 ± 12.4	0.29 ± 0.04	4.41 ± 0.68
FTH (n-type)	30.7 ± 3.6	5.28 ± 1.07	-0.63 ± 0.03
FTH (p-type)	30.6 ± 8.6	$5.65 \times 10^{-6} \pm 50$	0.74 ± 1537
MCz (n-type)	52.3 ± 2.6	0.96 ± 0.36	-0.58 ± 0.11
MCz (p-type)	16.3 ± 1.1	0.26 ± 0.25	0.50 ± 0.11

4.10 Comparison with 23 MeV and 23 GeV Proton Irradiations

Silicon detector designs with different materials, polarities, and geometries have been studied before using different particle irradiations and energies [8, 44, 46]. Here, we specifically compare our results with 800 MeV proton irradiation to 23 MeV and 23 GeV proton irradiations reported in [44].

The FZ material shows similar behavior after 23 MeV and 23 GeV proton irradiations. In both cases, the n-bulk FZ material with $200\mu m$ and $300\mu m$ undergo a space charge sign inversion at relatively lower fluences of less than 3×10^{14} MeV n_{eq}/cm^2 . Our results with 800 MeV proton irradiation are also consistent with this observation.

MCz- $200\mu m$ n-type material shows a space charge sign inversion after 23 MeV proton irradiation, while MCz- $200\mu m$ p-type material does not show an inversion. On the other hand, after 23 GeV proton irradiation, this behavior of MCz- $200\mu m$ is reversed; while p-bulk material undergoes a SCSI, the n-bulk material does not show an inversion. Comparing our results, we see that the 800 MeV proton irradiation shows a similar behavior to 23 MeV proton irradiations.

A qualitative comparison of proton irradiations at different energies (23 MeV, 800 MeV, and 23 GeV) shows that the changes in sensor properties such as depletion voltage and space charge sign inversion are similar at different proton beam energies for the FZ material. However, MCz silicon material shows differences as reported in [44] when the 23 MeV and 23 GeV proton irradiations are compared and we report 800 MeV irradiation results that are more consistent with 23 MeV irradiations (see Table 4.6).

Table 4.6: Space charge sign inversion in physically thinned FZ and MCz materials after proton irradiations at different energies.

SCSI	FTH (200 μm)		MCz (200 μm)	
	n-type	p-type	n-type	p-type
23 MeV	✓	✗	✓	✗
800 MeV	✓	✗	✓	✗
23 GeV	✓	✗	✗	✓

Chapter 5

Physics Object Definitions

The reconstruction and selection of physics objects for the analyses presented in this thesis are described in this chapter. The candidate physics objects (e.g. electrons, muons, and jets) from the collision data of the CMS detector are produced using reconstruction algorithms [47] that are approved by the relevant Physics Object Groups (POGs). Detector signals for physics processes of interest as well as the corresponding simulated events produced by Monte Carlo generators are passed through the same reconstruction algorithms.

5.1 Primary vertex and pile-up

A primary vertex (PV) is reconstructed from all tracks in the event that are compatible with the LHC beam spot in x,y plane. Reconstructed primary vertices are required to have a z position within 24 *cm* of the nominal detector origin, a radial position (ρ) within 2 *cm* of the beamspot, and the vertex fit must include more than four degrees of freedom. In the presence of multiple primary vertex candidates in an event, the vertex with the largest $\sum p_T^2$ is selected as *the* primary interaction vertex. The details of the primary vertex reconstruction in CMS can be found elsewhere (e.g., Ref. [48]).

The collision data contains a significant number of additional interactions per bunch crossing, an effect known as pileup. To correct for effects of having different pileup distributions in data and MC, distributions of the mean number of interactions per bunch crossing are created. Figure 5.1.1 (left) shows the data and MC histograms normalized to unit area from the 13 TeV analysis. MC events are reweighted according to the ratio histogram shown in Fig. 5.1.1 (right). The minimum bias cross section is set to 69 (69.4) mb for 13 (8) TeV collisions data. Uncertainties in pileup reweighting are based on shifting the minimum bias cross section by $\pm 5\%$. The number of primary vertices per event after pileup reweighting is shown in Fig. 5.1.2 for the 13 TeV analysis in Chapter 7.

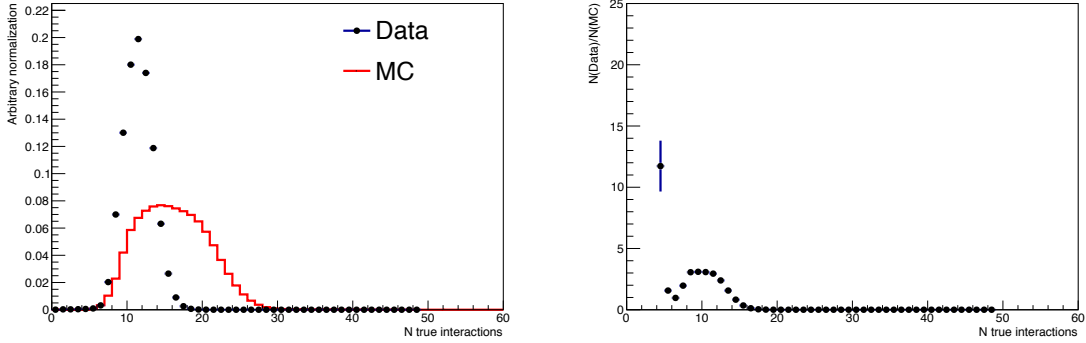


Figure 5.1.1: Distributions of (left) mean number of interactions per bunch crossing in data and MC at 13 TeV. The ratio of these histograms is shown in (right) and used to weight MC events.

5.2 Electrons

Electrons are identified with the use of a multivariate identification (MVA) algorithm provided by the EGamma POG. For the 13 TeV analysis, the selection is based on the non-triggering MVA identification [49] and a “tight” electron is defined to have an MVA discriminant passing the following criteria:

- $MVA > 0.967083$, $0.0 < |\eta| < 0.8$

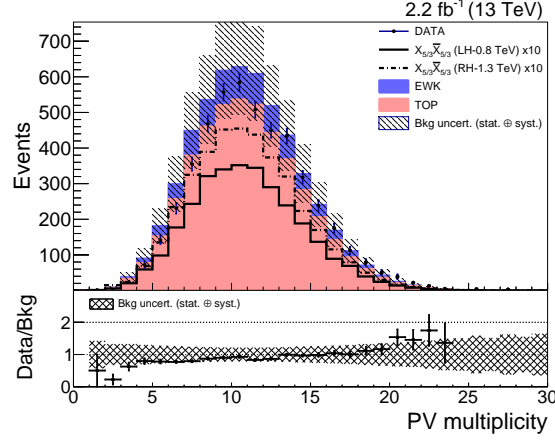


Figure 5.1.2: Distribution of the number of primary vertices per event after pileup reweighting at 13 TeV. Uncertainties include all statistical and systematic uncertainties described in sec. 7.7.

- $MVA > 0.929117, 0.8 < |\eta| < 1.479$
- $MVA > 0.726311, 1.479 < |\eta| < 2.4$

This working point has an estimated 80% efficiency for identifying an electron. We also use the 90% efficiency working point to define a “loose” electron with an MVA discriminant passing the following criteria:

- $MVA > 0.913286, 0.0 < |\eta| < 0.8$
- $MVA > 0.805013, 0.8 < |\eta| < 1.479$
- $MVA > 0.358969, 1.479 < |\eta| < 2.4$

The corresponding criteria for the 8 TeV analysis can be found in Ref. [50]. The loose lepton definition is used for the single lepton channels to reject events with a second reconstructed lepton.

In addition to satisfying electron ID criteria, we require electrons to be isolated using the relative isolation for the 8 TeV analysis and the mini-isolation variable for the 13 TeV analysis. Standard relative isolation is calculated by summing particle

flow candidates within a fixed cone around a lepton, correcting the sum for pileup effects, and dividing by the lepton transverse momentum. The p_T of all reconstructed PF candidates within a cone of radius $R = 0.3$ around the lepton (after correcting for pileup activity) must not exceed 12% of the electron p_T . Mini-isolation on the other hand uses a p_T -dependent cone size to increase efficiency at high energies, where jets are more likely to overlap [51]. For tight electrons, mini-isolation must be less than 0.1, and for loose electrons mini-isolation must be less than 0.4.

Preliminary efficiencies of the electron identification and mini-isolation working points were measured using the tag and probe method for the corresponding $X_{5/3}$ search in the same-sign dilepton final state [52]. A scale factor is defined as the ratio of data efficiency to MC efficiency, in bins of p_T and η . The scale factors are applied to MC events as weights, and we include a 1% systematic uncertainty for each of the ID and isolation scale factors. For the 8 TeV analysis, the corresponding scale factors are centrally computed by the EGamma POG and applied in the corresponding analysis.

5.3 Muons

Muons are selected using the "tight" and "loose" muon ID provided by the Muon POG [53, 54]. We select tight muons that pass the following criteria:

- Reconstructed as GlobalMuon with Particle-Flow muon ID
- $\chi^2/ndof < 10$
- Number of muon system hits > 0
- Number of chambers with matched segments > 1
- The minimum radial distance of the track with respect to the primary vertex $d_{XY} < 2$ mm

- The minimum longitudinal distance of the track with respect to the primary vertex $d_Z < 5$ mm
- Number of pixel hits > 0
- Number of tracker layers with hits > 5

Loose muons are selected that are reconstructed as a global or tracker muon with the particle-flow muon ID.

In addition to satisfying the ID requirements, the muons are required to be well-isolated, using relative isolation variable for both 8 TeV and 13 TeV analyses, as defined for the electrons before. In the 13 TeV analysis, the relative muon isolation is required to be less than 0.2 (0.4) for tight (loose) muons, where the relative isolation is calculated using a cone of radius $R = 0.4$ around muon. For the 8 TeV analysis, on the other hand, the relative isolation is calculated using $R = 0.3$ and required to be less than 0.12.

Efficiencies of the muon ID and isolation requirements were also calculated using the same technique as in the case of an electron, and we weight MC events by these scale factors to correct for discrepancies with the data.

5.4 Jets

Jets are reconstructed using the anti- k_T algorithm [55] with distance parameters of 0.4 (AK4) for 13 TeV and 0.5 (AK5) for 8 TeV analyses. Corrections for the contributions of pileup are made using the Charged Hadron Subtraction (CHS) method. Both the 8 and 13 TeV analyses require jets to pass the “loose” particle-flow jet ID with following requirements [56]:

- Neutral hadron fraction < 0.99
- Neutral electromagnetic fraction < 0.99

- Number of constituents > 1
- if $|\eta| < 2.4$, charged hadron fraction > 0
- if $|\eta| < 2.4$, charged multiplicity > 0
- if $|\eta| < 2.4$, charged electromagnetic fraction < 0.99 ,

In addition, the jets are required to have $p_T > 30$ GeV and $|\eta| < 2.4$ in the 13 TeV analysis, while in the 8 TeV analysis, they are selected if they have $p_T > 30(20)$ GeV and $|\eta| < 2.5$ in WH (ZH) channel.

Jets which overlap leptons have the lepton energy subtracted by matching lepton particle flow candidates to candidates within the jet and removing them. The jet energy is then corrected using the “L1FastJet”, “L2Relative”, and “L3Absolute” corrections from the recommended Jet Energy Corrections (JEC) [57, 58]. In data we also apply the “L2L3Residual” correction. Residual lepton-jet overlaps are also removed by requiring that the lepton and the closest jet to it be separated by $\Delta R > 0.4$.

5.5 b tagging

Jets resulting from the fragmentation and hadronization of b quarks are identified with the multivariate Combined Secondary Vertex algorithm [59]. Jets from b quarks and light quarks and gluons have discriminating properties. Using a combination of the information from calorimeters and tracker, the jets originating from b quarks can be distinguished from those of light quark or gluons. Longer lifetime of B hadrons ($\approx 1.5 ps$) for example can lead to a vertex that is displaced with respect to the primary vertex.

In the 13 TeV analysis, jets are labeled as b tagged if they have a `pfCombinedInclusiveSecondaryVertexV2BJetTags` discriminator value greater than 0.890 [60]. This

working point was chosen to have a mistag rate of approximately 1%. The efficiency for tagging true b hadron jets is approximately 65%, averaged over jet p_T . Figure 5.5.1 shows the measured efficiency and mistag rate of this working point in the $t\bar{t}$ MC sample, which are used to determine systematic uncertainties in the b tagging data to MC scale factors [60]. The scale factors are applied using the jet-by-jet b tagging status update method [61]. This method downgrades (upgrades) the tagged status of a random selection of jets if the scale factor is greater than (less than) 1.

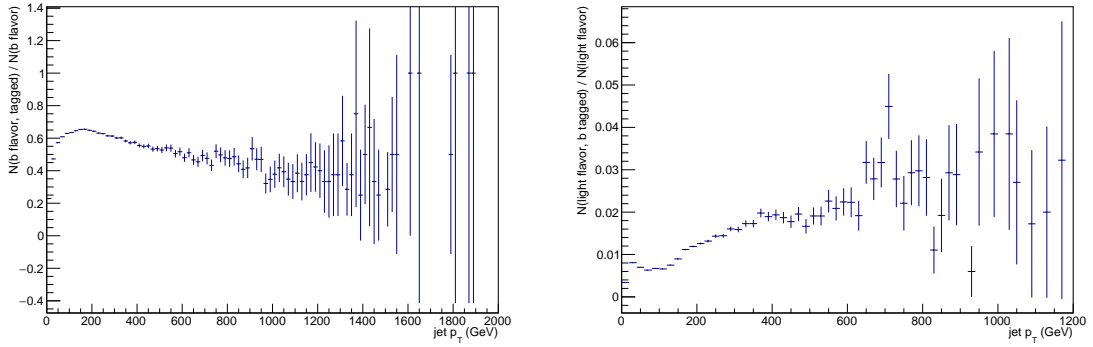


Figure 5.5.1: Distributions of (left) efficiency of tagging a jet with b quark flavor using the pfCombinedInclusiveSecondaryVertexV2BJetTags medium working point, and (right) efficiency of tagging a light flavor jet with the same working point. Both distributions are calculated using the $t\bar{t}$ MC sample for 13 TeV collisions.

The 8 TeV analysis uses different b-tagging working points on the CSV discriminant and the specific requirements are collected in Table 6.2.

5.6 Missing transverse energy

Missing transverse energy is the negative vector sum of the transverse momenta of all the objects in an event. Particle flow E_T^{miss} with Type-1 corrections is used in this analysis, and jet energy corrections and uncertainties are propagated to E_T^{miss} .

All data and MC events must pass a series of quality E_T^{miss} filters [62], including:

- HBHE noise filter

- HBHE isolated noise filter
- CSC tight halo filter, using the bad event list
- Bad EE supercrystal filter.

5.7 Large radius jets and substructure

Large radius jets, primarily used in the 13 TeV analysis, are reconstructed with the anti- k_T distance parameter 0.8 (AK8) and stored in the miniAOD format if they have $p_T > 200$ GeV. Decay products of heavy particles such as $t\bar{t}$ can have large Lorentz boost, and their subsequent decay products can merge into a single jet. An algorithm called “n-subjettiness” [63] creates jet shape variables that quantify the consistency of a jet with having n or fewer subjets (1, 2, 3, etc). Mass grooming techniques are used to remove soft jet constituents so that the mass of the hard constituents can be measured more clearly. The “pruning” [64] algorithm is currently used to identify boosted hadronic W boson decays, where the mass is corrected without L1 jet energy corrections. We require a W tagged jet to have $p_T > 200$ GeV, $|\eta| < 2.4$, pruned mass between 65 and 105 GeV, and the ratio of n-subjettiness variables $\tau_2/\tau_1 < 0.55$.

Differences in the pruned mass distribution and τ_2/τ_1 efficiencies between data and MC have been evaluated using $t\bar{t}$ MC with reconstructed W bosons matched to true W bosons from the MC generation [65]. The mean value of the fitted W mass peak in the pruned mass distribution agrees well in data and MC, with a ratio of 0.992 ± 0.005 . The width of the fitted peak is wider in data than MC, with a ratio of 1.12 ± 0.07 . The ratio of efficiencies for jets match to W bosons to pass $\tau_2/\tau_1 < 0.6$ is consistent with 1 within an uncertainty of 13%. Since both the pruned mass mean value and τ_2/τ_1 efficiencies agree with 1, only their uncertainties are applied to the W tag definition. The pruned jet mass resolution is applied to MC events, with a Gaussian smearing function with $\sigma = \sqrt{1.12^2 - 1}\sigma_{MC}$, where $\sigma_{MC} = 7.3$ GeV.

Chapter 6

Search for Anomalous Higgs Couplings in $VH(\rightarrow b\bar{b})$

6.1 Introduction and Theory

As discussed in Chapter 1, the newly discovered Higgs boson [20,21] completes a long search for the mechanism by which the electroweak symmetry is broken and helps complete the standard model; however, precision measurements are needed in order to confirm the compatibility of the Higgs boson with the predictions from the SM. The Higgs boson provides an opportunity to better understand the connection of the Higgs to the rest of the SM particles. For example, the decay of a Higgs boson to a pair of b quarks ($b\bar{b}$) has not yet been observed. Thus it is important to verify that this fermionic coupling is as predicted. The most sensitive mode to find the $H \rightarrow b\bar{b}$ decay is via associated production $q\bar{q} \rightarrow VH$ where V is either a W or Z boson. This diagram is shown in Fig. 6.1.1.

However, in addition to the observation of $h \rightarrow b\bar{b}$ this final state is also important in searching for new physics through anomalous Higgs couplings. By detailing the properties of the Higgs interactions with the SM particles, we can use it as a probe

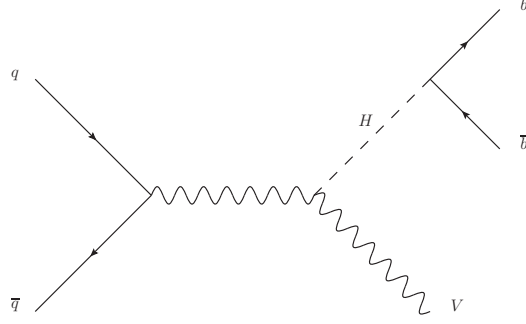


Figure 6.1.1: Higgs boson produced in association with a vector boson

into new physics through deviations from SM expectations. This final state, as can be seen from Fig. 6.1.1, also contains a coupling HVV to the vector bosons, which can be studied as well. Previous studies of anomalous couplings of the newly discovered Higgs boson to vector bosons [66–71], in order to understand the spin and parity of the H , conclude that the Higgs is likely to be spin-0 with SM-like couplings. The properties have already been studied in great detail where the Higgs is produced via gluon fusion and the Higgs is allowed to decay either to $\gamma + \gamma$, $Z^{(*)}/\gamma^* + Z^{(*)}/\gamma^*$, $W^{(*)} + W^{(*)}$. These studies show that the Higgs couplings are SM-like to within $O(30\%)$ but the precision of these studies needs to be improved. It has been shown in Ref. [72] that in associated production ($q\bar{q} \rightarrow VH$) and vector boson scattering ($q\bar{q} \rightarrow Hq\bar{q}$), the highly off-shell nature of the propagating vector boson(s) gives us strong sensitivity to anomalous couplings of the Higgs to vector bosons (aHVV). With enough data, these channels will provide the best sensitivity to search for aHVV.

In determining anomalous couplings, we take a model-independent approach. We start by defining a generic amplitude for a spin-0 boson coupling to vector bosons that is characterized by dimensionless couplings. Then we scan the coupling parameter space to determine the most likely values. In defining the amplitude, we follow the notation of previous CMS results and write the general scattering amplitude that describes interactions of a spin-zero boson with the gauge bosons, such as ZZ , WW ,

$Z\gamma$, $\gamma\gamma$, or gg , as

$$A(\text{HVV}) \sim \left[a_1^{\text{VV}} + \frac{\kappa_1^{\text{VV}} q_{V1}^2 + \kappa_2^{\text{VV}} q_{V2}^2}{(\Lambda_1^{\text{VV}})^2} \right] m_{V1}^2 \epsilon_{V1}^* \epsilon_{V2}^* + a_2^{\text{VV}} f_{\mu\nu}^{*(1)} f^{*(2),\mu\nu} + a_3^{\text{VV}} f_{\mu\nu}^{*(1)} \tilde{f}^{*(2),\mu\nu}, \quad (6.1.1)$$

In Eq. (6.1.1), $f^{(i),\mu\nu} = \epsilon_i^\mu q_i^\nu - \epsilon_i^\nu q_i^\mu$ is the field strength tensor of a gauge boson with momentum q_i and polarization vector ϵ_i ; $\tilde{f}^{(i),\mu\nu} = 1/2\epsilon^{\mu\nu\alpha\beta} f_{\alpha\beta}$ is the conjugate field strength tensor. Parity-conserving interactions of a scalar (pseudo-scalar) are parameterized by the couplings $a_{1,2}$ and Λ_1 (a_3). In the SM, the only non-vanishing coupling of the Higgs to ZZ or WW bosons at tree-level is a_1 , while a_2 is generated through radiative corrections. For final states with at least one massless gauge boson, such as $\gamma\gamma$, gg or $Z\gamma$, the SM interactions with the Higgs boson are loop-induced; these interactions are described by the coupling a_2 .

In this analysis we consider only the effects of the pseudoscalar coupling a_3 . It is enough, if we consider solely the separation of pure scalar and pseudoscalar hypotheses, to set the a_1 (or a_3) couplings to 1 and all other couplings to zero. However, to scan the allowed hypotheses, the physical effects of such anomalous couplings are parameterized as effective cross-sections and phases. Again we follow the convention of previous CMS results and we define:

$$f_{a3} = \frac{|a_3|^2 \sigma_3}{|a_1|^2 \sigma_1 + |a_3|^2 \sigma_3}, \quad \phi_{a3} = \arg\left(\frac{a_3}{a_1}\right), \quad (6.1.2)$$

where σ_i is the cross section of the process corresponding to $a_i = 1$, $a_{j \neq i} = 0$. When $f_{a3} = 0$, only the pure scalar SM hypothesis is considered while when $f_{a3} = 1$, only the pure pseudoscalar case is considered. In the absence of additional anomalous Higgs couplings, the signal strength parameter ($\mu = \sigma\mathcal{B}/\sigma\mathcal{B}|_{SM}$) is given by

$$\mu = \frac{|a_1|^2 \sigma_1 + |a_3|^2 \sigma_3}{\sigma_1}. \quad (6.1.3)$$

6.2 Analysis Strategy

We follow as closely as possible the CMS 8 TeV SM $Vh(\rightarrow b\bar{b})$ search [4]. We reuse techniques and code where applicable, so as to avoid unnecessary effort and ensure accuracy of the results; the b jet energy regression, BDT training, background modeling, object and event selection, etc., in Ref. [4] are all unchanged in this analysis.

Events are selected with the same criteria used in the SM search for the BDT-based analysis. In these events, we produce two dimensional templates for the backgrounds and 0^+ and 0^- signal hypotheses. The BDT makes up one dimension, separating both signal hypotheses from the background. The other dimension is chosen to discriminate between the 0^+ and 0^- hypotheses. Using these templates, we perform hypothesis testing to assess the compatibility of the data with the signal hypotheses.

We consider only the medium and high boost signal regions of the $W \rightarrow \ell\nu$ channel, and both signal regions of the $Z \rightarrow \ell\ell$ channel (which we will refer to as medium and high boost for consistency). Throughout, “ ℓ ” is used to denote e, μ .

In these selected events, we construct two dimensional templates that can discriminate between a scalar and pseudoscalar Higgs. Using these templates, we test between the pure scalar and pseudoscalar hypotheses, as well as mixed scalar-pseudoscalar hypotheses by constructing templates for intermediate values of f_{a3} . We perform a scan of f_{a3} , comparing these templates to data in order to constrain f_{a3} . Finally, a combination is performed with the gluon fusion $h \rightarrow VV$ results from Ref. [66].

6.3 Data and Monte Carlo

The same data and background Monte Carlo (MC) samples from the SM search are used in this analysis. We use the Hbb group step 2 ntuples. A total of 18.9 fb^{-1} of data is analyzed, collected from p-p collisions at a center-of-mass energy of 8 TeV with single electron, single muon, and double electron triggers, just as in the SM search.

In addition to the background samples analyzed in the SM search, we also analyzed a sample of $gg \rightarrow Zh$ events generated with POWHEG [73]. Les Houches Event (LHE) files were generated by the Hbb group for this process with $Z \rightarrow ee$ and $h \rightarrow bb$. We modified a subset of these events, replacing the electrons with muons. We then passed orthogonal sets of the ee and $\mu\mu$ $ggZh$ events ($\sim 100k$ each) through the standard showering/hadronization + reconstruction chain in CMSSW_5_3_2_patch5. The contribution in the signal region from decays with $Z \rightarrow \tau\tau$ are negligible. The sample names are listed in Table 6.1. The cross section used to normalize these samples is $\sigma_{gg \rightarrow Zh} \times BR(Z \rightarrow l^+ l^-) \times BR(h \rightarrow b\bar{b}) = 32.46 \text{ fb} \times 0.033658 \times 0.577 = 0.630 \text{ fb}$ [9,74].

The signal MC is generated with the LO matrix element generator JHUGEN [72, 75, 76] under the assumption of a SM-like, purely scalar (0^+) HVV coupling structure, as well as an anomalous, purely pseudoscalar (0^-) HVV coupling structure, and also in a 50/50 mix of 0^+ and 0^- . In the mixed sample, 50% of the cross section comes from the a_1 term, and the other 50% of the cross section comes from the a_3 term in Equation 6.1.1. The phase between these two couplings is chosen to be zero.

The parton level samples are interfaced to PYTHIA [77] for parton showering and hadronization. Detector simulation is performed with GEANT4 [78]. The signal samples assume $m_h = 125.6 \text{ GeV}$, and are listed in Table 6.1.

At NLO in α_{QCD} , the corrections to the VH production cross sections are the same as those in Drell-Yan [79]. At NNLO in α_{QCD} , the corrections are still mostly given by the Drell-Yan corrections [80] with contributions from diagrams in which the Higgs is produced through a heavy fermion loop [81]. In WH, these corrections

Table 6.1: Additional MC samples used in the analysis not described in Ref. [4].

Sample	HVV coupling
$W \rightarrow \ell \nu$	
/WHiggs0PToBB_M-125p6_8TeV-JHUGenV4-pythia6-tauola/ Summer12_DR53X-PU_S10_START53_V19-v1/AODSIM	0^+
/WHiggs0Mf05ph0ToBB_M-125p6_8TeV-JHUGenV4-pythia6-tauola/ Summer12_DR53X-PU_S10_START53_V19-v1/AODSIM	50/50
/WHiggs0MToBB_M-125p6_8TeV-JHUGenV4-pythia6-tauola/ Summer12_DR53X-PU_S10_START53_V19-v1/AODSIM	0^-
$Z \rightarrow \ell \ell$	
/ZHiggs0PToBB_M-125p6_8TeV-JHUGenV4-pythia6-tauola/ Summer12_DR53X-PU_S10_START53_V19-v1/AODSIM	0^+
/ZHiggs0Mf05ph0ToBB_M-125p6_8TeV-JHUGenV4-pythia6-tauola/ Summer12_DR53X-PU_S10_START53_V19-v1/AODSIM	50/50
/ZHiggs0MToBB_M-125p6_8TeV-JHUGenV4-pythia6-tauola/ Summer12_DR53X-PU_S10_START53_V19-v1/AODSIM	0^-
$gg \rightarrow Zh$	
/ZeeHbb_PHG/ zixu-ZeeHbb_PHG-RECO-c8f8ed334db8a7d6f56c62266b1dfa5b/USER	NA
/ZmmHbb_PHG/ zixu-ZmmHbb_PHG-RECO-c8f8ed334db8a7d6f56c62266b1dfa5b/USER	NA

are at the percent level [82], and are neglected. In ZH, these contributions are non-negligible, and their treatment is described below. NLO corrections in α_{EW} are also available [83]. We apply corrections up to NNLO in α_{QCD} and NLO in α_{EW} to our LO 0^+ MC. Furthermore, we assume these higher order corrections can also be applied in the 0^- case, and assign a systematic uncertainty to account for this assumption. The systematic uncertainty is discussed in Section 6.6.

The NLO α_{QCD} shape corrections, parameterized as a function of the generator level V transverse momentum, are derived from the ratio of the POWHEG [73] and the 0^+ JHUGEN MC samples. The resulting k-factors are shown in Fig. 6.3.1 based on WH and ZH MC. The signal MC samples are normalized to the same cross section used in the SM search, including contributions from terms up to NLO in α_{QCD} . The NNLO QCD and NLO electroweak corrections from the SM search, also parameterized as a function of the generator level V transverse momentum, are applied as well.

In all cases, the number of pileup interactions simulated in MC is reweighted to

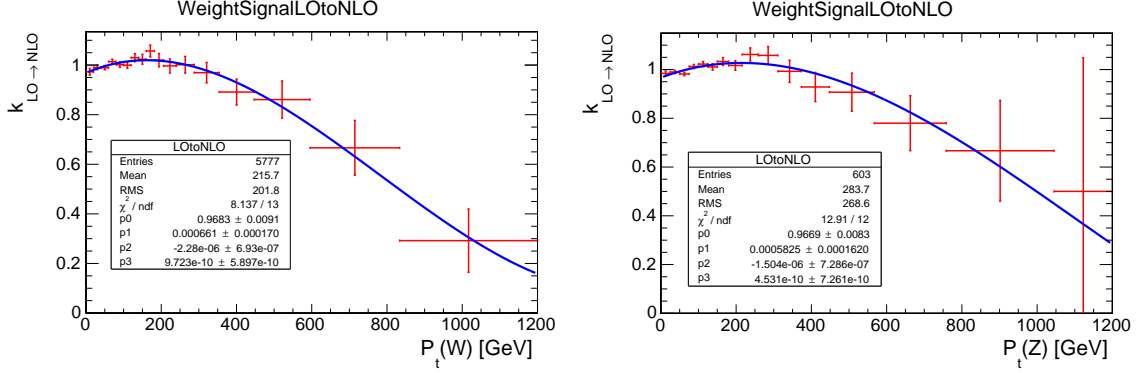


Figure 6.3.1: The ratio of the NLO POWHEG and LO JHUGEN V transverse momentum shapes, applied as a k-factor to signal MC. The k-factors are derived separately in WH (left) and ZH (right) MC.

reproduce the distribution observed in data.

6.4 Event Selection

Signal events are selected with the same set of cuts used in the BDT-based SM search, summarized in Table 6.2. These events are split into two boost regions for both the WH and ZH channels, defined by requirements on the V transverse momentum. With respect to the SM search, we have dropped the low boost region in the WH channel due to its negligible sensitivity to anomalous couplings.

Higgs candidates are constructed from the pair of jets with the largest \vec{p}_T sum. The b jet energy regression from the SM search is applied in order to improve the Higgs mass scale and resolution.

In the WH channel, we attempt to determine the neutrino p_z in order to fully reconstruct the W. We begin by assuming the neutrino \vec{p}_T is given by the \vec{E}_T^{miss} . We then use the W mass constraint, which yields a quadratic equation in the neutrino p_z . If the solutions to this equation are real, we choose the solution closest to the charged lepton p_z . Since the neutrinos in signal events do not generally have very large $|p_z|$, if the magnitude of this solution is greater than 300 GeV and the other solution has

Table 6.2: Event selection criteria. Numbers in parentheses refer to the high boost region.

Variable	WH	ZH
$m_{\ell\ell}$ [GeV]	–	75 – 105
$p_T(j_1)$ [GeV]	> 30	> 20
$p_T(j_2)$ [GeV]	> 30	> 20
$p_T(h)$ [GeV]	> 100	–
$m(h)$ [GeV]	< 250	40 – 250 (< 250)
$p_T(V)$ [GeV]	130 – 180 (> 180)	50 – 100 (> 100)
CSV_{max}	> 0.40	> 0.50 (> 0.244)
CSV_{min}	> 0.40	> 0.244
$N_{\text{additional lepton}}$	$= 0$	–
E_T^{miss} [GeV]	> 45	–
$\Delta\Phi(E_T^{\text{miss}}, \ell)$	$< \pi/2$	–

a smaller magnitude, we choose the other solution. Complex solutions can arise in the case of mismeasured charged lepton momentum or \vec{E}_T^{miss} . If the solutions to the quadratic equation are complex, we take the real part of the solutions as the neutrino p_z and rescale the neutrino p_T such that the W mass constraint is satisfied. Finally, the W candidate is formed from the sum of the resulting neutrino four momentum and that of the charged lepton.

6.5 Background Modeling

The background modeling is identical to that of the SM search.

The background normalization scale factors for $t\bar{t}$, V+light jets, V+b, and V+bb, derived in the SM search from a simultaneous fit to data in V+light flavor (V+LF), V+heavy flavor (V+HF), and $t\bar{t}$ control regions, are applied. Furthermore, both the observed V and top p_T distributions in data are softer than in MC. We therefore apply the p_T -dependent corrections derived in the SM search to the V+jets MC and also the $t\bar{t}$ MC for the WH channel.

The BDT discriminant and $m(\text{VH})$ distributions for signal, background, and data

in the various control regions of the WH and ZH channels are shown in Appendix A.1. The expected background is found to agree with the data within uncertainties. Although the ZH CRs are not split into medium and high boost regions, we show two plots for each CR/distribution pair with the binning used in the 2D templates for the medium and high boost SRs.

6.6 Systematic Uncertainties

All sources of systematic uncertainties considered in the SM search are again considered here. The systematic uncertainties considered are summarized in Table 6.3.

Due to the use of two dimensional templates for hypothesis testing, a number of bins have significant MC statistical uncertainty. We treat the statistical uncertainty on each bin as an additional nuisance parameter, uncorrelated among bins. To keep the computing resources at a reasonable level, we can't assign a nuisance parameter for each bin of every process. Instead, we consider nuisance parameters only for those bins with significant statistical uncertainty and significant signal content. We include a nuisance parameter for all bins of process i for which the relative statistical uncertainty ($\Delta N_i/N_i$) exceeds 15%, and the statistical uncertainty relative to the total background expectation ($\Delta N_i/N_{background}$) exceeds 7%, and the 0^+ or 0^- signal expectation is at least 2.5% of the total background expectation.

A slight mismodeling is observed in a sideband of the medium boost signal regions, as shown in Appendix A.5. The ratio of data to MC shows an excess at high $m(VH)$. The mismodeling is consistent with a linear trend. As a result, four additional “trend” nuisance parameters are included for each signal region (WH/ZH, medium boost/high boost) which allows for a linear transformation of the background model. These trend nuisances are correlated among the electron and muon channels, but not between boost region or WH/ZH channels. The size of the uncertainty is taken as twice the

Table 6.3: Summary of the sources of systematic uncertainty on the background and signal yields. The size of the uncertainties that only affect normalizations are given. Uncertainties that also affect the shapes are implemented with template morphing, a smooth vertical interpolation between the nominal shape and systematic shape variations.

Source	Pre-fit uncertainty
Normalization uncertainties	
Integrated luminosity	2.6%
Lepton reconstruction and trigger efficiency	3% per ℓ
Missing transverse energy scale and resolution	3%
Signal and background cross section (scale)	4–6%
Signal and background parton distribution functions	1%
0^+ (0^-) EW/QCD signal corrections	2%/5% (10%/5%)
$t\bar{t}$ and V+jets data-driven scale factors	10%
Single top quark cross section	15%
Diboson cross section	15%
$gg \rightarrow ZH$ cross section	+35% –25%
Normalization + shape uncertainties	
Jet energy scale	$\pm 1\sigma$
Jet energy resolution	$\pm 1\sigma$
b tagging efficiency	$\pm 1\sigma$
b tagging mistag rate	$\pm 1\sigma$
Simulated event statistics	$\pm 1\sigma$
Event simulation accuracy (V+jets and $t\bar{t}$)	Alternate event simulation
$m(VH)$ modeling	$\pm 2\times$ fitted slope

slope observed in the signal region sidebands.

The signal MC is generated at LO. We apply higher order corrections to the MC, up to NNLO in α_{QCD} and NLO in α_{EW} . These corrections are well defined in the case of a 0^+ SM-like Higgs boson, but are somewhat ambiguous in the general case of aHVV couplings. The 0^+ QCD corrections should apply as well in the 0^- case, so we apply the same QCD corrections and uncertainty to the 0^- MC. For the electroweak corrections, we again apply the same NLO corrections to the 0^- MC, but apply a systematic uncertainty the same size as the NLO effects.

6.7 Parameter Scan

We perform a scan over f_{a3} values from 0 (pure scalar) to 1 (pure pseudoscalar). At each point in the scan, we maximize the binned likelihood

$$\mathcal{L} = \prod_{i=1}^N \frac{n_i^{\text{sig}}(\vec{\zeta}) + n_i^{\text{bkg}}}{n_i!} e^{-n_i^{\text{sig}}(\vec{\zeta}) - n_i^{\text{bkg}}}, \quad (6.7.1)$$

where n_i^{sig} (n_i^{bkg}) is the expected number of signal (background) events and n_i is the observed number of events in bin i of N bins. The expected number of signal events depends on the anomalous coupling parameters, $\vec{\zeta}$. Statistical uncertainty and the systematic uncertainties described in Section 6.6 are introduced with nuisance parameters and constraint PDFs. Deviations from the global minimum in the negative log likelihood distribution, $-2\Delta\ln \mathcal{L}$, are used to quantify consistency of the mixed hypotheses with the data. Expected results are determined from a fit to an Asimov data set with the SM Higgs included ($\mu = 1$).

We perform two types of scans. One type of scan is highly optimistic, performed solely for comparison with the Tevatron result [71]. In these ‘‘Tevatron-style’’ scans μ^{WH} and μ^{ZH} are fixed to one. It is also assumed the a_1 couplings are related by $|a_1^{WW}|^2 = |a_1^{ZZ}|^2$ and the a_3 couplings by $|a_3^{WW}|^2 = |a_3^{ZZ}|^2 \Omega^{\text{ZH,WH}^{-1}}$, where

$$\Omega^{\text{ZH,WH}} = \frac{\sigma_3^{WH}/\sigma_1^{WH}}{\sigma_3^{ZH}/\sigma_1^{ZH}}. \quad (6.7.2)$$

This implies $f_{a3}^{WH} = f_{a3}^{ZH}$, which we will refer to jointly as f_{0-} .

We also perform scans similar to those in Ref [66]. In these ‘‘CMS-style’’ scans, we again assume $|a_1^{WW}|^2 = |a_1^{ZZ}|^2$, but for the anomalous couplings we instead assume $|a_3^{WW}|^2 = |a_3^{ZZ}|^2$. This implies

$$f_{a3}^{WH} = \left[1 + \frac{1}{\Omega^{\text{ZH,WH}}} \left(\frac{1}{f_{a3}^{ZH}} - 1 \right) \right]^{-1}. \quad (6.7.3)$$

This relation between the a_i also implies

$$\mu^{WH} = \mu^{ZH} \times [1 - f_{a3}^{ZH} + f_{a3}^{ZH} \Omega^{ZH,WH}] . \quad (6.7.4)$$

Equations 6.7.3 and 6.7.4 can also be used to relate $H \rightarrow VV$ and VH channels (with an appropriate change of superscripts), allowing for a combination of results between these channels. In CMS-style scans, we allow the μ parameters to float.

We perform four sets of CMS-style scans under various assumptions:

- A) all Higgs couplings are SM except the HWW coupling ($|a_3^{ZZ}| = 0$),
- B) all Higgs couplings are SM except the HZZ coupling ($|a_3^{WW}| = 0$),
- C) all Higgs couplings are SM except the HWW and HZZ couplings ($|a_3^{WW}|^2 = |a_3^{ZZ}|^2$),
- D) anomalous Higgs couplings (aside from aHWW and aHZZ) effect coupling strengths only ($|a_3^{WW}|^2 = |a_3^{ZZ}|^2$).

6.7.1 Combine Physics Model

We use the Combine package with a custom version of the HiggsJPC physics model to perform the f_{a3} scans. The physics model can be found here [84].

There are four Higgs production processes relevant to the analysis, shown in Fig. 6.7.1. The analysis is optimized to select events consistent with the quark initiated diagram in the upper left of Fig. 6.7.1. This process is represented in the physics model as

$$\mathcal{P}_{\text{sig}}(\vec{x}; \vec{\zeta}) = (1 - f_{a3}) \mathcal{P}_{0+}(\vec{x}) + f_{a3} \mathcal{P}_{0-}(\vec{x}) + \sqrt{f_{a3}(1 - f_{a3})} \mathcal{P}_{0+,0-}^{\text{int}}(\vec{x}; \phi_{a3}), \quad (6.7.5)$$

where \mathcal{P}_{0+} (\mathcal{P}_{0-}) is a luminosity-scaled template representing the differential cross

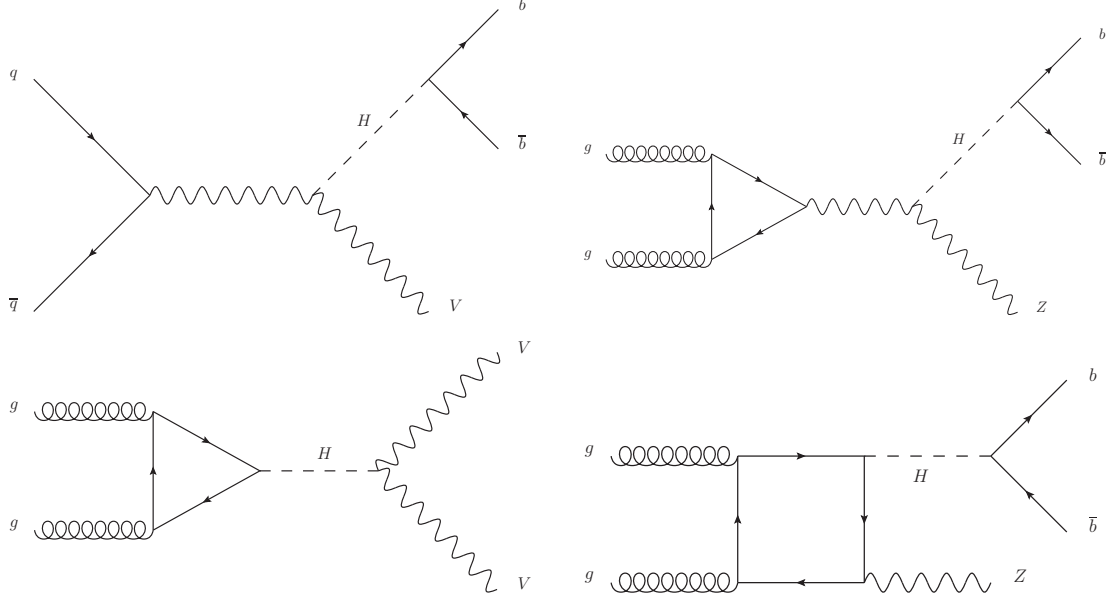


Figure 6.7.1: Various Feynman diagrams relevant to the analysis; quark initiated VH production (upper left), gluon initiated ZH production via a fermion triangle (upper right) and box (lower right), and gluon fusion with $H \rightarrow VV$ (lower left).

section times efficiency of a pure scalar (pseudoscalar), and $\mathcal{P}_{0^+,0^-}^{\text{int}}$ is a template which represents the effects of interference. In the VH analysis, the BDT discriminant and the $m(\text{VH})$ distributions are found to be insensitive to interference. Interference effects are therefore neglected. The $H \rightarrow VV$ process shown in the bottom left of Fig. 6.7.1 is represented similarly, but the interference effects are included (a phase of 0 is assumed).

The signal strength for $qq \rightarrow \text{VH}$ given in Eq. 6.1.3 is modified in the presence of additional anomalous Higgs couplings by a factor κ_b^2/κ_H^2 , where the κ_i are defined in Ref [85]. For $H \rightarrow VV$, the signal strength is modified by a factor κ_g^2/κ_H^2 . If $\kappa_b = \kappa_g$, the signal strength of the two channels are equal. Otherwise, the signal strengths are not related. We therefore enforce Eq. 6.7.4 (with a suitable change of superscripts) during the fits under assumptions A-C described above; whereas under assumption D, the normalizations of the VH and $H \rightarrow VV$ processes are not correlated.

The ZH process contains two additional gluon initiated diagrams. The box dia-

gram shown in the bottom right of Fig. 6.7.1 does not contain an HVV vertex, and therefore is not sensitive to the values of a_1 or a_3 . However, the triangle diagram shown in the upper right of Fig. 6.7.1 does contain an HZZ vertex. The $gg \rightarrow Z^*$ portion of the diagram is completely symmetric under a reversal of the direction of loop momentum flow. The a_1 (a_3) term in Eq. 6.1.1 is completely symmetric (anti-symmetric). Therefore, a potential pseudoscalar interaction has no contribution, as the process as a whole is completely anti-symmetric, and diagrams with the direction of loop momentum flow reversed cancel one another. This process therefore only depends on the value of a_1 .

Considered separately, the signal strength of the triangle (box) diagram is given by $|a_1^{ZZ}|^2 \times \kappa_b^2/\kappa_H^2$ ($\kappa_g^2 \times \kappa_b^2/\kappa_H^2$). The triangle diagram has the same κ_b^2/κ_H^2 -dependence as that of $qq \rightarrow ZH$. Therefore, even in the presence of additional anomalous Higgs couplings these two processes always share a correlated signal strength parameter. In principle, the signal strength of the box diagram should be fixed to 1 under assumptions A-C described above, and be a free parameter under scenario D. But we are unable to constrain the box normalization with the data at hand and therefore fix it to the SM cross section under all scenarios.

The signal strength parameters of the various processes are summarized in Table 6.4.

The two gluon initiated ZH diagrams interfere strongly with one another, and this interference is accounted for. We take the $gg \rightarrow ZH$ interaction to be of the form

$$\mathcal{P}_{ggZH}(\vec{x}; \vec{\zeta}) = b^2 \sigma_{\square} \mathcal{P}_{\square} + a_1^2 \sigma_{\triangle} \mathcal{P}_{\triangle} + a_1 b \times [\sigma_{\square+\triangle} \mathcal{P}_{\square+\triangle} - \sigma_{\square} \mathcal{P}_{\square} - \sigma_{\triangle} \mathcal{P}_{\triangle}], \quad (6.7.6)$$

where b is an effective coupling constant controlling the box term, the σ_i are the cross sections for the various processes when all couplings are one, and the \mathcal{P}_i are luminosity-scaled templates representing the differential cross section times efficiency

Table 6.4: Signal strength parameters for the various Higgs production processes. In a given row, μ values with a common subscript but primed are related via Eq. 6.7.4.

Scan	Assumption	μ_{VV} ($\kappa_g^2 \times \kappa_V^2 / \kappa_H^2$)	$\mu_{qq \rightarrow WH}$ ($\kappa_W^2 \times \kappa_b^2 / \kappa_H^2$)	$\mu_{qq \rightarrow ZH}$ ($\kappa_Z^2 \times \kappa_b^2 / \kappa_H^2$)	μ_{Δ} ($\kappa_Z^2 \times \kappa_b^2 / \kappa_H^2$)	μ_{\Box} ($\kappa_g^2 \times \kappa_b^2 / \kappa_H^2$)
Tevatron-style						
WH	aHWW only	X	1	1	1	1
ZH	aHZZ only	X	1	1	1	1
VH	aHVV only ($a_i^{WW} = a_i^{ZZ}$, $a_3^{WW} = a_3^{ZZ} \Omega_{ZH,WH}$)	X	1	1	1	1
CMS-style						
WH	aHWW only	X	μ_0	1	1	1
WW	aHWW only	μ_0	X	X	X	X
WH+WW	aHWW only	μ_0	1	1	1	1
ZH	aHZZ only	X	1	μ_0	$\mu_0(1 - f_{a3})$	1
ZZ	aHZZ only	μ_0	X	X	X	X
ZH+ZZ	aHZZ only	μ_0	1	μ_0	$\mu_0(1 - f_{a3})$	1
VH	aHVV only ($a_i^{WW} = a_i^{ZZ}$)	X	μ_0	μ_0	$\mu_0(1 - f_{a3})$	1
VV	aHVV only ($a_i^{WW} = a_i^{ZZ}$)	μ_0	X	X	X	X
VH+VV	aHVV only ($a_i^{WW} = a_i^{ZZ}$)	μ_0	μ_0'	μ_0	$\mu_0(1 - f_{a3})$	1
WH+WW	all aHXX allowed ($a_i^{WW} = a_i^{ZZ}$)	μ_1	μ_2	μ_3	$\mu_3(1 - f_{a3})$	1
ZH+ZZ	all aHXX allowed ($a_i^{WW} = a_i^{ZZ}$)	μ_1	μ_2	μ_3	$\mu_3(1 - f_{a3})$	1
VH+VV	all aHXX allowed ($a_i^{WW} = a_i^{ZZ}$)	μ_1	μ_2'	μ_2	$\mu_2(1 - f_{a3})$	1
2D						
WH	aHWW only	X	μ_0	1	1	1
ZH	aHZZ only	X	1	μ_0	$\mu_0(1 - f_{a3})$	1
VH	aHVV only ($a_i^{WW} = a_i^{ZZ}$)	X	μ_0'	μ_0	$\mu_0(1 - f_{a3})$	1

for the various processes. We generate LHE events with VBFNLO [86] for the box only ($a_1 = 0$, $b = 1$), the triangle only ($a_1 = 1$, $b = 0$), and the box plus triangle process including interference ($a_1 = 1$, $b = 1$). We can construct a template for any observable at gen-level for arbitrary a_1, b couplings from a linear combination of these three samples. A closure test which demonstrates this is shown in Fig. 6.7.2.

Using the generator-level m (ZH) distributions from these three samples, we construct event-by-event weights with which to reweight our SM box+triangle $gg \rightarrow ZH$ MC in order to obtain hypothetical box-only and triangle-only samples. Just as shown above, we can then construct a template for any observable at reconstructed-level for arbitrary a_1, b couplings from a linear combination of these three samples. In this way, we can allow the triangle signal strength to float, while always maintaining the correct interference between the two diagrams.

6.7.2 Presentation of results

For a given set of coupling constants, the physical observable f_{a3} varies for different processes as a result of the dependence on the σ_i in Eq. 6.1.2 (except in the limiting

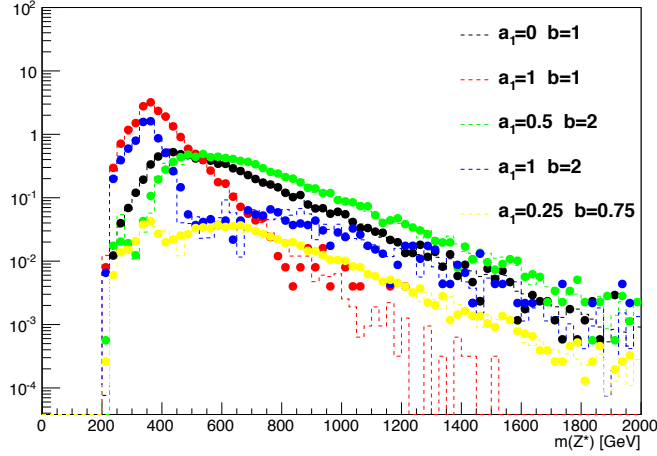


Figure 6.7.2: Closure test of the $gg \rightarrow ZH$ reweighting procedure. Histograms constructed directly from LHEs generated with various a_1 and b values (dots) are compared to those constructed from a linear combination of box-only, triangle-only, and box+triangle LHEs (dashed lines).

cases of $f_{a3} = 0$ and $f_{a3} = 1$). In the following, f_{a3} will be indexed to indicate the σ_i used in the definition. f_{a3} values calculated with respect to different processes are related via Eq. 6.7.3 with a substitution of the relevant superscripts. The results in terms of f_{a3}^{WW} and f_{a3}^{ZZ} can be compared to previous results [66]. We perform both one-dimensional profile likelihood scans of f_{a3} (where μ is profiled) and two-dimensional scans in the μ versus f_{a3} plane.

6.7.3 Templates

Although trained for a 0^+ signal, the BDT developed for the SM legacy analysis also efficiently separates the 0^- signal from the backgrounds, as shown for the WH channel in Fig. 6.7.3. The $m(\text{VH})$ distribution peaks at much larger values for the 0^- signal than it does for 0^+ , as shown in Fig. 6.7.4, again for the WH channel. Therefore, we construct 2D templates in the BDT discriminant vs $m(\text{VH})$ space. The region with large BDT discriminant is background depleted. Within this region, the low (high) $m(\text{VH})$ region is 0^+ (0^-) enhanced. The 2D templates for the signals,

total background, and data are shown in Fig. 6.7.5 in the $W \rightarrow e\nu$ channel, high boost region (see Appendix A.2 for the full set of the 2D templates). Example 1D projections of the 2D templates are shown in Fig. 6.7.6 for high boost region (see Appendix A.2 for the full set of the 1D projections). We use the exact BDT training from the SM search. We make use only of the BDT trained to reject all backgrounds, not the cascading background-specific BDTs used to categorize events in the SM search.

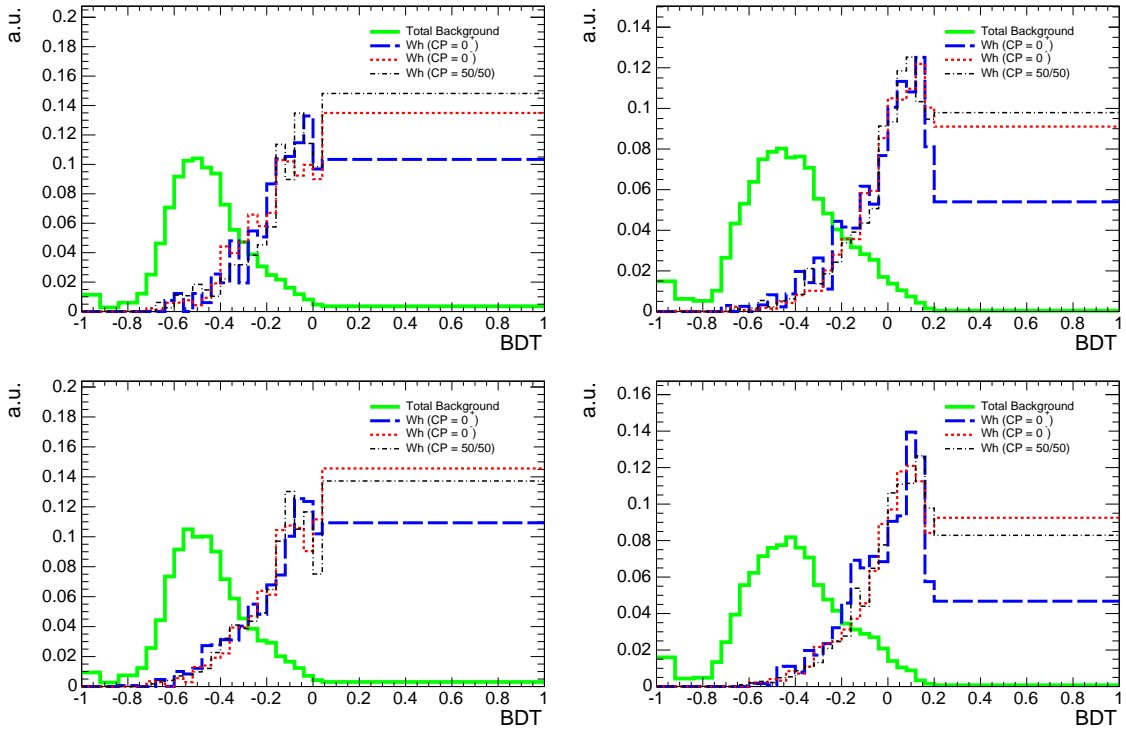


Figure 6.7.3: The shape of the BDT discriminant in selected events for the 0^+ , 0^- , and 50/50 signals compared to background, normalized to unit area. The top (bottom) row shows the electron (muon) channel. The left (right) column shows the medium (high) boost region.

The variable-width binning of the templates was chosen so all bins contain some background expectation, to avoid numerical issues related to identically zero background expectation. More details can be found in Appendix A.3.

The 2D templates are unrolled into 1D distributions, for use in Higgs combine

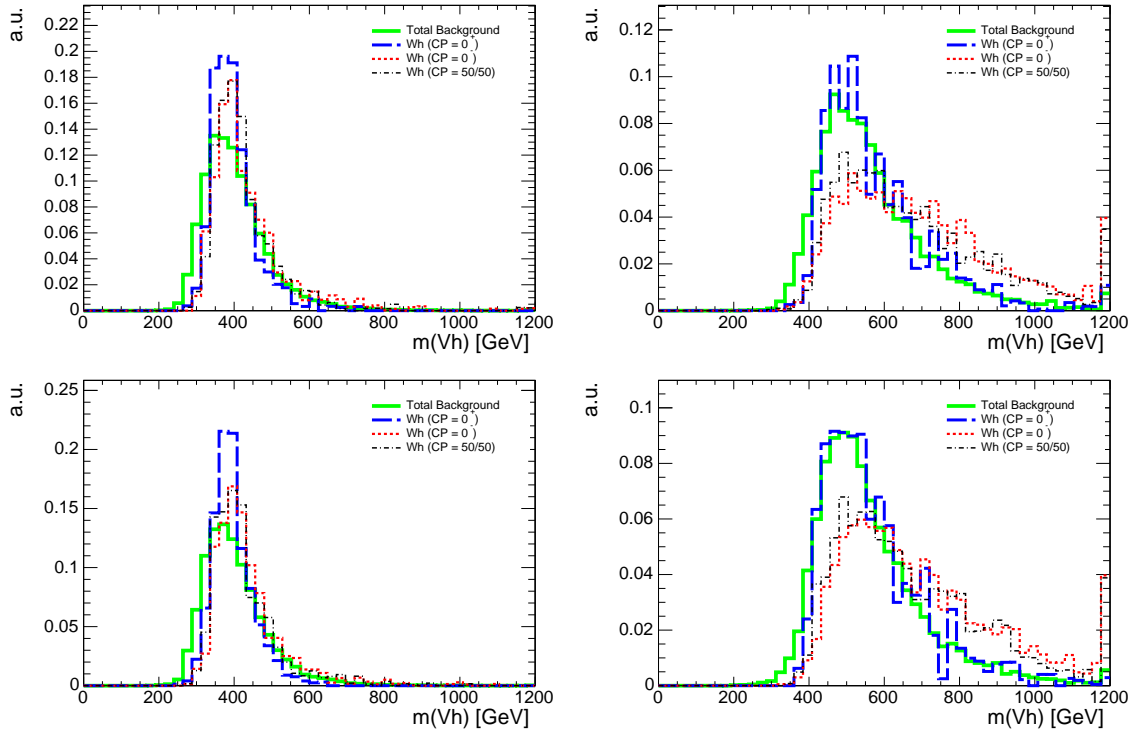


Figure 6.7.4: The shape of the $m(Vh)$ distribution in selected events for the 0^+ , 0^- , and 50/50 signals compared to background, normalized to unit area. The top (bottom) row shows the electron (muon) channel. The left (right) column shows the medium (high) boost region.

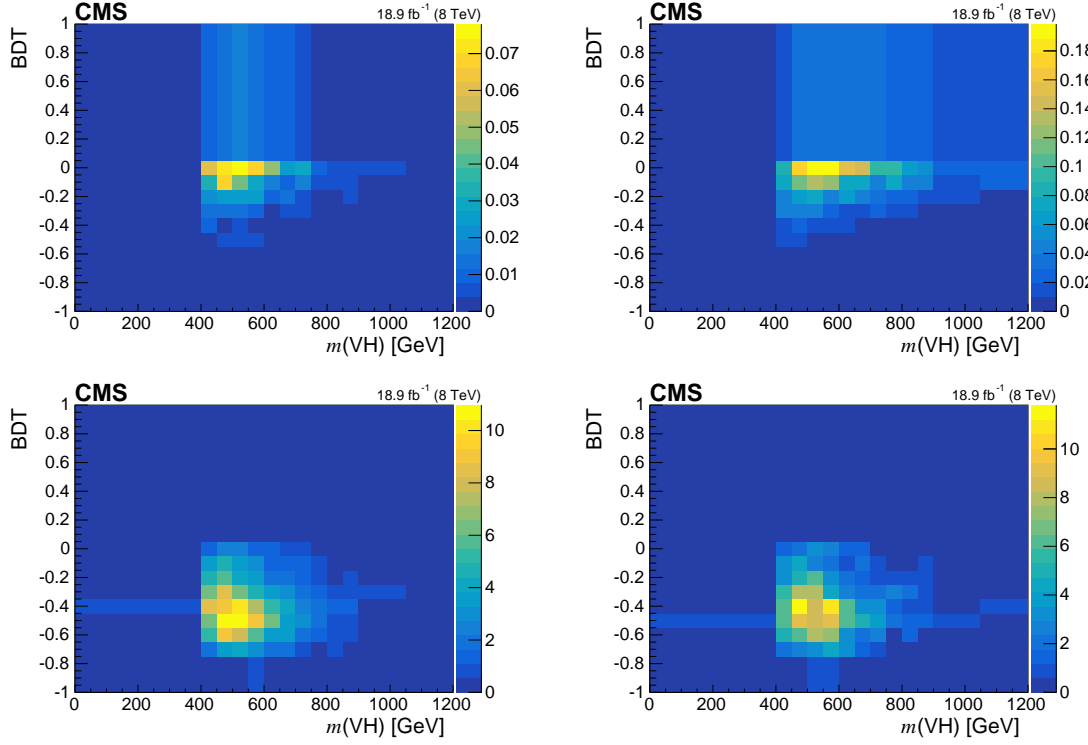


Figure 6.7.5: The 2D templates used for hypothesis testing in the $W \rightarrow e\nu$ channel, high boost region. From upper left to lower right: 0^+ signal, 0^- signal, total background, and data.

tools [87]. Given that the bins are treated as statistically independent with no bin-to-bin correlations, the unrolling does not effect the results. The unrolled templates are shown in Fig. 6.7.7 (the full set of unrolled templates are shown in Appendix A.2).

6.8 Results

6.8.1 Tevatron-Style Scans

The results of tevatron-style scans based exclusively on the WH and ZH channels, as well as the combination, are shown in Fig. 6.8.1. In all cases, the data exhibit a modest preference for intermediate values of f_{0-} . The best fit for f_{0-} and the 95% CL intervals of the fit are shown in Table 6.5.

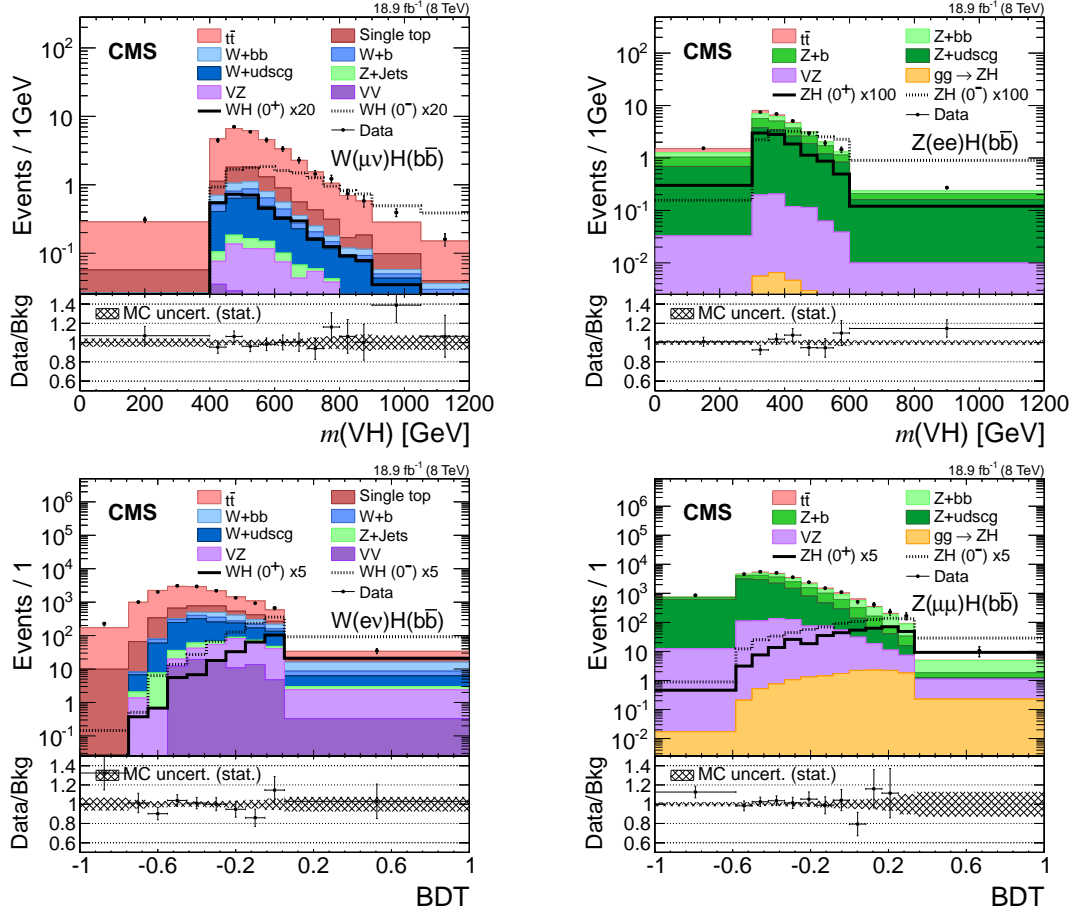


Figure 6.7.6: The distribution of (top) $m(\text{VH})$ in the (left) $W \rightarrow \mu\nu$ and (right) $Z \rightarrow ee$ channels and (bottom) BDT discriminant in the (left) $W \rightarrow e\nu$ and (right) $Z \rightarrow \mu\mu$ channels in selected events for the 0^+ , and 0^- signals compared to background, normalized to 18.9 fb^{-1} . All distributions are from the high boost region.

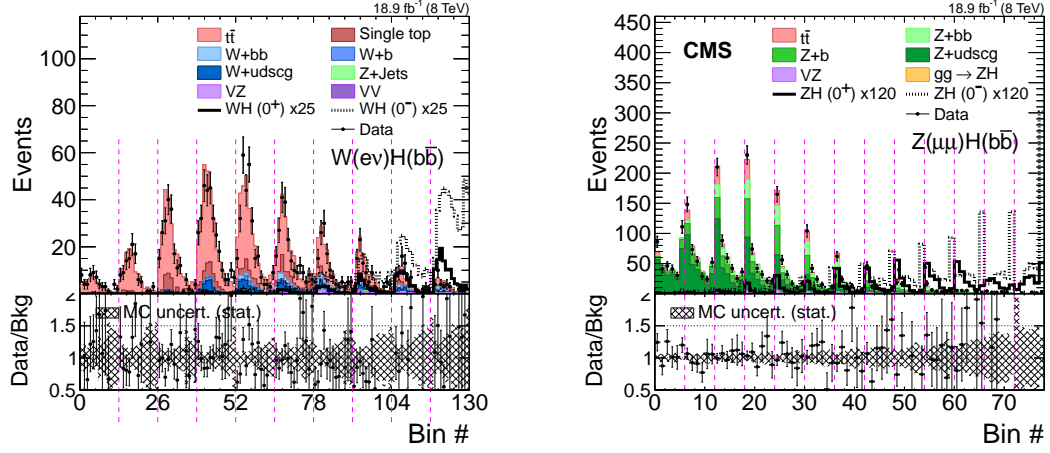


Figure 6.7.7: Unrolled 2D templates in the (left) $W \rightarrow e\nu$ and (right) $Z \rightarrow \mu\mu$ channels of the high boost region.

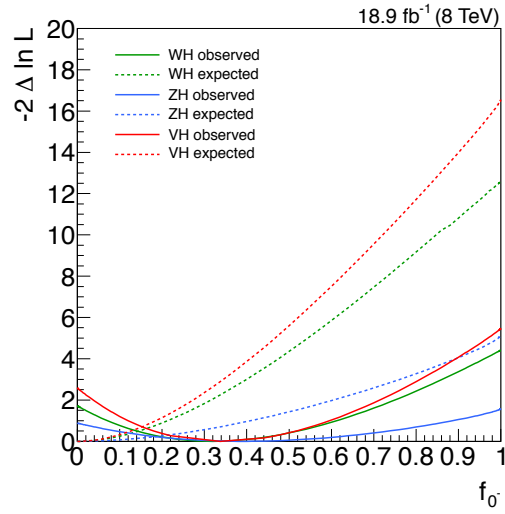


Figure 6.8.1: Results of the fixed- μ profile likelihood scans in the WH, ZH, and VH (WH +ZH) channels. The dashed (solid) line shows the expected (observed) $-2\Delta\ln\mathcal{L}$ value as a function of f_0 . Expected results are derived from Asimov data for a pure scalar Higgs with $\mu = 1$.

Table 6.5: The best fit value of f_{0-} and 95% CL intervals derived from fixed- μ profile likelihood scans. The ranges are truncated at the physical boundaries.

Channel	f_{0-} Best Fit	f_{0-} 95% CL Obs. (Exp.)
WH	$0.32^{+0.29}_{-0.25}$	$<0.95(0.46)$
ZH	$0.39^{+0.49}_{-0.39}$	$<1.0(0.87)$
VH	$0.34^{+0.26}_{-0.22}$	$<0.88(0.40)$

6.8.2 CMS-Style Scans

The results of CMS-style scans based only on the associated production channels are shown in Fig. 6.8.2. The WH (ZH) channel was then combined with the $H \rightarrow WW$ ($H \rightarrow ZZ$) channel to enhance the sensitivity to anomalous HWW (HZZ) interactions, without the need to introduce any assumption on the relationship between HWW and HZZ couplings. These results probing the HWW and HZZ couplings are shown in the top and bottom plots of Fig. 6.8.3, respectively. Finally, all four channels are combined under the assumption $a_i^{\text{HWW}} = a_i^{\text{HZZ}}$, with the results shown in Fig. 6.8.4. The best fit f_{a3} and 95% CL intervals are shown in Table 6.6. The results are shown in a slightly different format, also including the expected 68% CL intervals in Table 6.7.

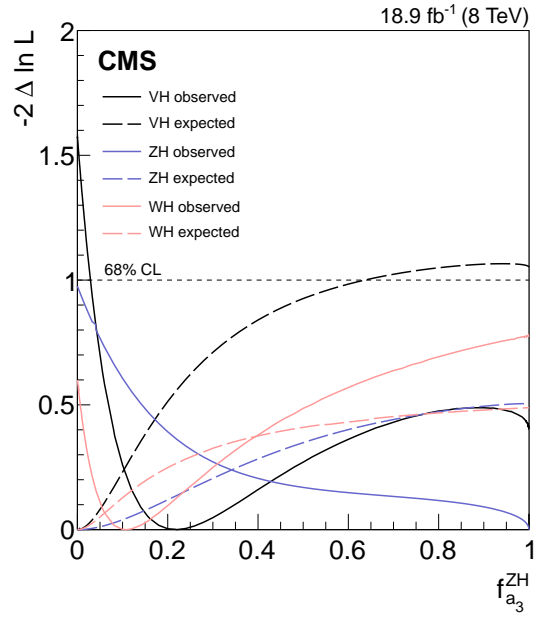


Figure 6.8.2: Results of the floating- μ profile likelihood scans for the WH and ZH channels, as well as their combination (VH). The dotted (solid) lines show the expected (observed) $-2\Delta\ln\mathcal{L}$ value as a function of $f_{a_3}^{ZH}$. Expected results are derived from Asimov data for a pure scalar Higgs with $\mu = 1$. The horizontal dashed line represents the 68% CL.

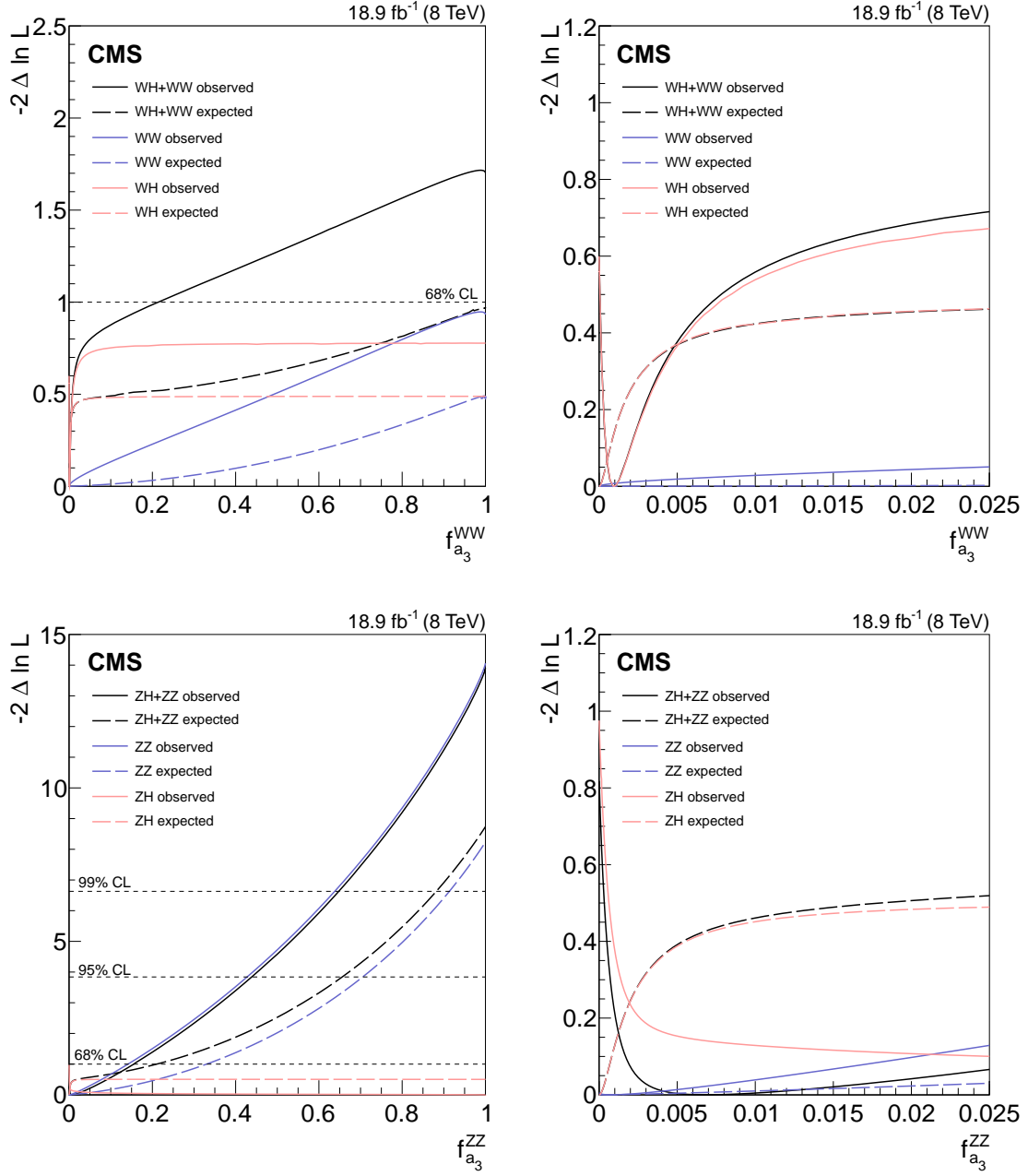


Figure 6.8.3: Results of the floating- μ profile likelihood scans for the VH and $H \rightarrow VV$ channels, plus their combination. The top (bottom) plots show results which exclusively depend on the HWW (HZZ) couplings. The dotted (solid) lines show the expected (observed) $-2\Delta\ln\mathcal{L}$ value as a function of (top) f_{a3}^{WW} and (bottom) f_{a3}^{ZZ} . The full range of f_{a3} is shown on the left, with the low f_{a3} region highlighted on the right. Expected results are derived from Asimov data for a pure scalar Higgs with $\mu = 1$. The horizontal dashed lines represent the 68%, 95%, and 99% CL.

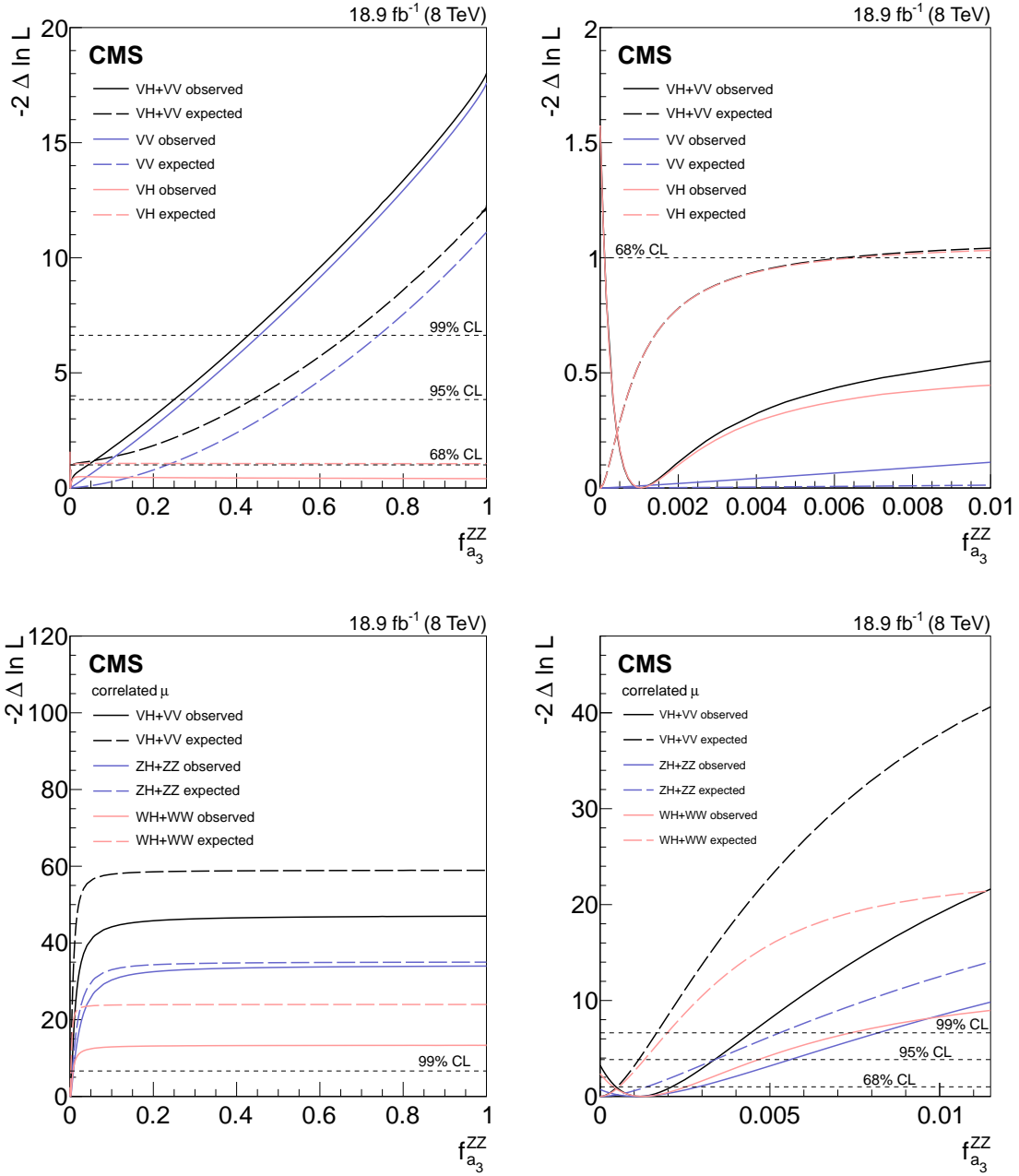


Figure 6.8.4: Results of the floating- μ profile likelihood scans for the VH and $H \rightarrow VV$ channels, as well as their combination. The dotted (solid) lines show the expected (observed) $-2\Delta\ln\mathcal{L}$ value as a function of f_{a3}^{ZZ} . The full range of f_{a3}^{ZZ} is shown on the left, with the low f_{a3}^{ZZ} region highlighted on the right. The bottom plots contain the results of correlated- μ scans. Expected results are derived from Asimov data for a pure scalar Higgs with $\mu = 1$. The horizontal dashed lines represent the 68%, 95%, and 99% CL. In the legends, VH refers to the combination of the WH and ZH channels, and VV refers to the combination of the $H \rightarrow WW$ and $H \rightarrow ZZ$ channels.

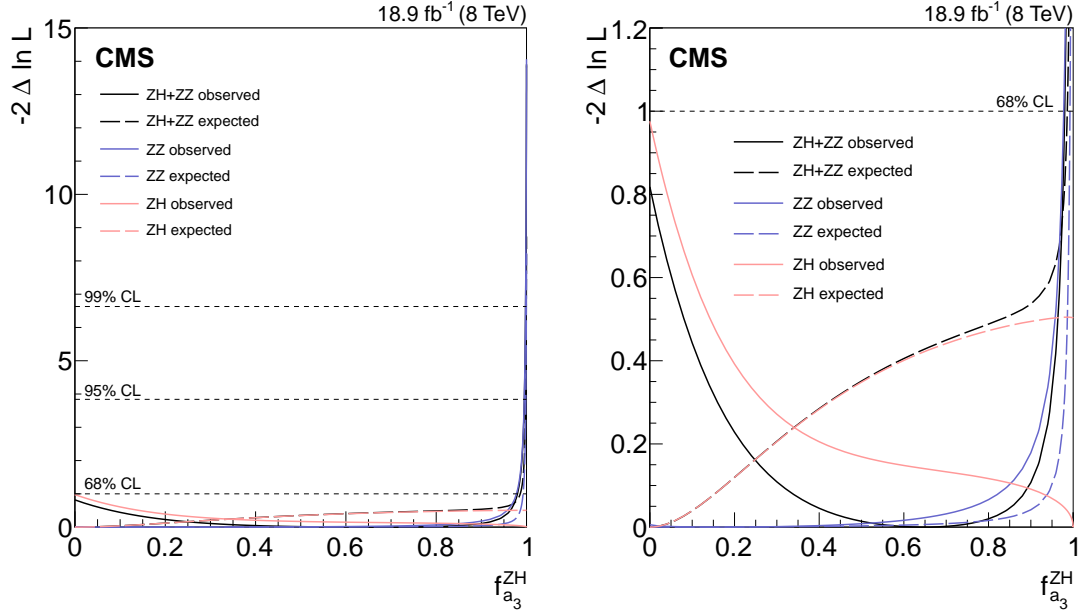


Figure 6.8.5: Results of the floating- μ profile likelihood scans for the ZH and $H \rightarrow ZZ$ channels, as well as their combination. These channels exclusively probe the HZZ coupling, and therefore the results do not include any assumption on the relationship between the HWW and HZZ couplings. The dotted (solid) lines show the expected (observed) $-2\Delta\ln\mathcal{L}$ value as a function of f_{a3}^{ZH} . Expected results are derived from Asimov data for a pure scalar Higgs with $\mu = 1$. The horizontal dashed lines are shown, representing the 68% and 95% CL.

Table 6.6: The best fit values of f_{a3} and 95% CL intervals derived from floating- μ profile likelihood scans. The ranges are truncated at the physical boundaries. All scans which involve both VH and $H \rightarrow VV$ channels are performed with and without enforcing the correlation between the μ parameters given in Equation 6.7.4.

Channel	Best Fit		95% CL Obs. (Exp.)	
WH	$f_{a3}^{\text{WH}} = 0.14^{+0.86}_{-0.14}$	$f_{a3}^{\text{WW}} = 0.00096^{+0.99904}_{-0.00096}$	$f_{a3}^{\text{WH}} < 1.0$ (1.0)	$f_{a3}^{\text{WW}} < 1.0$ (1.0)
ZH	$f_{a3}^{\text{ZH}} = 1.0^{+0.0}_{-1.0}$	$f_{a3}^{\text{ZZ}} = 1.0^{+0.0}_{-1.0}$	$f_{a3}^{\text{ZH}} < 1.0$ (1.0)	$f_{a3}^{\text{ZZ}} < 1.0$ (1.0)
VH	$f_{a3}^{\text{ZH}} = 0.22^{+0.78}_{-0.19}$	$f_{a3}^{\text{ZZ}} = 0.00106^{+0.99894}_{-0.00094}$	$f_{a3}^{\text{ZH}} < 1.0$ (1.0)	$f_{a3}^{\text{ZZ}} < 1.0$ (1.0)
Correlated μ parameters				
WH + $H \rightarrow \text{WW}$	$f_{a3}^{\text{WH}} = 0.31^{+0.17}_{-0.19}$	$f_{a3}^{\text{WW}} = 0.0026^{+0.0027}_{-0.0018}$	$f_{a3}^{\text{WH}} < 0.63$ (0.32)	$f_{a3}^{\text{WW}} < 0.0098$ (0.0027)
ZH + $H \rightarrow \text{ZZ}$	$f_{a3}^{\text{ZH}} = 0.23^{+0.21}_{-0.23}$	$f_{a3}^{\text{ZZ}} = 0.0011^{+0.0018}_{-0.0011}$	$f_{a3}^{\text{ZH}} < 0.60$ (0.48)	$f_{a3}^{\text{ZZ}} < 0.0056$ (0.0034)
VH + $H \rightarrow \text{VV}$	$f_{a3}^{\text{ZH}} = 0.24^{+0.12}_{-0.13}$	$f_{a3}^{\text{ZZ}} = 0.00118^{+0.00092}_{-0.00072}$	$f_{a3}^{\text{ZH}} < 0.48$ (0.23)	$f_{a3}^{\text{ZZ}} < 0.0034$ (0.0011)
Uncorrelated μ parameters				
WH + $H \rightarrow \text{WW}$	$f_{a3}^{\text{WH}} = 0.13^{+0.85}_{-0.13}$	$f_{a3}^{\text{WW}} = 0.00088^{+0.21318}_{-0.00088}$	$f_{a3}^{\text{WH}} < 1.0$ (1.0)	$f_{a3}^{\text{WW}} < 1.0$ (1.0)
ZH + $H \rightarrow \text{ZZ}$	$f_{a3}^{\text{ZH}} = 0.64^{+0.34}_{-0.64}$	$f_{a3}^{\text{ZZ}} = 0.0067^{+0.1487}_{-0.0067}$	$f_{a3}^{\text{ZH}} < 0.995$ (0.998)	$f_{a3}^{\text{ZZ}} < 0.44$ (0.66)
VH + $H \rightarrow \text{VV}$	$f_{a3}^{\text{ZH}} = 0.21^{+0.71}_{-0.19}$	$f_{a3}^{\text{ZZ}} = 0.00102^{+0.04236}_{-0.00091}$	$f_{a3}^{\text{ZH}} < 0.989$ (0.995)	$f_{a3}^{\text{ZZ}} < 0.25$ (0.44)

The power of the associated production channels at constraining anomalous HVV couplings is demonstrated in Fig. 6.8.2. Although the expected exclusion of anomalous couplings in these channels is only at the $\sim 68\%$ CL level, these channels are sensitive to very small values of f_{a3}^{ZZ} . Whereas, measurements in the $H \rightarrow VV$ channels demonstrate strong sensitivity at larger values of f_{a3}^{ZZ} . Furthermore, the sensitivity to anomalous couplings is enhanced significantly in a combination of the VH and $H \rightarrow VV$ channels, particularly in the absence of additional anomalous couplings.

6.8.3 2D Scans

The results of two-dimensional scans in the μ^{ZH} versus f_{a3}^{ZH} plane are shown in Figs. 6.8.6, 6.8.7, and 6.8.8. The scan prefers smaller μ^{ZH} values with increasing f_{a3}^{ZH} as a result of increasing signal efficiency.

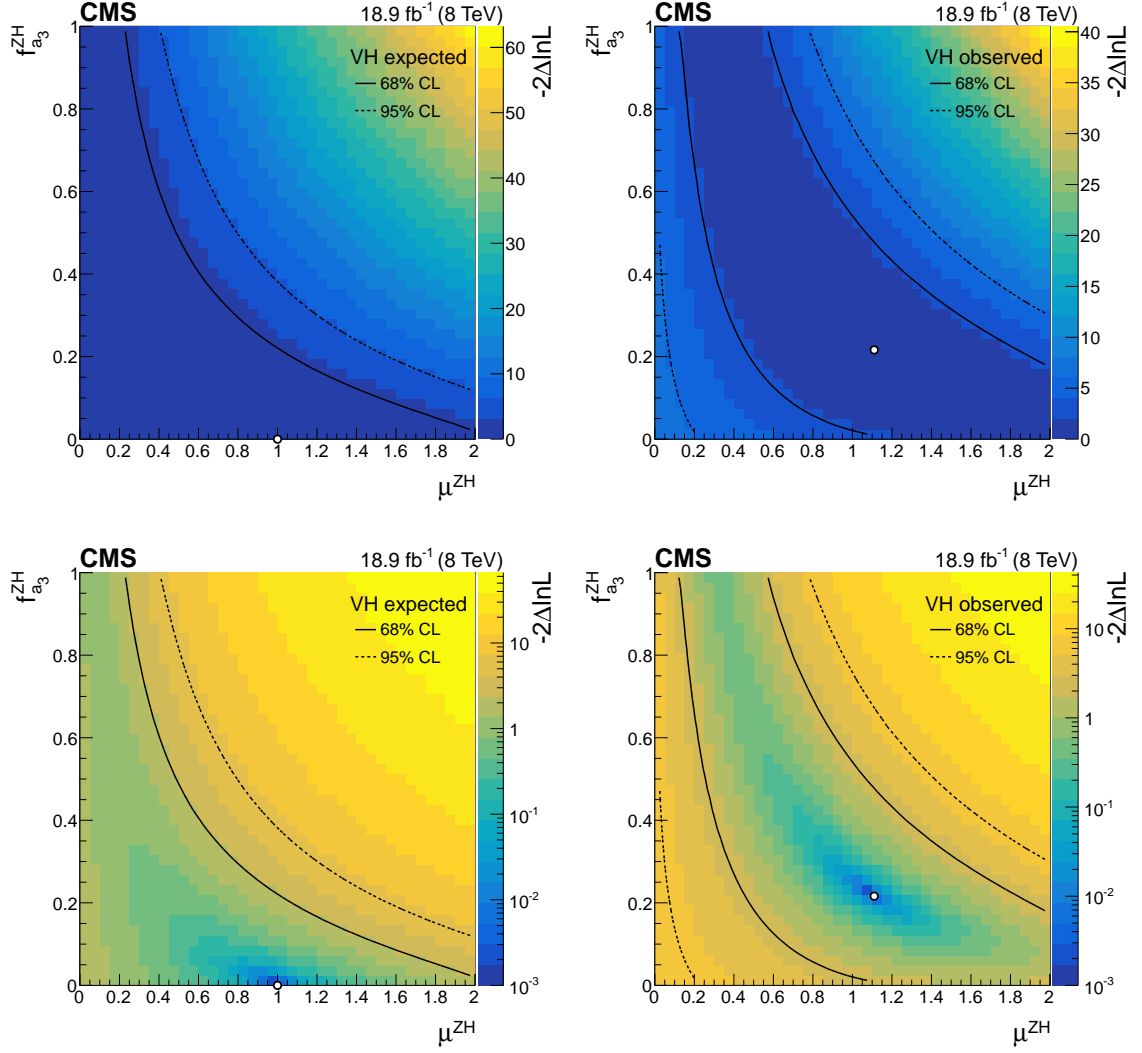


Figure 6.8.6: Results of expected (left) and observed (right) two-dimensional profile likelihood scans in the μ^{ZH} versus f_{a3}^{ZH} plane using the combination of WH and ZH channels. The z -axis represents $-2\Delta\ln\mathcal{L}$ calculated with respect to the global minimum with a linear (log) scale on the top (bottom) row. The scan minimum is indicated by a white dot. The 68% and 95% CL contours at $-2\Delta\ln\mathcal{L} = 2.30$ and 5.99, respectively, are shown. Expected results are derived from Asimov data for a pure scalar Higgs with $\mu = 1$.

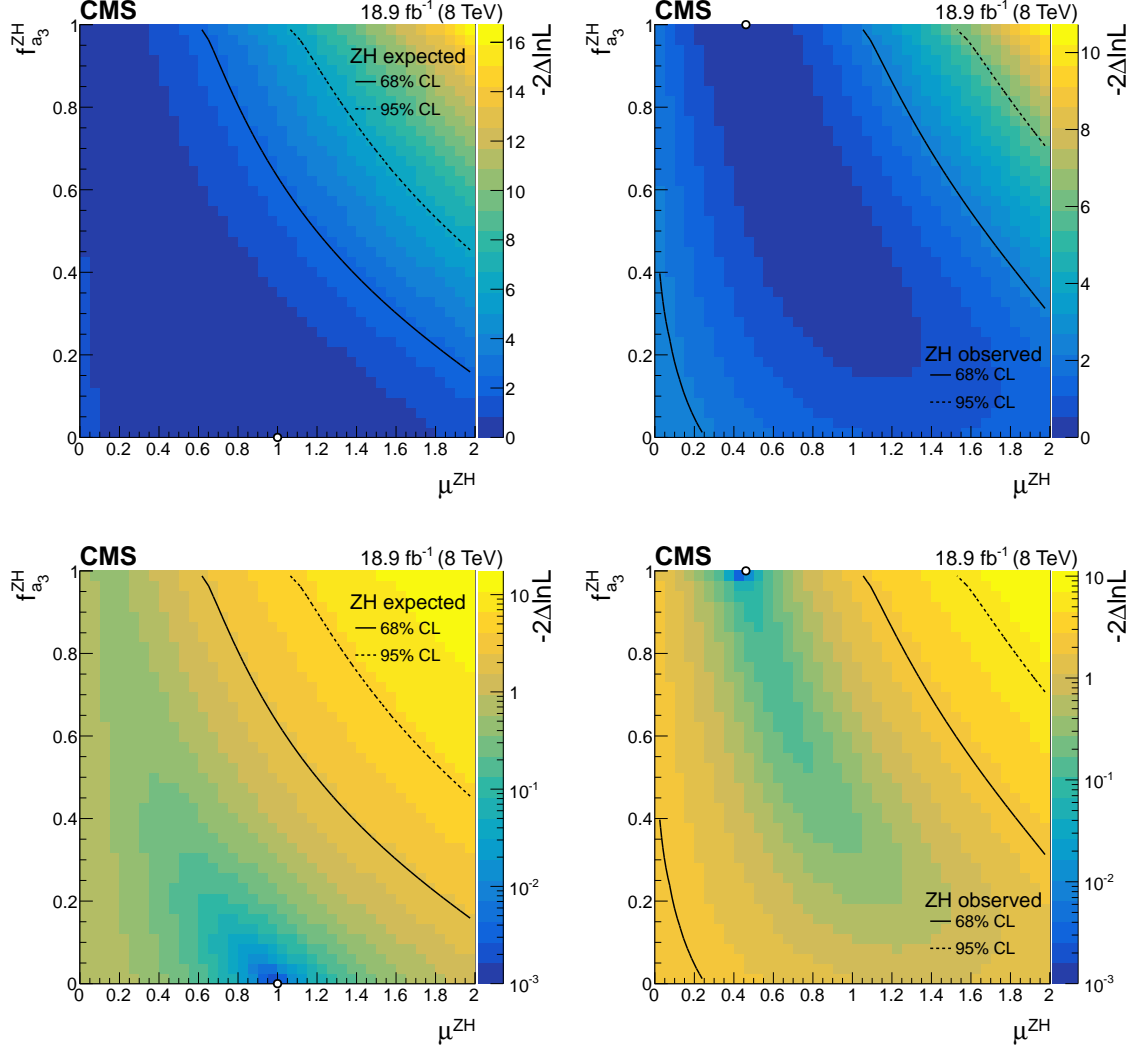


Figure 6.8.7: Results of expected (left) and observed (right) two-dimensional profile likelihood scans in the μ^{ZH} versus f_{a3}^{ZH} plane using the ZH channel. The z -axis represents $-2\Delta\ln\mathcal{L}$ calculated with respect to the global minimum with a linear (log) scale on the top (bottom) row. The scan minimum is indicated by a white dot. The 68% and 95% CL contours at $-2\Delta\ln\mathcal{L} = 2.30$ and 5.99, respectively, are shown. Expected results are derived from Asimov data for a pure scalar Higgs with $\mu = 1$.

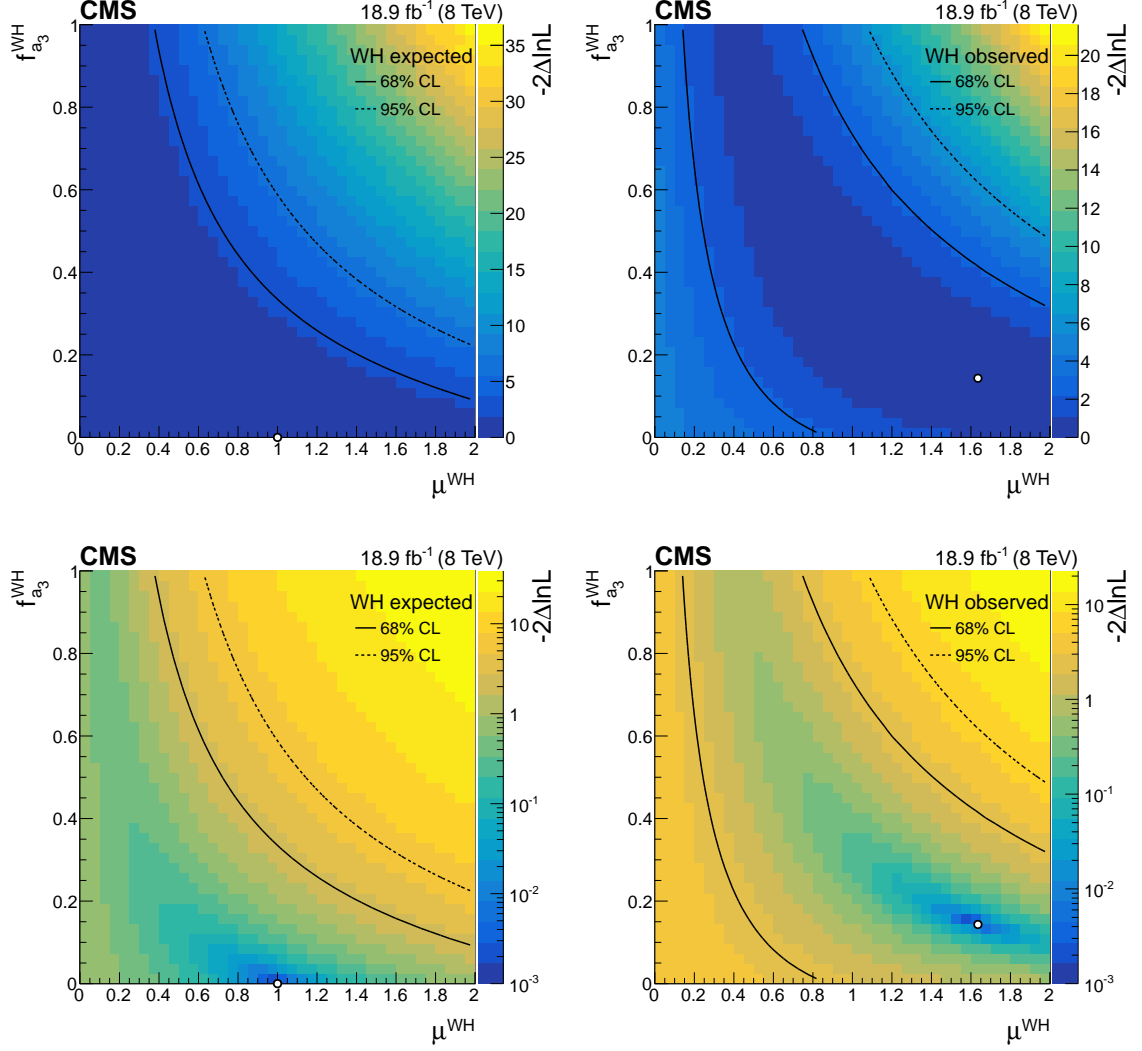


Figure 6.8.8: Results of expected (left) and observed (right) two-dimensional profile likelihood scans in the μ^{WH} versus f_{a3}^{WH} plane using the WH channel. The z -axis represents $-2\Delta\ln\mathcal{L}$ calculated with respect to the global minimum with a linear (log) scale on the top (bottom) row. The scan minimum is indicated by a white dot. The 68% and 95% CL contours at $-2\Delta\ln\mathcal{L} = 2.30$ and 5.99 , respectively, are shown. Expected results are derived from Asimov data for a pure scalar Higgs with $\mu = 1$.

Table 6.7: The observed and expected intervals derived from floating- μ profile likelihood scans. Parentheses contain 68% CL intervals, and brackets contain 95% CL intervals. The ranges are truncated at the boundaries $0 < f_{a3} < 1$. All scans which involve both VH and $H \rightarrow VV$ channels are performed with and without enforcing the correlation between the μ parameters given in Equation 6.7.4.

Channel	Parameter	Expected	Observed
WH	f_{a3}^{WH}	0 (0, 1) [0, 1]	0.14 (0, 1) [0, 1]
ZH	f_{a3}^{ZH}	0 (0, 1) [0, 1]	1.0 (0, 1) [0, 1]
VH	f_{a3}^{ZH}	0 (0, 0.64) [0, 1]	0.22 (0.029, 1) [0, 1]
Correlated μ parameters			
WH + $H \rightarrow WW$	f_{a3}^{WW}	0 (0, 0.0012) [0, 0.0027]	0.0026 (0.00082, 0.0053) [0, 0.0098]
ZH + $H \rightarrow ZZ$	f_{a3}^{ZZ}	0 (0, 0.0014) [0, 0.0034]	0.0011 (0, 0.0029) [0, 0.0056]
VH + $H \rightarrow VV$	f_{a3}^{ZZ}	0 (0, 0.00050) [0, 0.0011]	0.00118 (0.00047, 0.0021) [0, 0.0034]
Uncorrelated μ parameters			
WH + $H \rightarrow WW$	f_{a3}^{WW}	0 (0, 1) [0, 1]	0.00088 (0, 0.21) [0, 1]
ZH + $H \rightarrow ZZ$	f_{a3}^{ZZ}	0 (0, 0.21) [0, 0.66]	0.0067 (0, 0.16) [0, 0.44]
VH + $H \rightarrow VV$	f_{a3}^{ZZ}	0 (0, 0.0062) [0, 0.44]	0.00102 (0.00011, 0.043) [0, 0.25]

6.8.4 Form Factor Scans

In general, the coupling parameters can depend on kinematic invariants of the two vector bosons [72, 75, 76]. In this analysis, such a dependence is ignored for a Higgs particle with a mass of 125 GeV [75]. However, in this section, we consider the effect of this dependence on the f_{a3} scans and modify Eq. 6.1.1 by introducing a form-factor dependence of the pseudo-scalar coupling parameter, a_3 ,

$$\frac{1}{(1 + \frac{q_1^2}{\Lambda^2})^2(1 + \frac{q_2^2}{\Lambda^2})^2} \quad (6.8.1)$$

where q_1 and q_2 are the four-momenta of the intermediate and the decay vector bosons, respectively, and Λ is the energy scale of new physics. Figure 6.8.9 shows f_{a3} scans after form factor re-weighting for a wide range of Λ values between 1 TeV and 10 TeV. Figure 6.8.9 shows the form factor scans where the signal strength is allowed to float

(CMS-style). The sensitivity to anomalous couplings in the VH analysis is reduced for a new physics scale Λ smaller than 10 TeV.

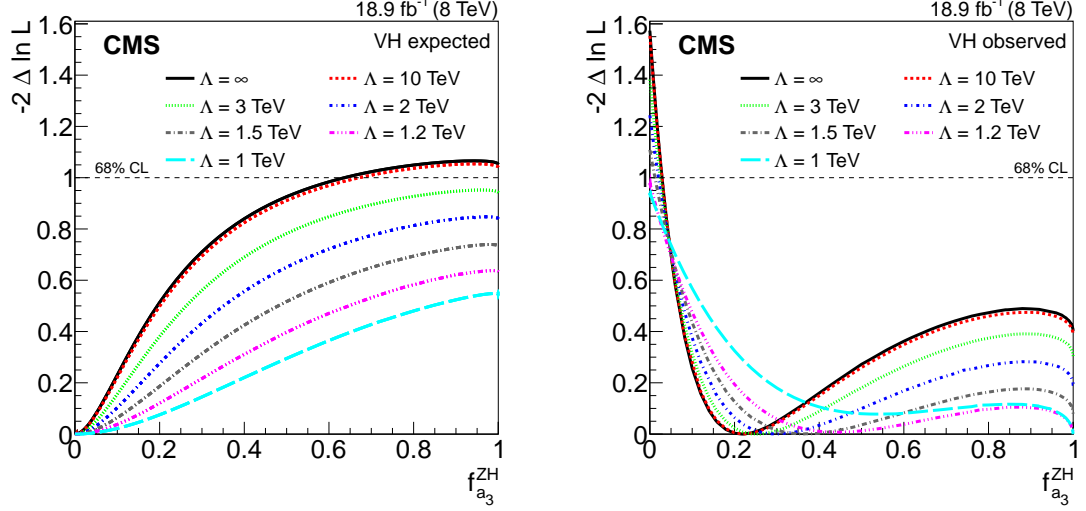


Figure 6.8.9: Results of CMS-style expected (left) and observed (right) f_{a3} scans based on a combination of the WH and ZH channels, shown for various new physics scales Λ .

6.9 Conclusion

In summary, a search has been performed for anomalous HVV interactions in 8 TeV pp data collected with the CMS detector. This is the first study at the LHC in associated Higgs production. Profile-likelihood scans are performed to evaluate the consistency of data with various effective pseudoscalar cross section fractions, f_{a3} . The observed results are consistent with the SM prediction of a scalar Higgs boson. Based on a combination of WH and ZH channels, a value of $f_{a3}^{ZZ} = 0.00106^{+0.99894}_{-0.00094}$ is observed. The sensitivity from the associated Higgs production channels alone is not sufficient to constrain the f_{a3} at 95% CL. However, in a combination with the $H \rightarrow VV$ channels, when assuming the absence of additional anomalous Higgs couplings, a value of $f_{a3}^{ZZ} = 0.00118^{+0.00092}_{-0.00072}$ is obtained, with $f_{a3}^{ZZ} > 0.0034$ excluded at a 95% CL.

Chapter 7

Search for Heavy Top Quark Partners with Charge $5/3$

7.1 Motivation

As discussed before, a long search for the Higgs boson predicted from the electroweak symmetry breaking mechanism has been completed with the discovery made by ATLAS and CMS experiments [20–22]. The studies so far have shown that the new boson is compatible with the SM expectations (as discussed in Chapter 6); however, its mass gets quadratically divergent contributions mainly from the top quark, the heaviest particle in the SM, when corrections applied for higher energies such as the Plank energy scale. This causes the so-called Hierarchy Problem, as the divergence of the Higgs mass-squared would cause its mass to be much bigger. There are several theories that attempt to address this problem, such as Little Higgs and Composite Higgs models in which the spontaneously broken symmetry is enhanced [88–90]. With the enhanced symmetry new states emerge known as heavy fermionic top-partners. We focus on pair production of such particles with electric charge $5e/3$ ($X_{5/3}$) as predicted in some of the composite Higgs models [90]. The first experimental exclusion limits on the production cross section for masses up to 800 GeV have been placed with 8 TeV data at CMS in same-sign dilepton channel [91, 92].

We analyze the events where the $X_{5/3}$ is pair produced with its antiparticle via

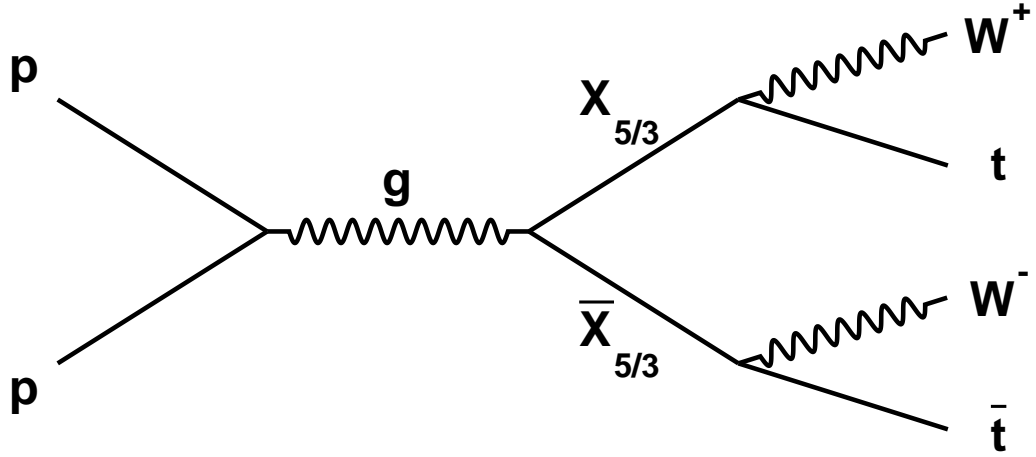


Figure 7.1.1: Pair production of $X_{5/3}$ and its decay into a top quark and a W boson.

the strong interaction. Each $X_{5/3}$ decays into a top quark and a W boson (tW). This is shown in Fig. 7.1.1. In the final state we are interested in, we require one of the W bosons to decay into a lepton (electron or muon) and a neutrino, while the other three W bosons decay hadronically. This particular final state has not been explored before at the LHC as it is a difficult channel to study with overwhelming hadronic activity in the final state. In this work, we show that this channel can make an important contribution to the $X_{5/3}$ search at the higher center-of-mass energy which LHC has been operating, by making use of the boosted topologies.

7.2 Data and Monte Carlo

7.2.1 Data Samples

The data sample used in this analysis corresponds to 2.2 fb^{-1} of integrated luminosity and was collected at a center-of-mass energy of 13 TeV with 25 ns bunch spacing. The standard CMS selection of good runs and luminosity sections was applied by using the officially recommended JSON files. The data samples used in this analysis are listed in Table 7.1 along with their corresponding integrated luminosities.

Table 7.1: Data sample definitions.

Primary Dataset	Reconstruction Group	Int. Lumi [pb^{-1}]
SingleMuon	Run2015C-05Oct2015-v1	17.23
SingleMuon	Run2015D-05Oct2015-v1	2197.96
SingleMuon	Run2015D-PromptReco-v4	
SingleElectron	Run2015C-05Oct2015-v1	17.23
SingleElectron	Run2015D-05Oct2015-v1	2197.96
SingleElectron	Run2015D-PromptReco-v4	

7.2.2 Background Samples

The background Monte Carlo (MC) samples used in this analysis are listed in Table 7.2. MC was generated with 25 ns bunch spacing corresponding to LHC 2015 p-p collisions. MC background processes were produced using MADGRAPH 5 [93], POWHEG v2 [73], and MG5_AMCNLO (v5_2.2.2) [94]. Pythia8 [95] was used to simulate parton showering, hadronization, and the underlying event. Next-to-next-to-leading order (NNLO) or NLO cross sections were used, where available. Detector simulation was performed with GEANT4 [78].

All samples generated with MG5_AMCNLO contain events with negative weights, introduced to cancel out double counting of next-to-leading-order correction factors during parton showering [96]. These weights are applied event-by-event in histograms and are also summed to find the effective number of events in each sample.

The $t\bar{t}$ MC samples consist of three mass bins: $M(t\bar{t}) > 350$ GeV, $700 \text{ GeV} < M(t\bar{t}) < 1000$ GeV, and $M(t\bar{t}) > 1000$ GeV. The sample with $M(t\bar{t}) > 350$ GeV is split based on the mass of the initially generated top-antitop pair, and events with mass from $700 - 1000$ GeV or greater than 1000 GeV are added to the respective binned samples. This procedure increases the number of events in the binned samples when calculating the normalization factor.

To simplify both limit setting and plot visualization, background samples are grouped into three categories: QCD, Top, and Electroweak. The QCD group contains all H_T binned QCD samples. The Top group is dominated by $t\bar{t}$ but also contains

Table 7.2: Background MC sample definitions.

Background	Generators	Cross Section [pb]
DYJetsToLL_M-50	amcatnloFXFX-pythia8	6025^{+228}_{-226} [97]
WJetsToLNu_HT-100to200	madgraphMLM-pythia8	1627.5 ± 1.5 [97]
WJetsToLNu_HT-200to400	madgraphMLM-pythia8	435.24 ± 0.24 [97]
WJetsToLNu_HT-400to600	madgraphMLM-pythia8	59.18 ± 0.09 [97]
WJetsToLNu_HT-600to800	madgraphMLM-pythia8	14.58 ± 0.01 [97]
WJetsToLNu_HT-800to1200	madgraphMLM-pythia8	6.66 ± 0.02 [97]
WJetsToLNu_HT-1200to2500	madgraphMLM-pythia8	1.61 ± 0.004 [97]
WJetsToLNu_HT-2500toInf	madgraphMLM-pythia8	0.0390 ± 0.0001 [97]
WW	pythia8	$118.7^{+3.0}_{-2.6}$ [98]
WZ	pythia8	66.1 ± 2.7 [98]
ZZ	pythia8	31.8 ± 1.6 [98]
TT	powheg-pythia8	832^{+40}_{-46} [97]
TT_Mtt-700to1000	powheg-pythia8	$76.5^{+3.7}_{-4.2}$ [97]
TT_Mtt-1000toInf	powheg-pythia8	$20.8^{+1.0}_{-1.1}$ [97]
ST_t-channel_4f_leptonDecays	amcatnlo-pythia8	$70.7^{+2.9}_{-2.5}$ [97]
ST_s-channel_4f_leptonDecays	amcatnlo-pythia8	$11.36^{+0.44}_{-0.48}$ [99]
ST_tW_top_5f_inclusiveDecays	powheg-pythia8	35.6 ± 1.9 [99]
ST_tW_antitop_5f_inclusiveDecays	powheg-pythia8	35.6 ± 1.9 [99]
TTWJetsToLNu	amcatnloFXFX-madspin-pythia8	0.204 ± 0.002 [97]
TTWJetsToQQ	amcatnloFXFX-madspin-pythia8	0.406 ± 0.002 [97]
TTZToQQ	amcatnlo-pythia8	0.5307 ± 0.001 [97]
TTZToLLNuNu_M-10	amcatnlo-pythia8	0.253 ± 0.001 [97]
QCD_HT-100to200	madgraphMLM-pythia8	27850000 [97]
QCD_HT-200to300	madgraphMLM-pythia8	1717000 [97]
QCD_HT-300to500	madgraphMLM-pythia8	351300 [97]
QCD_HT-500to700	madgraphMLM-pythia8	31630 [97]
QCD_HT-700to1000	madgraphMLM-pythia8	6802 [97]
QCD_HT-1000to1500	madgraphMLM-pythia8	1206 [97]
QCD_HT-1500to2000	madgraphMLM-pythia8	120.4 [97]
QCD_HT-2000toInf	madgraphMLM-pythia8	25.24 [97]

single top backgrounds and the rare SM processes $t\bar{t}W$ and $t\bar{t}Z$. The Electroweak group, labeled “EWK”, is dominated by $W + \text{jets}$ but also contains the Drell Yan and diboson samples.

7.2.3 Signal Samples

The $X_{5/3}$ signal samples are produced with Madgraph 5, MadSpin [100], and Pythia 8 for both left-handed (LH) and right-handed (RH) coupling scenarios. Madgraph 5 was used for the production of $X_{5/3}$ and its immediate decay into a top quark and a W boson. For the decays of the top quark and W boson, MadSpin was used [101].

The full list of signal samples used in this analysis is given in Table 7.3 along with their cross sections [102].

Table 7.3: $X_{5/3}$ signal MC samples for both LH and RH chiralities at various mass points. These samples were generated with inclusive decays of the $X_{5/3}$.

Signal	Generators	Cross Section [pb]
X53X53_M-700_LH	madgraph-pythia8	0.442
X53X53_M-700_RH	madgraph-pythia8	0.442
X53X53_M-800_LH	madgraph-pythia8	0.190
X53X53_M-800_RH	madgraph-pythia8	0.190
X53X53_M-900_LH	madgraph-pythia8	0.0877
X53X53_M-000_RH	madgraph-pythia8	0.0877
X53X53_M-1000_LH	madgraph-pythia8	0.0427
X53X53_M-1000_RH	madgraph-pythia8	0.0427
X53X53_M-1100_LH	madgraph-pythia8	0.0217
X53X53_M-1100_RH	madgraph-pythia8	0.0217
X53X53_M-1200_LH	madgraph-pythia8	0.0114
X53X53_M-1200_RH	madgraph-pythia8	0.0114
X53X53_M-1300_LH	madgraph-pythia8	0.00618
X53X53_M-1300_RH	madgraph-pythia8	0.00618
X53X53_M-1400_LH	madgraph-pythia8	0.00342
X53X53_M-1400_RH	madgraph-pythia8	0.00342
X53X53_M-1500_LH	madgraph-pythia8	0.00193
X53X53_M-1500_RH	madgraph-pythia8	0.00193
X53X53_M-1600_LH	madgraph-pythia8	0.00111
X53X53_M-1600_RH	madgraph-pythia8	0.00111

7.3 Event Selection

Event selection is performed by reading events from the miniAOD [103] file format with the LJMet software framework [104]. Data events are considered for selection if they were recorded during runs included in the certified data set defined by the following JSON file:

Cert_246908-260627_13TeV_PromptReco_Collisions15_25ns_JSON.txt.

Electron events are triggered in data using the HLT_Ele27_eta2p1_WPLoose_Gsf path, while the corresponding MC trigger path is HLT_Ele27_eta2p1_WP75_Gsf.

Muon events on the other hand are triggered in data and MC using the HLT_IsoMu27 path. Both the electron and muon triggers were unprescaled during 2015 data taking. To correct for differences in trigger efficiency we apply MC scale factors calculated in Ref. [105] using the tag and probe method.

The single lepton final state includes events with one charged lepton, usually from the decay of a W boson. Events are selected that contain exactly one tight electron or muon with $p_T > 40$ GeV, and no loose electrons or muons with $p_T > 10$ GeV.

Fig. 7.3.1 shows distributions of electron and muon p_T and pseudorapidity.

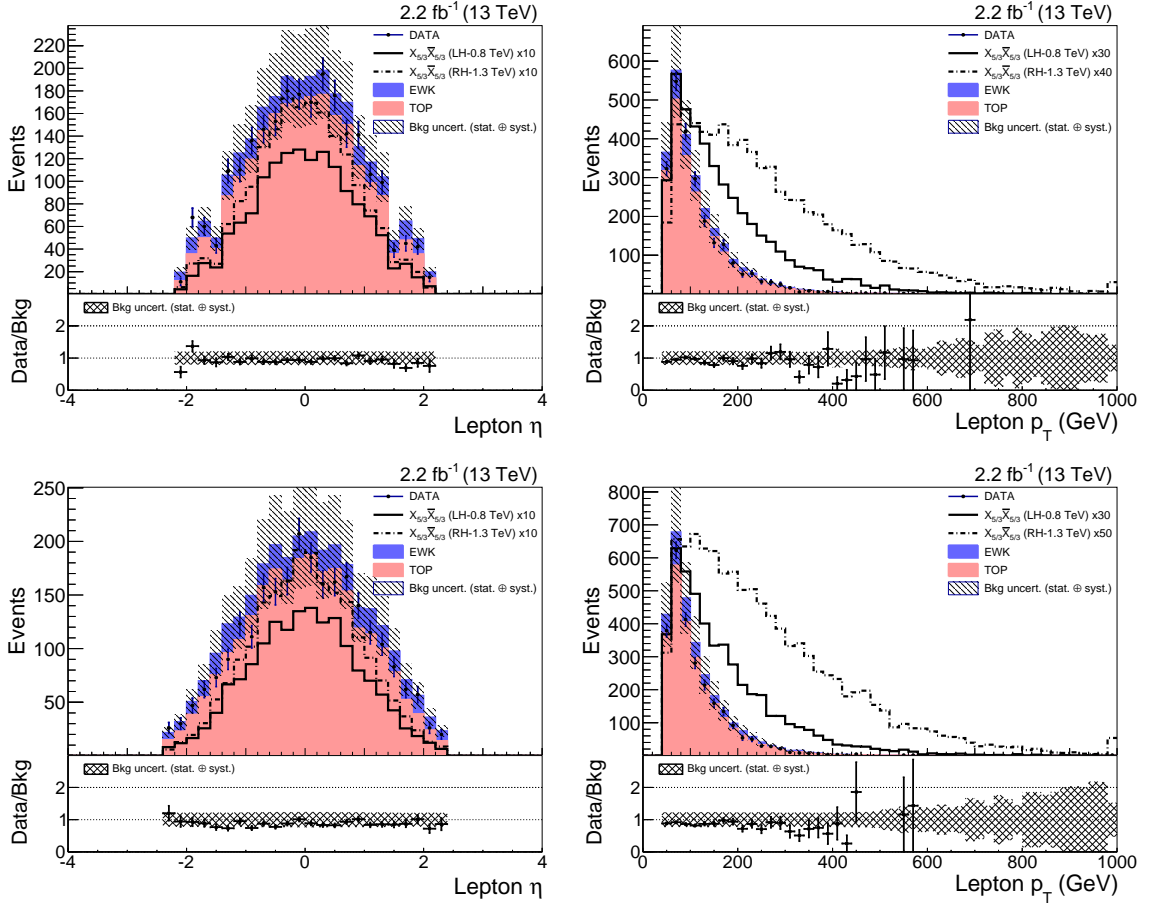


Figure 7.3.1: Distributions of (top) electron and (bottom) muon, showing (left) $|\eta|$ and (right) p_T in data and MC after the initial selection. Uncertainties include all statistical and systematic uncertainties described in Section 7.7.

We select events with at least 3 jets, where the highest corrected jet p_T is greater

than 200 GeV, and the second highest jet p_T is greater than 90 GeV. Distributions of jet p_T and $|\eta|$ are shown in Fig. 7.3.2. The jet p_T distribution is split into the contributions from each of the four highest p_T jets in Fig. 7.3.3. At least one of the jets is required to be b tagged. Figure 7.3.4 shows the number of AK4 jets and b tagged jets.

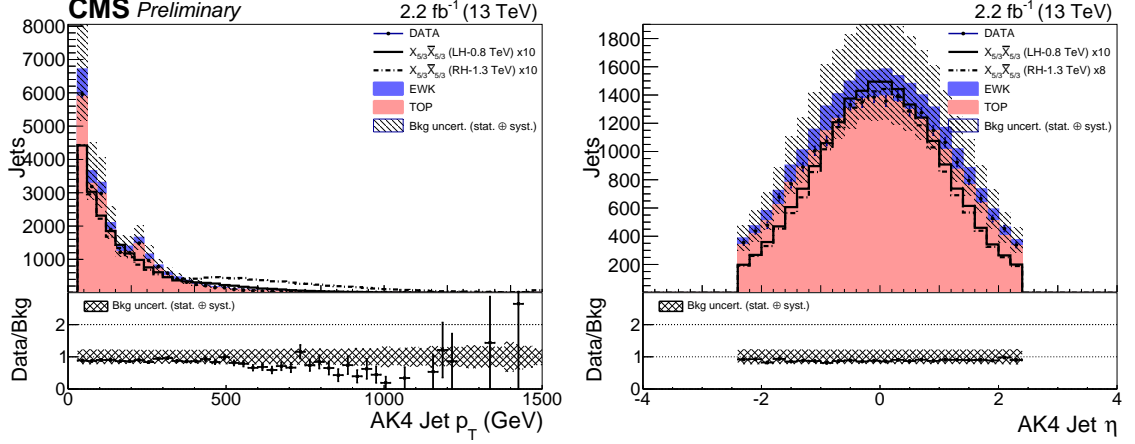


Figure 7.3.2: Distributions of (left) p_T and (right) $|\eta|$ of all AK4 jets with $p_T > 30$ GeV in data and MC after the initial selection. Uncertainties include all statistical and systematic uncertainties described in Section 7.7.

E_T^{miss} must be greater than 60 GeV in selected events, to reduce the number of multijet background events. Figure 7.3.5 shows the E_T^{miss} , H_T (the scalar sum of AK4 jet p_T), and S_T (the scalar sum of the H_T , E_T^{miss} , and lepton p_T) distributions.

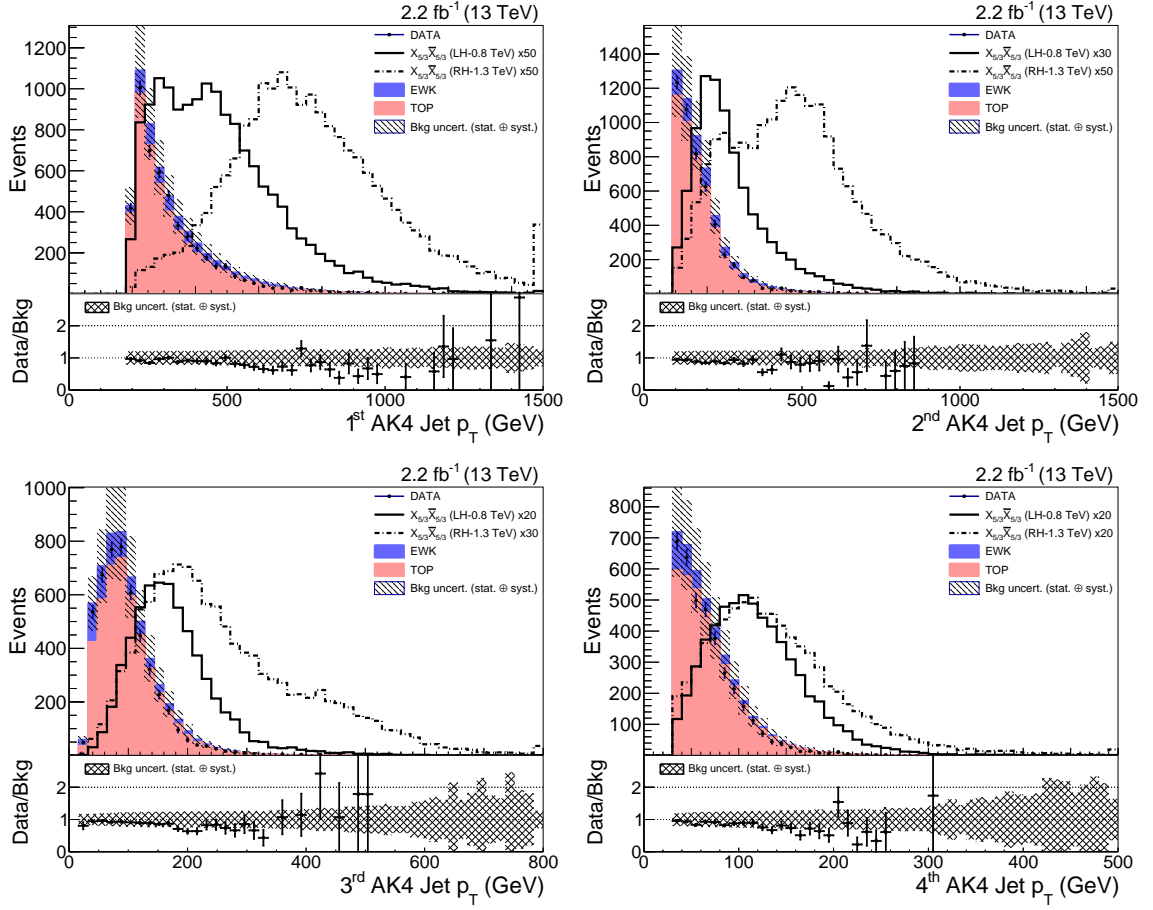


Figure 7.3.3: Distributions of p_T for the four highest p_T jets in data and MC after the initial selection. Uncertainties include all statistical and systematic uncertainties described in Section 7.7.

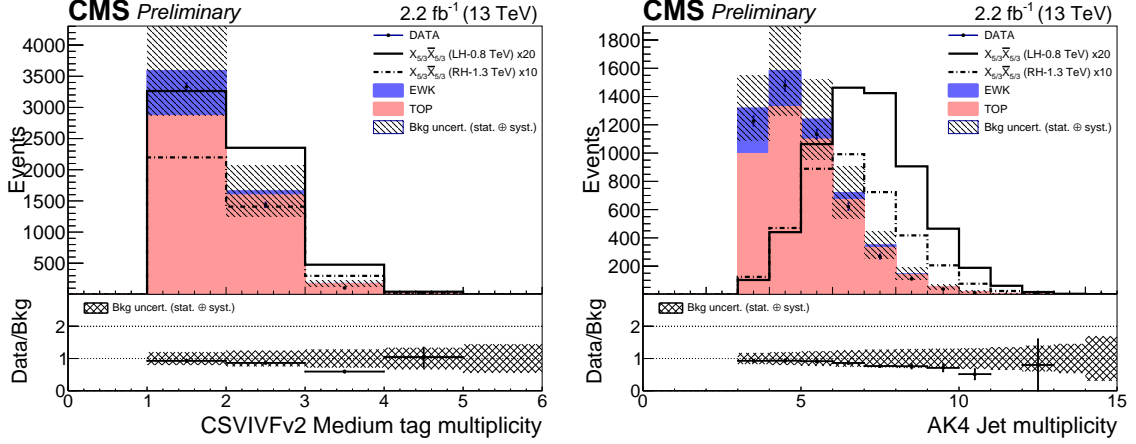


Figure 7.3.4: Distributions of (left) the number of AK4 jets and (right) the number passing the medium b tag working point in data and MC after the initial selection. Uncertainties include all statistical and systematic uncertainties described in Section 7.7.

Table 7.4 lists the yields of data and MC with the initial selection cuts, which are summarized below:

- 1 tight, isolated electron or muon with $p_T > 50\text{GeV}$
- 0 loose leptons with $p_T > 10\text{GeV}$
- 3 or more AK4 jets with $|\eta| < 2.4$ and $p_T > 200, 90, \text{ and } 30\text{GeV}$
- 1 or more b tagged jet with $|\eta| < 2.4$
- $E_T^{miss} > 100\text{GeV}$

7.4 Categorization and Discriminants

7.4.1 Event Categories

To maximize the sensitivity to the presence of $X_{5/3}$, events are divided into 8 categories based on lepton flavor (e, μ), the number of b tagged AK4 jets (1, 2+), and the number of boosted W tagged jets (0, 1+). Distributions of AK8 jet p_T and $|\eta|$

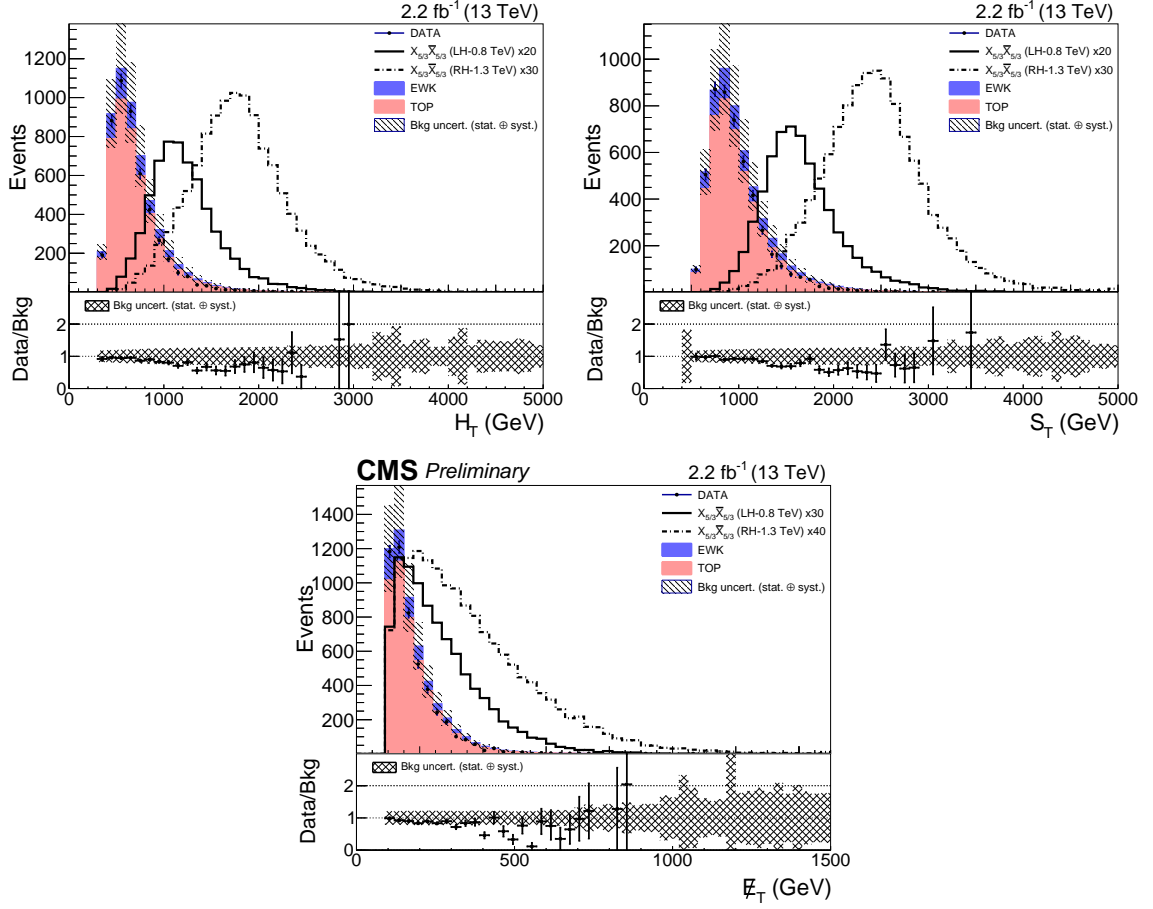


Figure 7.3.5: Distributions of (top left) H_T , (top right) S_T , and (bottom) E_T^{miss} in data and MC after the initial selection. Uncertainties include all statistical and systematic uncertainties described in Section 7.7.

Table 7.4: Observed (expected) number of data (background) events in electron and muon channels after the initial selection cuts, with an integrated luminosity of 2.2 fb^{-1} . Uncertainties include all statistical and normalization uncertainties described in Table 7.8.

Sample	Electron channel	Muon channel	Combined
LH $X_{5/3}$ (0.8 TeV)	27.6 ± 1.6	30.6 ± 1.8	58.2 ± 3.3
RH $X_{5/3}$ (1.3 TeV)	1.13 ± 0.07	1.27 ± 0.07	2.40 ± 0.14
EWK	360 ± 80	450 ± 120	810 ± 200
Top	2180 ± 330	2450 ± 440	4630 ± 740
QCD	13.0 ± 8.2	0.3 ± 0.3	13.3 ± 8.3
Total Bkg	2550 ± 350	2890 ± 470	5450 ± 790
Data	2362	2523	4885
Data/Bkg	0.92 ± 0.13	0.87 ± 0.14	0.9 ± 0.13

as well as the number of AK8 jets are shown in Fig. 7.4.1. Distributions of the W tagging variables and number of tagged jets are shown in Fig. 7.4.2.

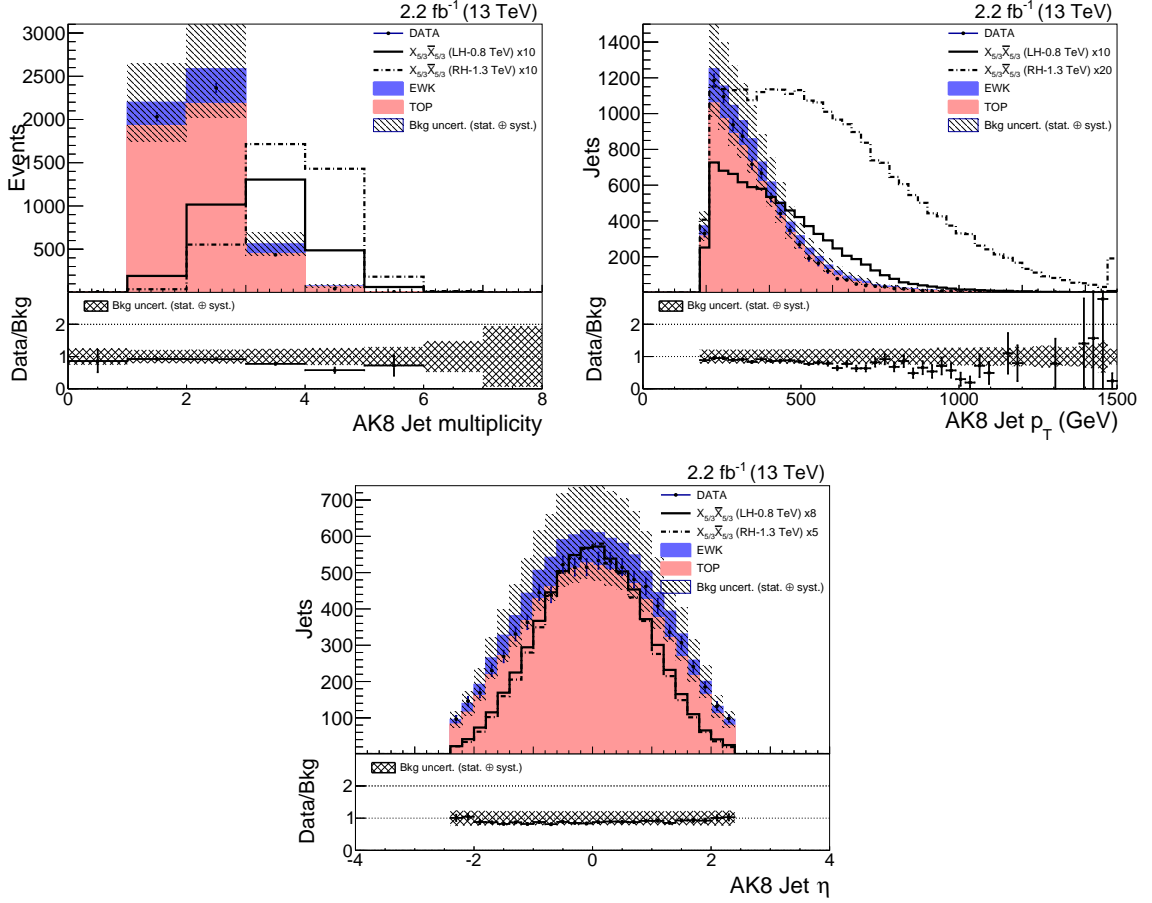


Figure 7.4.1: Distributions of (left) the number of AK8 jets, (right) AK8 jet p_T , and (bottom) AK8 jet $|\eta|$ in data and MC after the initial selection. Uncertainties include all statistical and systematic uncertainties described in Section 7.7.

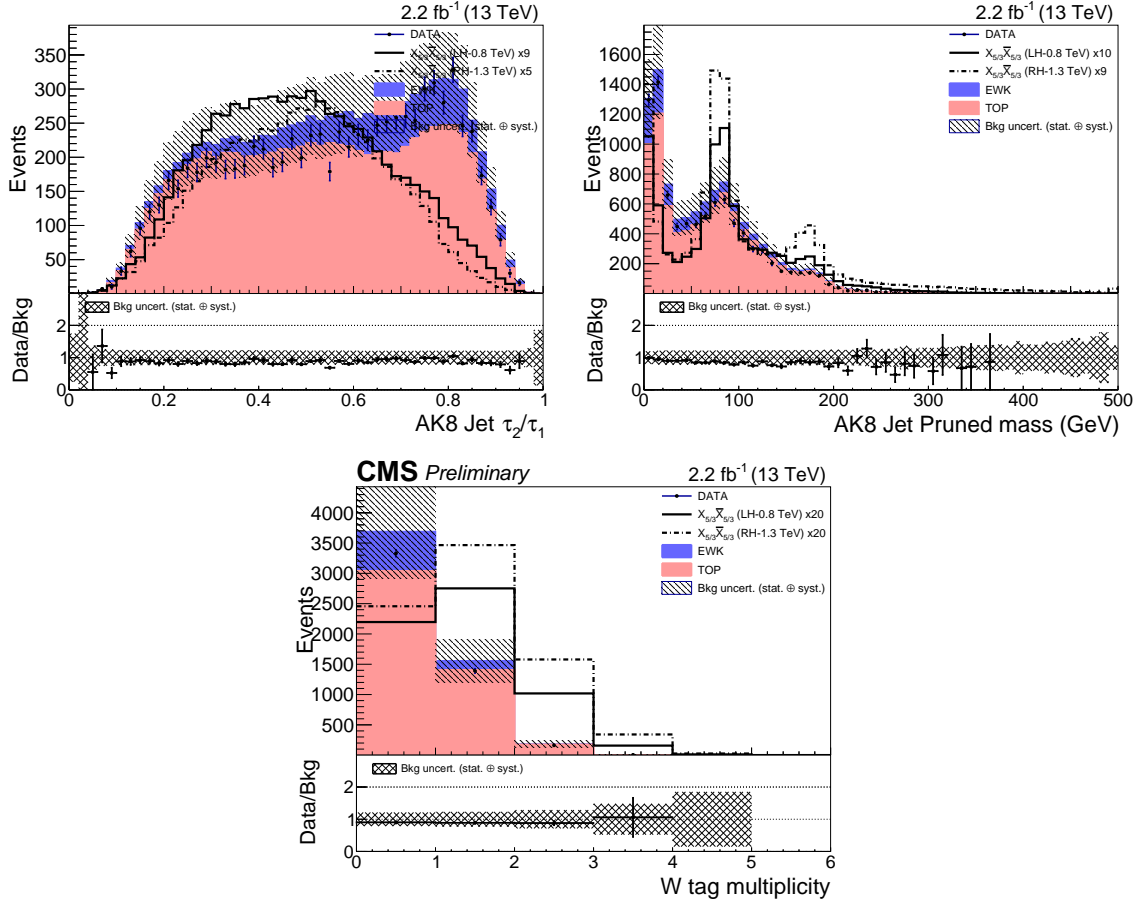


Figure 7.4.2: Distributions of (left) the n-subjettiness τ_2/τ_1 ratio, (right) AK8 jet pruned mass, and (bottom) the number of W tagged jets in data and MC after the initial selection. Uncertainties include all statistical and systematic uncertainties described in Section 7.7.

7.4.2 Discriminating Variables

Event selection is optimized using S_T as the discriminating variable in a procedure described in Section 7.5. The optimized event selection changes the following requirements compared to preselection:

- p_T (lepton) > 80 GeV
- number of AK4 jets ≥ 4

Because of discrepancies between data and MC that were later seen by another analysis [106] as well, we explored alternative variables to the S_T discriminant that are less sensitive to discrepancy sources. The first of two alternate discriminating variables is the mass constructed from the lepton (ℓ) and b-tagged jet, labeled $M(\ell, b)$. In the case of more than one b-tagged jet, the minimum mass from the possible pairs of lepton and b-tagged jet is used, labeled $\min[M(\ell, b)]$.

Another discriminating variable is the mass of the $X_{5/3}$ pair obtained by combining the four vectors of the leptonic W boson and all AK4 jets in the event with $p_T > 30$ GeV: $M[W(\ell, \nu) + \text{all AK4 jets}]$. The reconstruction of the neutrino 4-momentum vector follows the prescription described in Ref. [107]. Following this technique, the missing transverse energy is used to obtain the xy -components of the neutrino momentum, and the z -component is calculated using a W boson mass constraint (80.4 GeV). This constraint leads to a quadratic equation in $|p_z^\nu|$. In the case of two real solutions, for W reconstruction, the solution with the minimum $|p_z^\nu|$ is chosen. In case of a complex solution, the real part is assigned to $|p_z^\nu|$, and the p_T of the neutrino is computed, taking the solution which gives the mass of the W boson closest to 80.4 GeV.

The final results are computed using the $\min[M(\ell, b)]$ discriminant, as the $X_{5/3}$ pair mass variable was also found to be sensitive to data/MC discrepancies, after a simple optimization on the value of $\Delta R(\ell, \text{sub-leading jet})$. The additional cut is:

$\Delta R(\ell, \text{sub-leading jet}) > 1$. Figure 7.4.3 shows the distributions of $\min[M(\ell, b)]$, $M[W(\ell, \nu) + \text{all AK4 jets}]$, and $\Delta R(\ell, \text{sub-leading jet})$ after the initial analysis selection.

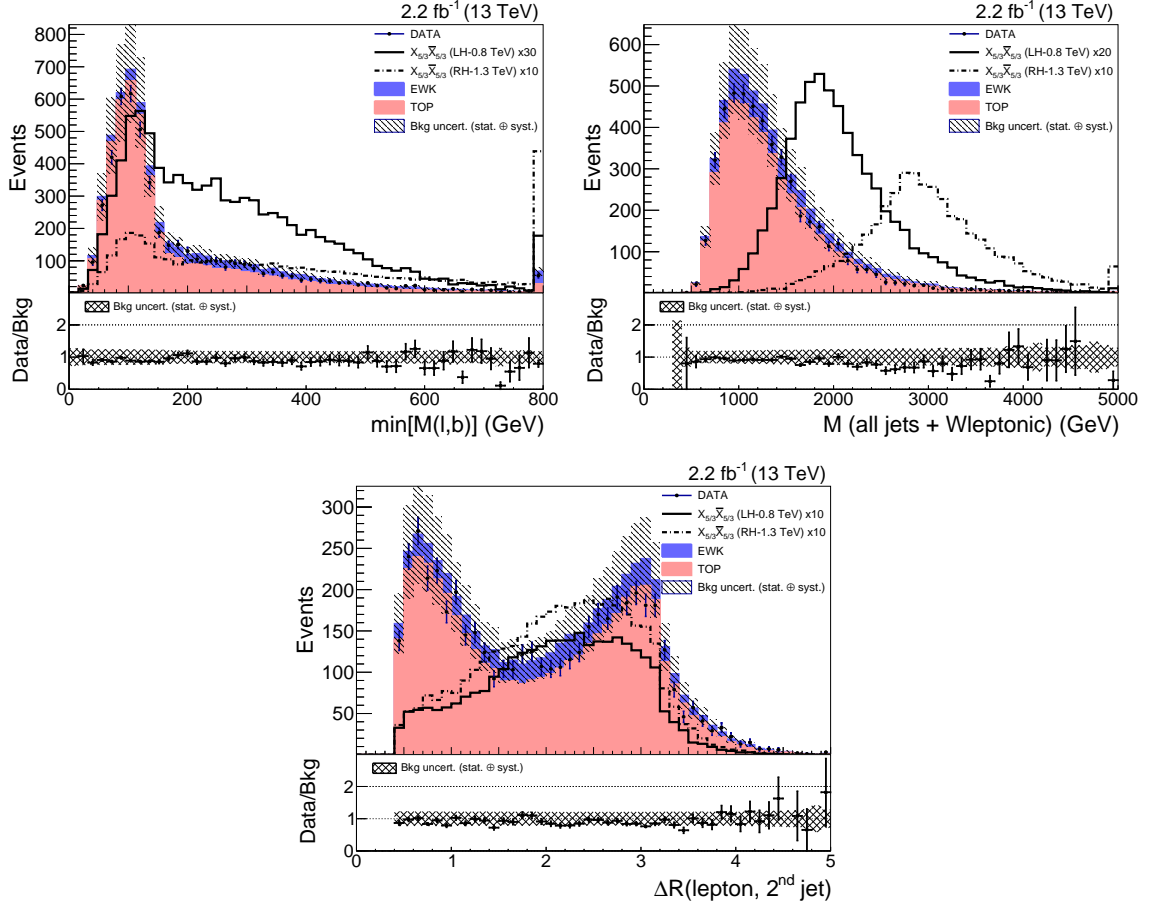


Figure 7.4.3: Distributions of (left) $\min[M(\ell, b)]$, (right) $M[W(\ell, \nu) + \text{all AK4 jets}]$, and (bottom) $\Delta R(\ell, \text{sub-leading jet})$ in data and MC after the initial selection. Uncertainties include all statistical and systematic uncertainties described in Section 7.7.

7.5 Selection Optimization

The Theta program [108] uses Bayesian statistics to calculate the 95% CL upper limit on the cross section of the left-handed $X_{5/3}$ particle at each simulated mass point (700 – 1600 GeV). Analysis cuts are optimized by maximizing the intersection of the limit curve with a curve defined by the theoretical predictions for the cross sections. Because kinematic cuts are often correlated, all permutations of the following cuts are considered:

- p_T (lepton) > [50, 60, 80, 100] GeV
- p_T (leading jet) > [200, 250, 300, 450] GeV
- p_T (sub-leading jet) > [90, 150, 300] GeV
- E_T^{miss} > [100, 150, 200, 250] GeV
- Number of jets > [4, 5, 6]

The optimization procedure creates distributions of S_T for each signal and background MC sample in each category, normalizing the background samples based on their cross section, number of events, and an integrated luminosity of 1.28 fb^{-1} . Owing to computational limitations, during the optimization study an inflated normalization uncertainty of 20% is used for each of the background processes instead of the systematic uncertainties affecting the shape and/or normalization of the distribution listed in Table 7.8.

The results of a preliminary optimization are shown in Fig. 7.5.1, comparing 95% CL expected limits with the theoretical prediction curve. In Fig. 7.5.2, certain kinematic variables are varied while the others are held fixed. After optimization with the categories described above, the best set of kinematic cuts are found to be:

- p_T (lepton) > 80 GeV
- p_T (leading jet) > 200 GeV
- p_T (sub-leading jet) > 90 GeV
- $E_T^{miss} > 100$ GeV
- Number of AK4 jets ≥ 4

While the optimization results prefer high jet multiplicities (see upper-right plot in Fig. 7.5.2), we do not require high jet multiplicities because of Data-MC discrepancies.

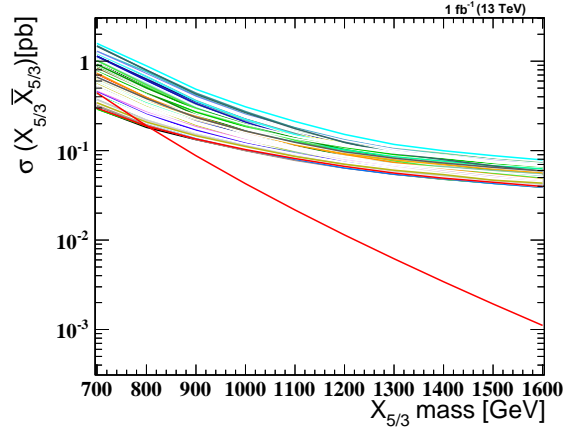


Figure 7.5.1: Optimization results, from varying all combinations of selection cuts.

7.6 Background Modeling

In order to cross check the background modeling, we consider two control regions (CR); "W+jets" and " $t\bar{t}$ " CRs, which are the two dominant background processes in

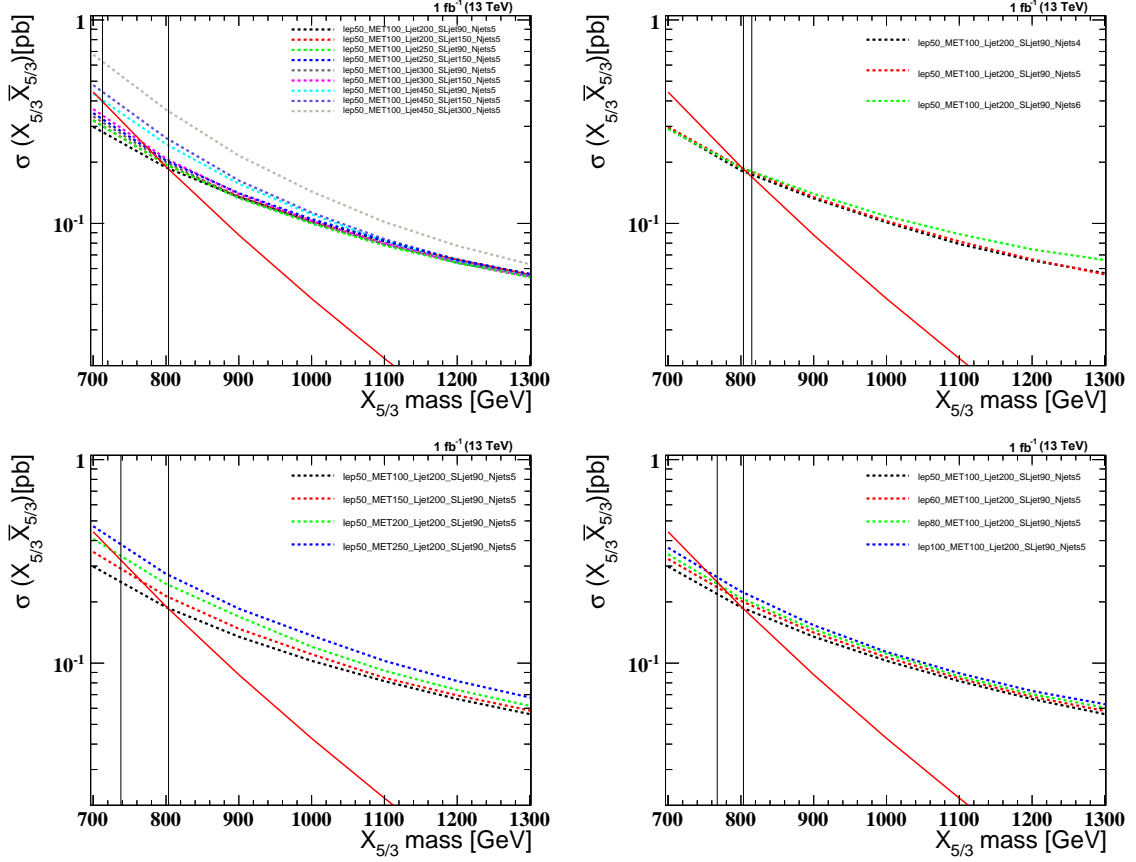


Figure 7.5.2: Optimization results from varying (top left) jet p_T , (top right) number of jets, (bottom left) E_T^{miss} , and (bottom right) lepton p_T . In each plot the other cuts are held constant at the optimal cut points returned by the algorithm.

Table 7.5: Definitions of W+jets and $t\bar{t}$ control regions.

Selection	$t\bar{t}$	W + jets
$p_T(\text{lepton})$	$> 80 \text{ GeV}$	$> 80 \text{ GeV}$
$p_T(\text{leading jet})$	$> 200 \text{ GeV}$	$> 200 \text{ GeV}$
$p_T(\text{sub-leading jet})$	$> 90 \text{ GeV}$	$> 90 \text{ GeV}$
$/E_T$	$> 100 \text{ GeV}$	$> 100 \text{ GeV}$
Number of AK4 jets	≥ 4	≥ 4
Number of b tagged jets	≥ 1	$= 0$
$\Delta R(\ell, \text{sub-leading jet})$	< 1	< 1

this analysis. In order to define these CRs, we invert the signal region requirement of $\Delta R(\ell, \text{sub-leading jet}) > 1$ and modify the number of b-tagged jets to maximize W+jets or $t\bar{t}$ background processes. The CR selections are listed in Table 7.5.

In both control regions we categorize the events depending on the lepton flavour and the number of W-tagged jets or b-tagged jets. In the $t\bar{t}$ CR, each lepton flavour is split into categories with exactly 1 b-tagged jet, or 2 or more b-tagged jets, while in the W+jets CR, we require 0 b-tagged jets and categorize electron and muon channels into 0 W-tagged jets or 1 or more W-tagged jets.

The $\min[M(\ell, b)]$ distributions from each category are shown in Fig. 7.6.1 (Fig. 7.6.2) for the $t\bar{t}$ (W+jets) control region, and the corresponding yields for data and background samples are listed in Tables 7.6 and 7.7. In all plots and tables, uncertainty bands include statistical uncertainty and all systematic uncertainties described in Section 7.7 except for those estimated from any data to MC disagreement in these CRs. The corresponding $\min[M(\ell, b)]$ distributions in each CR after combining electron and muon channels are shown in Fig. 7.6.3.

7.7 Systematic Uncertainties

Systematic uncertainties were evaluated in two ways:

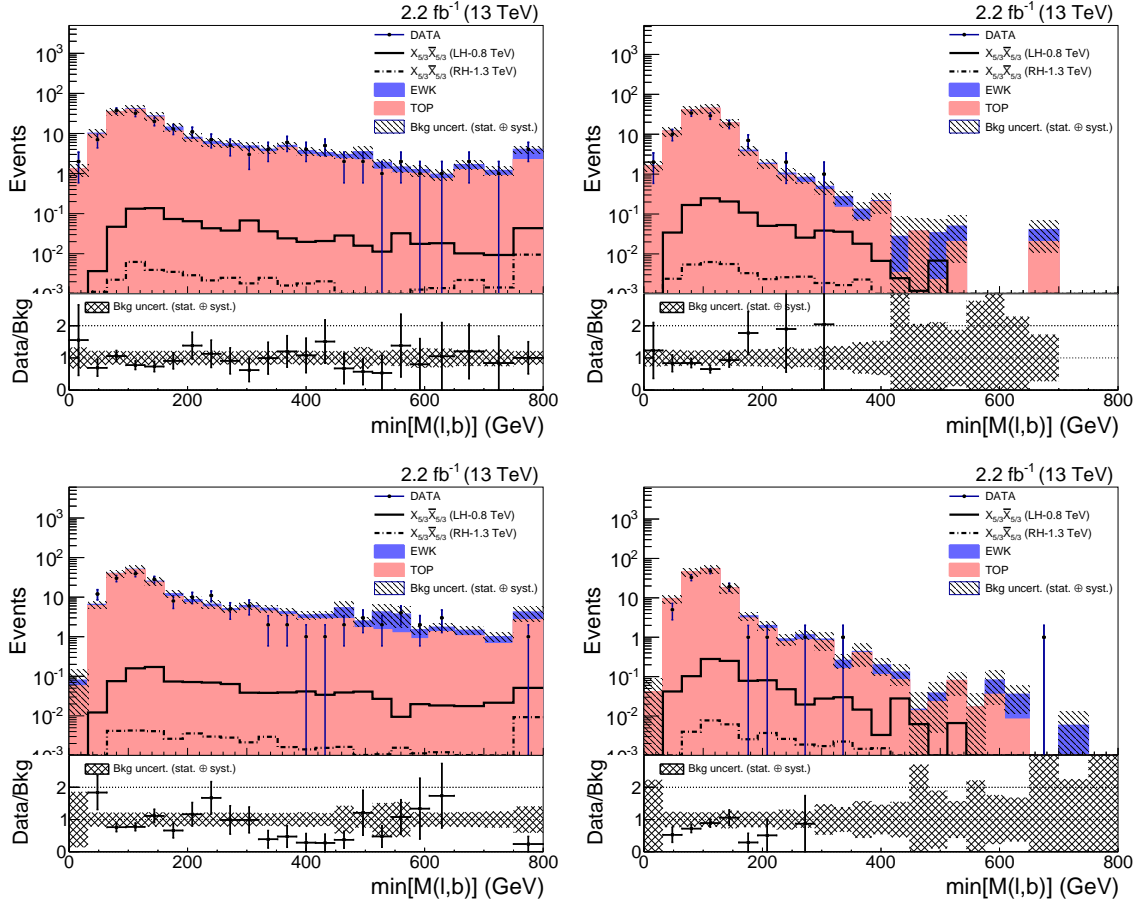


Figure 7.6.1: Distributions of $\min[M(\ell, b)]$ in the $t\bar{t} + \text{jets}$ control region, for (top/bottom) electron/muon plus (left/right) 1/2+ b tag categories. Uncertainties include all uncertainties except those derived from data/MC agreement in the CR.

Table 7.6: Observed (expected) number of data (background) events in the $t\bar{t}$ + jets control region, with an integrated luminosity of 2.2 fb^{-1} . Uncertainties include statistical and all normalization uncertainties except those derived from data/MC agreement in the CR.

Sample	$e + \text{jets, 1 b tag}$	$e + \text{jets, 2+ b tags}$
LH $X_{5/3}$ (0.8 TeV)	0.860 ± 0.072	1.004 ± 0.081
RH $X_{5/3}$ (1.2 TeV)	0.065 ± 0.005	0.074 ± 0.006
EWK	20.2 ± 2.8	2.63 ± 0.39
Top	165 ± 13	124 ± 10
QCD	0.23 ± 0.22	< 0.2
Total Bkg	186 ± 14	127 ± 10
Data	169	103
Data/Bkg	0.91 ± 0.10	0.81 ± 0.10
Sample	$\mu + \text{jets, 1 b tag}$	$\mu + \text{jets, 2+ b tags}$
LH $X_{5/3}$ (0.8 TeV)	1.097 ± 0.087	1.019 ± 0.082
RH $X_{5/3}$ (1.2 TeV)	0.083 ± 0.006	0.076 ± 0.006
EWK	25.0 ± 4.1	3.0 ± 1.7
Top	174 ± 14	134 ± 11
QCD	< 0.2	< 0.2
Total Bkg	199 ± 16	137 ± 11
Data	171	110
Data/Bkg	0.86 ± 0.09	0.80 ± 0.10

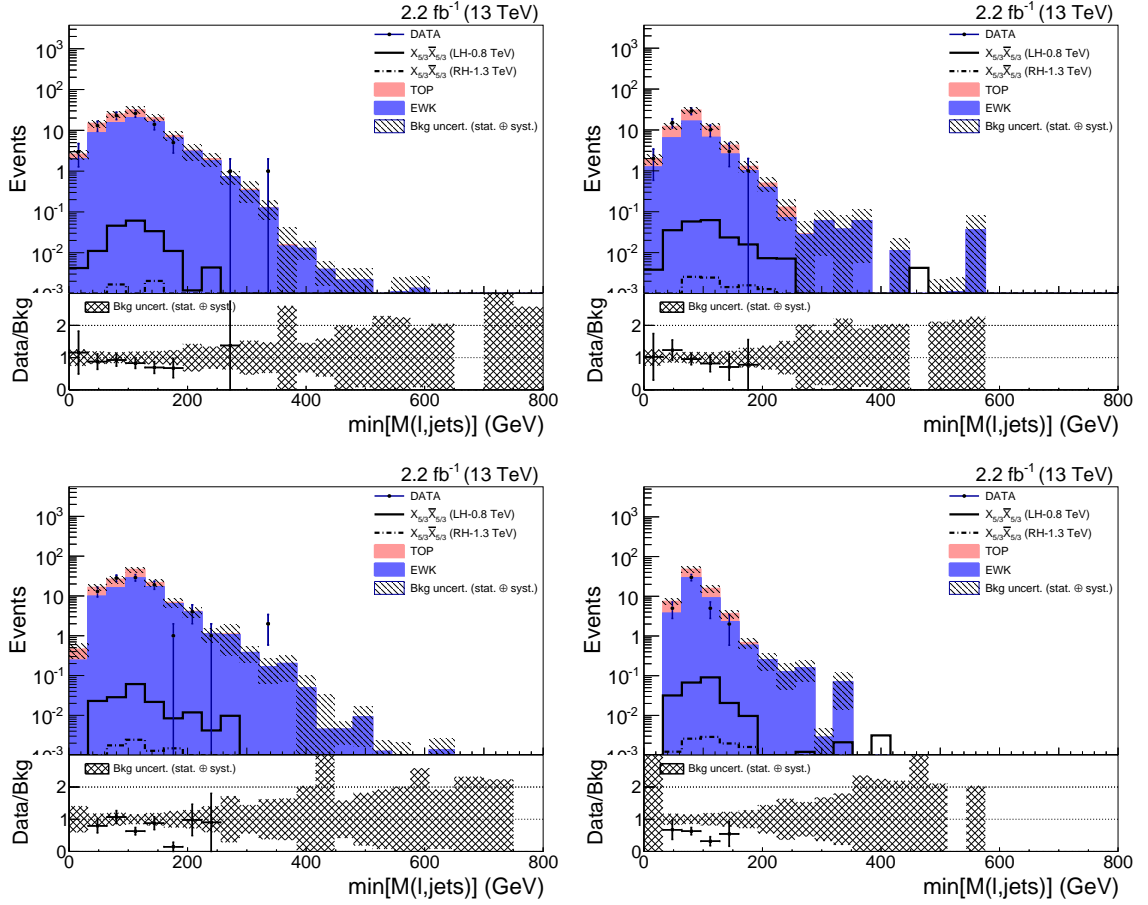


Figure 7.6.2: Distributions of $\min[M(\ell, b)]$ in the W + jets control region, for (top/bottom) electron/muon plus (left/right) 0/1+ W tag categories. Uncertainties include all uncertainties except those derived from data/MC agreement in the CR.

Table 7.7: Observed (expected) number of data (background) events in the W+jets control region, with an integrated luminosity of 2.2 fb^{-1} . Uncertainties include statistical and all normalization uncertainties except those derived from data/MC agreement in the CR.

Sample	$e + \text{jets, 0 W tags}$	$e + \text{jets, 1+ W tags}$
LH $X_{5/3}$ (0.8 TeV)	0.177 ± 0.026	0.214 ± 0.029
RH $X_{5/3}$ (1.2 TeV)	0.014 ± 0.002	0.022 ± 0.002
EWK	75.9 ± 6.8	32.4 ± 3.5
Top	34.0 ± 2.9	28.6 ± 2.6
QCD	6.7 ± 5.5	0.111 ± 0.091
Total Bkg	117 ± 10	61.1 ± 5.0
Data	86	60
Data/Bkg	0.74 ± 0.10	0.98 ± 0.15
Sample	$\mu + \text{jets, 0 W tags}$	$\mu + \text{jets, 1+ W tags}$
LH $X_{5/3}$ (0.8 TeV)	0.169 ± 0.025	0.226 ± 0.030
RH $X_{5/3}$ (1.2 TeV)	0.015 ± 0.002	0.026 ± 0.003
EWK	83.4 ± 6.9	45.1 ± 5.1
Top	40.1 ± 3.5	31.3 ± 2.8
QCD	0.011 ± 0.013	< 0.01
Total Bkg	123.4 ± 9.0	76.3 ± 6.6
Data	97	42
Data/Bkg	0.79 ± 0.10	0.55 ± 0.10

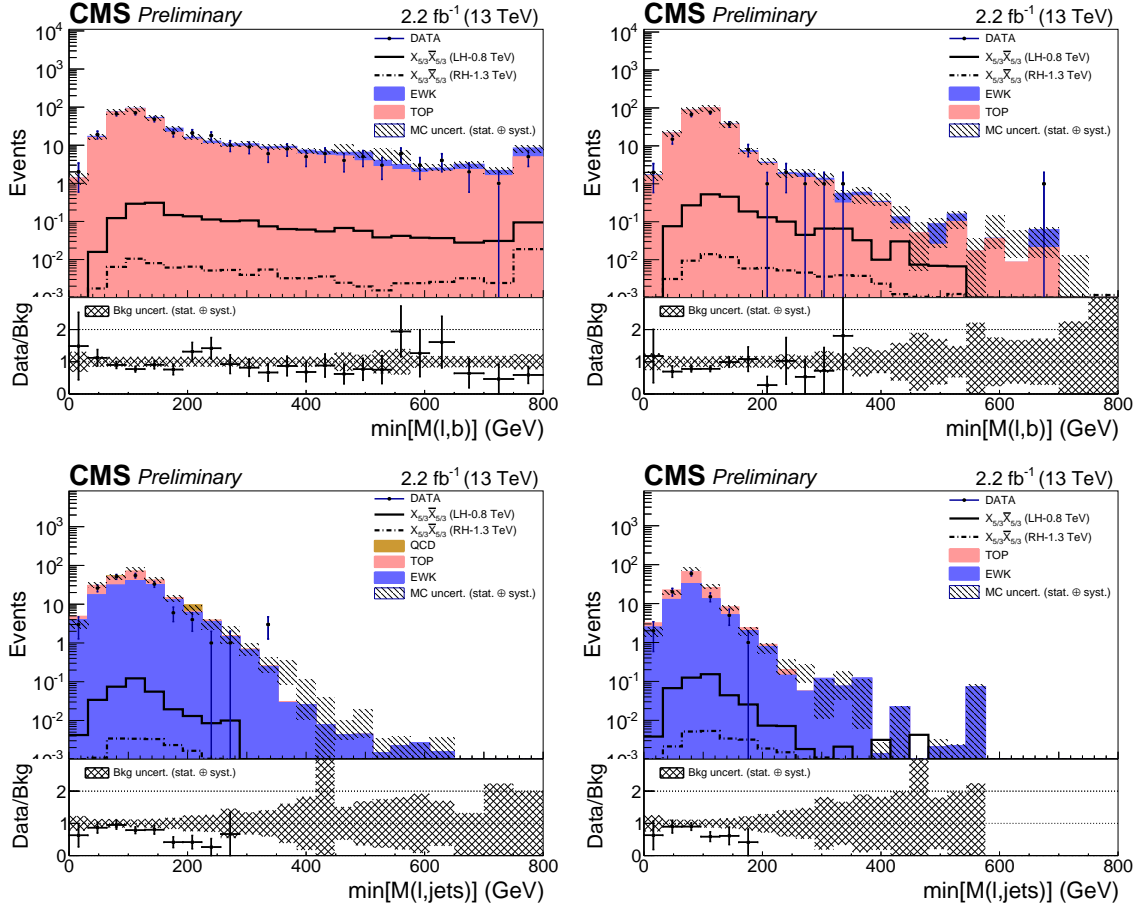


Figure 7.6.3: Distributions of $\min[M(\ell, b)]$ in the (top) $t\bar{t} + \text{jets}$ control region, for one b tagged jet (top left) and 2+ b tagged jets (top right) categories, and of $\min[M(\ell, b)]$ in the V + jets control region, for zero W tagged (bottom left) and 1+ W tagged jet (bottom right) categories for combined electron and muon event samples. Uncertainties include statistical and all systematic uncertainties except those which are derived from the control regions. For each category, the QCD contribution is not displayed if it is less than 0.5% of the total background.

7.7.1 Uncertainty in the normalization

This category includes uncertainties in the integrated luminosity, theoretical cross-sections and branching fractions, object identification efficiencies, and trigger efficiencies. Normalization uncertainties for luminosity (4.6% as recommended by the Lumi POG) and background sample cross section uncertainties (Table 7.2) are applied directly to the discriminating distributions. We assume an uncertainty of 50% in the cross sections of leading-order QCD samples. We also apply 1% uncertainties for lepton ID and isolation scale factors, and a 3% uncertainty for trigger efficiency scale factors. Because of data/MC discrepancies in the control regions discussed in Section 7.6, extra normalization uncertainties are added based on the tagging category, and averaged over the lepton flavour: 11-19% for the Top background group, and 24% for the EWK group. These uncertainties are applied independently to the tagging categories during limit calculation, but for figures and tables they are averaged across the categories to 14% (24%) uncertainties in the TOP (EWK) group. All uncertainties of this type have the same value regardless of event selection, either by definition, or by observation in the case of the modeling uncertainties.

7.7.2 Uncertainties in the shape of the distributions

This category includes the uncertainties from the jet energy scale (JEC), jet energy resolution (JER), b tagging and light quark mistagging efficiencies [60], W tagging uncertainties, event pileup conditions, parton distribution functions, parton shower energy scale, renormalization energy scale, and factorization energy scale. These were evaluated by raising and lowering the respective uncertainty by one standard deviation and creating the corresponding new discriminant shapes by repeating the whole analysis. Top quark p_T reweighting was evaluated according to the prescription in Ref. [109], and while central values of top quark p_T are not adjusted, the difference between central and reweighted values are added as a one-sided systematic

uncertainty. Shape uncertainties are evaluated event-by-event, so they are calculated independently for each type of event selection. Details of these uncertainties for the signal and background samples are shown in the Table 7.8.

Table 7.8: Summary of all systematic uncertainties considered.

Source	Uncertainty	Signal	Background
Normalization only			
Luminosity	4.6%	Yes	All
Trigger Efficiency	3%	Yes	All
Lepton efficiencies	1%	Yes	All
“Top bkg”: $t\bar{t}$, Single top, $t\bar{t}+W/Z$ cross-sections	5.5%	No	
“EWK bkg”: W +jets, Diboson cross sections	5%	No	
“Top bkg” modeling, based on the CR	11-19%	No	
“EWK bkg” modeling, based on the CR	24%	No	
QCD multijet cross-sections	50%	No	
Shape and Normalization			
Jet Energy Scale	$\pm\sigma(p_T, \eta)$	Yes	All
Jet Energy Resolution	$\pm\sigma$	Yes	All
b tagging	$\pm\sigma$	Yes	All
W tagging: mass resolution	$\pm\sigma$	Yes	All
W tagging: mass scale	$\pm\sigma$	Yes	All
W tagging: τ_2/τ_1	$\pm\sigma$	Yes	All
Top p_T	$\Delta(\text{weighted, nominal})$	No	$t\bar{t}$
Pileup	$\sigma_{\text{minbias}} \pm 5\%$	Yes	All
Parton Shower Scale	$\pm\sigma$	No	$t\bar{t}$, single top
Shape only			
PDF	$\pm\sigma$	Yes	All
Renormalization Scale	$\pm\sigma$	Yes	All
Factorization Scale	$\pm\sigma$	Yes	All

Figures 7.7.1 - 7.7.3 show the $\pm 1\sigma$ variations of these systematic shapes on the total background, using the selection cuts determined from the optimization procedure for the discriminant variable $\min[M(\ell, b)]$.

7.8 Results

We consider the $\min[M(\ell, b)]$ distributions in order to discriminate signal from background and, in the absence of signal, set limits on the $X_{5/3}$ cross section.

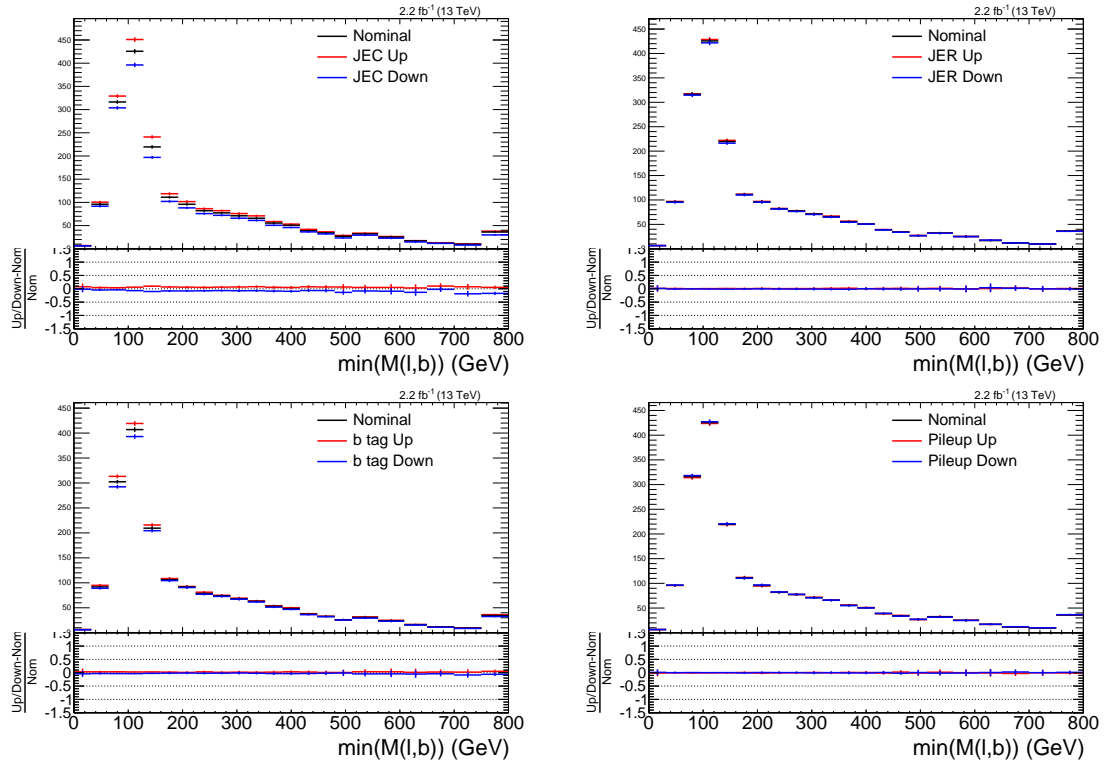


Figure 7.7.1: Distributions of $\min[M(\ell, b)]$ for total background with $\pm 1\sigma$ variations for (top-left) jet energy scale, (top-right) jet energy resolution, (bottom-left) b tag scale factor, and (bottom-right) pileup reweighting uncertainties after combining all channels.

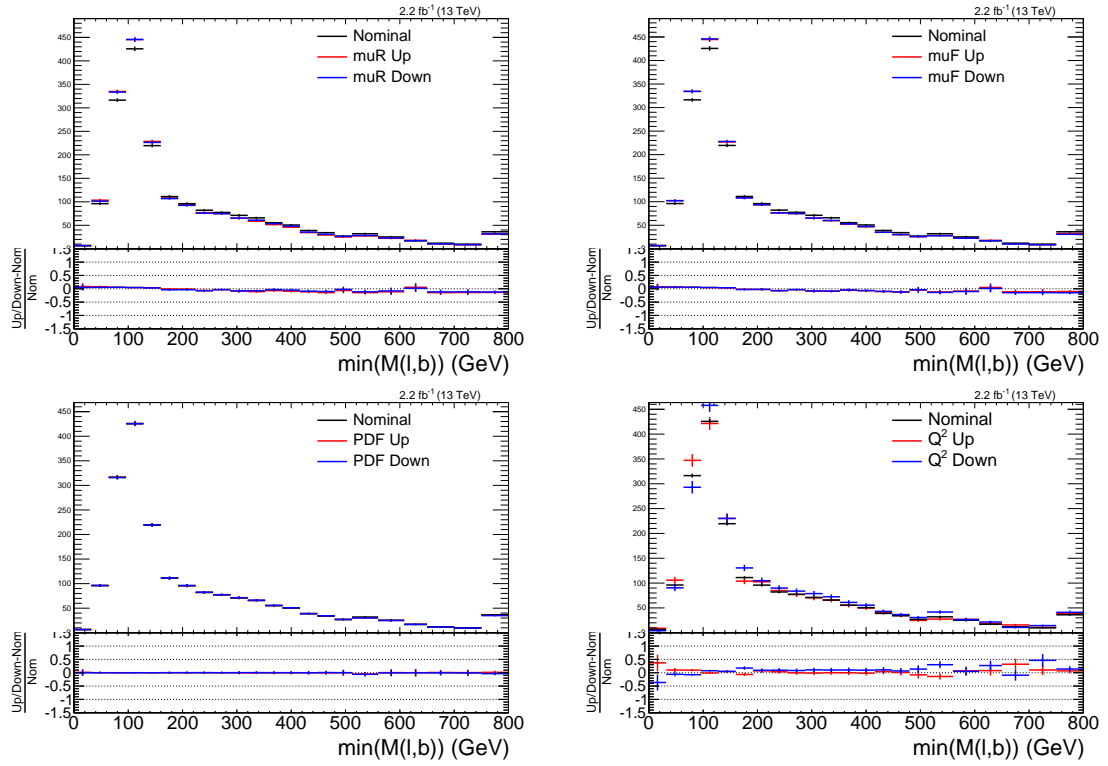


Figure 7.7.2: Distributions of $\min[M(\ell, b)]$ for total background with $\pm 1\sigma$ variations for (top-left) renormalization scale, (top-right) factorization scale, (bottom-left) PDF uncertainties, and (bottom-right) parton shower energy scale after combining all channels.

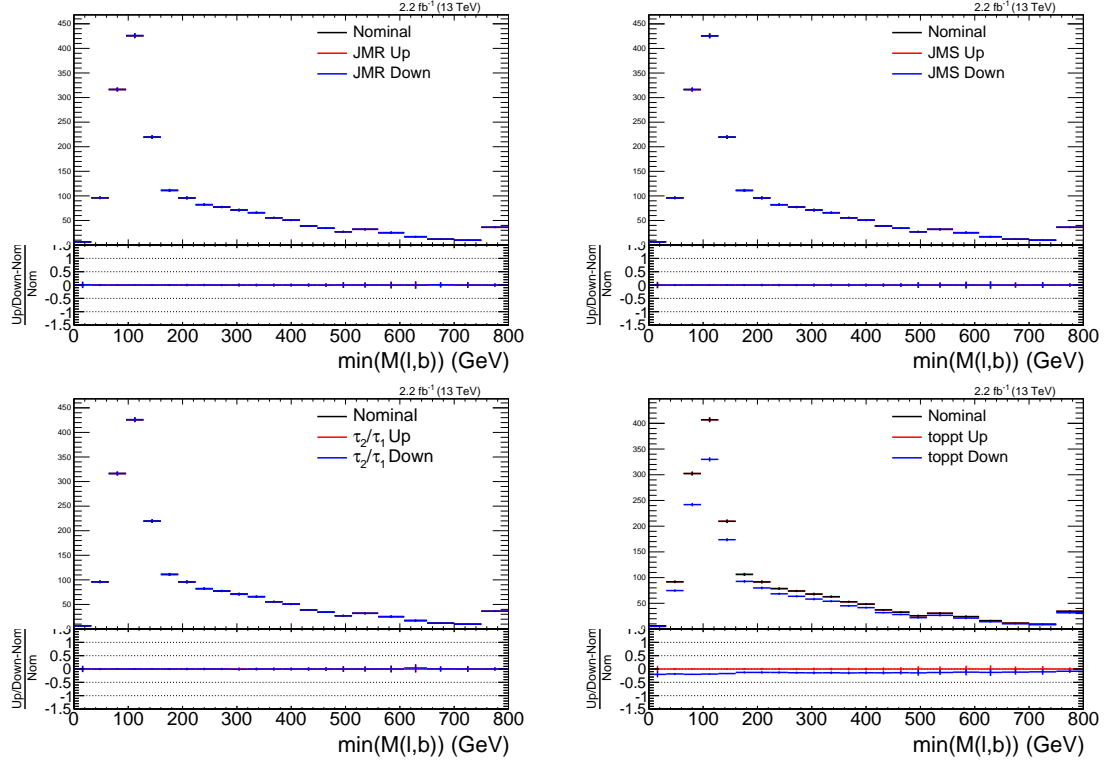


Figure 7.7.3: Distributions of $\min[M(\ell, b)]$ for total background with $\pm 1\sigma$ variations for (top-left) pruned jet mass resolution, (top-right) pruned jet mass scale, (bottom-left) τ_2/τ_1 efficiency uncertainty, and (bottom-right) top quark p_T reweighting.

7.8.1 Kinematics with optimized selection

As described in Section 7.5, the optimized event selection increases the lepton p_T requirement to 80 GeV, and increases the number of jets requirement to four or more. Figs. 7.8.1 and 7.8.2 show the lepton and jet kinematics after the optimized selection cuts are applied. Distributions of b-tagged and W-tagged jet multiplicities, which form event categories for limit calculation, are shown in Fig. 7.8.3, and Fig. 7.8.4 shows the distributions of $\min[M(\ell, b)]$ and $\Delta R(\ell, \text{sub-leading jet})$. Event yields in the analysis categories are listed in Table 7.9.

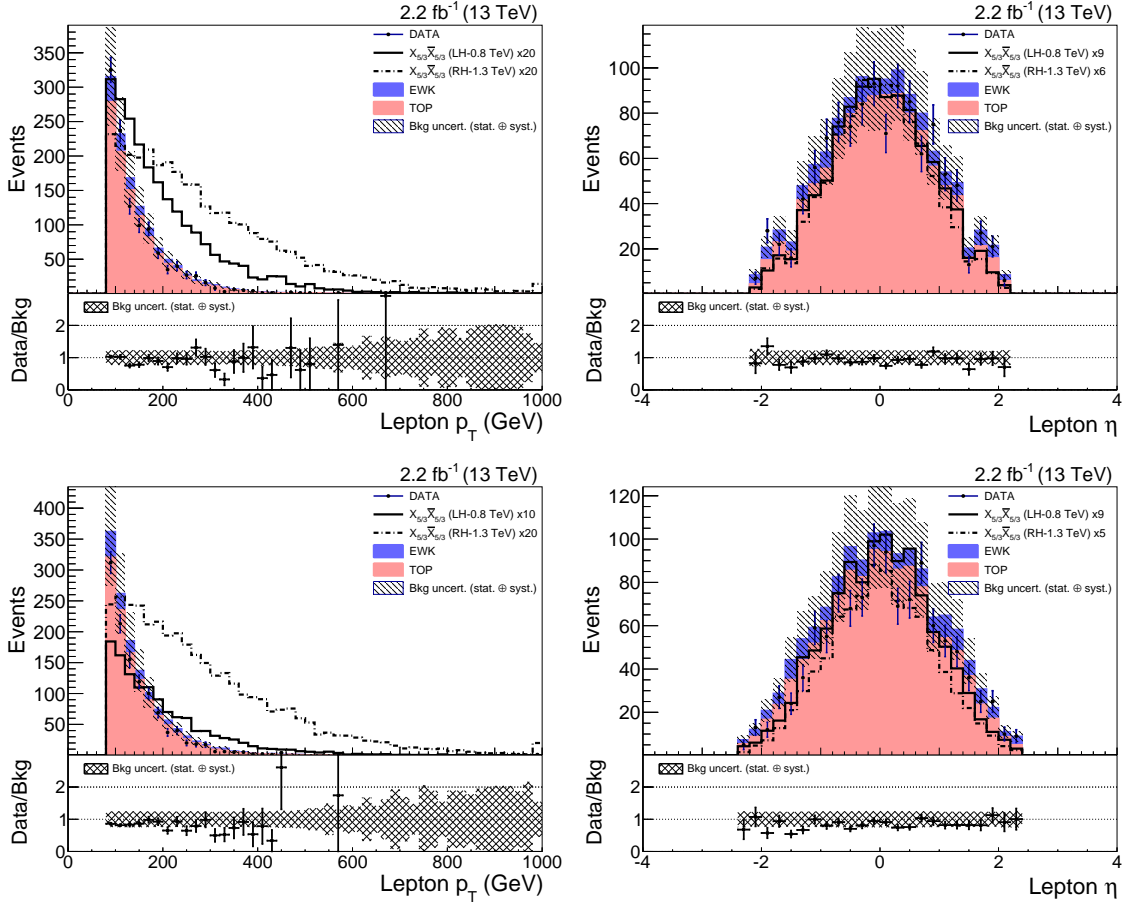


Figure 7.8.1: Distributions of (left) lepton p_T and (right) $|\eta|$ in (top) electron and (bottom) muon channels in data and MC after the optimized selection. Uncertainties include all statistical and systematic uncertainties.

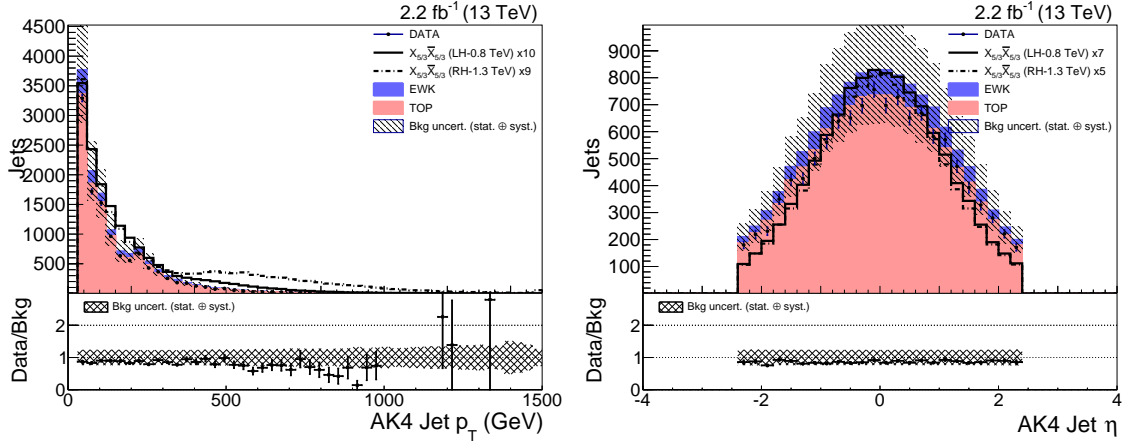


Figure 7.8.2: Distributions of (left) p_T (right) $|\eta|$ of all AK4 jets with $p_T > 30$ GeV in data and MC after the optimized selection. Uncertainties include all statistical and systematic uncertainties.

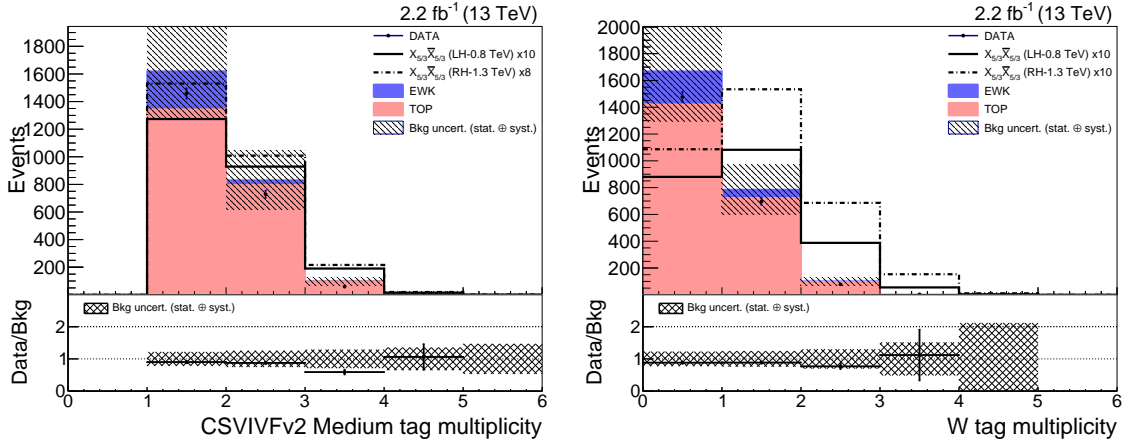


Figure 7.8.3: Distributions of b-tagged and W-tagged jet multiplicity in data and MC after the optimized selection. Uncertainties include all statistical and systematic uncertainties.

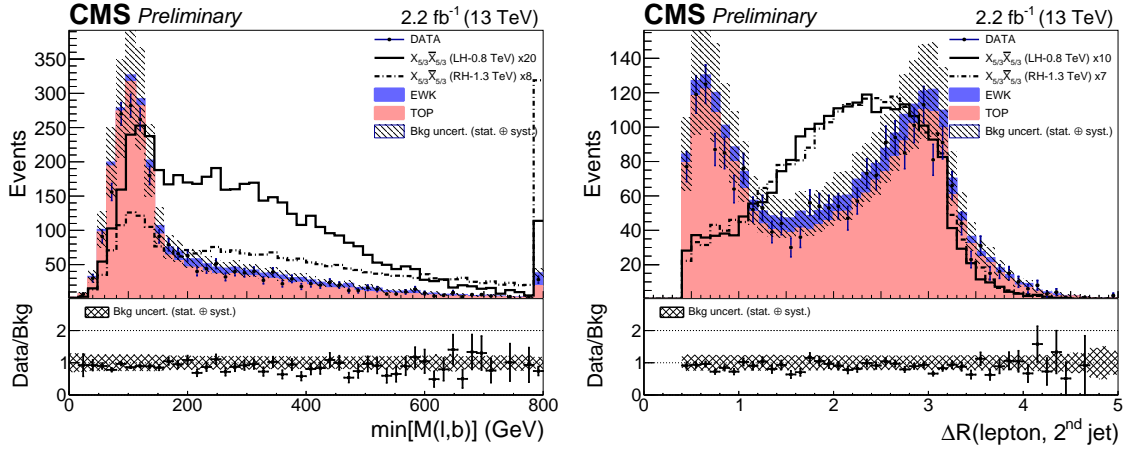


Figure 7.8.4: Distribution of $\min[M(\ell, b)]$ in data and MC after the optimized selection. Uncertainties include all statistical and systematic uncertainties.

Table 7.9: Observed (expected) number of data (background) events when requiring lepton $p_T > 80$ GeV and 4 or more AK4 jets, but before applying the final cuts on $\Delta R(\ell, \text{sub-leading jet})$. Uncertainties include all statistical and normalization uncertainties (Table 7.8).

Sample	$e + \text{jets}$	$\mu + \text{jets}$	Combined
LH $X_{5/3}$ (0.8 TeV)	21.8 ± 1.3	23.9 ± 1.4	45.7 ± 2.6
RH $X_{5/3}$ (1.3 TeV)	1.00 ± 0.06	1.11 ± 0.06	2.12 ± 0.12
EWK	146 ± 33	168 ± 45	315 ± 80
Top	1060 ± 160	1180 ± 210	2240 ± 360
QCD	2.3 ± 2.1	< 2	2.3 ± 2.1
Total Bkg	1210 ± 170	1350 ± 220	2560 ± 370
Data	1120	1134	2254
Data/Bkg	0.92 ± 0.13	0.84 ± 0.14	0.88 ± 0.13

Table 7.10: Expected (observed) number of background (data) events for the electron channel in the four analysis categories, with an integrated luminosity of 2.2 fb^{-1} . Uncertainties include all statistical and normalization uncertainties (Table 7.8).

Sample	0 W, 1 b	0 W, 2+ b	1+ W, 1 b	1+ W, 2+ b
LH $X_{5/3}$ (0.8 TeV)	3.94 ± 0.25	3.35 ± 0.22	6.80 ± 0.41	5.84 ± 0.36
RH $X_{5/3}$ (1.2 TeV)	0.291 ± 0.018	0.224 ± 0.014	0.649 ± 0.038	0.538 ± 0.032
EWK	84 ± 21	11.6 ± 3.1	23.9 ± 6.6	3.5 ± 1.2
Top	309 ± 42	198 ± 41	158 ± 22	108 ± 22
QCD	2.0 ± 2.0	0.006 ± 0.006	0.001 ± 0.001	< 0.001
Total Bkg	394 ± 49	209 ± 41	182 ± 23	112 ± 22
Data	376	186	189	94
Data/Bkg	0.95 ± 0.13	0.89 ± 0.19	1.04 ± 0.15	0.84 ± 0.19

7.8.2 Kinematics with final event selection

On top of the final selection described in Section 7.5, we introduce an additional selection requirement of $\Delta R(\ell, \text{sub-leading jet}) > 1$. This requirement is intended to create a background depleted signal region, and backgrounds were studied in control regions defined by inverting this cut. Figs. 7.8.5 and 7.8.6 show the lepton and jet kinematics after optimized selection cuts are applied. The jet p_T distribution is split into contributions from the four highest p_T jets in Fig. 7.8.7. Figure 7.8.8 shows distributions of E_T^{miss} , H_T , and S_T . Distributions of b-tagged and W-tagged jet multiplicities, which form event categories for limit calculation, are shown in Fig. 7.8.9. Finally, Fig. 7.8.10 shows the distributions of $\min[M(\ell, b)]$ and $\Delta R(\ell, \text{sub-leading jet})$.

7.8.3 Categorized discriminant templates

In Figs. 7.8.11 - 7.8.13, the $\min[M(\ell, b)]$ distributions used in the limit calculation are shown for each category in the electron, muon, and combined lepton channels. The $\min[M(\ell, b)]$ distributions are given variable sized bins. Event yields after the final selection cuts are given in Tables 7.10 - 7.11.

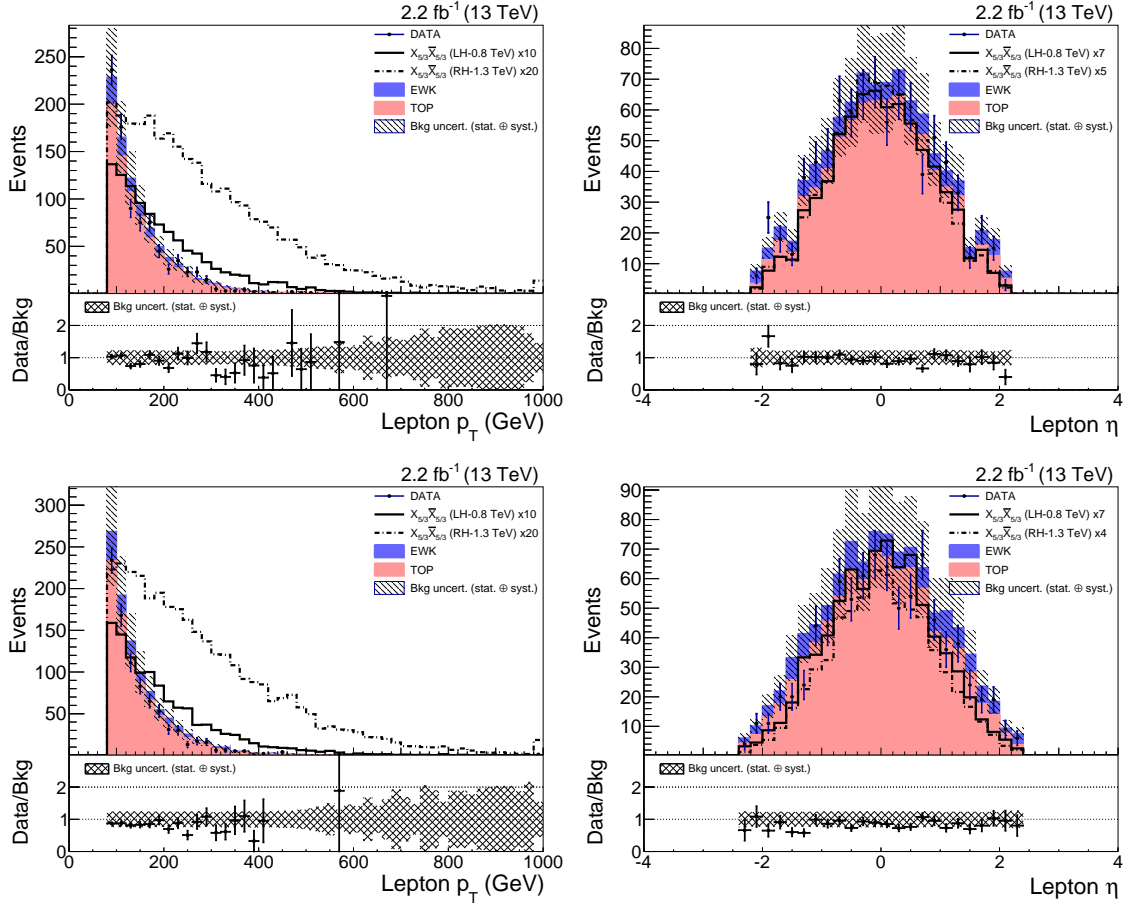


Figure 7.8.5: Distributions of (left) lepton p_T and (right) $|\eta|$ in (top) electron and (bottom) muon channels in data and MC after the final selection for the $\min[M(\ell, b)]$ discriminant. Uncertainties include all statistical and systematic uncertainties.

Table 7.11: Expected (observed) number of background (data) events for the muon channel in the four analysis categories, with an integrated luminosity of 2.2 fb^{-1} . Uncertainties include all statistical and normalization uncertainties (Table 7.8).

Sample	0 W, 1 b	0 W, 2+ b	1+ W, 1 b	1+ W, 2+ b
LH $X_{5/3}$ (0.8 TeV)	4.09 ± 0.26	3.69 ± 0.24	7.35 ± 0.44	6.68 ± 0.41
RH $X_{5/3}$ (1.2 TeV)	0.307 ± 0.019	0.262 ± 0.017	0.732 ± 0.043	0.579 ± 0.035
EWK	101 ± 26	14.2 ± 3.8	23.9 ± 6.2	3.6 ± 1.0
Top	355 ± 48	223 ± 46	178 ± 24	114 ± 24
QCD	< 1	< 1	< 1	< 1
Total Bkg	456 ± 57	237 ± 46	202 ± 26	117 ± 24
Data	392	214	158	88
Data/Bkg	0.86 ± 0.12	0.90 ± 0.19	0.78 ± 0.12	0.75 ± 0.17

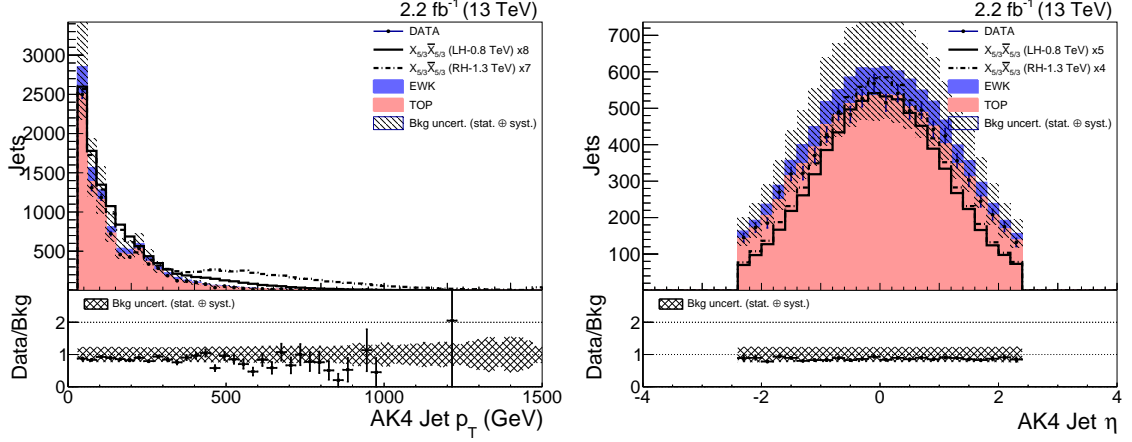


Figure 7.8.6: Distributions of (left) p_T (right) $|\eta|$ of all AK4 jets with $p_T > 30$ GeV in data and MC after the final selection for the $\min[M(\ell, b)]$ discriminant. Uncertainties include all statistical and systematic uncertainties.

7.8.4 Final results

After the optimized selection cuts, no significant excess above the SM expectations is observed in data. Using the Theta program [108], we apply Bayesian statistics with a flat prior on the signal cross-section to calculate 95% CL upper limits on the production cross section for $pp \rightarrow X_{5/3} \bar{X}_{5/3} \rightarrow tW^+ \bar{t}W^-$ for both left- and right-handed $X_{5/3}$ at each simulated mass point. Figure 7.8.14 shows the expected and observed limits as a function of $X_{5/3}$ mass, for an integrated luminosity of 2.2 fb^{-1} . Comparing the experimental upper limits to the theoretical predictions [102], we obtain the 95% confidence level (CL) lower limit on the observed (expected) mass of the $X_{5/3}$. For the left-handed $X_{5/3}$ both the observed lower mass limit is obtained to be 715 GeV, very close to the expected limit. For the right-handed $X_{5/3}$, the observed and expected exclusion limit is 700 GeV. These serve as the first limits at the LHC on the $X_{5/3}$ pair production in the single lepton channel.

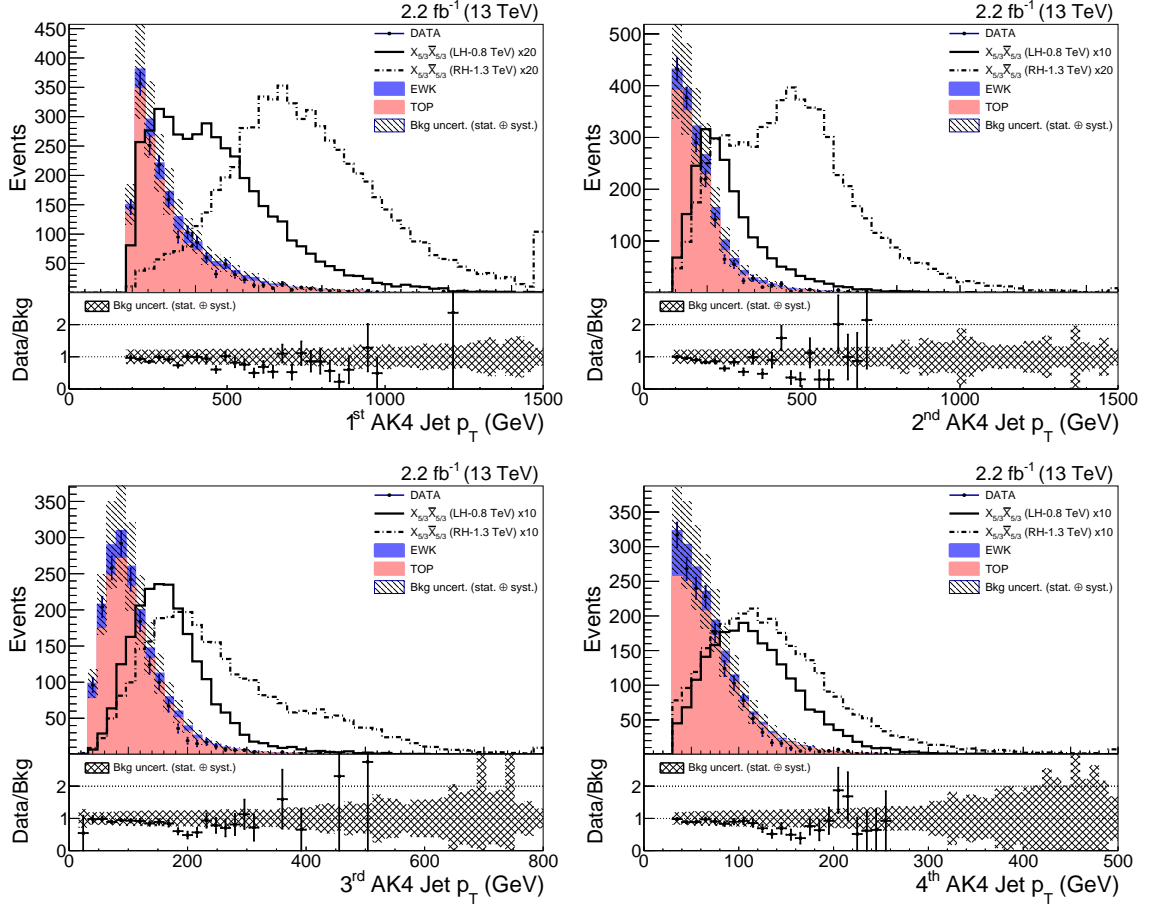


Figure 7.8.7: Distributions of p_T for the four highest p_T jets in data and MC after the final selection for the $\min[M(\ell, b)]$ discriminant. Uncertainties include all statistical and systematic uncertainties.

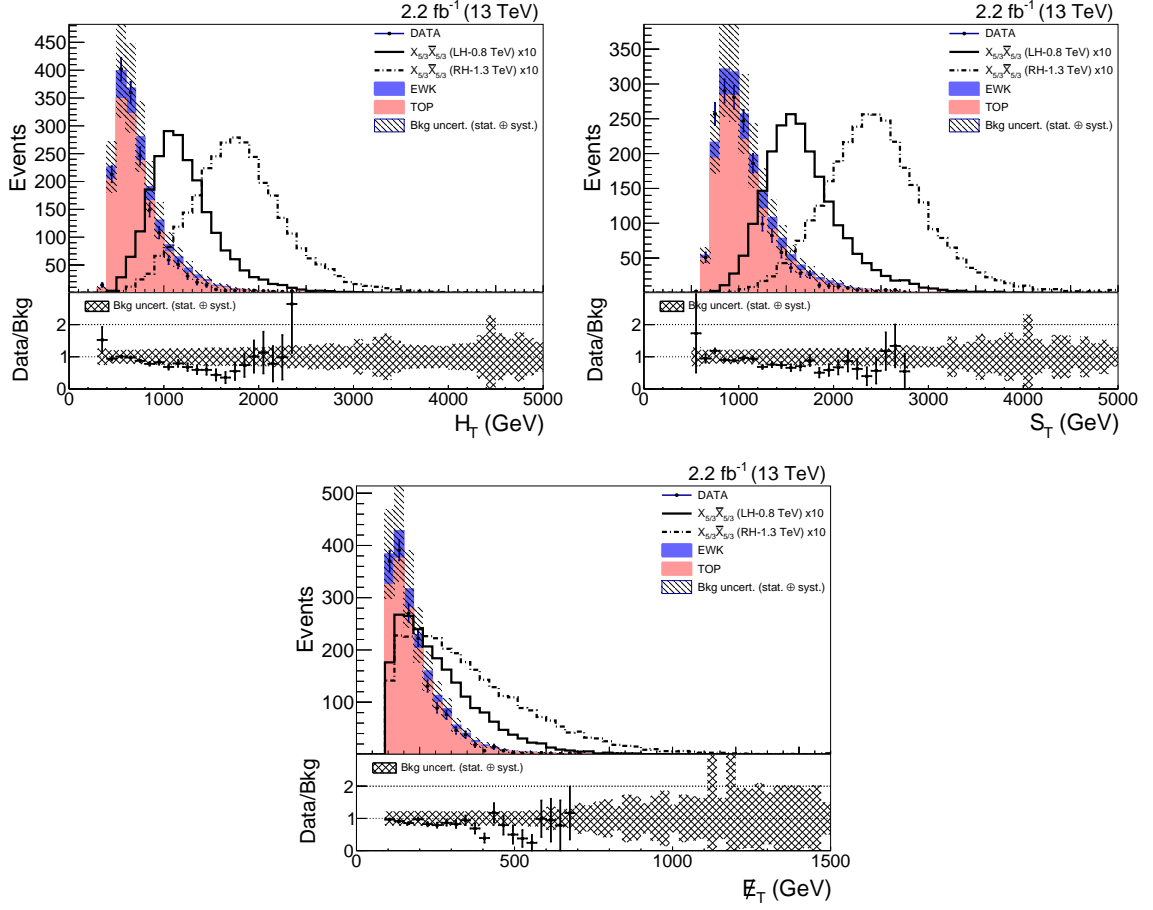


Figure 7.8.8: Distributions of (left) H_T , (right) S_T , and E_T^{miss} in data and MC after the final selection for the $\min[M(\ell, b)]$ discriminant. Uncertainties include all statistical and systematic uncertainties.

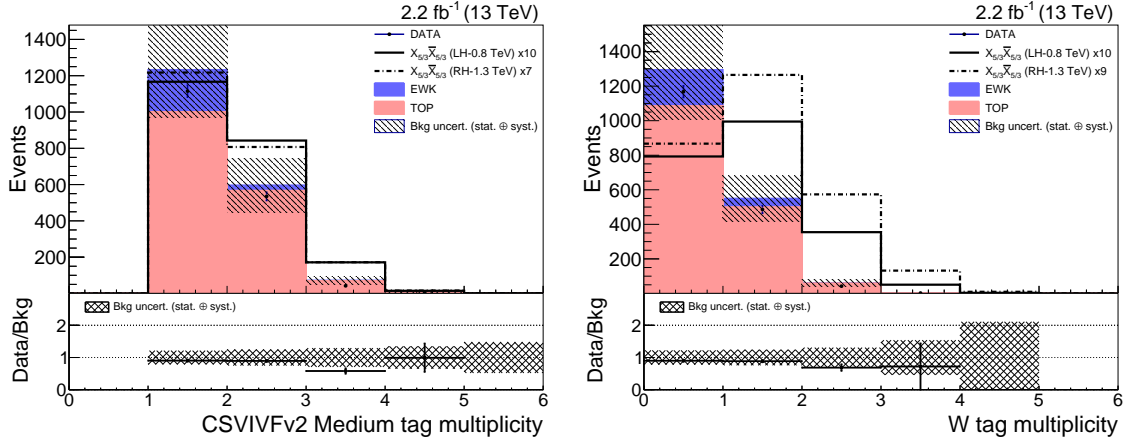


Figure 7.8.9: Distributions of b tagged and W tagged jet multiplicity in data and MC after the final selection for the $\min[M(\ell, b)]$ discriminant. Uncertainties include all statistical and systematic uncertainties.

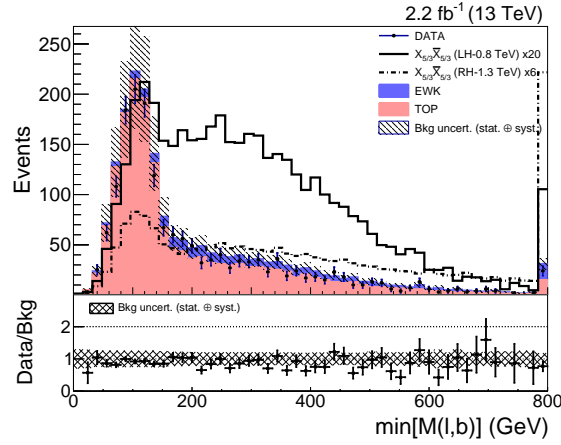


Figure 7.8.10: Distribution of $\min[M(\ell, b)]$ in data and MC after the final selection for the $\min[M(\ell, b)]$ discriminant. Uncertainties include all statistical and systematic uncertainties.

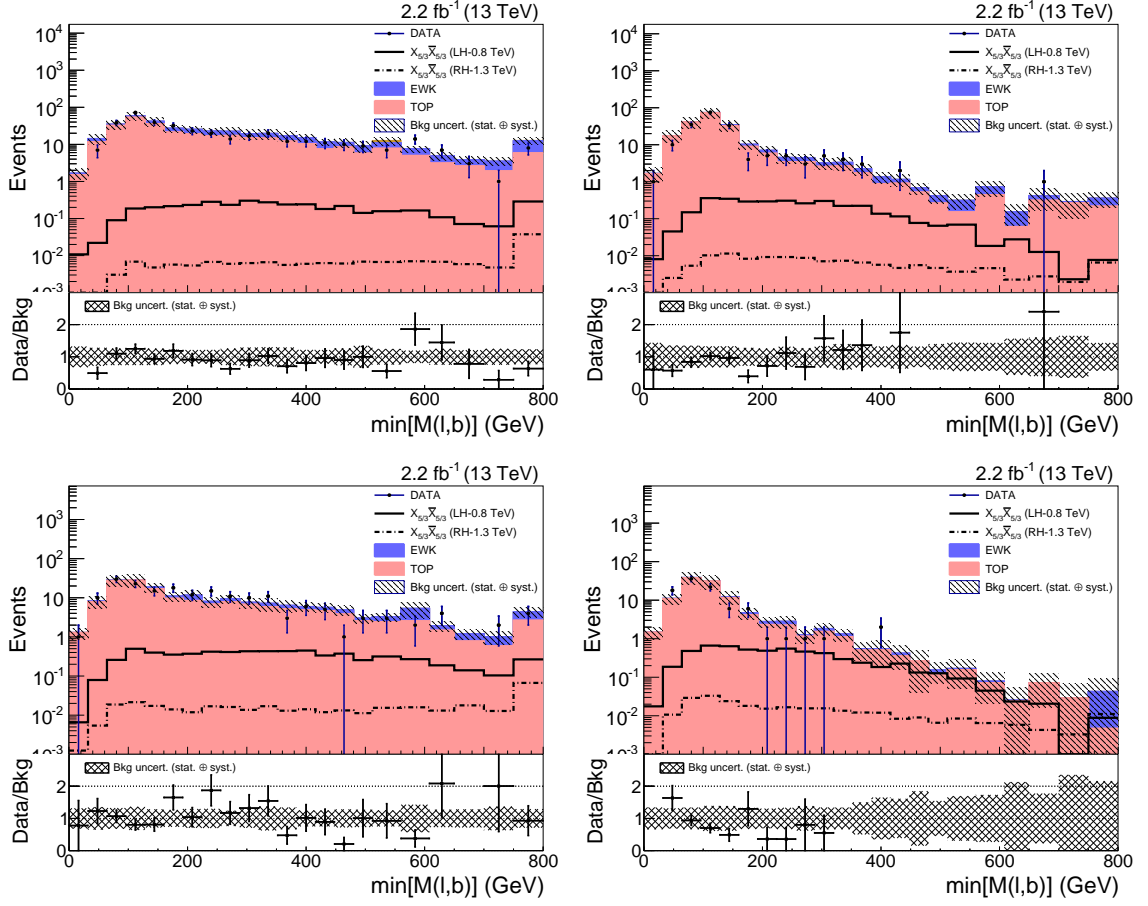


Figure 7.8.11: Distributions of $\min[M(\ell, b)]$ in the electron channel in categories with (top) 0 or (bottom) 1+ boosted W-tagged jets and (left) 1 or (right) 2+ b-tagged AK4 jets. Uncertainties include all statistical and systematic uncertainties.

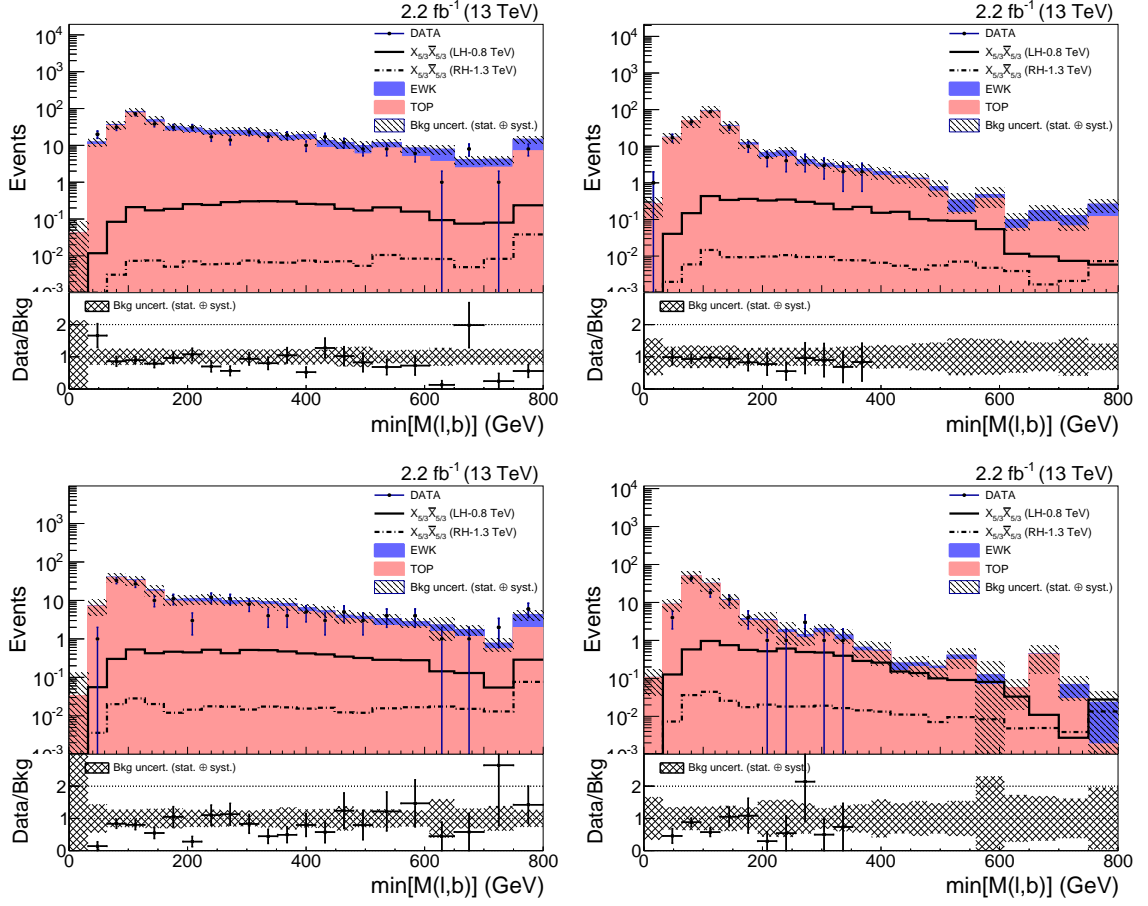


Figure 7.8.12: Distributions of $\min[M(\ell, b)]$ in the muon channel in categories with (top) 0 or (bottom) 1+ boosted W-tagged jets and (left) 1 or (right) 2+ b-tagged AK4 jets. Uncertainties include all statistical and systematic uncertainties.

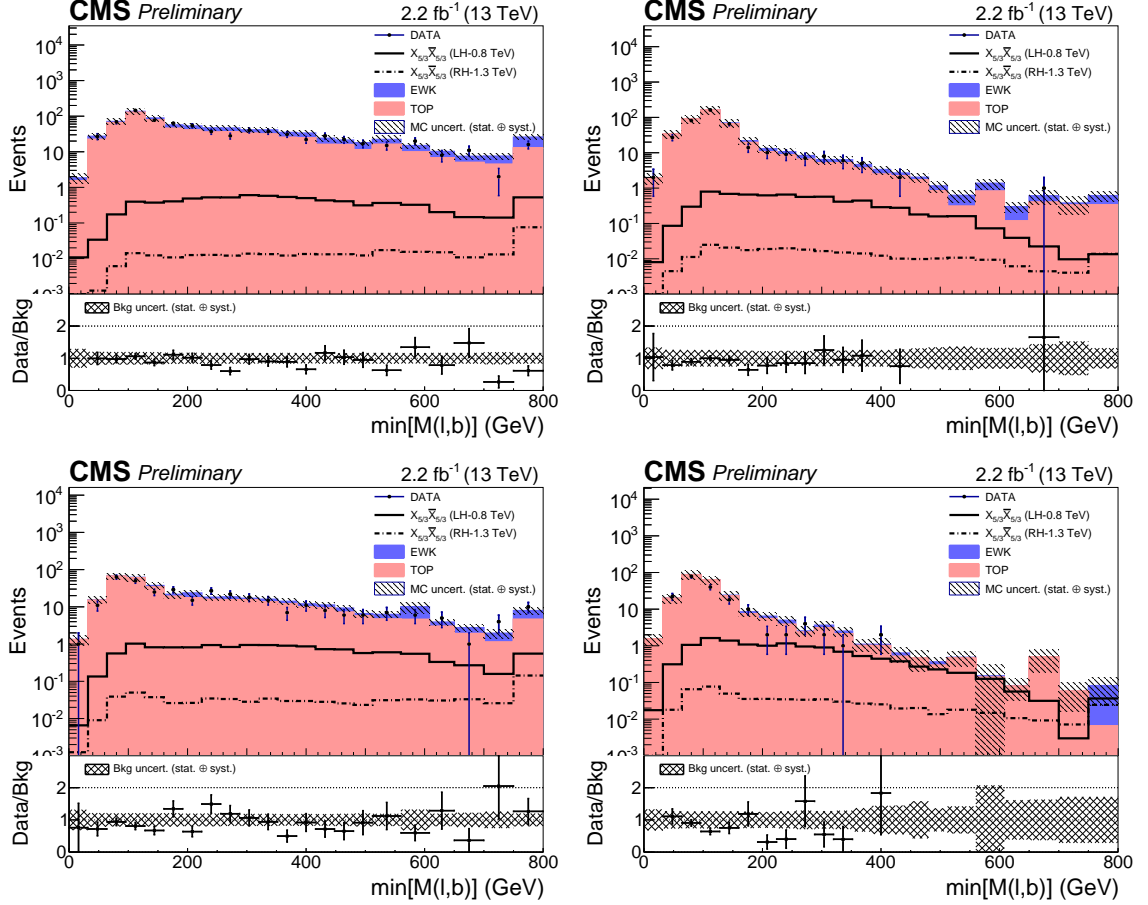


Figure 7.8.13: Distributions of $\min[M(\ell, b)]$ for combined electron and muon channels in categories with (top) 0 or (bottom) 1+ boosted W-tagged jets and (left) 1 or (right) 2+ b-tagged AK4 jets. Uncertainties include all statistical and systematic uncertainties. For each category, the QCD contribution is not displayed if it is less than 0.5% of the total background.

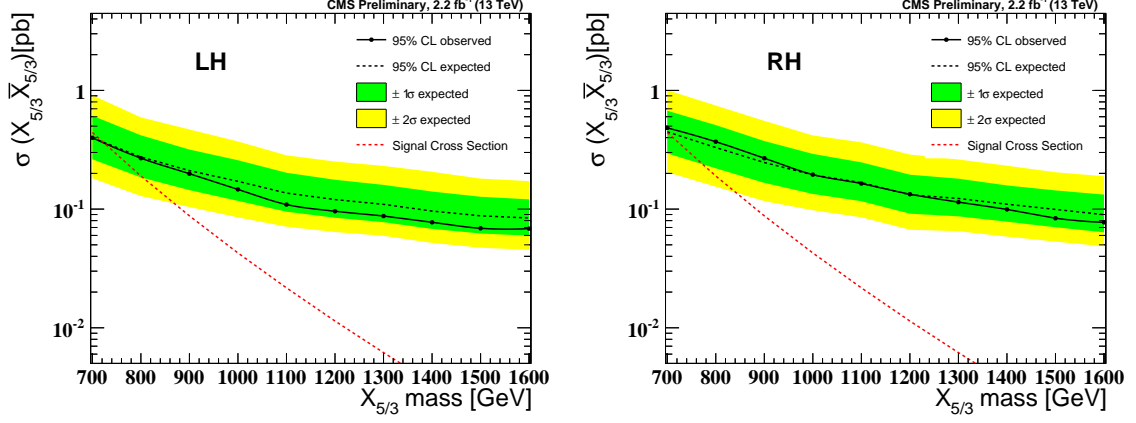


Figure 7.8.14: 95% CL expected and observed upper limits (Bayesian) on the cross section of (left) left-handed and (right) right-handed $X_{5/3}$, after combining electron/muon, 0/1+ W-tagged jets, and 1/2+ b-tagged jets channels at an integrated luminosity of 2.2 fb^{-1} .

7.9 Combination with Same-Sign Dilepton Channel

This search was also performed in the same-sign dilepton channel where the two W bosons arising from one of the $X_{5/3}$ particles decay into same-sign leptons while the other two W bosons decay inclusively. A combination of the results [30] from the analyses of the two final states is shown in Fig. 7.9.1. The observed (expected) exclusion limits on the mass of a right handed $X_{5/3}$ is obtained to be 960 (900) GeV. For the left handed $X_{5/3}$ signal, the observed (expected) lower limit on the mass is 940 (860) GeV. These are the strongest limits on the $X_{5/3}$ mass so far, improving the previous constraints set by CMS at $\sqrt{s} = 8 \text{ TeV}$.

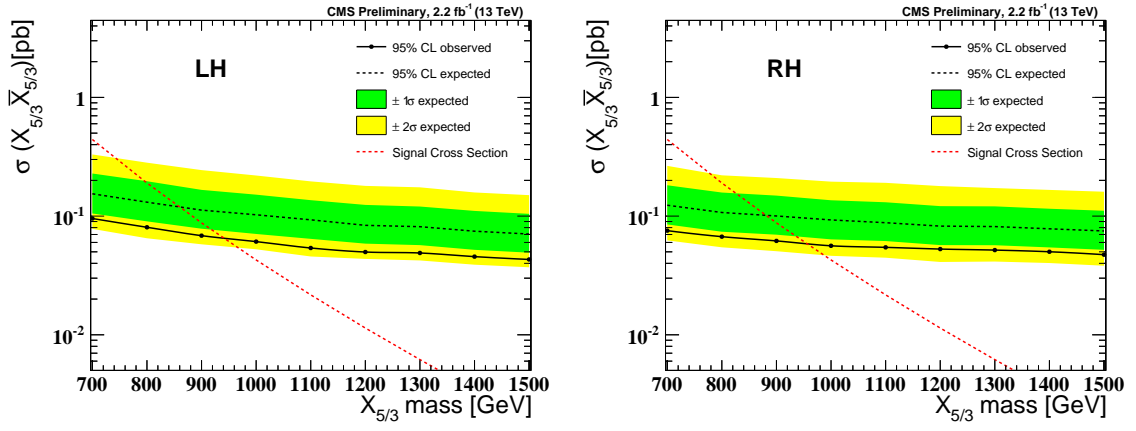


Figure 7.9.1: 95% CL expected and observed upper limits (Bayesian) after combining the same-sign dileptons, and the lepton+jets signatures for an integrated luminosity of 2.2 fb^{-1} for left handed (left) and right handed (right) $X_{5/3}$ signals.

Chapter 8

Summary and Outlook

In this dissertation, two searches for new physics have been presented using the data collected by the CMS detector at two different center of mass energies.

In the first part, the first search for anomalous Higgs couplings to vector bosons in the associated production channel with the Higgs boson decaying to a pair of bottom quarks at the LHC is presented using the data collected from proton-proton collisions in 2012 at a center-of-mass energy of 8 TeV. We demonstrated the power of the associated Higgs production channel in constraining very small anomalous couplings for the future analysis of a larger data set. The sensitivity from the associated Higgs production channel alone is not sufficient to constrain the effective pseudoscalar cross section fractions, f_{a3} , at 95% CL. However, in combination with the previous results from the $H \rightarrow VV$ channels, when assuming the absence of additional anomalous Higgs couplings, a value of $f_{a3}^{ZZ} = 0.00118^{+0.00092}_{-0.00072}$ is obtained, with $f_{a3}^{ZZ} > 0.0034$ excluded at 95% CL [29].

A full simulation projection for Run 2 of the LHC at $\sqrt{s} = 13$ TeV has also been performed. In the projection, a total integrated luminosity of 100 fb^{-1} is assumed. Figure 8.0.1 shows the profile-likelihood scans for the associated production channels. In the associated Higgs production channel alone, $f_{a3}^{ZZ} > 3.6 \times 10^{-3}$ is expected to be excluded at 95% CL.

In the second part of this dissertation, a search for a heavy fermionic partner

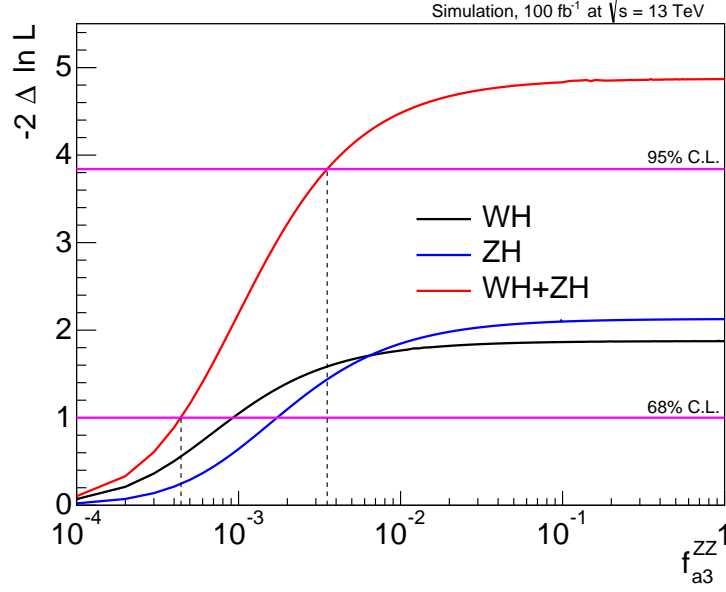


Figure 8.0.1: Results of expected profile likelihood scans for the WH and ZH channels, as well as their combination (WH + ZH), corresponding to 100 fb^{-1} at $\sqrt{s} = 13 \text{ TeV}$. The horizontal magenta lines represent the 68% and 95% CL.

of the top quark with an electrical charge of $5/3$ in the lepton + jets channel is presented using the data collected from proton-proton collisions in 2015 at a center-of-mass energy of 13 TeV. With the pair production channel, using the lepton + jets final state alone, $X_{5/3}$ masses below 715 GeV (700 GeV) are excluded at 95% CL for left-handed (right-handed) $X_{5/3}$. These serve as the first limits at the LHC on $X_{5/3}$ pair production in the lepton + jets channel. In a combination with the same-sign dilepton channel, the observed (expected) lower limit on the $X_{5/3}$ mass is obtained to be 960 (900) GeV for the right-handed signal and 940 (860) GeV for the left-handed signal [30], improving the previous constraints set by CMS at $\sqrt{s} = 8 \text{ TeV}$ [92].

In addition to boosted topologies of hadronically decaying W bosons which were explored in this dissertation, the decay products of top quarks in the final states of $X_{5/3}$ pair production can also be boosted. The sensitivity of the lepton + jets channel can, therefore, be improved more with the help of boosted top tagging with

additional data that is being collected at the LHC during 2016. In a combination with the same-sign dilepton final state, a hypothetical $X_{5/3}$ with a mass below ~ 1 TeV can be excluded at the LHC using the full Run 2 data at $\sqrt{s} = 13$ TeV. The two searches presented in this dissertation have important role in exploring new physics in the new energy regime at the LHC.

Bibliography

- [1] C. Barth, “Performance of the CMS Tracker under Irradiation”. PhD thesis, Karlsruhe Institute of Technology (KIT), 2013.
- [2] L. Rossi and O. Brüning, “High Luminosity Large Hadron Collider A description for the European Strategy Preparatory Group”, Technical Report CERN-ATS-2012-236, CERN, Geneva, Aug, 2012.
- [3] C. García-Argos, “A Silicon Strip Detector for the Phase II High Luminosity Upgrade of the ATLAS Detector at the Large Hadron Collider”. PhD thesis, Valencia U., 2015. [arXiv:1501.02903](#). [doi:10.17181/CERN.K7MD.N3VZ](#).
- [4] CMS Collaboration Collaboration, “Search for the standard model Higgs boson produced in association with a W or a Z boson and decaying to bottom quarks”, *Phys.Rev.* **D89** (2014) 012003, [doi:10.1103/PhysRevD.89.012003](#), [arXiv:1310.3687](#).
- [5] Wikipedia, “Standard Model — Wikipedia, The Free Encyclopedia”, 2016. [Online; accessed 6-May-2016].
- [6] P. Langacker, “Introduction to the Standard Model and Electroweak Physics”, in *Proceedings of Theoretical Advanced Study Institute in Elementary Particle Physics on The dawn of the LHC era (TASI 2008)*, pp. 3–48. 2010. [arXiv:0901.0241](#). [doi:10.1142/9789812838360_0001](#).

- [7] CMS Collaboration, “The CMS experiment at the CERN LHC”, *JINST* **3** (2008) S08004, doi:10.1088/1748-0221/3/08/S08004.
- [8] M. Moll, “Radiation Damage in Silicon Particle Detectors”. PhD thesis, University of Hamburg, 1999.
- [9] Particle Data Group Collaboration, “Review of Particle Physics”, *Chin. Phys.* **C38** (2014) 090001, doi:10.1088/1674-1137/38/9/090001.
- [10] D. Griffiths, “Introduction to Elementary Particles”. Wiley, 2008.
- [11] C. N. Yang and R. L. Mills, “Conservation of Isotopic Spin and Isotopic Gauge Invariance”, *Phys. Rev.* **96** (Oct, 1954) 191–195, doi:10.1103/PhysRev.96.191.
- [12] S. L. Glashow, “Partial Symmetries of Weak Interactions”, *Nucl. Phys.* **22** (1961) 579–588, doi:10.1016/0029-5582(61)90469-2.
- [13] S. Weinberg, “A Model of Leptons”, *Phys. Rev. Lett.* **19** (1967) 1264–1266, doi:10.1103/PhysRevLett.19.1264.
- [14] J. Goldstone, A. Salam, and S. Weinberg, “Broken Symmetries”, *Phys. Rev.* **127** (1962) 965–970, doi:10.1103/PhysRev.127.965.
- [15] S. L. Glashow, J. Iliopoulos, and L. Maiani, “Weak Interactions with Lepton-Hadron Symmetry”, *Phys. Rev.* **D2** (1970) 1285–1292, doi:10.1103/PhysRevD.2.1285.
- [16] A. Salam and J. C. Ward, “Weak and electromagnetic interactions”, *Il Nuovo Cimento (1955-1965)* **11** (1959), no. 4, 568–577, doi:10.1007/BF02726525.
- [17] P. W. Higgs, “Broken Symmetries and the Masses of Gauge Bosons”, *Phys. Rev. Lett.* **13** (Oct, 1964) 508–509, doi:10.1103/PhysRevLett.13.508.

- [18] F. Englert and R. Brout, “Broken Symmetry and the Mass of Gauge Vector Mesons”, *Phys. Rev. Lett.* **13** (Aug, 1964) 321–323,
doi:10.1103/PhysRevLett.13.321.
- [19] G. S. Guralnik, C. R. Hagen, and T. W. B. Kibble, “Global Conservation Laws and Massless Particles”, *Phys. Rev. Lett.* **13** (Nov, 1964) 585–587,
doi:10.1103/PhysRevLett.13.585.
- [20] CMS Collaboration, “Observation of a new boson at a mass of 125 GeV with the CMS experiment at the LHC”, *Phys. Lett. B* **716** (Jul, 2012) 30–61. 59 p.
- [21] ATLAS Collaboration, “Observation of a new particle in the search for the Standard Model Higgs boson with the ATLAS detector at the LHC”,
Phys.Lett. **B716** (2012) 1–29, doi:10.1016/j.physletb.2012.08.020,
arXiv:1207.7214.
- [22] ATLAS, CMS Collaboration, “Combined Measurement of the Higgs Boson Mass in pp Collisions at $\sqrt{s} = 7$ and 8 TeV with the ATLAS and CMS Experiments”, *Phys. Rev. Lett.* **114** (2015) 191803,
doi:10.1103/PhysRevLett.114.191803, arXiv:1503.07589.
- [23] Super-Kamiokande Collaboration Collaboration, “Evidence for Oscillation of Atmospheric Neutrinos”, *Phys. Rev. Lett.* **81** (Aug, 1998) 1562–1567,
doi:10.1103/PhysRevLett.81.1562.
- [24] SNO Collaboration Collaboration, “Measurement of the Rate of $\nu_e + d \rightarrow p + p + e^-$ Interactions Produced by 8B Solar Neutrinos at the Sudbury Neutrino Observatory”, *Phys. Rev. Lett.* **87** (Jul, 2001) 071301,
doi:10.1103/PhysRevLett.87.071301.
- [25] M. Gell-Mann, “The Eightfold Way: A Theory of strong interaction symmetry”, *CTSL-20, TID-12608* (1961).

- [26] M. Gell-Mann, “A Schematic Model of Baryons and Mesons”, *Phys. Lett.* **8** (1964) 214–215, doi:10.1016/S0031-9163(64)92001-3.
- [27] M. Herrero, “The Standard model”, *NATO Sci. Ser. C* **534** (1999) 1–59, doi:10.1007/978-94-011-4689-0_1, arXiv:hep-ph/9812242.
- [28] O. W. Greenberg, “Spin and Unitary Spin Independence in a Paraquark Model of Baryons and Mesons”, *Phys. Rev. Lett.* **13** (1964) 598–602, doi:10.1103/PhysRevLett.13.598.
- [29] CMS Collaboration, “Combined search for anomalous pseudoscalar HVV couplings in $VH(H \rightarrow b\bar{b})$ production and $H \rightarrow VV$ decay”, *Phys. Lett.* **B759** (2016) 672–696, doi:10.1016/j.physletb.2016.06.004, arXiv:1602.04305.
- [30] CMS Collaboration, “Search for top quark partners with charge 5/3 at $\sqrt{s} = 13$ TeV”, *CMS Physics Analysis Summary* **CMS-PAS-B2G-15-006** (2015).
- [31] O. S. Brüning et al., “LHC Design Report”. CERN, Geneva, 2004.
- [32] CMS Collaboration, “The CMS experiment at the CERN LHC”, *JINST* **3** (2008) S08004, doi:10.1088/1748-0221/3/08/S08004.
- [33] P. Adzic, “Energy resolution of the barrel of the CMS Electromagnetic Calorimeter”, *Journal of Instrumentation* **2** (2007), no. 04, P04004.
- [34] M. Moll, E. Fretwurst, and G. Lindström, “Leakage current of hadron irradiated silicon detectors - material dependence”, *Nuclear Instruments and Methods in Physics Research Section A: Accelerators, Spectrometers, Detectors and Associated Equipment* **426** (1999), no. 1, 87 – 93, doi:http://dx.doi.org/10.1016/S0168-9002(98)01475-2.

- [35] A. Chilingarov, “Temperature dependence of the current generated in Si bulk”, *Journal of Instrumentation* **8** (2013), no. 10, P10003.
- [36] CMS Collaboration, “TWiki: CMS Strip Tracker Radiation Damage Monitoring”, 2016. (CMS internal content).
- [37] G. Battistoni et al., “The FLUKA code: Description and benchmarking”, *AIP Conf. Proc.* **896** (2007) 31–49, doi:10.1063/1.2720455. [,31(2007)].
- [38] G. Antchev et al., “First measurement of the total proton-proton cross section at the LHC energy of $\sqrt{s}=7$ TeV”, *Europhys. Lett.* **96** (2011) 21002, doi:10.1209/0295-5075/96/21002, arXiv:1110.1395.
- [39] TOTEM Collaboration, “Cross sections and forward multiplicities measurements with TOTEM”, *PoS DIS2013* (2013) 066.
- [40] CMS Collaboration Collaboration, “Measurement of the inelastic proton-proton cross section at $\sqrt{s} = 13$ TeV”, Technical Report CMS-PAS-FSQ-15-005, CERN, Geneva, 2016.
- [41] A. Collaboration, “Letter of Intent for the Phase-II Upgrade of the ATLAS Experiment”, Technical Report CERN-LHCC-2012-022. LHCC-I-023, CERN, Geneva, Dec, 2012.
- [42] J. Butler et al., “Technical Proposal for the Phase-II Upgrade of the CMS Detector”, Technical Report CERN-LHCC-2015-010. LHCC-P-008, CERN, Geneva. Geneva, Jun, 2015. Upgrade Project Leader Deputies: Lucia Silvestris (INFN-Bari), Jeremy Mans (University of Minnesota) Additional contacts: Lucia.Silvestris@cern.ch, Jeremy.Mans@cern.ch.
- [43] Hamamatsu Photonics K.K., “Hamamatsu Photonics K.K (HPK)”, 2016. [Online; accessed 5-May-2016].

- [44] J. Erfle, “Irradiation study of different silicon materials for the CMS tracker upgrade”. PhD thesis, U. Hamburg, Dept. Phys., 2014.
- [45] J. Metcalfe, M. Hoferkamp, and S. Seidel, “Annealing effects on depletion voltage and capacitance of Float Zone and Magnetic Czochralski silicon diodes after 800 MeV proton exposure”, in *IEEE Nuclear Science Symposium Medical Imaging Conference*, pp. 608–611. Oct, 2010.
doi:10.1109/NSSMIC.2010.5873831.
- [46] G. Kramberger et al., “Performance of silicon pad detectors after mixed irradiations with neutrons and fast charged hadrons”, *Nuclear Instruments and Methods in Physics Research Section A: Accelerators, Spectrometers, Detectors and Associated Equipment* **609** (2009), no. 2-3, 142 – 148,
doi:http://dx.doi.org/10.1016/j.nima.2009.08.030.
- [47] CMS Collaboration, “Particle-Flow Event Reconstruction in CMS and Performance for Jets, Taus, and MET”, *CMS Physics Analysis Summary CMS-PAS-PFT-09-001* (2009).
- [48] CMS Collaboration, “Description and performance of track and primary-vertex reconstruction with the CMS tracker”, *JINST* **9** (2014), no. 10, P10009, doi:10.1088/1748-0221/9/10/P10009, arXiv:1405.6569.
- [49] CMS Collaboration, “TWiki: MVA Electron Identification Run2”, 2015. (CMS internal content).
- [50] CMS Collaboration, “TWiki: MVA Electron ID”, 2012. (CMS internal content).
- [51] CMS Collaboration, “Alternatives to Standard Isolation for 13TeV”, 2015. (CMS internal content).

- [52] A. Avetisyan et al., “Search for top quark partners with charge $5e/3$ in the same-sign dilepton final state with CMS detector”, (2015). (CMS internal content).
- [53] CMS Collaboration, “TWiki: Baseline Muon Selection”, 2012. (CMS internal content).
- [54] CMS Collaboration, “TWiki: Muon ID Run2”, 2015. (CMS internal content).
- [55] M. Cacciari, G. P. Salam, and G. Soyez, “The Anti- $k(t)$ jet clustering algorithm”, *JHEP* **0804** (2008) 063, [arXiv:hep-ph/0802.1189](#).
- [56] CMS Collaboration, “TWiki: Jet Identification”. (CMS internal content).
- [57] CMS Collaboration, “TWiki: Introduction to Jet Energy Corrections at CMS”. (CMS internal content).
- [58] CMS Collaboration, “TWiki: Recommended Jet Energy Corrections and Uncertainties for Data and MC”, 2015. (CMS internal content).
- [59] C. Weiser, “A Combined Secondary Vertex Based B-Tagging Algorithm in CMS”, Technical Report CMS-NOTE-2006-014, CERN, Geneva, Jan, 2006.
- [60] CMS Collaboration, “TWiki: Usage of b Tag Objects for 13TeV Data with 25ns bunch spacing and 74X reconstruction”, 2015. (CMS internal content).
- [61] CMS Collaboration, “TWiki: Methods to apply b-tagging efficiency scale factors”, 2015. (CMS internal content).
- [62] CMS Collaboration, “TWiki: MET Filters for Run II”, 2015. (CMS internal content).

- [63] J. Thaler and K. Van Tilburg, “Maximizing Boosted Top Identification by Minimizing N-subjettiness”, *JHEP* **1202** (2012) 093,
doi:10.1007/JHEP02(2012)093, arXiv:1108.2701.
- [64] S. Ellis, C. Vermilion, and J. Walsh, “Techniques for improved heavy particle searches with jet substructure”, *Phys. Rev. D* **80** (2009).
- [65] CMS Collaboration, “Top Tagging with New Approaches”, *CMS Physics Analysis Summary* **CMS-PAS-B2G-16-002** (2016).
- [66] CMS Collaboration Collaboration, “Constraints on the spin-parity and anomalous HVV couplings of the Higgs boson in proton collisions at 7 and 8 TeV”, arXiv:1411.3441.
- [67] (CMS Collaboration) Collaboration, “Measurement of the properties of a Higgs boson in the four-lepton final state”, *Phys. Rev. D* **89** (May, 2014) 092007, doi:10.1103/PhysRevD.89.092007.
- [68] CMS Collaboration Collaboration, “Measurement of Higgs boson production and properties in the WW decay channel with leptonic final states”, *JHEP* **1401** (2014) 096, doi:10.1007/JHEP01(2014)096, arXiv:1312.1129.
- [69] CMS Collaboration Collaboration, “Observation of the diphoton decay of the Higgs boson and measurement of its properties”, arXiv:1407.0558.
- [70] ATLAS Collaboration Collaboration, “Evidence for the spin-0 nature of the Higgs boson using ATLAS data”, *Phys.Lett.* **B726** (2013) 120–144,
doi:10.1016/j.physletb.2013.08.026, arXiv:1307.1432.
- [71] TEVNPH Working Group Collaboration, “Combined CDF and D0 Constraints on Models for the Higgs Boson with Exotic Spin and Parity”,.

- [72] I. Anderson et al., “Constraining anomalous HVV interactions at proton and lepton colliders”, *Phys.Rev.* **D89** (2014) 035007,
doi:10.1103/PhysRevD.89.035007, arXiv:1309.4819.
- [73] S. Frixione, P. Nason, and C. Oleari, “Matching NLO QCD computations with Parton Shower simulations: the POWHEG method”, *JHEP* **11** (2007) 070,
doi:10.1088/1126-6708/2007/11/070.
- [74] LHC Higgs Cross Section Working Group Collaboration, “Handbook of LHC Higgs Cross Sections: 3. Higgs Properties”, doi:10.5170/CERN-2013-004,
arXiv:1307.1347.
- [75] S. Bolognesi et al., “On the spin and parity of a single-produced resonance at the LHC”, *Phys.Rev.* **D86** (2012) 095031,
doi:10.1103/PhysRevD.86.095031, arXiv:1208.4018.
- [76] Y. Gao et al., “Spin determination of single-produced resonances at hadron colliders”, *Phys.Rev.* **D81** (2010) 075022,
doi:10.1103/PhysRevD.81.075022, arXiv:1001.3396.
- [77] S. M. T. Sjostrand and P. Z. Skands, “PYTHIA 6.4 Physics and Manual”, *JHEP* **0605** (2006) doi:10.1088/1126-6708/2006/05/026.
- [78] S. Agostinelli et al., “Geant4—a simulation toolkit”, *Nuclear Instruments and Methods in Physics Research Section A: Accelerators, Spectrometers, Detectors and Associated Equipment* **506** (7, 2003) 250–303,
doi:http://dx.doi.org/10.1016/S0168-9002(03)01368-8.
- [79] T. Han and S. Willenbrock, “QCD correction to the $p p \rightarrow W H$ and $Z H$ total cross-sections”, *Phys.Lett.* **B273** (1991) 167–172,
doi:10.1016/0370-2693(91)90572-8.

- [80] W. van Neerven and E. Zijlstra, “The $O(\alpha_S^2)$ corrected Drell-Yan K-factor in the DIS and $\overline{\text{MS}}$ schemes”, *Nuclear Physics B* **382** (1992), no. 1, 11 – 62, doi:[http://dx.doi.org/10.1016/0550-3213\(92\)90078-P](http://dx.doi.org/10.1016/0550-3213(92)90078-P).
- [81] O. Brein, R. Harlander, M. Wiesemann, and T. Zirke, “Top-quark mediated effects in hadronic Higgs-Strahlung”, *The European Physical Journal C* **72** (2012), no. 2, doi:[10.1140/epjc/s10052-012-1868-6](https://doi.org/10.1140/epjc/s10052-012-1868-6).
- [82] S. Dittmaier et al., “Handbook of LHC Higgs Cross Sections: 2. Differential Distributions”, doi:[10.5170/CERN-2012-002](https://doi.org/10.5170/CERN-2012-002), arXiv:[1201.3084](https://arxiv.org/abs/1201.3084).
- [83] M. Ciccolini, S. Dittmaier, and M. Kramer, “Electroweak radiative corrections to associated WH and ZH production at hadron colliders”, *Phys.Rev.* **D68** (2003) 073003, doi:[10.1103/PhysRevD.68.073003](https://doi.org/10.1103/PhysRevD.68.073003), arXiv:[hep-ph/0306234](https://arxiv.org/abs/hep-ph/0306234).
- [84] CMS Collaboration, “Physics Model”, 2015. (CMS internal content).
- [85] CMS Collaboration, “Precise determination of the mass of the Higgs boson and tests of compatibility of its couplings with the standard model predictions using proton collisions at 7 and 8 TeV”, arXiv:[1412.8662](https://arxiv.org/abs/1412.8662).
- [86] K. Arnold et al., “VBFNLO: A Parton level Monte Carlo for processes with electroweak bosons”, *Comput.Phys.Commun.* **180** (2009) 1661–1670, doi:[10.1016/j.cpc.2009.03.006](https://doi.org/10.1016/j.cpc.2009.03.006), arXiv:[0811.4559](https://arxiv.org/abs/0811.4559).
- [87] CMS Collaboration, “TWiki: Documentation of the RooStats-based statistics tools for Higgs PAG”, 2015. (CMS internal content).
- [88] M. Schmaltz and D. Tucker-Smith, “Little Higgs review”, *Ann.Rev.Nucl.Part.Sci.* **55** (2005) 229–270, doi:[10.1146/annurev.nucl.55.090704.151502](https://doi.org/10.1146/annurev.nucl.55.090704.151502), arXiv:[hep-ph/0502182](https://arxiv.org/abs/hep-ph/0502182).

- [89] M. Schmaltz, “Physics beyond the standard model (theory): Introducing the little Higgs”, *Nucl. Phys. Proc. Suppl.* **117** (2003) 40–49, [arXiv:hep-ph/0210415](#).
- [90] A. D. Simone, O. Matsedonskyi, R. Rattazzi, and A. Wulzer, “A First Top Partnew Hunter’s Guide”, *JHEP* **1304** (2013).
- [91] ATLAS Collaboration, “Analysis of events with b-jets and a pair of leptons of the same charge in pp collisions at $\sqrt{s} = 8\text{TeV}$ with the ATLAS detector”, *JHEP* **1510** (2015) 1–36, [doi:10.1007/JHEP10\(2015\)150](#), [arXiv:1504.04605](#).
- [92] CMS Collaboration, “Search for top-quark partners with charge 5/3 in the same-sign dilepton final state”, *Phys.Rev.Lett.* **112** (2014), no. 17, 171801, [doi:10.1103/PhysRevLett.112.171801](#), [arXiv:1312.2391](#).
- [93] J. Alwall et al., “MadGraph 5: going beyond”, *Journal of High Energy Physics* **2011** (2011) 1–40, [doi:10.1007/JHEP06\(2011\)128](#).
- [94] J. Alwall et al., “The automated computation of tree-level and next-to-leading order differential cross sections, and their matching to parton shower simulations”, *JHEP* **07** (2014) 079, [doi:10.1007/JHEP07\(2014\)079](#), [arXiv:1405.0301](#).
- [95] T. Sjöstrand, S. Mrenna, and P. Skands, “A Brief Introduction to PYTHIA 8.1”, *Comput. Phys. Comm.* **178** (2008).
- [96] CMS Collaboration, “Single-top t-channel: Run II working meeting”, 2015. (CMS internal content).
- [97] CMS Collaboration, “TWiki: Summary table of samples produced for the 1 Billion campaign, with 25ns bunch-crossing”, 2015. (CMS internal content).

- [98] CMS Collaboration, “TWiki: Standard Model Cross Sections for CMS at 13 TeV”, 2015. (CMS internal content).
- [99] CMS Collaboration, “TWiki: Single Top Cross Sections”, 2015. (CMS internal content).
- [100] P. Artoisenet, R. Frederix, O. Mattelaer, and R. Rietkerk, “Automatic spin-entangled decays of heavy resonances in Monte Carlo simulations”, *JHEP* **03** (2013) 015, doi:10.1007/JHEP03(2013)015, arXiv:1212.3460.
- [101] A. Avetisyan et al., “Search for top quark partners with charge $5e/3$ in the same-sign dilepton final state with CMS detector”, (2015). (CMS internal content).
- [102] O. Matsedonskyi, G. Panico, and A. Wulzer, “On the Interpretation of Top Partners Searches”, *JHEP* **1412** (2014) 097, doi:10.1007/JHEP12(2014)097, arXiv:1409.0100.
- [103] CMS Collaboration, “TWiki: Workbook MiniAOD”, 2015. (CMS internal content).
- [104] CMS Collaboration, “TWiki: LJMet for Run 2”, 2015. (CMS internal content).
- [105] D. Abercrombie et al., “Search for Dark Matter produced in association with top quark pairs”, (2015). (CMS internal content).
- [106] CMS Collaboration, “Search for pair production of vector-like T quarks in the lepton plus jets final state”, *CMS Physics Analysis Summary* **CMS-PAS-B2G-16-002** (2016).
- [107] CMS Collaboration, “Search for a W' boson decaying to a bottom quark and a top quark in pp collisions at $\sqrt{s} = 7$ TeV”, *Phys. Lett.* **B718** (2013) 1229–1251, doi:10.1016/j.physletb.2012.12.008, arXiv:1208.0956.

- [108] T. Müller, J. Ott, and J. Wagner-Kuhr, “theta - a framework for template-based modeling and inference”,. http://www-ekp.physik.uni-karlsruhe.de/~ott/theta/testing/html/theta__auto__intro.html.
- [109] CMS Collaboration, “Measurement of the differential cross section for top quark pair production in pp collisions at $\sqrt{s} = 8 \text{ TeV}$ ”, *Eur. Phys. J.* **C75** (2015), no. 11, 542, doi:10.1140/epjc/s10052-015-3709-x, arXiv:1505.04480.

Appendix A

Chapter 6 Appendix

A.1 Control Region Plots

The BDT discriminant and m (VH) distributions for signal, background, and data in the various control regions of the WH channel are shown in Figs. A.1.1, A.1.2, A.1.5, A.1.6, A.1.9, and A.1.10. Similarly, the distributions for the ZH channel are shown in Figs. A.1.3, A.1.4, A.1.7, A.1.8, A.1.11, and A.1.12.

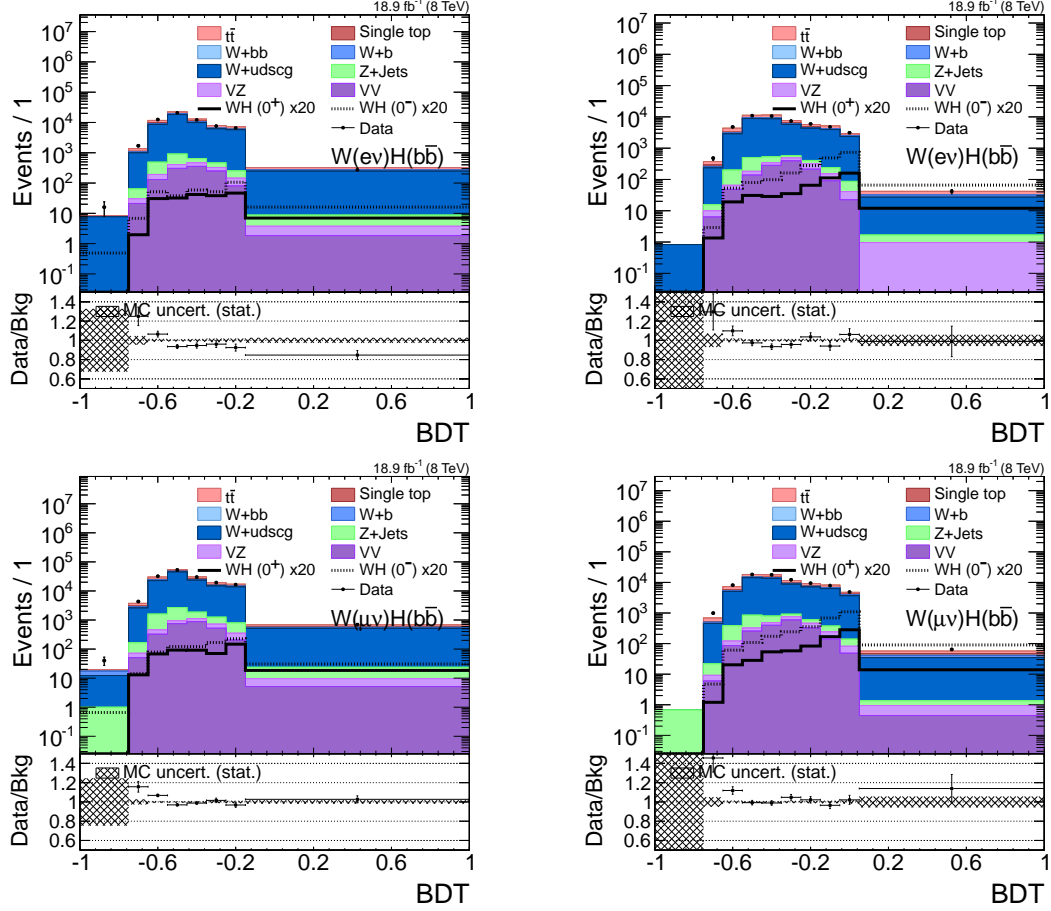


Figure A.1.1: The distribution of the BDT discriminant in the W+LF control region for the 0^+ and 0^- signals, expected background, and data. The top (bottom) row shows the electron (muon) channel. The left (right) column shows the medium (high) boost region. The binning choice is from the 2D templates in the corresponding signal regions.

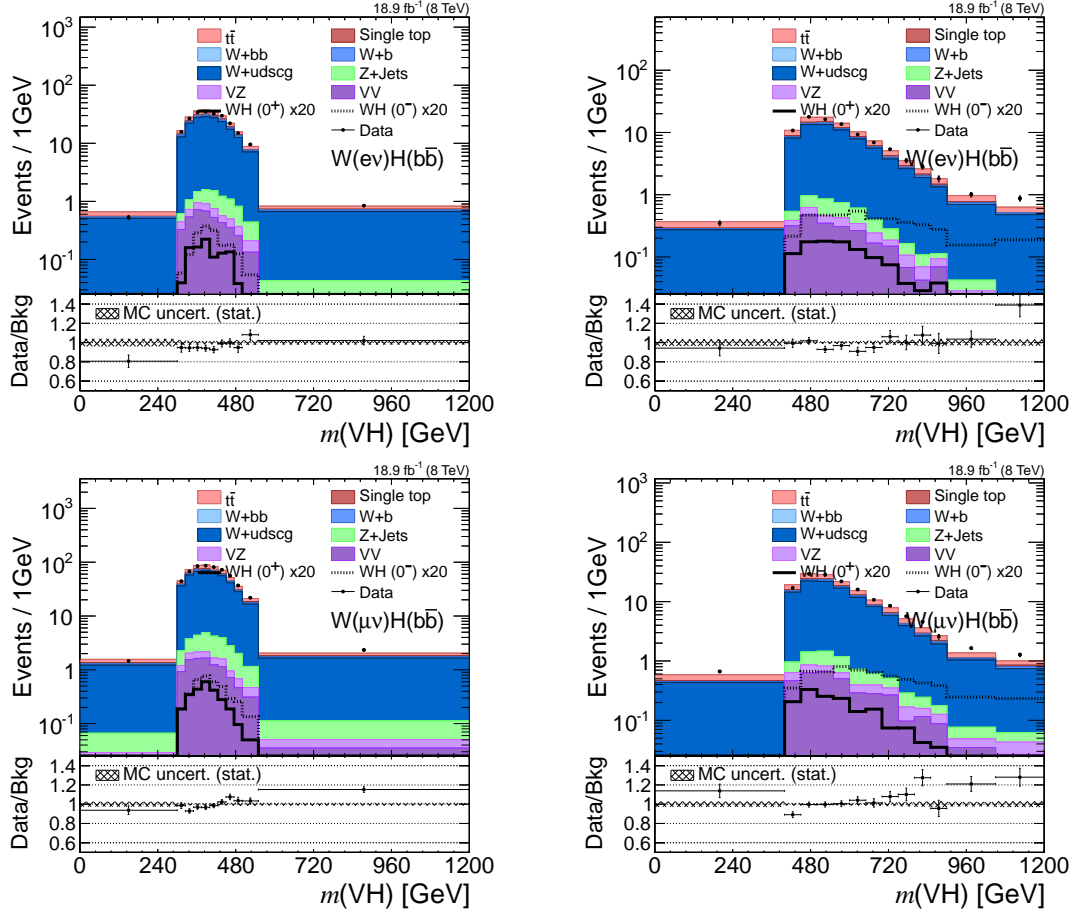


Figure A.1.2: The $m(VH)$ distribution in the $W+LF$ control region for the 0^+ and 0^- signals, expected background, and data. The top (bottom) row shows the electron (muon) channel. The left (right) column shows the medium (high) boost region. The binning choice is from the 2D templates in the corresponding signal regions.

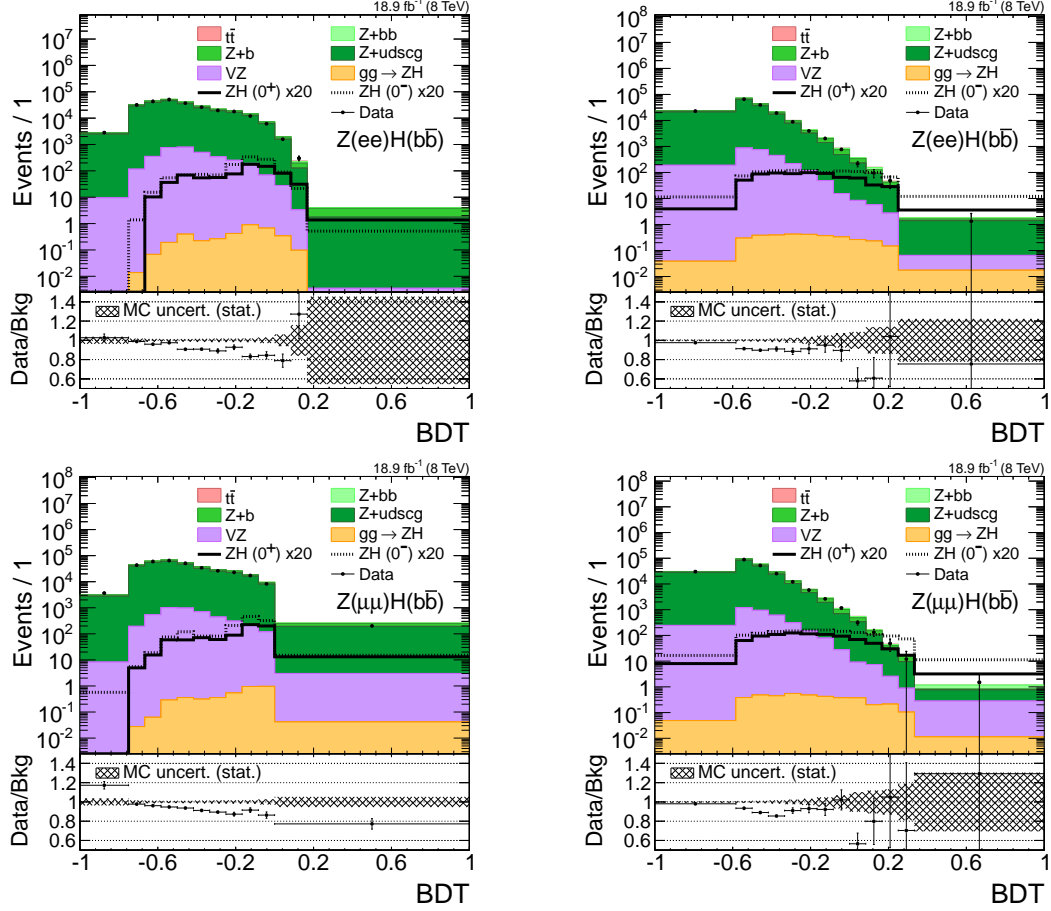


Figure A.1.3: The distribution of the BDT discriminant in the Z+LF control region for the 0^+ and 0^- signals, expected background, and data. The top (bottom) row shows the electron (muon) channel. The left (right) column shows the medium (high) boost region. The binning choice is from the 2D templates in the corresponding signal regions.

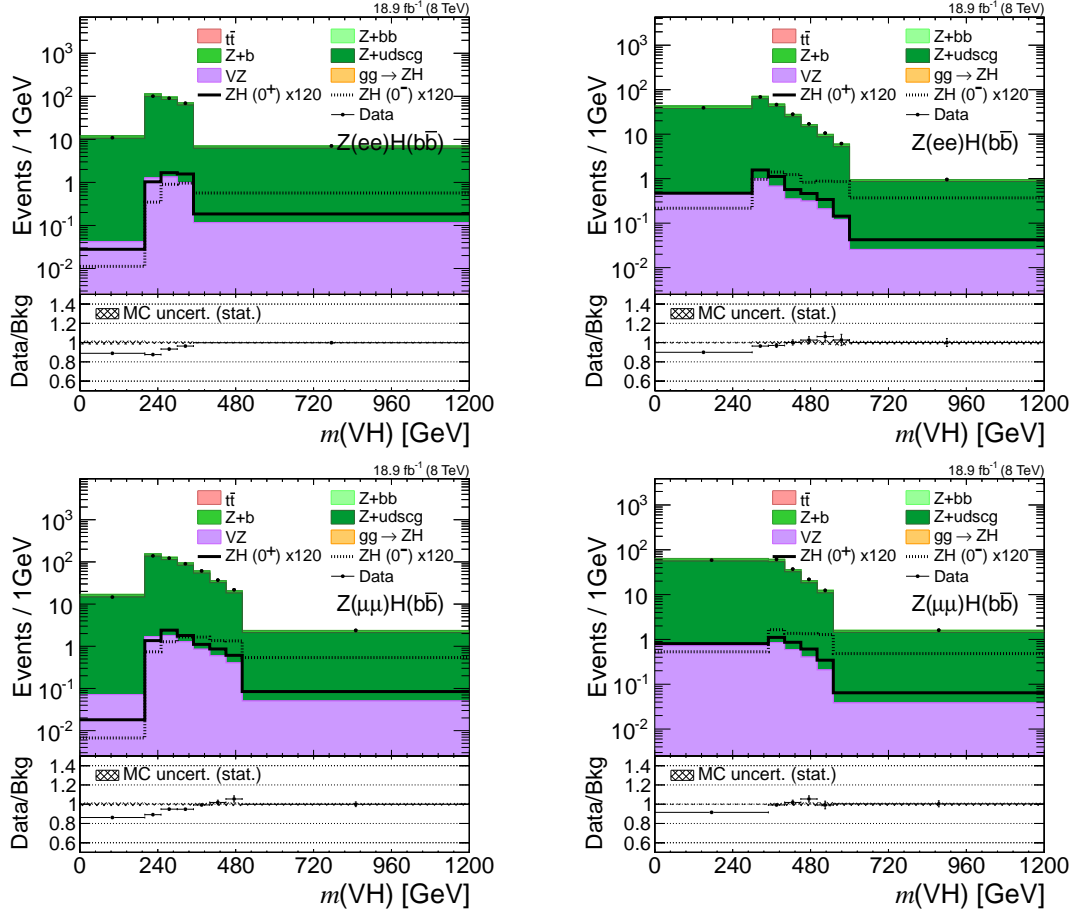


Figure A.1.4: The $m(VH)$ distribution in the Z+LF control region for the 0^+ and 0^- signals, expected background, and data. The top (bottom) row shows the electron (muon) channel. The left (right) column shows the medium (high) boost region. The binning choice is from the 2D templates in the corresponding signal regions.

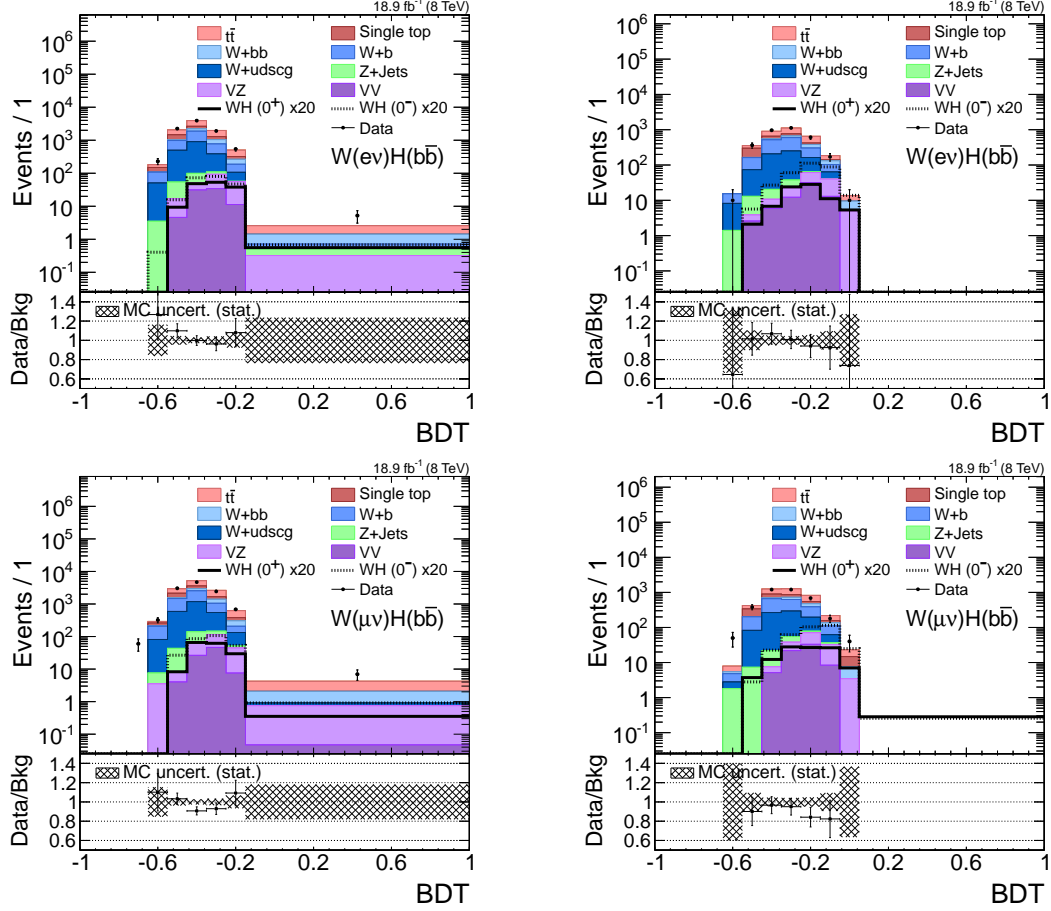


Figure A.1.5: The distribution of the BDT discriminant in the W+HF control region for the 0^+ and 0^- signals, expected background, and data. The top (bottom) row shows the electron (muon) channel. The left (right) column shows the medium (high) boost region. The binning choice is from the 2D templates in the corresponding signal regions.

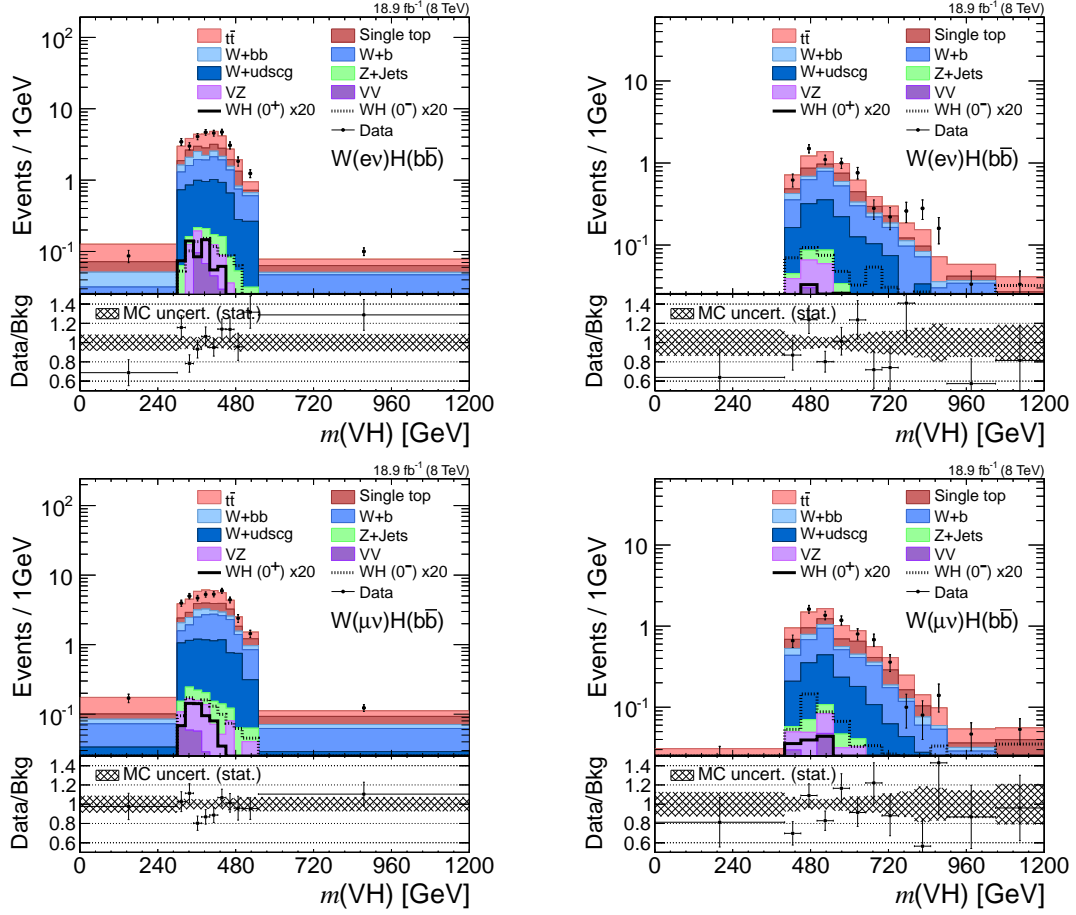


Figure A.1.6: The $m(VH)$ distribution in the $W+HF$ control region for the 0^+ and 0^- signals, expected background, and data. The top (bottom) row shows the electron (muon) channel. The left (right) column shows the medium (high) boost region. The binning choice is from the 2D templates in the corresponding signal regions.

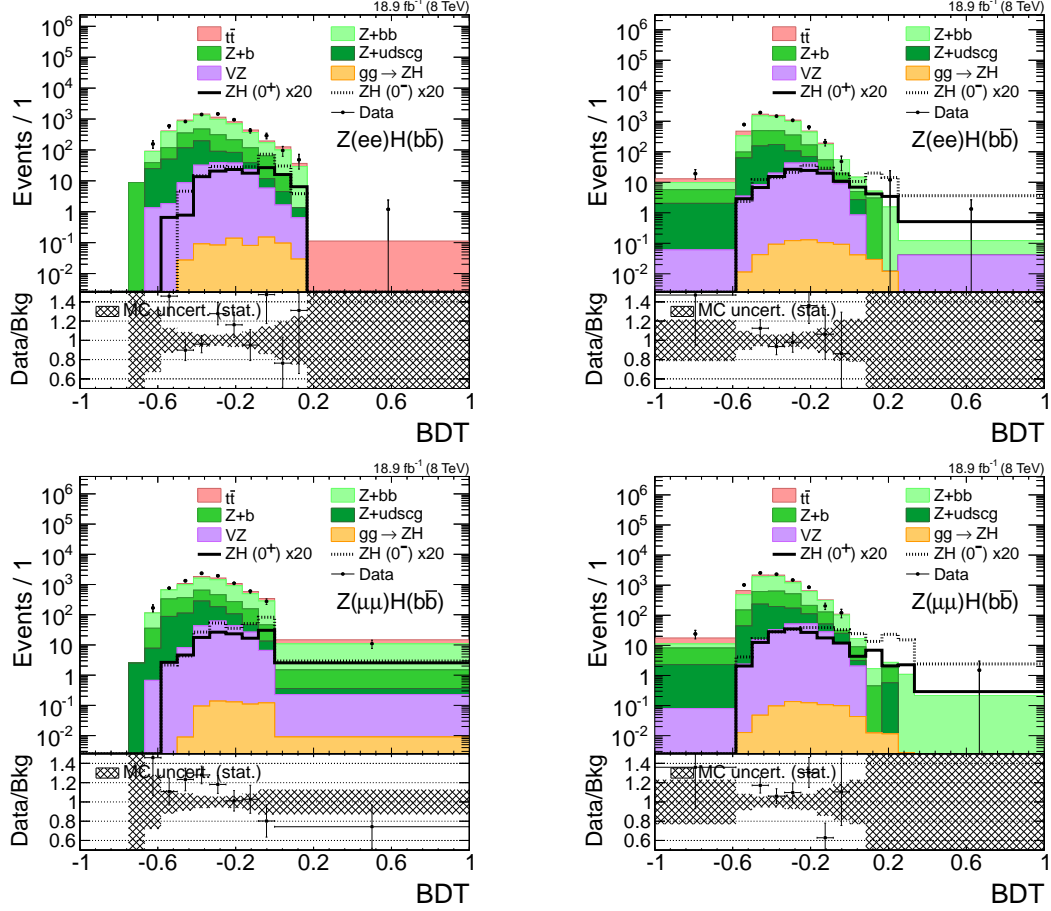


Figure A.1.7: The distribution of the BDT discriminant in the Z+HF control region for the 0^+ and 0^- signals, expected background, and data. The top (bottom) row shows the electron (muon) channel. The left (right) column shows the medium (high) boost region. The binning choice is from the 2D templates in the corresponding signal regions.

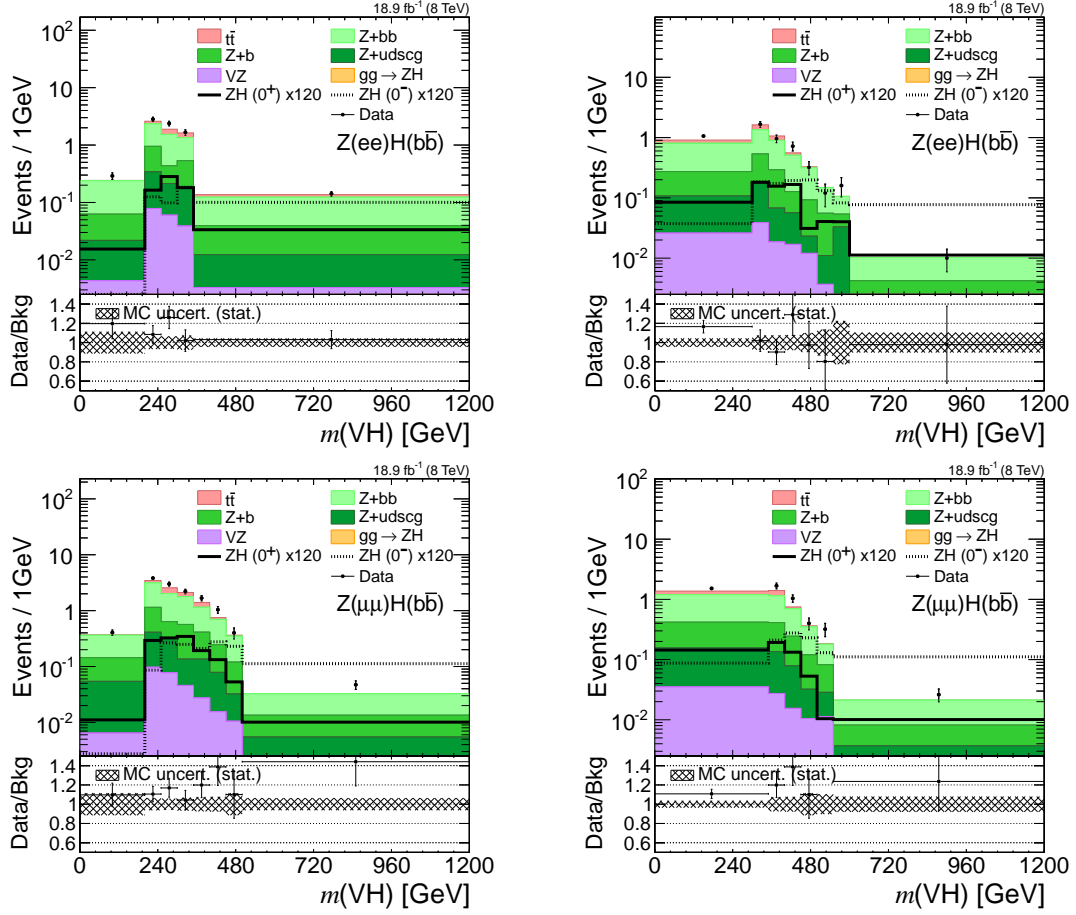


Figure A.1.8: The $m(VH)$ distribution in the Z+HF control region for the 0^+ and 0^- signals, expected background, and data. The top (bottom) row shows the electron (muon) channel. The left (right) column shows the medium (high) boost region. The binning choice is from the 2D templates in the corresponding signal regions.

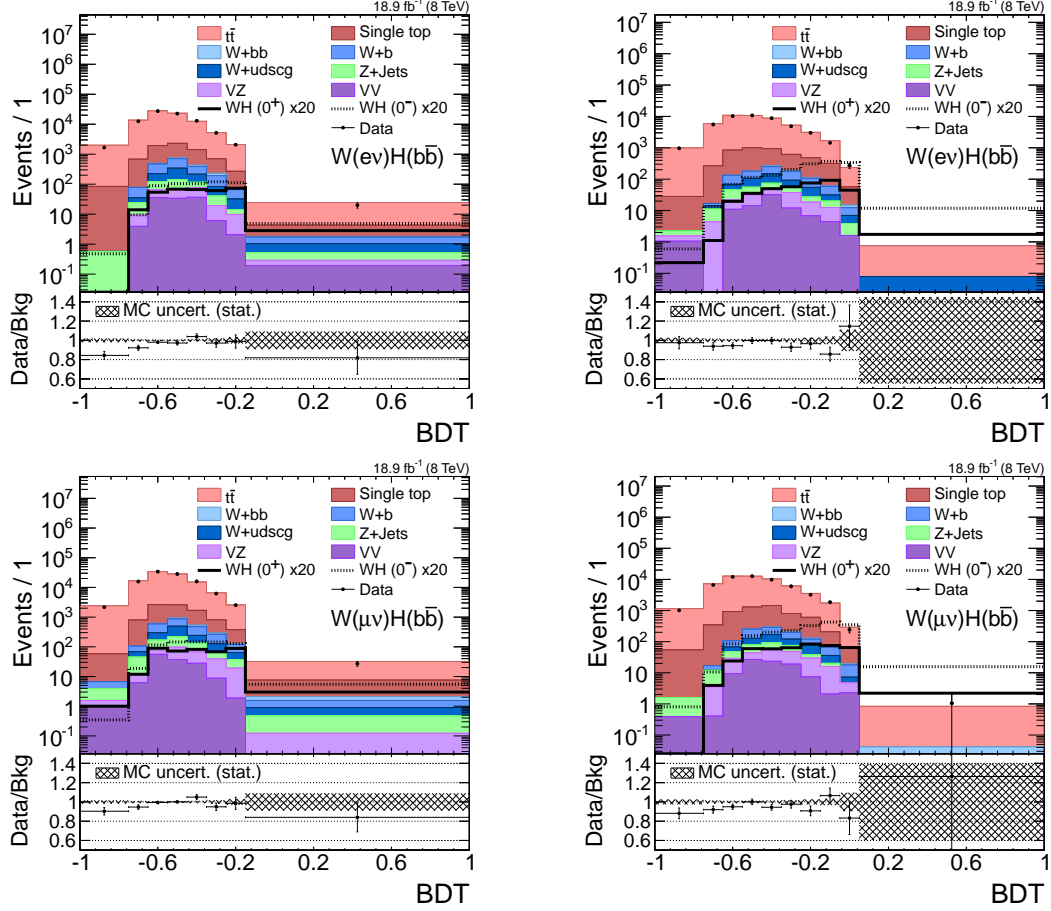


Figure A.1.9: The distribution of the BDT discriminant in the $t\bar{t}$ control region of the WH channel for the 0^+ and 0^- signals, expected background, and data. The top (bottom) row shows the electron (muon) channel. The left (right) column shows the medium (high) boost region. The binning choice is from the 2D templates in the corresponding signal regions.

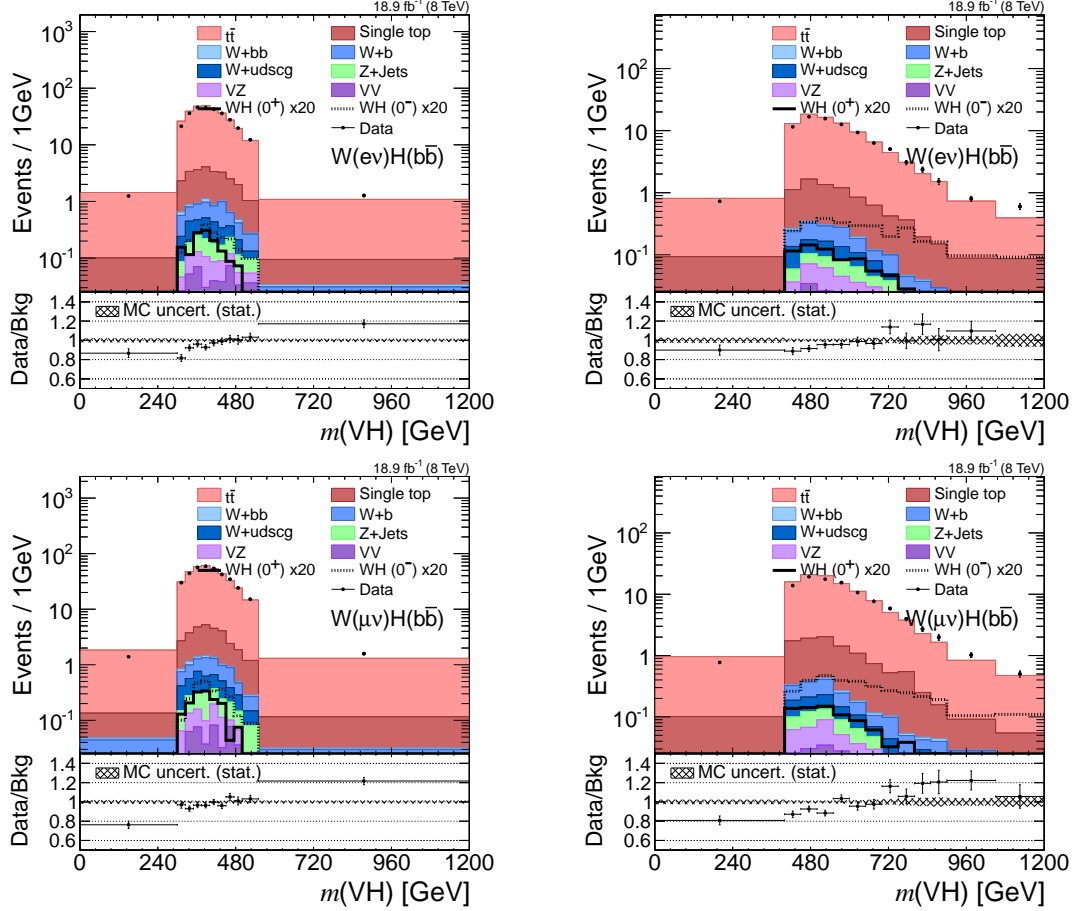


Figure A.1.10: The $m(VH)$ distribution in the $t\bar{t}$ control region of the WH channel for the 0^+ and 0^- signals, expected background, and data. The top (bottom) row shows the electron (muon) channel. The left (right) column shows the medium (high) boost region. The binning choice is from the 2D templates in the corresponding signal regions.

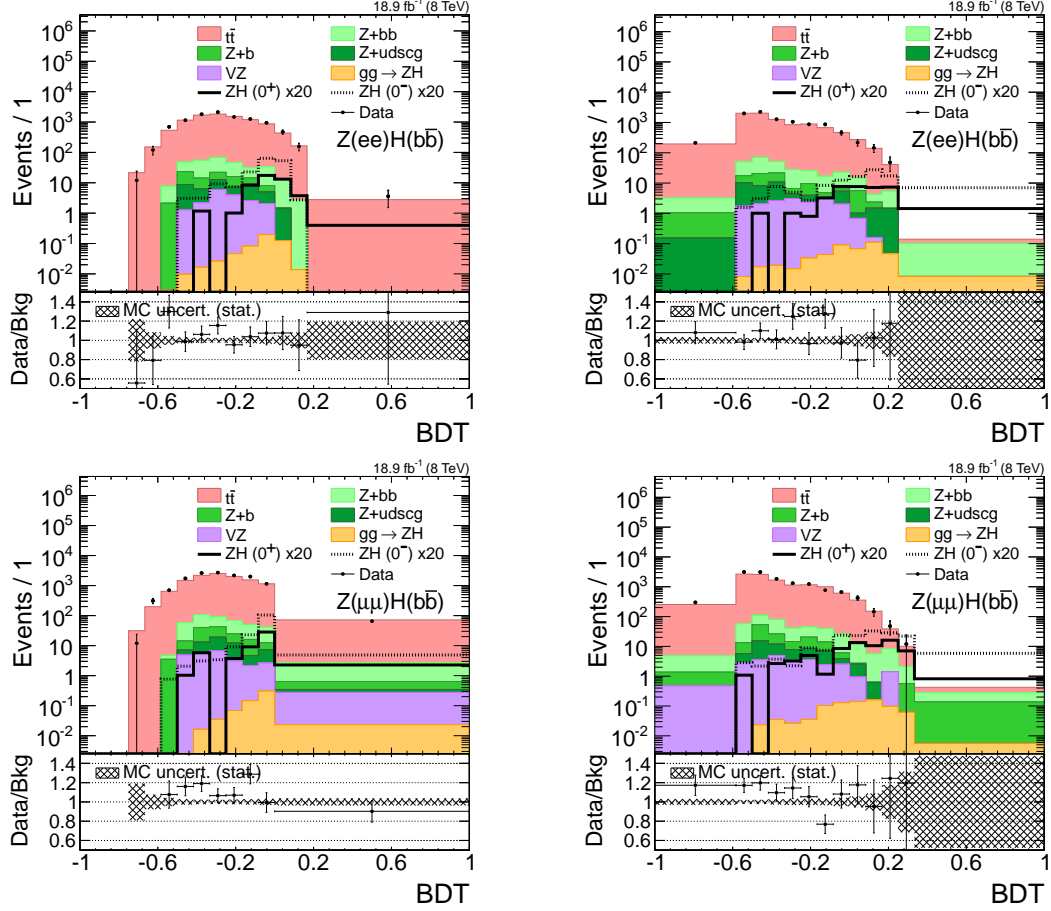


Figure A.1.11: The distribution of the BDT discriminant in the $t\bar{t}$ control region of the ZH channel for the 0^+ and 0^- signals, expected background, and data. The top (bottom) row shows the electron (muon) channel. The left (right) column shows the medium (high) boost region. The binning choice is from the 2D templates in the corresponding signal regions.

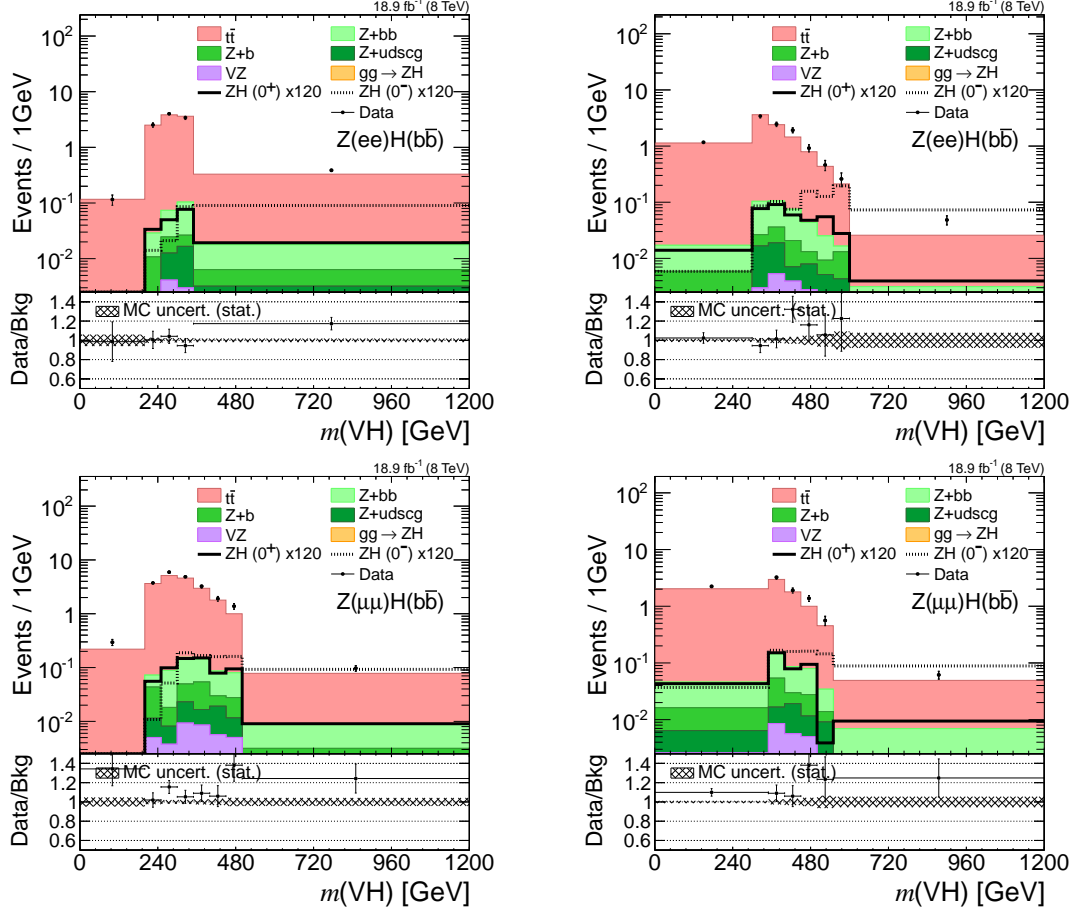


Figure A.1.12: The $m(\text{VH})$ distribution in the $t\bar{t}$ control region of the ZH channel for the 0^+ and 0^- signals, expected background, and data. The top (bottom) row shows the electron (muon) channel. The left (right) column shows the medium (high) boost region. The binning choice is from the 2D templates in the corresponding signal regions.

A.2 Signal Region Plots

The 2D templates for signal, background, and data in the signal regions are shown in Figs. A.2.1, A.2.2, A.2.3, A.2.4, A.2.5, A.2.6, A.2.7, and A.2.8. The corresponding 1D distributions for each component of the 2D templates (i.e., $m(\text{VH})$ and BDT) are shown in Figs. A.2.9, A.2.10, A.2.11, and A.2.12. The 2D templates are unrolled into 1D distributions and are shown in Figs. A.2.13 and A.2.14.

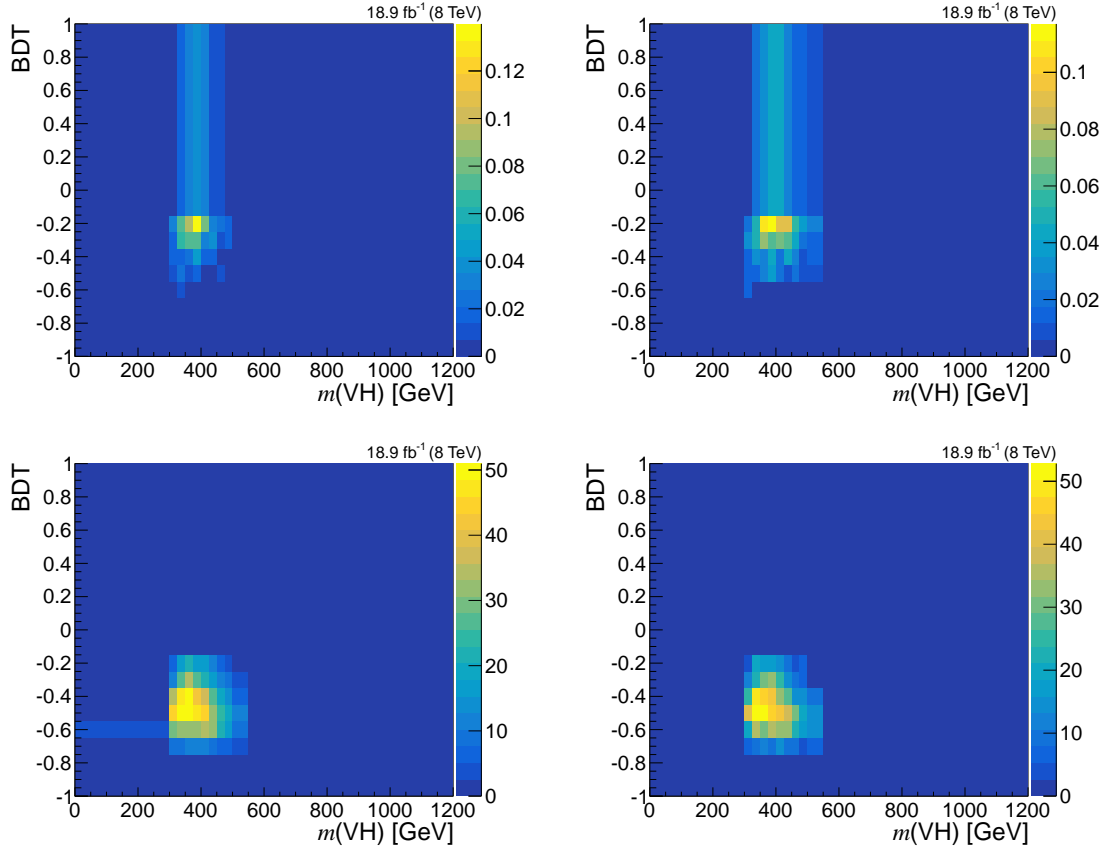


Figure A.2.1: The 2D templates used for profile likelihood scans in the $W \rightarrow e\nu$ channel, medium boost region. From upper left to lower right: 0^+ signal, 0^- signal, total background, and data.

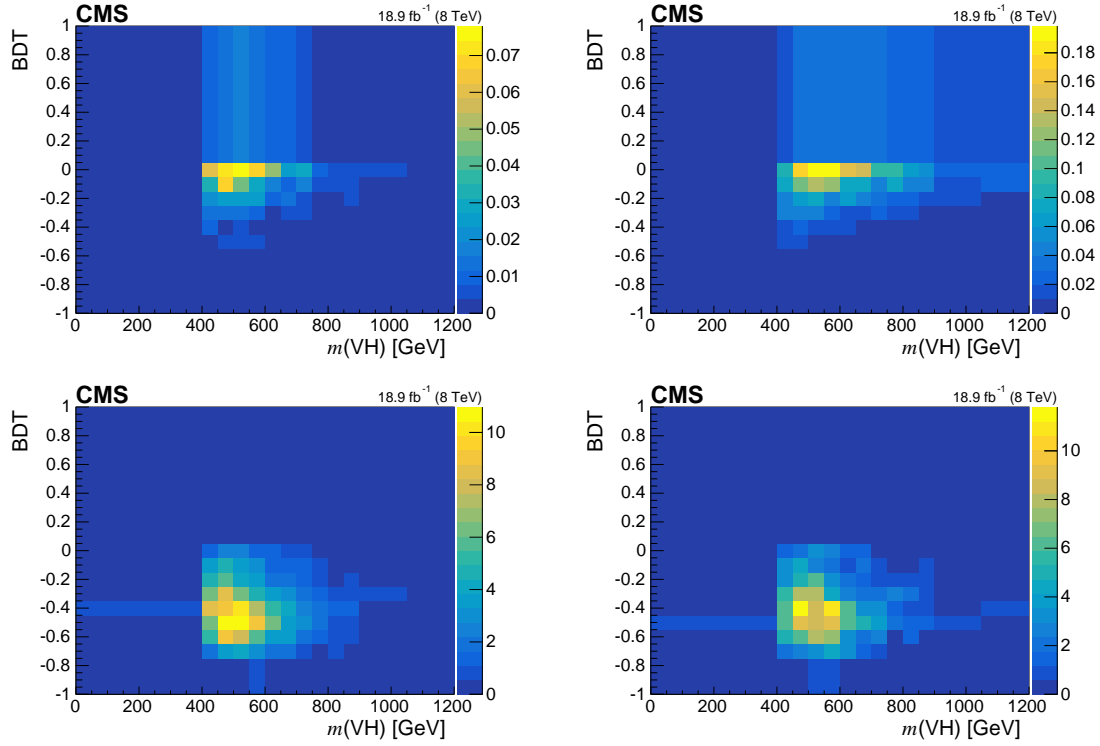


Figure A.2.2: The 2D templates used for profile likelihood scans in the $W \rightarrow e\nu$ channel, high boost region. From upper left to lower right: 0^+ signal, 0^- signal, total background, and data.

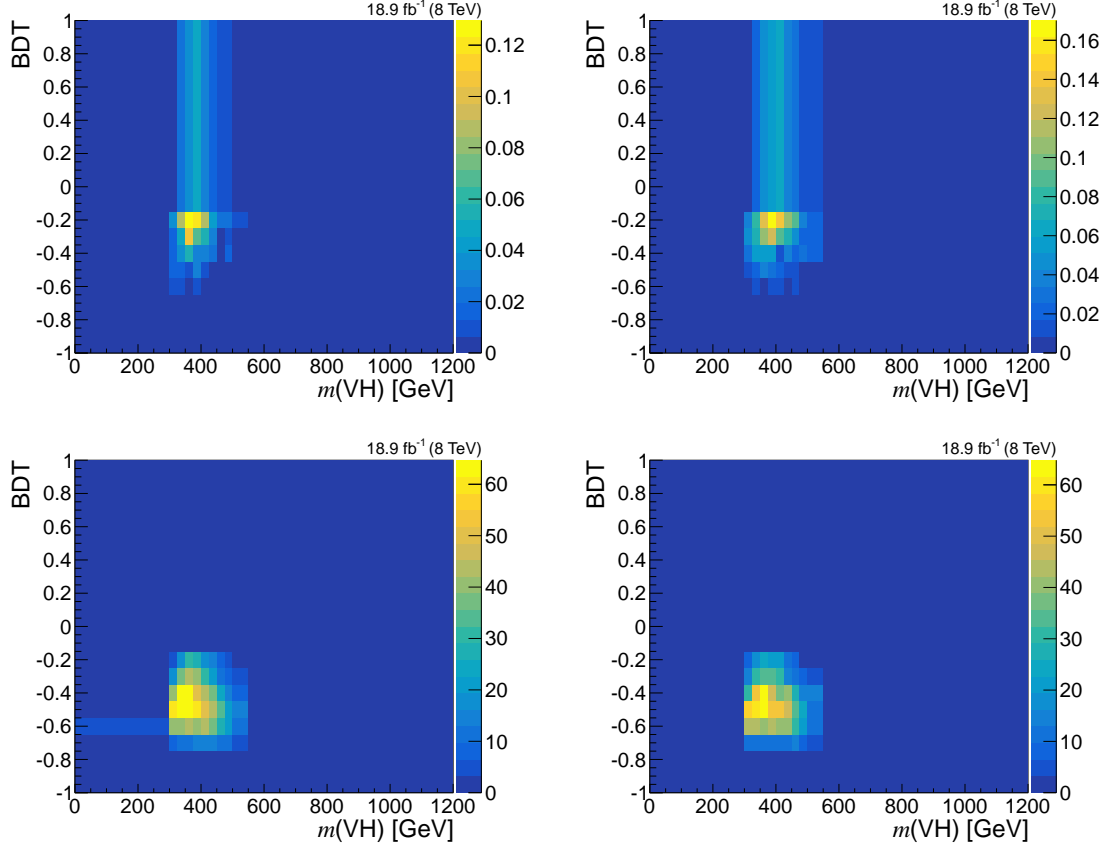


Figure A.2.3: The 2D templates used for profile likelihood scans in the $W \rightarrow \mu\nu$ channel, medium boost region. From upper left to lower right: 0^+ signal, 0^- signal, total background, and data.

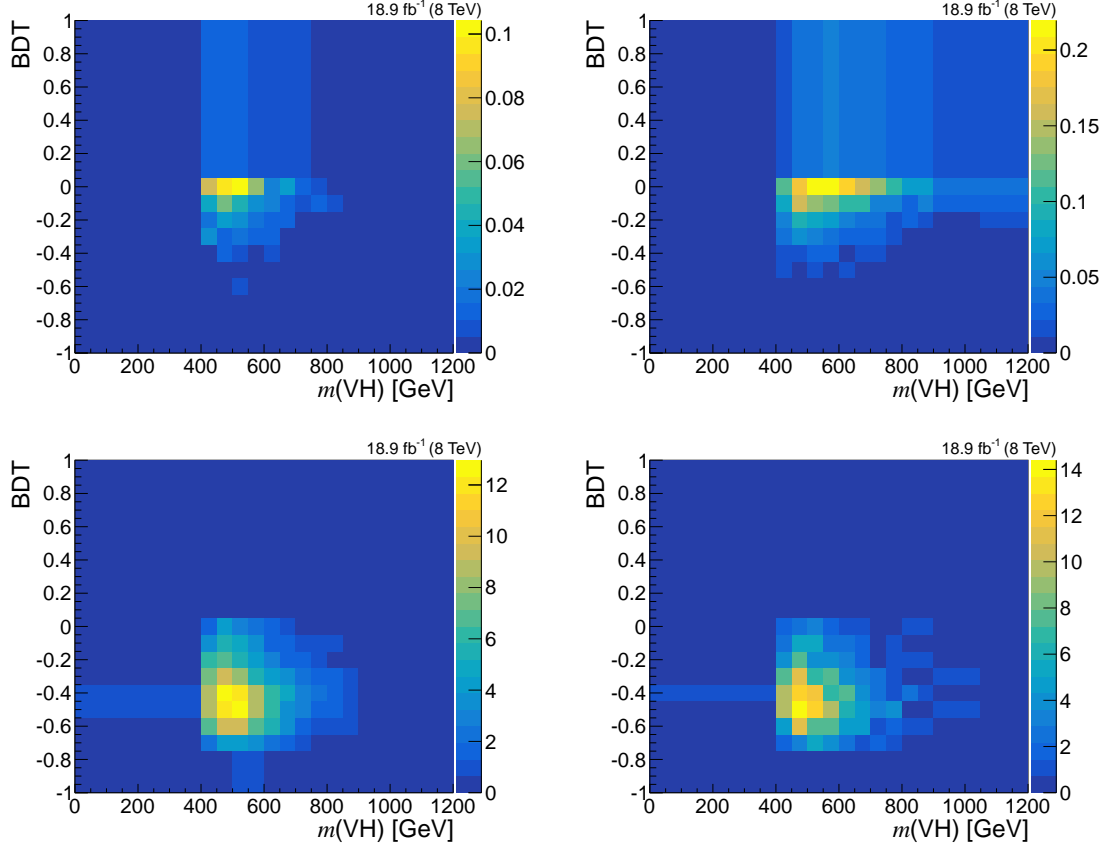


Figure A.2.4: The 2D templates used for profile likelihood scans in the $W \rightarrow \mu\nu$ channel, high boost region. From upper left to lower right: 0^+ signal, 0^- signal, total background, and data.

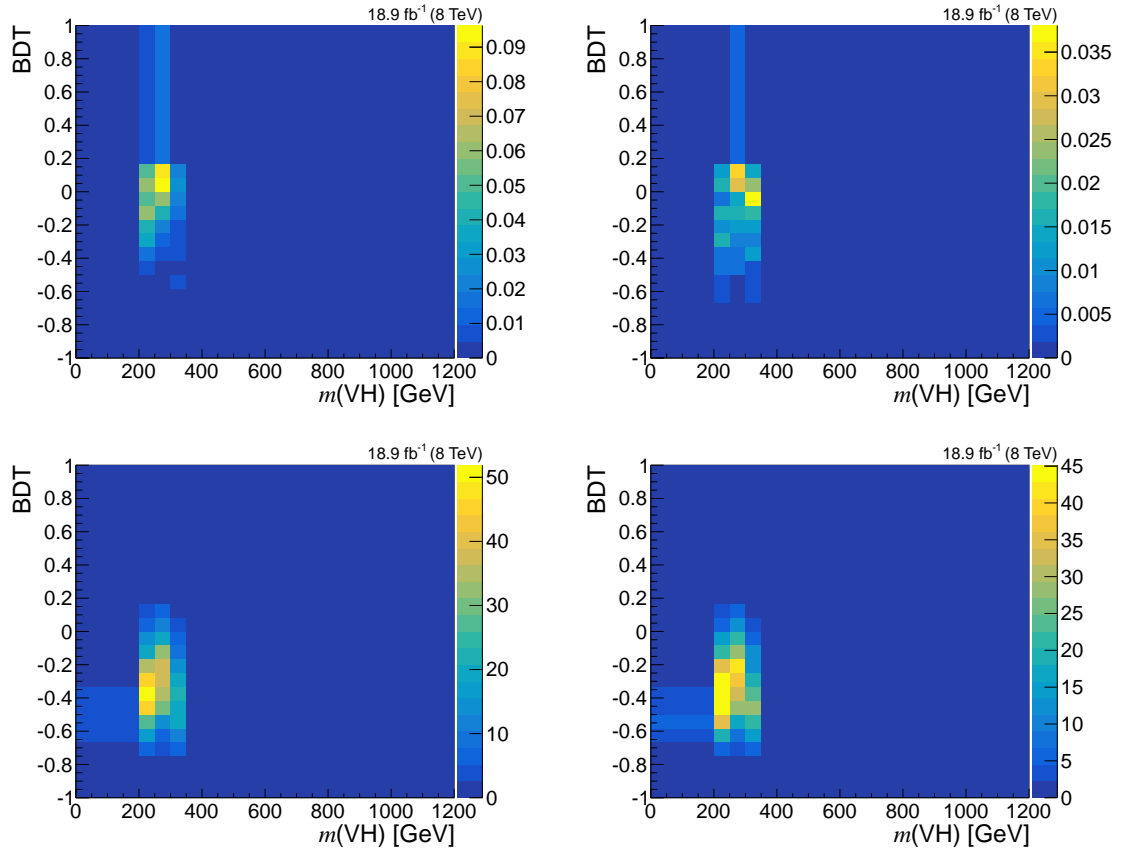


Figure A.2.5: The 2D templates used for profile likelihood scans in the $Z \rightarrow ee$ channel, medium boost region. From upper left to lower right: 0^+ signal, 0^- signal, total background, and data.

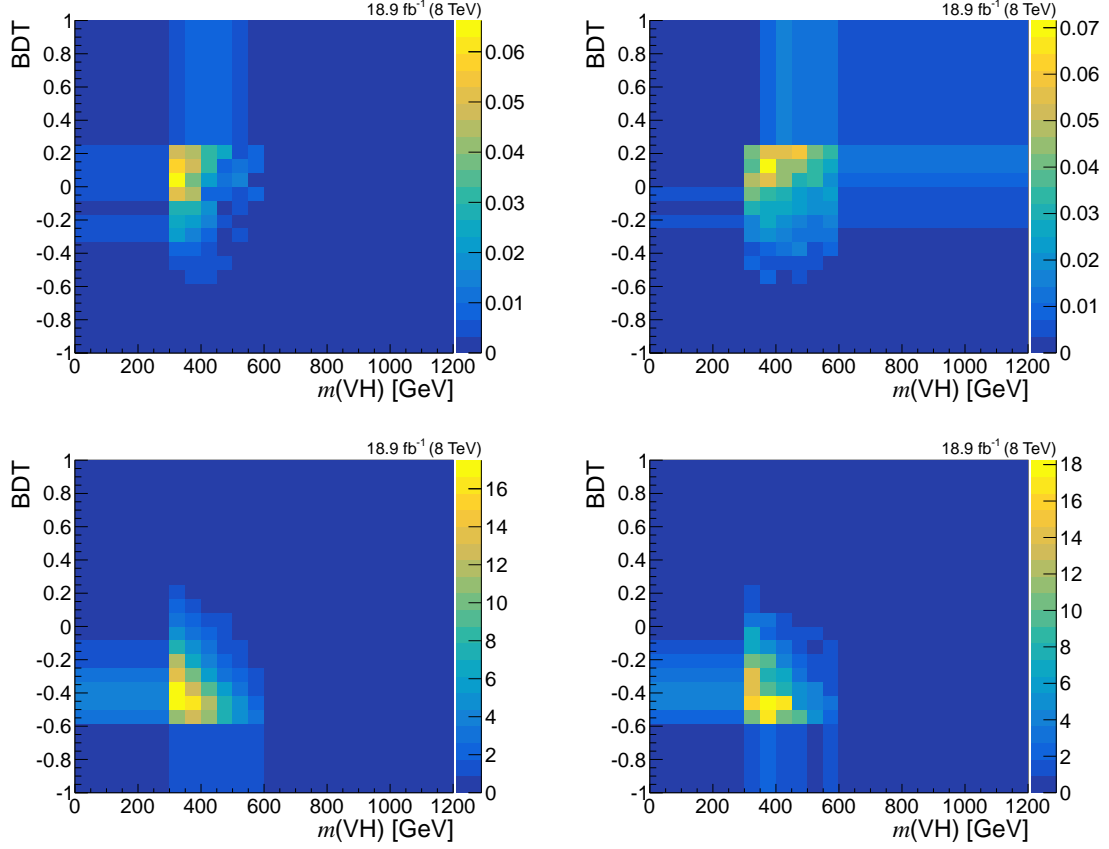


Figure A.2.6: The 2D templates used for profile likelihood scans in the $Z \rightarrow ee$ channel, high boost region. From upper left to lower right: 0^+ signal, 0^- signal, total background, and data.

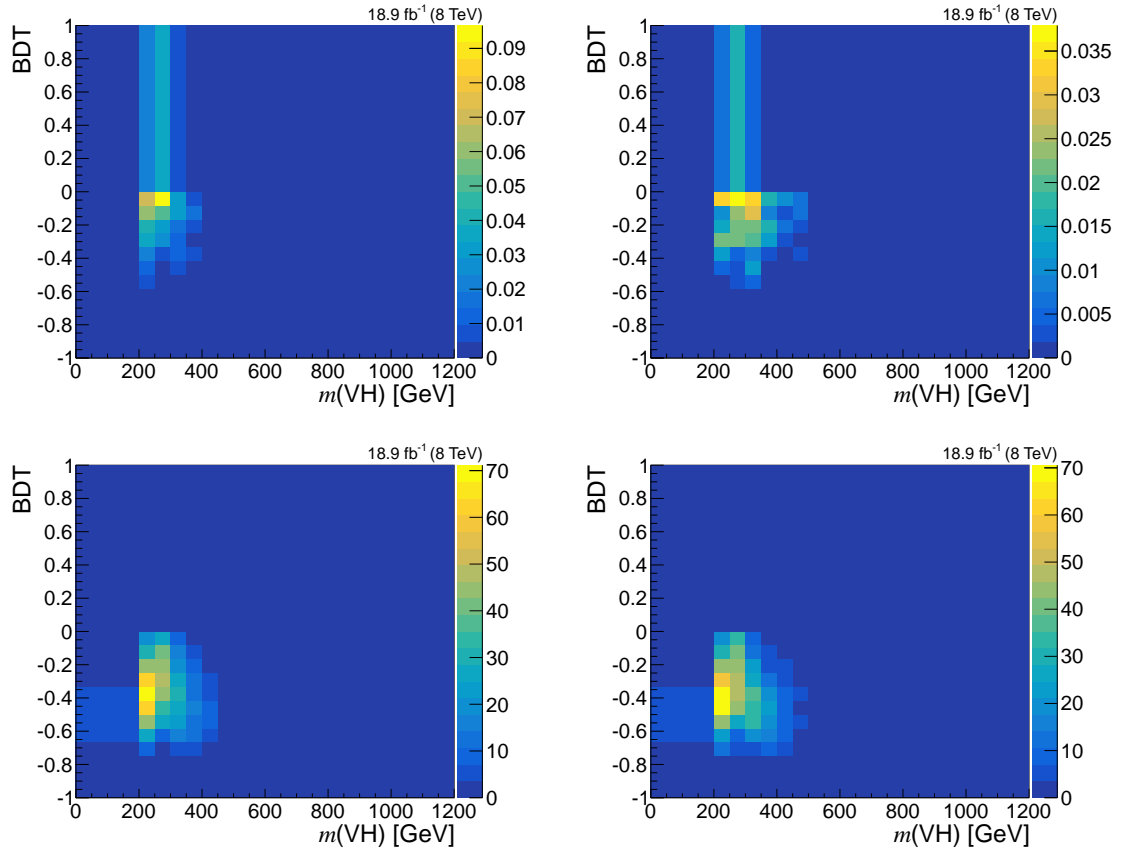


Figure A.2.7: The 2D templates used for profile likelihood scans in the $Z \rightarrow \mu\mu$ channel, medium boost region. From upper left to lower right: 0^+ signal, 0^- signal, total background, and data.

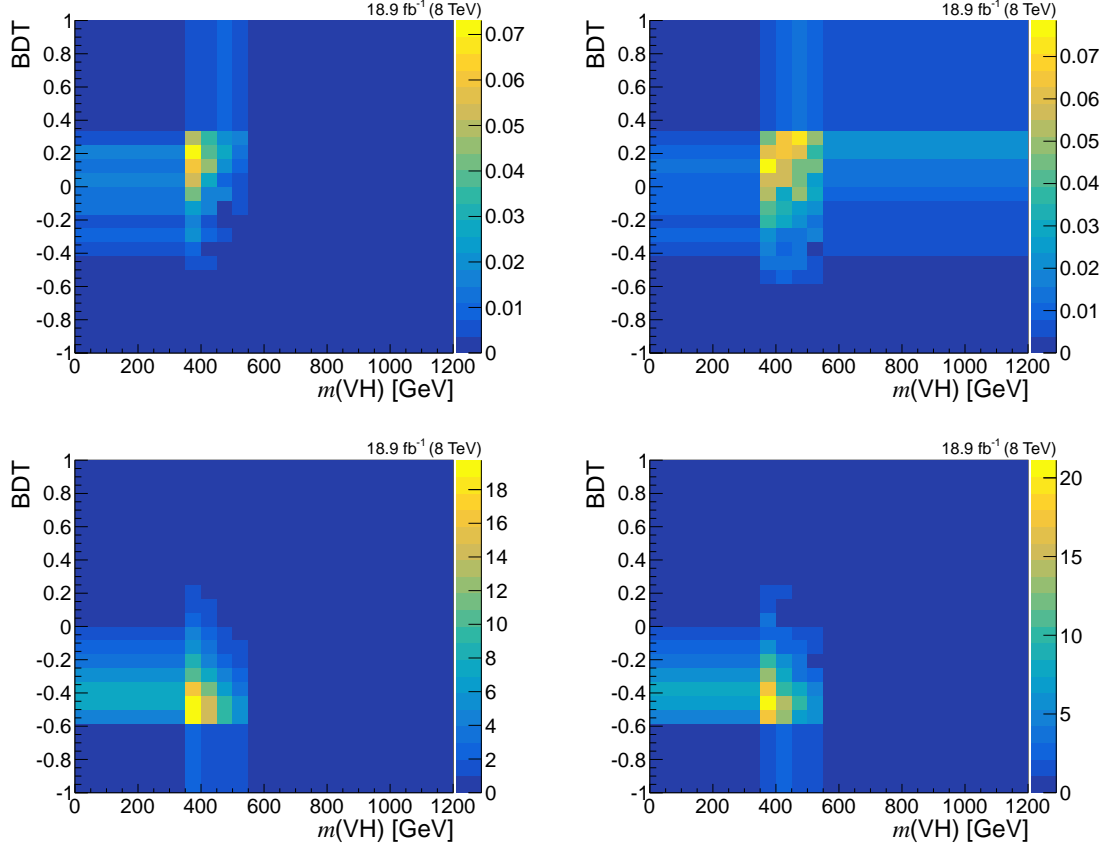


Figure A.2.8: The 2D templates used for profile likelihood scans in the $Z \rightarrow \mu\mu$ channel, high boost region. From upper left to lower right: 0^+ signal, 0^- signal, total background, and data.

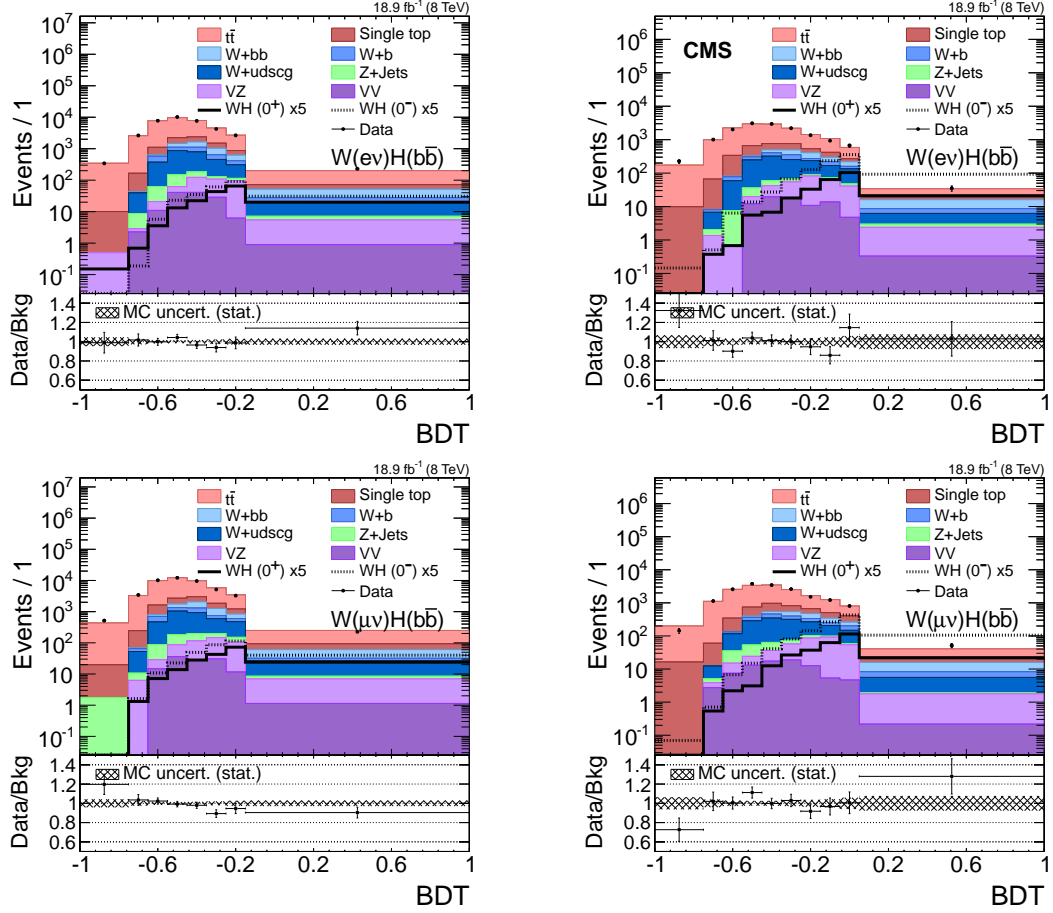


Figure A.2.9: The distribution of the BDT discriminant in selected events in the WH channel for the 0^+ and 0^- signals compared to background, normalized to 18.9 fb^{-1} . The top (bottom) row shows the electron (muon) channel. The left (right) column shows the medium (high) boost region.

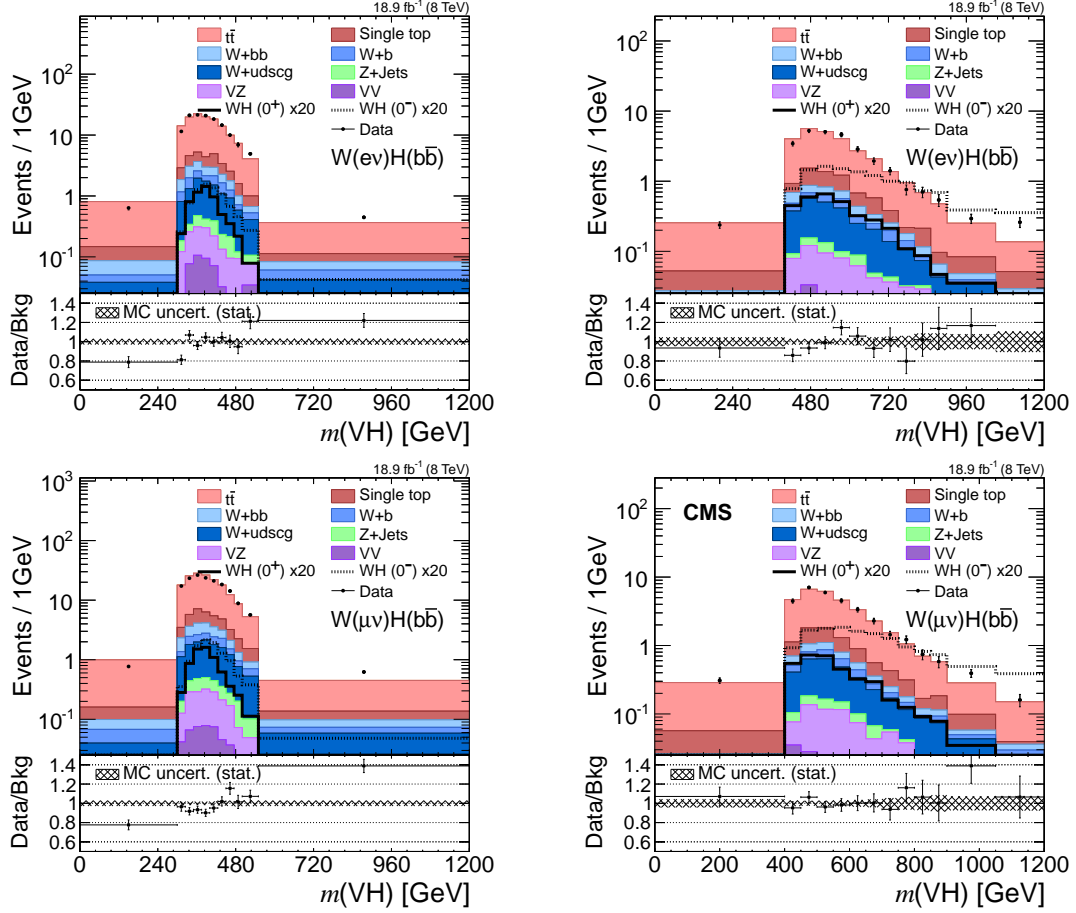


Figure A.2.10: The $m(VH)$ distribution in selected events in the WH channel for the 0^+ and 0^- signals compared to background, normalized to $18.9 fb^{-1}$. The top (bottom) row shows the electron (muon) channel. The left (right) column shows the medium (high) boost region.

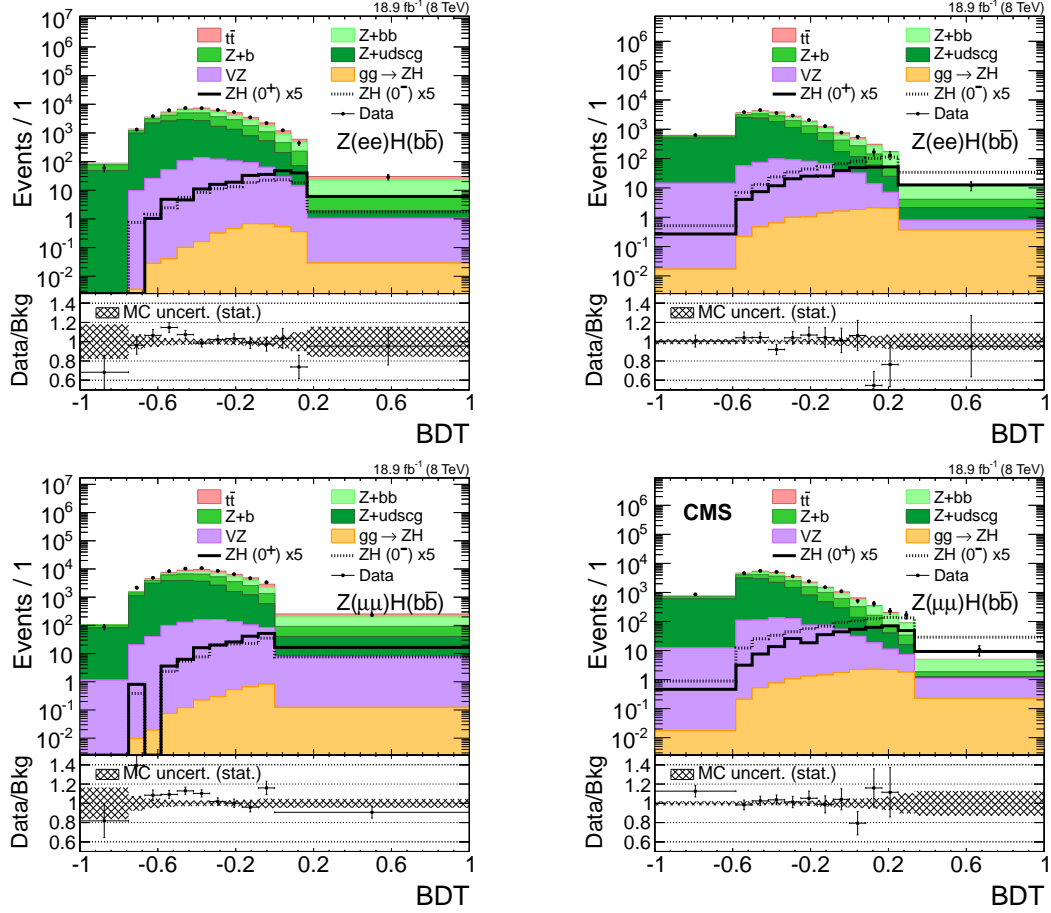


Figure A.2.11: The distribution of the BDT discriminant in selected events in the ZH channel for the 0^+ and 0^- signals compared to background, normalized to $18.9fb^{-1}$. The top (bottom) row shows the electron (muon) channel. The left (right) column shows the medium (high) boost region.

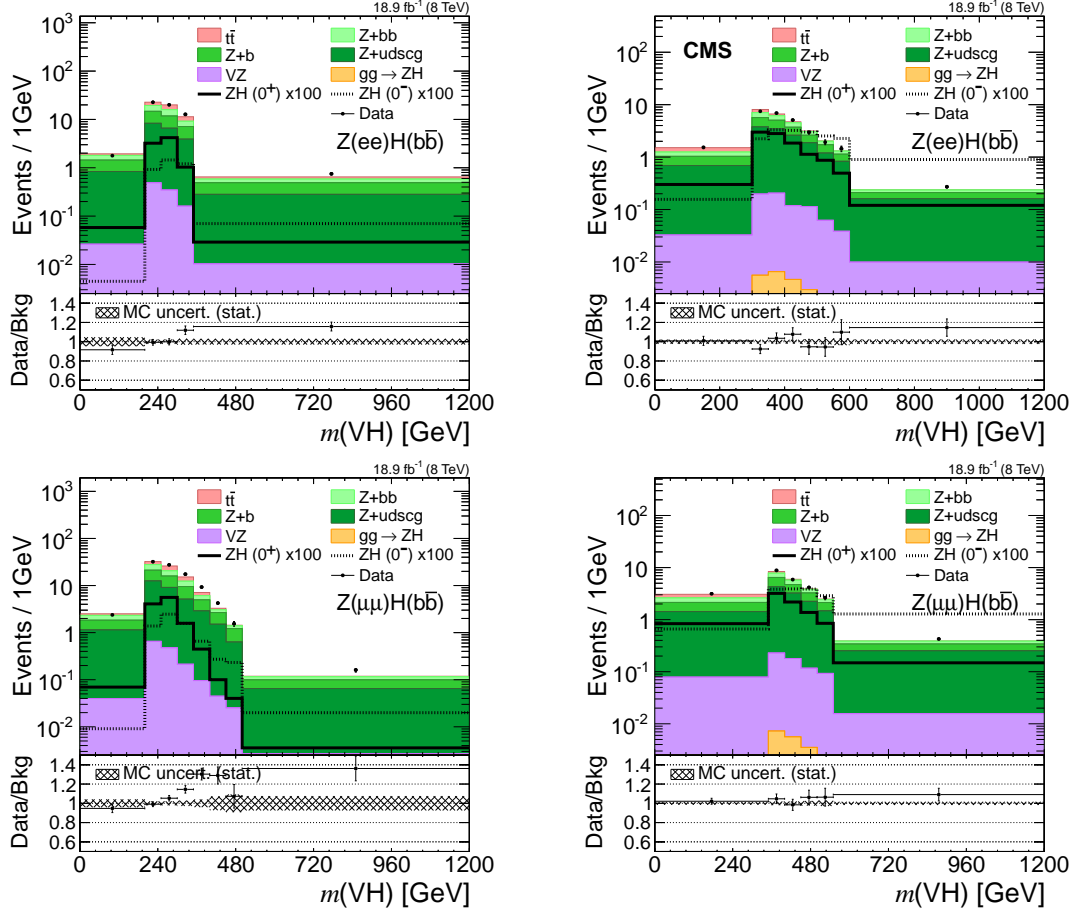


Figure A.2.12: The $m(VH)$ distribution in selected events in the ZH channel for the 0^+ and 0^- signals compared to background, normalized to $18.9 fb^{-1}$. The top (bottom) row shows the electron (muon) channel. The left (right) column shows the medium (high) boost region.

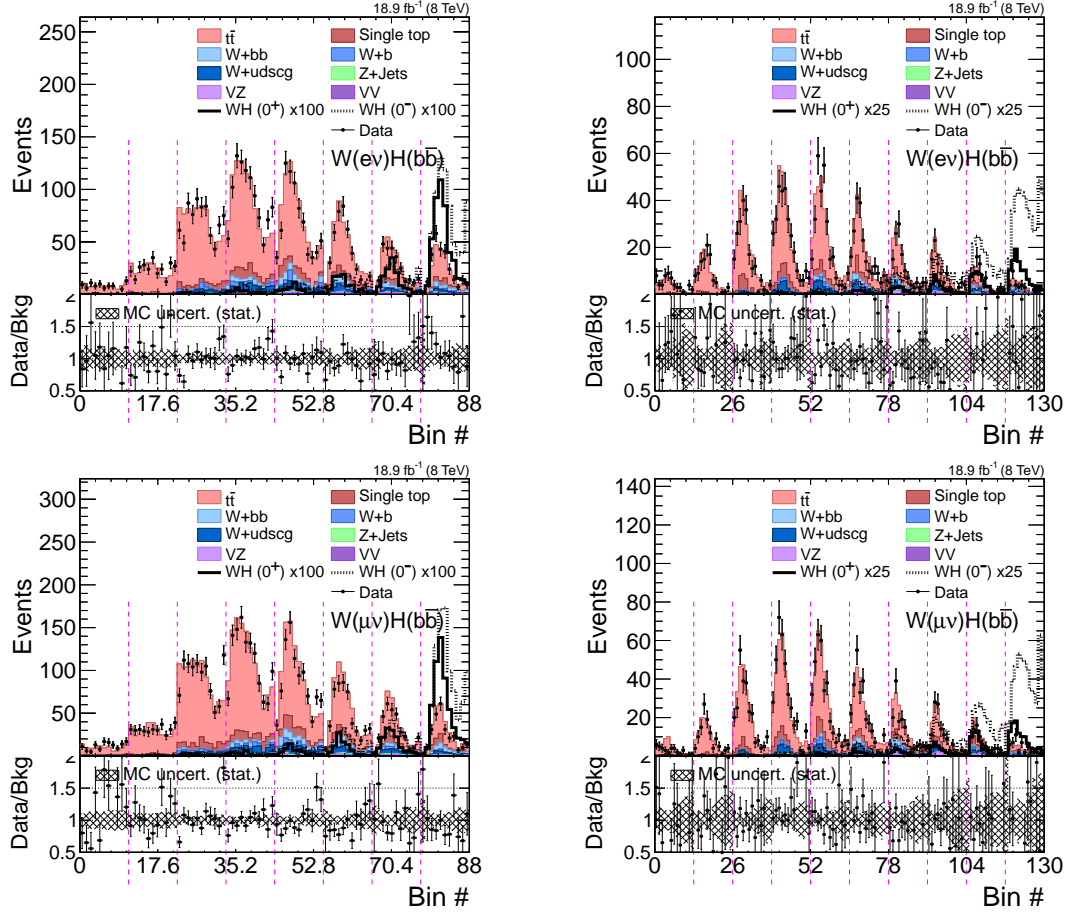


Figure A.2.13: Unrolled 2D templates in the WH channel. The top (bottom) row shows the electron (muon) channel. The left (right) column shows the medium (high) boost region.

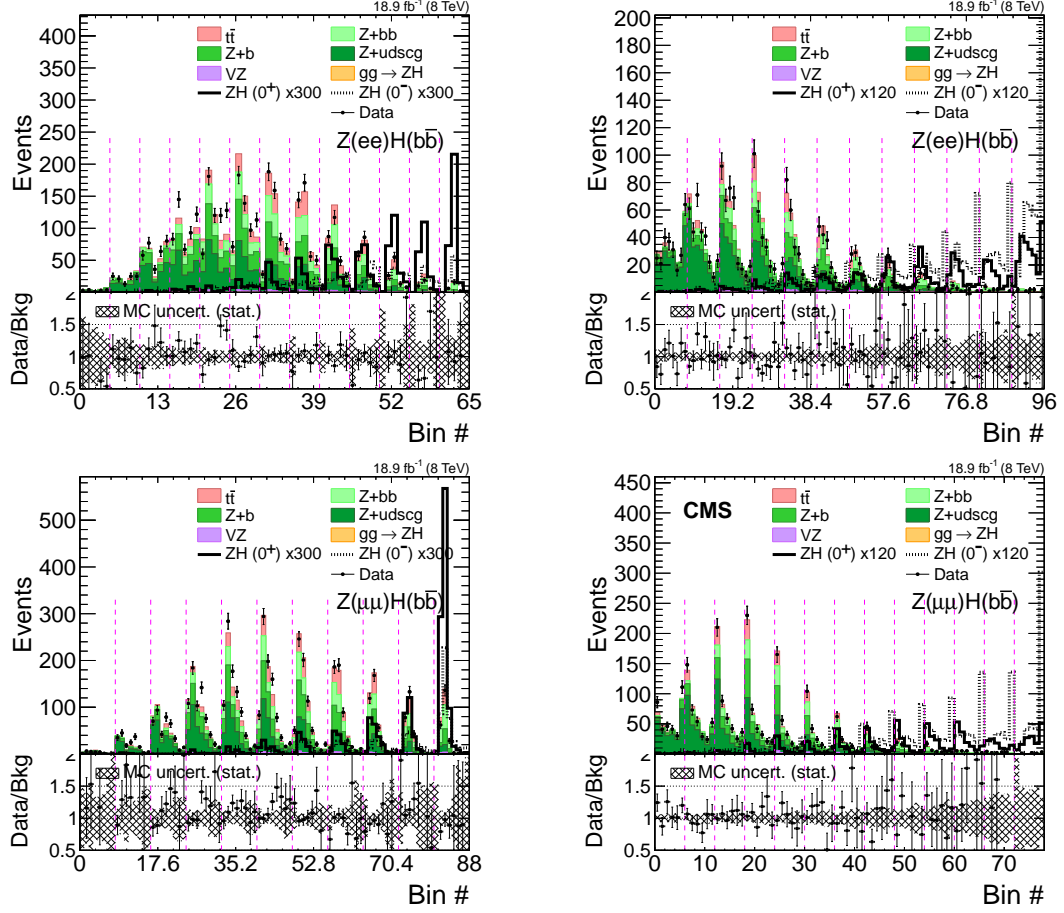


Figure A.2.14: Unrolled 2D templates in the ZH channel. The top (bottom) row shows the electron (muon) channel. The left (right) column shows the medium (high) boost region.

A.3 Template Binning and Statistical Uncertainty

In order to avoid numerical issues in Combine, we choose variable width bins for the background and signal templates such that all bins are populated with non-zero background expectation. By ensuring that all bins are populated by background, we ensure all bins in all potential hypotheses (background-only, 0^+ , 0^-) are populated.

We begin with uniform binning in both template dimensions, as shown in the left side of Fig. A.3.1. We then find a rectangular area that satisfies three conditions:

- All bins within the rectangle are populated by background

- All columns of bins above and below the rectangle must contain some background expectation
- All rows of bins to the left and right of the rectangle must contain some background expectation

We then merge bins in each row (column) to the left/right (above/below) the rectangle. If only a subset of bins in all rows/columns must be merged in order to ensure non-zero background, this is preferred over merging the entire row/column, as can be seen in the double-width column just to the right of the rectangle in Fig. A.3.1. The bins inside the rectangle are left as is. This ensures all bins are populated by background. The resulting rebinned histogram is shown in the right side of Fig. A.3.1.

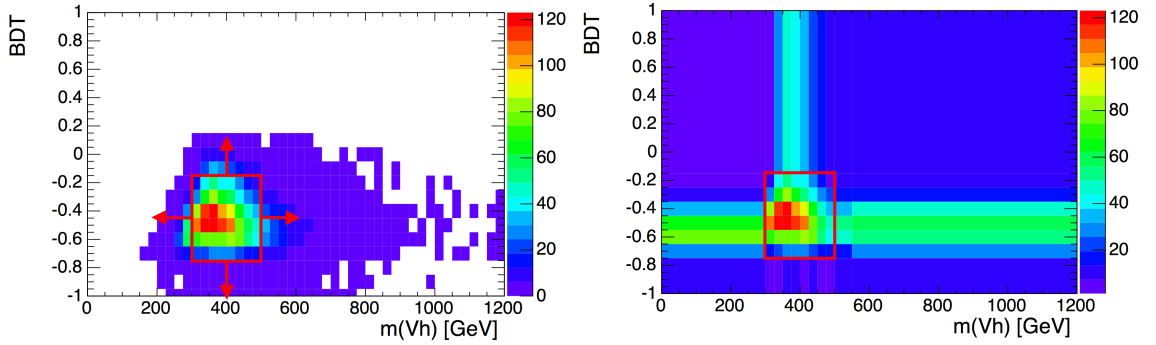


Figure A.3.1: Total background distribution in the medium boost $W \rightarrow e\nu$ channel, before (left) and after (right) rebinning in order to ensure non-zero background expectation in every bin.

After this procedure, some bins contain significant statistical uncertainty. For all bins where either 0^+ or 0^- signals represent at least 2.5% of the total background expectation, a statistical nuisance is included for every background or signal template which possess a relative statistical uncertainty greater than 15% AND greater than 7% statistical uncertainty relative to the total background expectation. These nuisance parameters are uncorrelated relative to one another.

A.4 Fit Validation

In order to validate the profile likelihood fits used in the f_{a3} scans, we created data templates with signal injected for various values of f_{a3} . We then performed observed scans with these templates. The results are shown in Fig. A.4.1. As seen from the fit results, we get a minimum at the injected f_{a3} value; thus the fits show no bias.

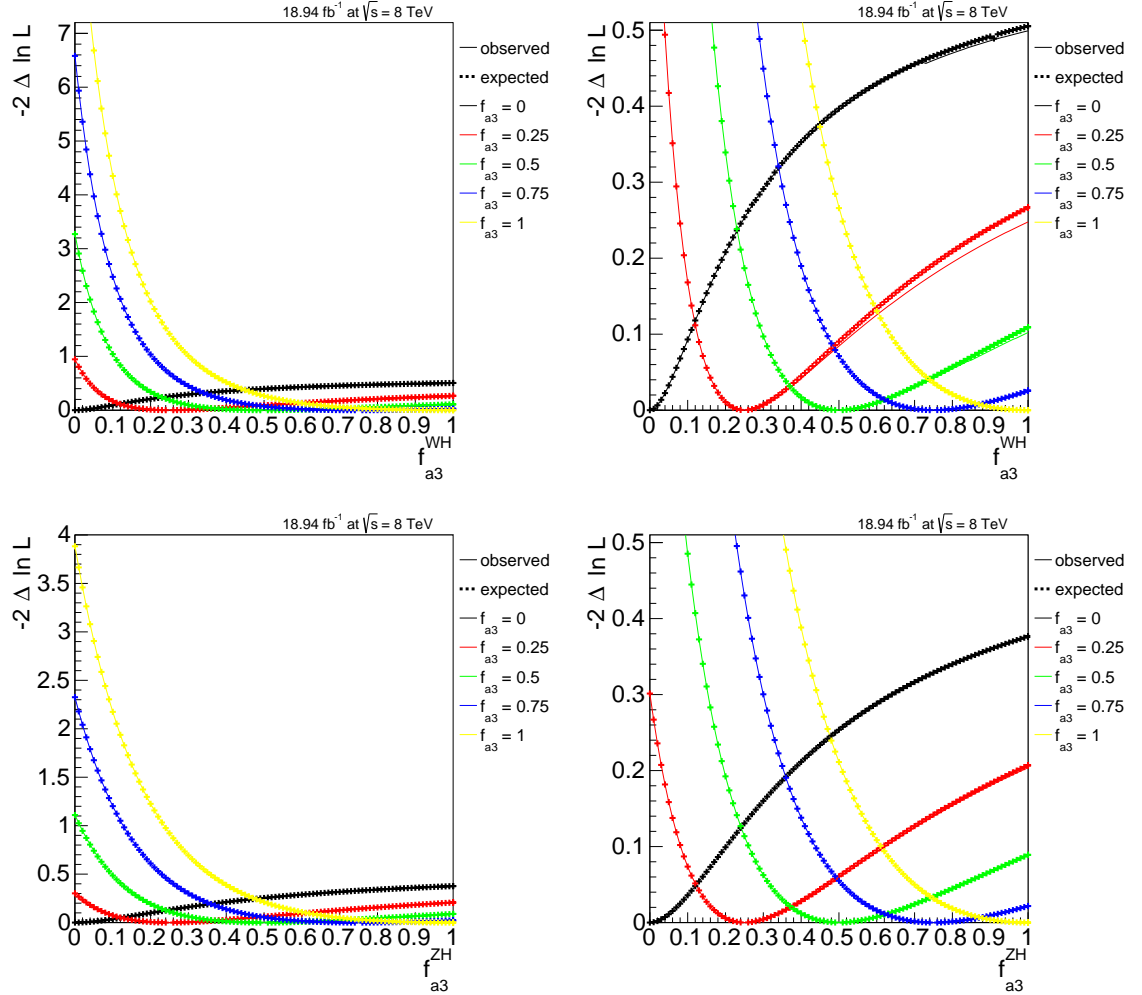


Figure A.4.1: Results of observed scans to data with signal injected at various values of f_{a3} . The top (bottom) left plot shows the results from WH (ZH) channel only. A zoom into the y-axis is also shown on the right.

A.5 Background Modeling Crosscheck

We show here $m(\text{VH})$ plots in the signal region with a cut on the value of the BDT discriminant to enhance ($\text{BDT} > -0.3$) or suppress ($\text{BDT} < -0.3$) the signal. The signal-depleted plots are shown in Figs. A.5.1 and A.5.3. The signal-enriched plots are shown in Figs. A.5.2 and A.5.4. We also show linear fits to the $m(\text{VH})$ data/background distributions with $\text{BDT} < -0.3$ in Fig. A.5.5. No sign of background mismodeling is observed in the high boost signal-depleted plots, where the overwhelming bulk of the sensitivity is obtained. A nuisance parameter is added to the physics model which allows for a linear correction of the background templates in accord with the fitted ratios in each SR.

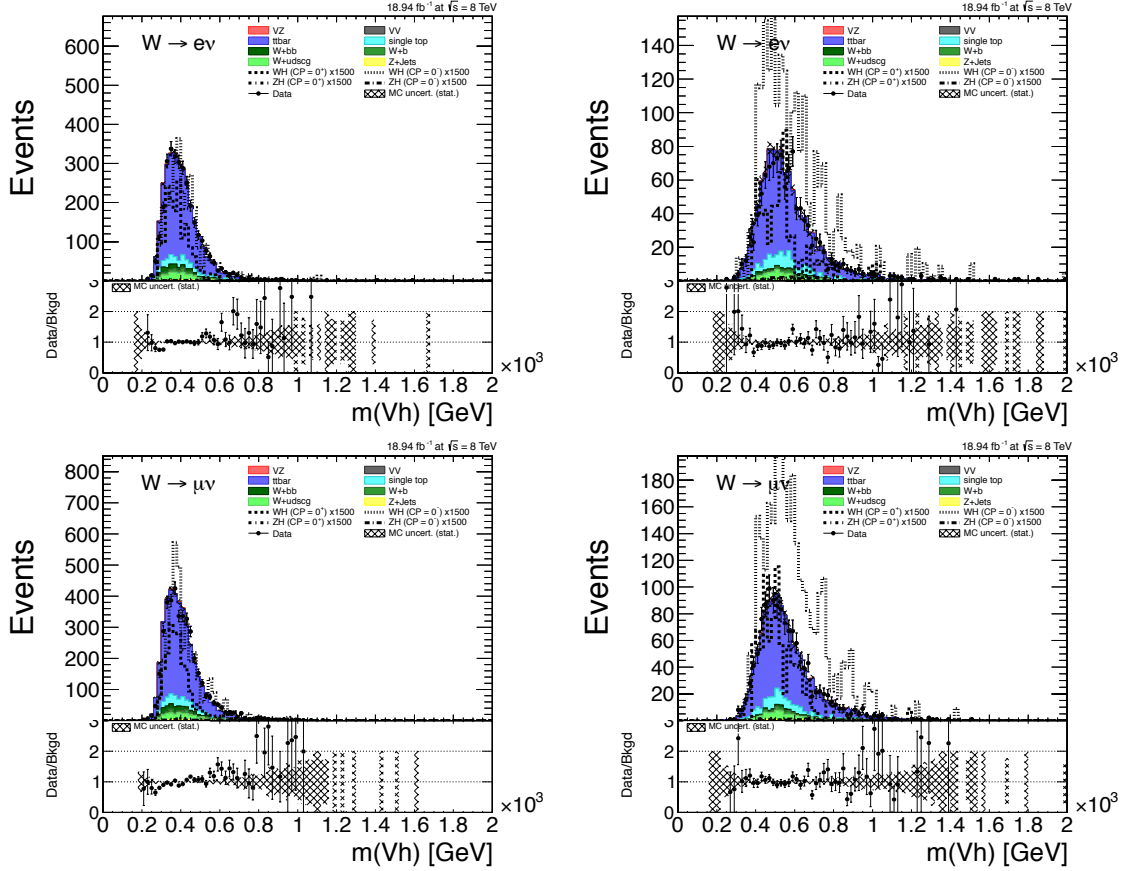


Figure A.5.1: The $m(VH)$ distribution in the WH signal regions, with the requirement that the BDT discriminant is smaller than -0.3. The top (bottom) row shows the electron (muon) channel. The left (right) column shows the medium (high) boost region.

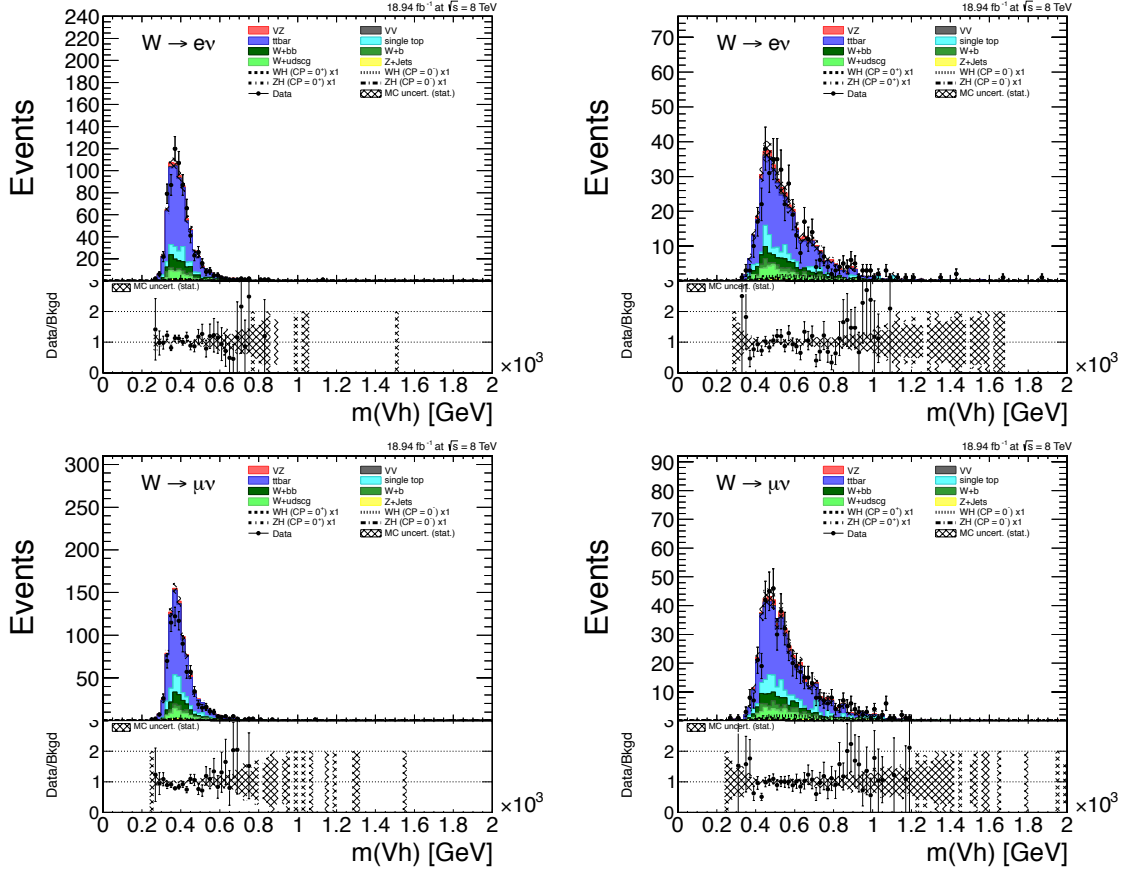


Figure A.5.2: The $m(VH)$ distribution in the WH signal regions, with the requirement that the BDT discriminant is greater than -0.3. The top (bottom) row shows the electron (muon) channel. The left (right) column shows the medium (high) boost region.

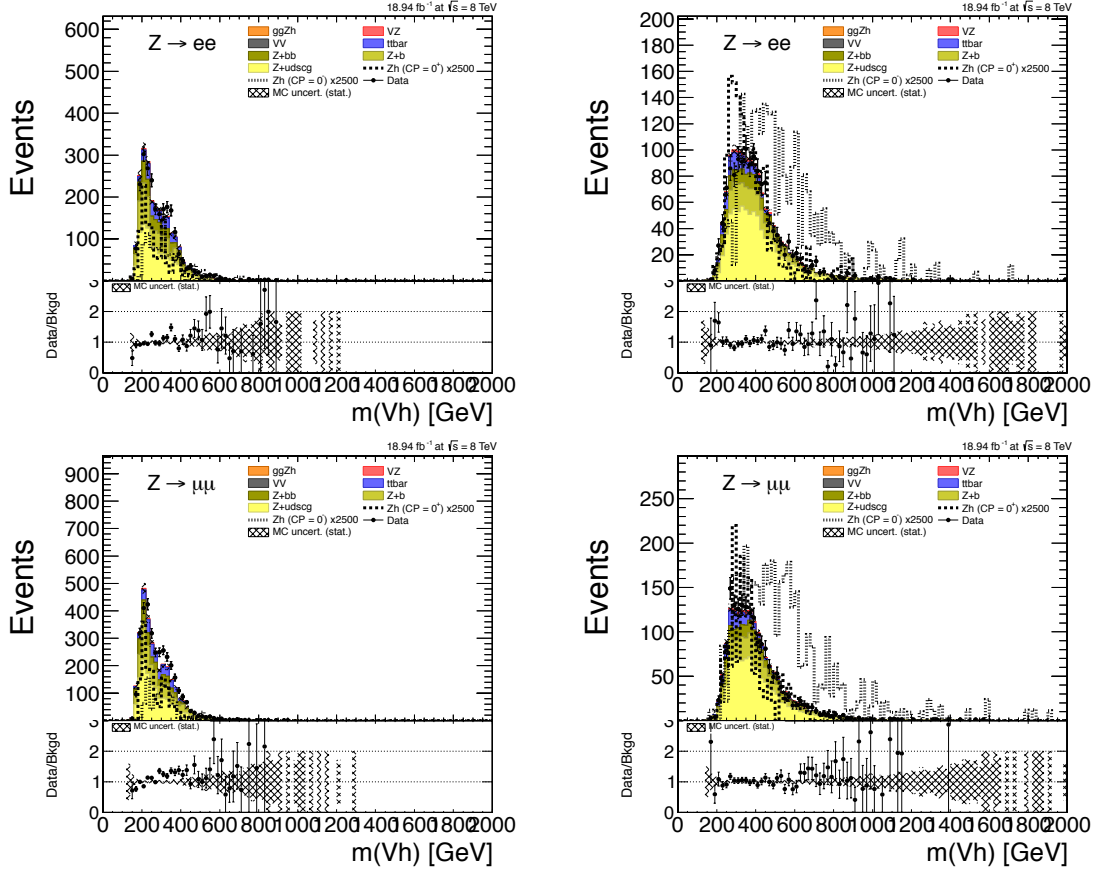
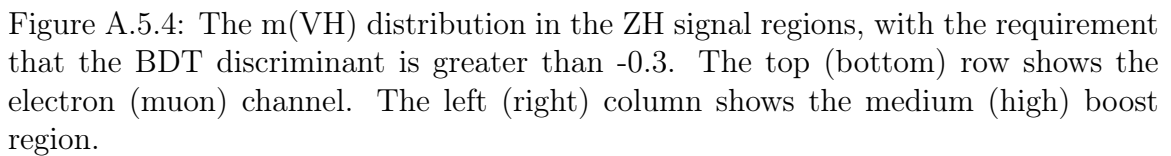


Figure A.5.3: The $m(VH)$ distribution in the ZH signal regions, with the requirement that the BDT discriminant is smaller than -0.3. The top (bottom) row shows the electron (muon) channel. The left (right) column shows the medium (high) boost region.



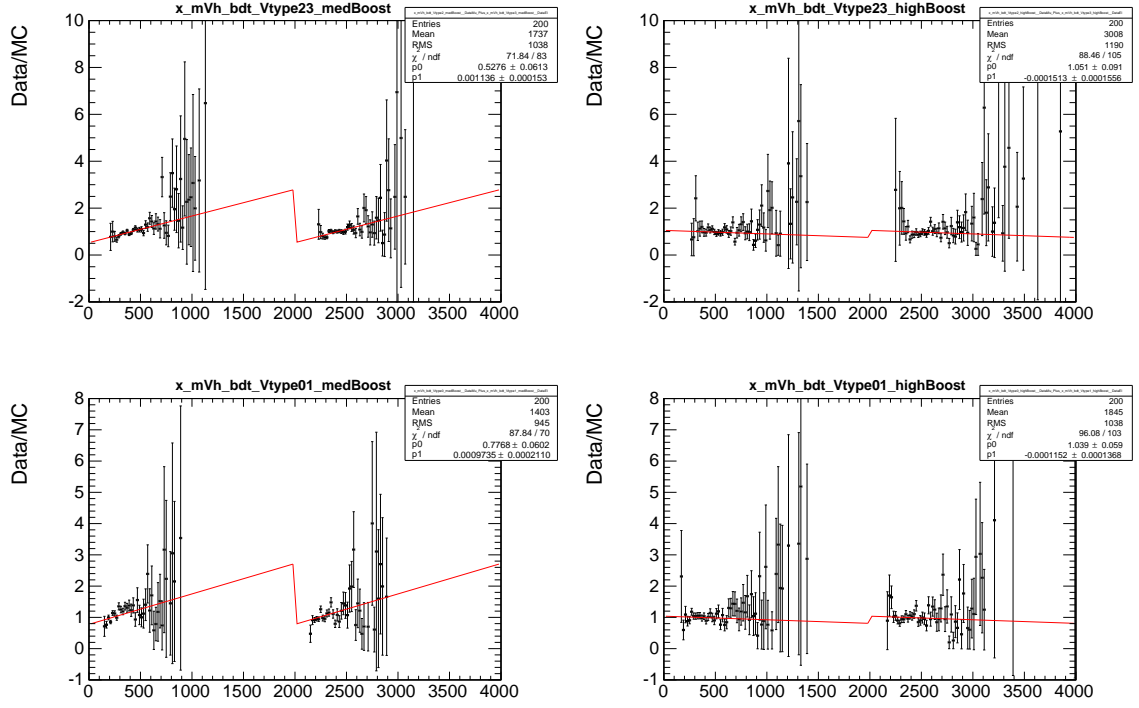


Figure A.5.5: Simultaneous fits to the $m(\text{VH})$ data/background ratio across the electron and muon channels, in the medium (left) and high (right) boost signal regions with $\text{BDT} < -0.3$. The top plots show the WH channel, while the bottom plots show the ZH channel. The left (right) half of each plot shows the data/background ratio vs $m(\text{VH})$ from 0 to 2 TeV in the muon (electron) channel. A nuisance parameter is added to the physics model which allows for a linear correction of the background templates in accord with the fitted ratios in each SR.